# ANISOTROPIC MORPHOLOGIES AND PROPERTIES IN PERFLUOROSULFONATE IONOMER-BASED MATERIALS

Jong Keun Park

Dissertation submitted to the faculty of the Virginia Polytechnic Institute and State University in partial fulfillment of the requirements for the degree of

DOCTOR OF PHILOSOPHY
in
Macromolecular Science and Engineering

Robert B. Moore, chairman
Timothy E. Long
Judy S. Riffle
Kenneth A. Mauritz
S. Richard Turner

December 09, 2009
Blacksburg, Virginia

Keywords: perfluorosulfonate ionomers, Nafion®, anisotropic morphology, proton exchange membrane, orientation, crystallinity, uniaxial stretching, electroactive polymer, ionic polymer-metal composite (IPMC)

# ABSTRACT

# ANISOTROPIC MORPHOLOGIES AND PROPERTIES IN PERFLUOROSULFONATE IONOMER-BASED MATERIALS

Jong Keun Park

The overall goal of this investigation was to elucidate specific structure-property relationships in perfluorosulfonate ionomers (PFSIs)-related materials. The project can be broken into two primary foci. First, we explored the current state of understanding related to morphology-property relationships in PFSIs with specific attention to the nano-scale organization of the ionic and crystalline domains. Specifically, the effect of uniaxial orientation on the structure and transport properties of Nafion® membranes was examined. Small angle X-ray scattering (SAXS) experiments on dry membranes that were uniaxially elongated showed a strong anisotropic morphology which was shown to persist over the swelling process without a significant relaxation. Herman's order parameters for the ionomer peak were strongly influenced by uniaxial deformation, which supports the presence of cylindrical rather than spherical morphology for ionic domains. Comparison of the water diffusion coefficients between unoriented and oriented samples revealed that uniaxial deformation of Nafion® membranes essentially enhances transport ability in one direction (i.e., the parallel to draw direction) and suppresses in the other two directions (i.e., two orthogonal directions relative to the stretching direction). Based on 1-dimensional analyses of oriented SAXS patterns at the azimuthal angle $90^{o}$, three recent models (lamellar model, semicrystalline rod-like model and fringed-micelle model) for the morphology of PFSIs were critically evaluated. The loss of meridional scattering, different orientation behavior of the crystalline and ionic domains, and inherent chain stiffness

precludes the possibility of a chain-folded lamellar morphology. While the inter-aggregate dimensions remain constant at high draw ratios, the inter-crystalline spacings decrease significantly. Coupled with the distinctly different orientation behavior, these observations preclude the existence of crystallites solely within rod-like aggregates. While the worm-like ionic channel model was able to explain the behavior of SAXS and wide angle X-ray scattering (WAXS) relatively well, this model also had limitations such as (1) crystalline domains directly linked to the ionic domain (and thus a lack of amorphous domains) and (2) a presence of only a single ionic channel between two neighboring crystallites.

Second, electroactive materials, specifically ionic polymer-metal composites (IPMCs) that undergo bending motions with the stimulus of a relatively weak electric field were fabricated. To understand the role of the nanoscale morphology of the membrane matrix in affecting the actuation behavior of IPMC systems, we evaluated actuation performance of IPMCs subjected to uniaxial orientation. The PFSI nanostructure altered by uniaxial orientation mimicked the fibrillar structure of biological muscle tissue and yielded a new anisotropic actuation response. It was evident that IPMCs cut from films oriented *perpendicular* to the draw direction yielded displacement values that were significantly *greater* than that of unoriented IPMCs. In contrast, IPMCs cut from films oriented *parallel* to the draw direction appeared to resist bending and yield displacement values that were *much less* than that of the unoriented IPMC. This anisotropic actuation behavior was attributed to the contribution of the nanoscale morphology to the bulk bending modulus. Overall, this study clearly demonstrated, for the first time, the importance of the nanoscale morphology in affecting/controlling the actuation behavior in IPMC systems.

## ACKNOWLEDGEMENTS

First of all, I would like to express my gratitude to my esteemed research advisor, Dr. Robert B. Moore, for his unflagging encouragement, guidance, and also friendship throughout my entire graduate studies at both the University of Southern Mississippi (USM) and Virginia Tech (VT). This dissertation would not have been possible without his expert support. I would also like to thank all of the members of the Moore Research Group of the past (Shawn Osborn, Kirt Page, Bret Calhoun, Robert Bourne, and Ju-Myung Song) and the present (Sonya Benson, Gilles Divoux, Angela Osborn, Ninad Dixit, Scott Forbey, and Bing Yan) for their assistance and support during my graduate school.

I wish to thank my committee members at USM (Drs. Kenneth Mauritz, Sergei Nazarenko, Marek Urban, and Charles Hoyle) and at VT (Drs. Kenneth Mauritz, Timothy Long, Judy Riffle, and Richard Turner) for their valuable guidance and discussions. In particular, I would like to thank the staff members, Dr. William Jarrett, Jim Bridges, Steve Selph, and Laura Fosselman at USM and Tammy Jo Hiner, Mary Jane Smith, Carla Slebodnick, and John Burleson for their invaluable assistance.

I also gratefully acknowledge all the institutional support that I have received throughout my entire graduate careers. I thank the Department of Polymer Science at USM for supporting me with generous fellowships and also for a tremendous and rigorous 1$^{st}$ year graduate education. I also thank the National Science Foundation for the support that I received while working on this project. I would also like to extend my special thanks to the following national labs, NIST Center for Neutron Research (NCNR), Advanced Photon Source (APS) in Argonne National Laboratory, National Synchrotron Light Source (NSLS) in Brookhaven National Laboratory, and

Pohang Accelerator Laboratory (PAL) in South Korea for giving me the opportunities to visit their facilities and conduct numerous experiments during my graduate school.

Finally, I want to thank my parents (Dong Gue Park, and Duk Soon Cha), my sister (Mi Ra Park) and brother (Jong Hyun Park) for their support and encouragement. I most want to thank my wife, Min Oh Lim, for her love, sacrifice, thoughtfulness, and kind indulgence.

## TABLE OF CONTENTS

## LIST OF FIGURES

## LIST OF TABLES

## LIST OF EQUATIONS

# CHAPTER I

# SCIENTIFIC BACKGROUND: PERFLUOROSULFONATE IONOMERS

## A. Introduction

Perfluorosulfonate ionomers (PFSIs) have attracted a great attention over the past several decades due to their extensive applications ranging from chlor-alkali cells[1], water electrolyzers[2], batteries[3], fuel cells[4,5] to artificial muscles[6]. Their excellent chemical and thermal stability, as well as permselective ion transport are attributed to the chemical architecture of PFSIs which, in general, is characterized by polytetrafluoroethylene (PTFE) backbone segments and randomly distributed perfluoroether side chains bearing sulfonate groups. Nafion® (Figure I-1a), being the first perfluorinated ionomer, was developed and produced by E. I. DuPont de Nemours and Company.[7] Dow Chemical also developed a perfluorinated ionomer with a similar chemical structure to Nafion®, but with a much shorter side chain length.[8,9] This PFSI is now commercially available from Solvay Solexis under the trade name of Hyflon Ion® (Figure I-1b). Most recently, 3M has introduced a perfluorinated ionomer (Figure I-1c) with an intermediate side chain length between Nafion® and the Hyflon Ion®.[10] The presence of PTFE segments renders these materials semicrystalline character while the pendant groups containing the sulfonate moieties tend to phase separate from the PTFE matrix into microdomains (i.e. ionic aggregates).[5] It should be pointed out that the size and chemical nature of the sulfonate terminated pendant group strongly influence the crystallization behavior of the PTFE backbone and also ionic aggregation.[11,12] Nafion®, being the benchmark material in the chlor-alkali industry, fuel cells, and artificial muscles, will be the focus of the current review and later experimental parts.

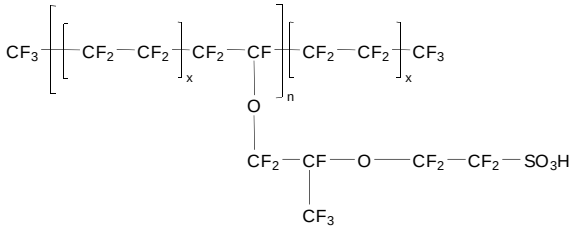

**a) Nafion®**

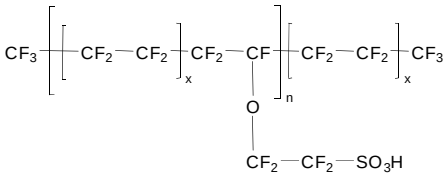

**b) Hyflon Ion®**

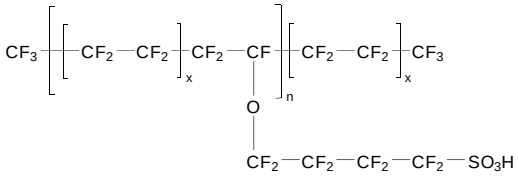

**c) 3M Ionomer**

**Figure I-1**. Structure of (a) Nafion®, (b) Hyflon Ion®, and (c) 3M ionomer

## B. Synthesis and Processing of PFSIs

Synthesis of the long-chain perfluorinated ionomer, Nafion® will be described in this chapter. To synthesize Nafion®, tetrafluoroethylene (TFE) is first reacted with sulfur trioxide ($SO_3$), creating a cyclic sulfone.[4,13] Rearrangement of the sulfone followed by reaction with hexafluoropropylene epoxide produce sulfonylfluoride adducts. Upon heating in the presence of sodium carbonate ($Na_2CO_3$), these adducts give a sulfonylfluoride vinylether. Subsequent copolymerization of this vinylether and TFE is typically carried out in perfluorocarbon solvents using perfluorinated free radical initiators such as perfluoroperoxides to form the high molecular weight resin. After polymerization, copolymer of TFE and fluorinated vinyl ether can be melt-processed into various forms, such as sheets or tubes, by standard methods, prior to hydrolysis to the ionomer.[5] A recipe for hydrolysis of the sulfonyl fluoride form after melt-processing involves a solution of 15 wt % KOH, 35 wt % dimethylsulfoxide (DMSO), and 50 wt %

deionized water (DI) at 80 $^{o}$C for 30 min or longer depending on membrane or pellet thickness.[4,14]

More recently, due to the necessity for thin membranes in modern proton exchange membrane fuel cell (PEMFC) applications, the current industrial membrane processing procedures have shifted from high-temperature melt extrusion to relatively low-temperature dispersion-casting method.[15] The dispersion-casting procedure involves applying the polymer dispersion onto a supporting film, drying both materials, applying a cover-sheet, and winding onto a master roll. While the new dispersion-casting membranes exhibited several crucial advantages such as (1) less contamination, (2) increased overall production rates and (3) improved thickness control and uniformity when compared to their extruded counterparts, it has been reported that these new membranes exhibit physical properties that are significantly different from the old extruded membranes.[15] For example, new, dispersion-cast Nafion® NRE212CS undergoes disintegration in boiling methanol, however as-received, extruded Nafion® remains in tack in boiling methanol even after several hours.[16]

### C. Models for the Morphology of Nafion®

The PFSI, particularly Nafion®, is a copolymer of tetrafluoroethylene and generally less than 15 mol % of perfluorovinylether units terminated with sulfonic acid functionalities.[5] With a sufficient length of polytetrafluoroethylene (PTFE) segments between side chains, Nafion® can organize into crystalline domains having the unit cell dimensions essentially identical to that of pure PTFE.[17] The degree of crystallinity in Nafion® has been shown to vary with equivalent weight (EW, the grams of dry polymer per equivalent of sulfonic acid units) with generally less than ca. 10 wt % in 1100 equivalent weight of Nafion®.[18,19] Greater efforts, however, have been

given to the unique nanophase-separated morphology observed upon aggregation of the polar, ionic side chains within the matrix of hydrophobic PTFE.[20-22] These ionic clusters, and specifically their shape, order, spatial distribution and connectivity, precisely define the supramolecular organization and function of this technologically important material as an ionic conductor.[23,24]

Numerous investigations were focused on characterizing the complex, nanophase-separated morphology, which has amorphous, crystalline and ionic domains, by employing mostly small-angle scattering of X-ray (SAXS) and neutron (SANS) techniques.[5,17,19-21,25-36] Specifically, there is a scattering maximum (often called the ionomer peak) appearing in SAXS/SANS profiles of this material at ca. $q$ = 0.2 Å$^{-1}$ which corresponds to a Bragg spacing of ca. 50Å.[5] This scattering maximum has been attributed to scattering from the ionic aggregates dispersed in the PTFE matrix. Numerous structural models have been proposed to account for the origin of the ionomer peak.

**(1) Cluster-network model**

In the early 1980's, Hsu and Gierke contemplated the most extensively referenced cluster-network model for perfluorinated ionomers based on small-angle X-ray scattering (SAXS) and transport studies.[19,22] The model proposes that hydrophilic ionic groups are phase-separated from the hydrophobic fluorocarbon matrix to form nearly spherical domains, essentially an inverted micelle-type structure. These spherical ionic aggregates were proposed to spatially locate on a paracrystalline cubic lattice and the SAXS maximum in Nafion® was attributed to inter-particle correlation between the neighboring aggregates. To reconcile the permselective transport properties of water-swollen Nafion®, Gierke et al. also proposed narrow (1 nm), sulfonate group-lined channels connecting the adjacent aggregates. (Figure I-2) The

channels serve to create a connected network of aggregates giving rise to percolation pathways across the membrane.

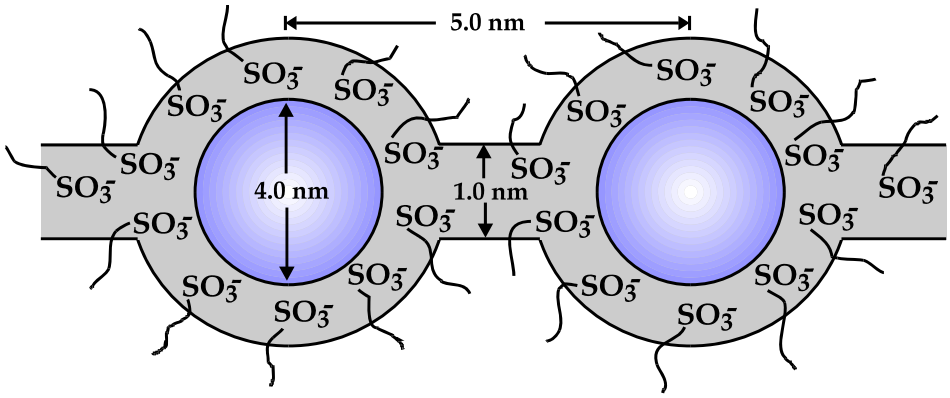


**Figure I-2.** Cluster-network model by Gierke et al. (Reprinted with permission from ref[22] *Journal of Membrane Science*, **13**, 307 (1983). Copyright 1983, Elsevier.)

Based on simple space-filling consideration, the authors also calculated the cluster diameter, the number of sulfonate sites per cluster, and the number of water molecules per cluster as a function of water content, equivalent weight (EW) and cation form.[19] It turned out that for 1200 EW $Na^+$-form Nafion®, the cluster diameter, the exchange sites per cluster, and the number of water molecules per exchange site increased linearly with increasing water content. The model also proposed the possibility of slight morphological reorganization during solvent swelling. Upon hydration, the ionic domains became larger, but this growth was accompanied by a redistribution of the ionic sulfonate groups, which led to fewer clusters in the fully hydrated Nafion®. This study also showed that with increasing equivalent weight (EW), the cluster diameter, number of ion exchange sites per cluster and water per exchange site all decreased. They attributed this trend to the higher crystallinity and greater polymer stiffness with increasing EW, which would hinder formation of ionic clusters. Lastly, effects of neutralizing cations ($H^+$, $Li^+$, $Na^+$, $K^+$, $Rb^+$, and $Cs^+$) on cluster morphology in 1200 EW Nafion® were investigated. With increasing cation weight, the cluster diameter and water per exchange site decreased while the

number of exchange sites per cluster increased. This behavior was explained by less hydrophilicity of the heavier cations which would bind more tightly to the sulfonate exchange sites.

**(2) Local order model**

The local-order model, first proposed by Dreyfus et al., is another model relying on inter-particle scattering to define the spatial distribution of spherical ionic aggregates in Nafion®.[21] The local environment around a given aggregate is proposed to have a tetrahedral symmetry, 4 aggregates located at a distance D. The model predicts a liquid-like distribution of aggregates at distances greater than αD from the original aggregate, where $\alpha > 1$. The model was found to satisfactorily reproduce the SANS profiles of Nafion® membranes ranging from dry material to a water volume fraction of 0.26. Gebel and Lambard later employed the local order model to fit the scattering profiles of water swollen Nafion® membranes finding good agreement between experiment and model at a water volume fraction of 0.29.[37] Incorporation of a Debye-Bueche correlation length of 80 Å enabled the model to fit both the ionomer peak and the small angle upturn.

**(3) Lamellar model**

By reevaluating previous SAXS results[19] obtained during swelling and deswelling experiments, Litt proposed the lamellar model (Figure I-3) as the Nafion® morphology instead of the Cluster-Network model by Gierke.[26] Litt pointed out that a structural reorganization of spherical ionic clusters required to explain a linear relationship between SAXS peak position and water contents implies an inevitable restructuring of the matrix, too, which is not a simple process. In this model, the low angle scattering maximum (i.e., the ionomer peak) is attributed to

the correlation between thin, lamellar PTFE-like crystallites separated by hydrophilic ionic clusters that are planar and locally parallel. Simple absorption of water into hydrophilic domains separates the lamellae and thus increasing the *d*-spacing. The overall swelling is restricted by the tie molecules that interconnect the lamellae. The amorphous, tie chains become extended, assuming a high energy conformation as the polymer swells, exerting a retractile force to restore the dry state structure. Due to the presence of these tie chains between lamellae, swelling and deswelling should be completely reversible, without undergoing any major reorganization of the ionic clusters and the matrix. While this simple structural model is able to describe the swelling and deswelling behaviors of Nafion® on a nanometer scale, the recent solid state NMR work by Schmidt-Rohr[38] indicated that backbone chains in Nafion® are quite stiff in nature, and thus a chain-folding phenomenon required to make a lamellar-type crystal is difficult to expect.[20] More importantly, this model fails to explain another scattering maximum typically observed in SAXS and SANS profiles at ca. 0.05 $Å^{-1}$, which is attributed to the correlation between crystalline domains.[5]

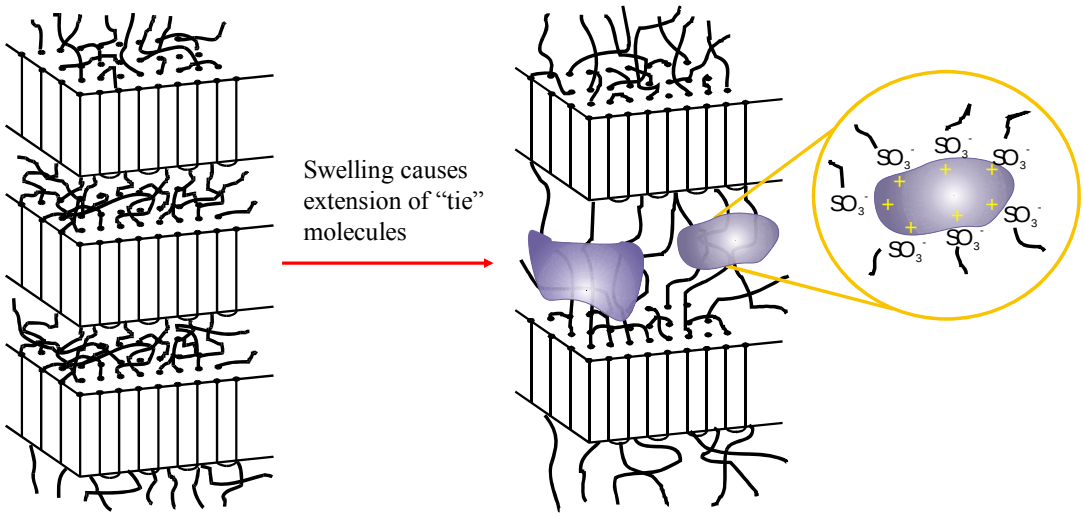


**Figure I-3.** Lamellar model for Nafion® proposed by Litt[26]

**(4) Sandwich-like model**

Based on synchrotron SAXS experiments on Nafion® membranes swollen with water and methanol, Haubold et al. proposed a slightly modified version of the lamellar model, where the basic structural element was proposed to be a "sandwich" geometry, as shown in Figure I-4.[29] The outer part (the "shell") of the sandwich is consisted of side chains along with sulfonate groups while the inner part (the "core") of the sandwich is filled with swelling solvents, water-methanol. In this model, percolation pathways through which protons and water molecules may travel are provided by arranging the structural elements to be juxtaposed in a linear fashion such that the solvent-containing cores form a continuous channel. The authors also fitted the obtained SAXS results using the particle structure factor for a rectangular parallelepiped to obtain meaningful structural information, such as core thickness (*c*), total shell thickness (*s*) and lateral dimensions (*a* and *b*) of the parallelepiped. Based on the model fits, the basic structure element was found to have lateral dimensions *a* and *b* between the values of 15 and 45 Å, and the combined thickness of the sandwich, $c + s$, was about 60 Å. Furthermore, fitted values of *s*, *c, a,* and *b* were shown to depend strongly on the volume percent of methanol in water. It is interesting to note that increasing methanol content led to smaller core thickness while it caused side-chains in the shell region to extend significantly. While the sandwich model is able to describe the swelling behavior of Nafion® on a nanometer scale, it is a rather local structure and fails to describe another important structural parameter, PTFE-like crystals.

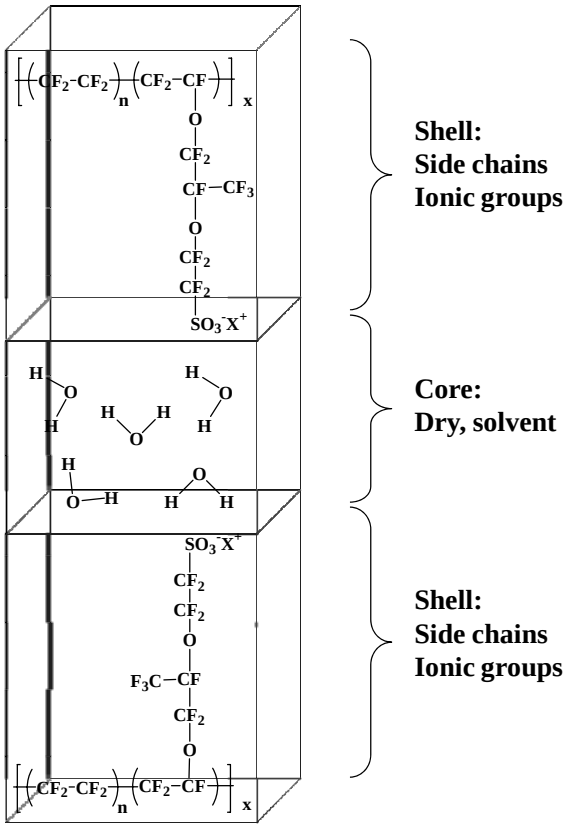


**Figure I-4.** Sandwich-like model proposed by Haubold et al. (Reprinted with permission from ref[29] *Electrochimica Acta*, **46**, 1559 (2001). Copyright 2001, Elsevier)

## (5) Structural Evolution Model

Along with SAXS/SANS results and conductivity measurements, Gebel proposed the evolution of PFSI structure from the complete dry state through the water-swollen state to ultimate dissolution state.[28] Inspired by previous investigations which evidenced the presence of rod-like structure in PFSI solution,[39,40] the overall objective of this study was to picture continuous morphological transition that Nafion® membranes would undergo from the completely dry state to final dissolution state. The structural evolution of Nafion® morphology as a function of water content is illustrated in Figure I-5. In the dry state, Nafion® morphology is

characterized by isolated, spherical ionic aggregates with a diameter of ca. 15 Å and an average inter-aggregate distance of ca. 27 Å. Upon hydration (with a water volume fraction lower than $\Phi_w$ = 0.2), spherical ionic aggregates swell encasing pools of water with ionic functionalities segregated to the polymer-water interface minimizing interfacial energy. At low water content, the water pool diameter is close to 20 Å while the inter-ionic aggregate distance is ca. 30 Å and the extremely low conductivity values indicated that they are still isolated clusters. With a water volume fraction increasing to ca. $\Phi_w$ = 0.2, the percolation pathways were developed in the membrane as indicated by the large increase of the ionic conductivity. At this level of hydration, the Nafion® morphology corresponds to spherical ionic domains connected with water-filled cylinders dispersed within the PTFE matrix which is reminiscent of the Cluster-Network model by Gierke et al.[19] As $\Phi_w$ increases above 0.5, an inversion of the structure was suggested such that the membrane structure appears as a network of interconnected rods dispersed in water. Ultimately, as the membrane dissolves into solution, the interconnected rod-like ionic aggregates become separated to yield a colloidal dispersion of isolated rods (with a radius of 25 Å).

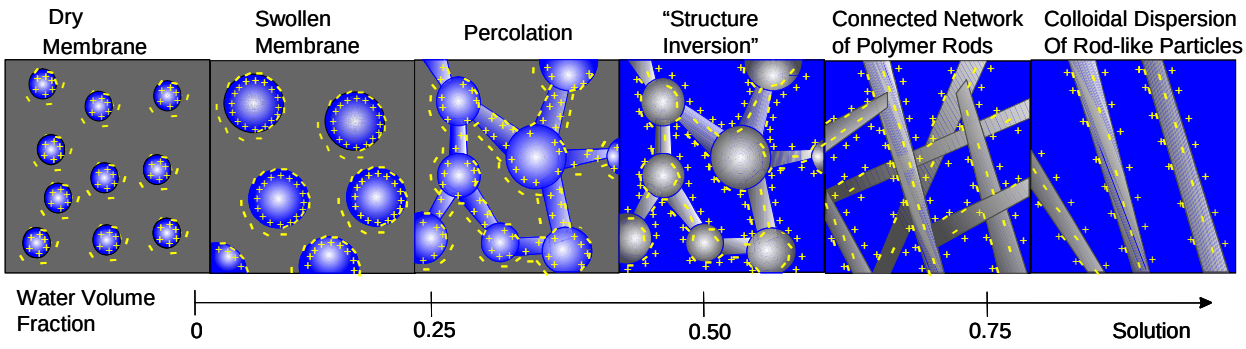


**Figure I-5.** Structure evolution of Nafion® morphology from dry membrane to dissolution state proposed by Gebel. (Reprinted with permission from ref[28] *Polymer*, **41**, 5829 (2000). Copyright 2000, Elsevier)

**(6) Elongated Polymer Aggregate Model**

Rubatat et al. used small-angle X-ray and neutron scattering and ultra small-angle X-ray scattering (USAXS) techniques to probe the structure of water-swollen Nafion® membranes over the length scale ranging from 10 to 10000 Å.[31,41] Combined USAXS and SAXS results showed (1) the extended small-angle upturn behavior which is attributed to long-range heterogeneities in electron density, (2) the low angle scattering maximum attributed to supralamellar dimensions of the crystalline domains, and (3) the ionomer peak attributed to inter-ionic aggregate correlation. Closer examination of the scattering profile also revealed that there are two distinct regimes of decreasing intensity, a $q^{-1}$ power law at low angles and a $q^{-4}$ power law at high angles. While the high angle behavior ($q^{-4}$ power law decay) is characteristic of a sharp interface between scattering particle and matrix,[42] the low angle behavior ($q^{-1}$ power law decay) is usually modeled as the scattering from elongated, rod-like objects.[42] Based on the observed $q^{-1}$ regime between $10^{-3}$ and $5 \times 10^{-1}$ Å$^{-1}$, a length (L) and a diameter (D) of the rod-like aggregate were estimated to be D ≈ 60 Å, and L ≥ 1000 Å.[31]

SAXS profiles were also acquired on water-swollen Nafion® membranes with a polymer volume fraction ($\Phi_p$) varying between 0.95 and 0.15. It was obvious that the $q$-positions of the crystalline and ionic peaks were systematically shifted to lower $q$ region as the polymer volume fraction decreased. It was pointed out that the general features of the scattering profiles were essentially the same for all samples, which supported the assumption that the swelling process simply involves a dilution of the scattering entities without inducing a strong structural reorganization of the ionic cluster morphology unlike it was suggested by Gebel.[28] The authors also plotted the characteristic (Bragg) distances, $2\pi/q^*$, corresponding to the ionomer and crystalline peaks as a function of polymer volume fractions, and noticed two microscopic

swelling regimes which agrees well with Gebel's work.[28] For polymer volume fraction ($\Phi_p$) lower than 0.6, the ionomer peak position followed a power law in $\Phi^{-0.5}$ suggesting a dilution of cylindrical shaped particles. For polymer volume fractions ($\Phi_p$) higher than 0.6, the ionomer peak position was observed to follow a power law close to $\Phi^{-1.0}$ in agreement with the previous investigations.[17,25,26]

According to examination of the very small-angle upturn profile using a Debye-Bueche analysis, it was proposed that the correlation length on the 800 Å scale corresponded to "bundle" of rod-like particles dispersed through the matrix with random orientation, though particles within the bundle remain oriented.[31,37,41] (Figure I-6) It was further suggested that the rod-like aggregates were composed of relatively aligned backbone chains with pendant sulfonate groups decorating the surface of the cylindrical aggregate.[31]

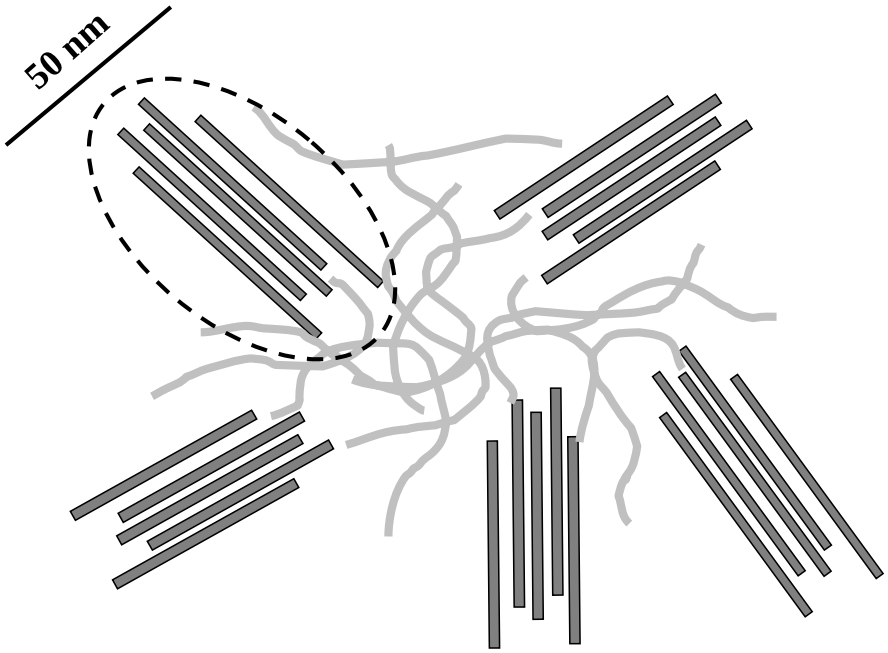


**Figure I-6.** Elongated polymeric aggregate model proposed by Rubatat and coworkers. (Reprinted with permission from ref[41] *Macromolecules*, **37**, 7772 (2004). Copyright 2004, American Chemical Society)

**(7) Worm-like Channel Model**

Following the work by Grenoble group[31,32], Kim *et al*. studied various Nafion® membranes with SANS to evaluate the effects of relative humidity (RH), processing method (melt-extrusion and solution-casting), prehistory and membrane thickness on the nanoscale structure at room temperature.[34] In an agreement with Rubatat et al., thin extruded samples showed an extended I ($q$) ~ $q^{-1}$ power law behavior from ca. 0.008 to 0.1 Å$^{-1}$. Based on this observation, the existence of a local cylindrical structure was postulated and the hydrated ionic clusters in Nafion® were suggested to be worm-like channels as shown in Figure I-7. Although both the elongated rod-like model and Kim's worm-like model are based on the I ($q$) ~ $q^{-1}$ power law observation, the proximity of the crystalline component to the ionic domains differs significantly. Unlike the elongated rod-like model where crystallites remain within the rod-like ionic domains and thus correlation of the crystalline peaks does not lie across the ionic domains, the worm-like model suggests that crystallites are dispersed between rod-like ionic domains and thus correlation of the inter-crystalline peak lies across the ionic domains. Furthermore, Kim et al. went on to discuss the possible structure of the crystalline component in Nafion®. Although no definitive evidence was provided, fringed-micelle-like crystal was preferred over the lamellar-like due to polymerization of crystallizable PTFE segments in a random fashion as opposed to a blocky fashion. Based on a complete random copolymerization, an EW of 1100 would yield a PTFE repeating unit of approximately 6.57, or twelve to fourteen $CF_2$ units in the backbone capable of crystallization. Backbone chains with a short linear chain sequence may crystallize in a fringed micelle structure. It should be pointed out in this study that thicker extruded samples and membranes prepared by solution-casting method did not show the I ($q$) ~ $q^{-1}$ power law behavior. Thus proposing a morphological model based on a slope in the small-angle scattering

profile needs to be critically checked. Uniquely Nafion® is characterized by 3-component systems, namely ionic, crystalline and amorphous domains giving rise to two distinct scattering peaks in SAXS/SANS profiles. Thus it should be clarified first whether the power law is attributed to the ionic or crystalline component.

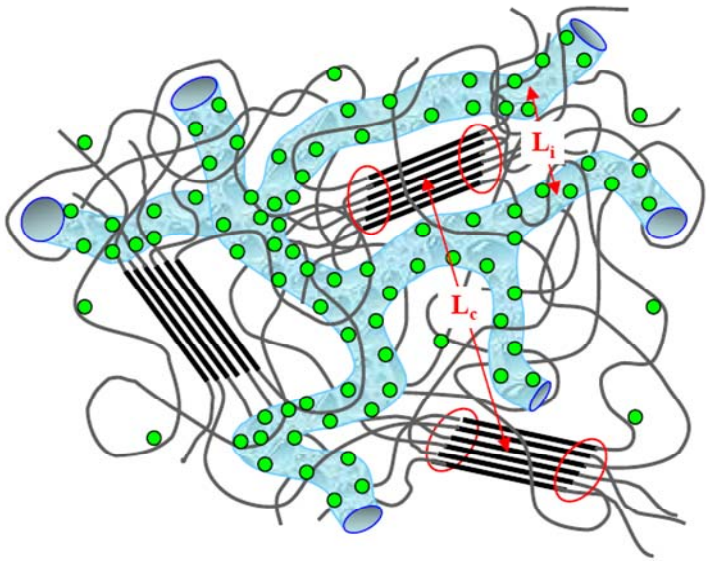


**Figure I-7**. Worm-like channel model by Kim et al. (Reprinted with permission from ref[34] *Macromolecules*, **39**, 4775 (2006). Copyright 2006 American Chemical Society)

### (8) Locally-Parallel Water Channel Model

Inspired by the I ($q$) ~ $q^{-1}$ power law observed in the small-angle scattering profile for the as-received, extruded Nafion®, Schmidt-Rohr and Chen have recently proposed a parallel cylindrical water-channel model for the morphology of Nafion® based on the simulation of various SAXS studies. The algorithm used to simulate various SAXS experiments involved first defining the scattering density ρ(x), on a cubic or rectangular lattice, and then calculating the scattering intensity I ($q$) by using two or three dimensional discrete (fast) Fourier transformations.

A representation of the parallel water-channel model of Nafion® can be seen in Figure I-8. In order to develop the images seen in Figure I-8, the authors assumed a hydration level of 20 vol % or 11 wt % water. Figure I-8a displays the top and side view of a single inverted micelle with the hydrophilic side chains facilitating a water channel through the center and the hydrophobic backbone of the polymer constructing the cylinder wall. Based on a 20 vol % of water, the simulated water channel diameters ranged from 1.8 to 3.5 nm with an average of 2.4 nm. Figure I-8b shows how several inverted micelle cylinders would approximately pack in a hexagonal fashion. Figure I-8c displays a cross-sectional view of scattering density, $\rho(x)$, perpendicular to the channel axes. The water channels are displayed in white, Nafion® amorphous regions are gray, and Nafion® crystallites are black. The Nafion® crystallites used in the water-channel model simulation accounted for 13 vol %, were approximately 2-5 nm in thickness, and had x-y aspect ratios of 1 to 1.8. It is important to point out that crystals are also elongated and approximately cylindrical in shape. This allows that ~3/4 of the scattered intensity at small $q$ is originated from crystallites. Simulation with nearly cubic crystalline blocks instead of long crystals resulted in too little intensity at small $q$ due to the $q^0$ powder law for cubes or spheres. Elongated crystals are suggested to be parallel to the water channels and thus help align the water cylinders. Based on the SAXS simulations, the water-channel model accurately depicted changes in the scattering profile with various water volumes, percent crystallinity, and changes in the thickness of the polymer layer surrounding the inverted micelle cylinders. An accurate depiction of and the Porod region of $q^{-4}$ at large $q$ values was shown versus reported experimental data on the acid form Nafion® by Rubatat et al. As a comparison to the water-channel model, simulations of small-angle scattering for other models of the Nafion® nanostructure were also performed, but failed to reproduce the experimental data. For example,

the most referenced Gierke's cluster-network model resulted in the ionomer peaks that are too sharp. Furthermore, it showed I ($q$) ~ $q^0$ power law at small $q$, which is indeed expected for spheres, rather than the experimentally observed I ($q$) ~ $q^{-1}$ power law.

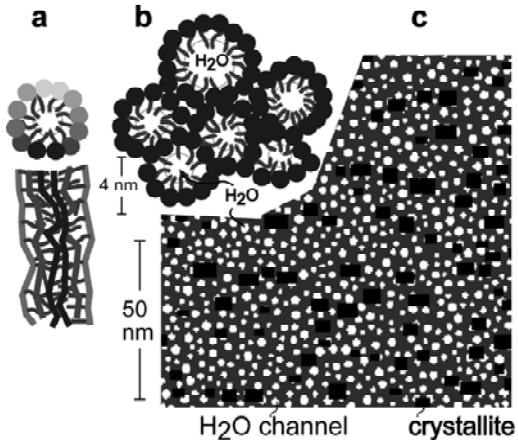


**Figure I-8.** Parallel water-channel model by Schmidt-Rohr (a) Top view and side view of an inverted-micelle cylinder, with the polymer backbones on the outside the ionic water channel (b) the approximately hexagonal packing of several inverted micelles cylinders, (c) cross-sections of scattering density distribution. (Reprinted with permission from ref[20] *Nature Materials*, **7**, 75 (2008). Copyright 2008, Nature Publishing Group)

## D. Post-Processing Method

Two principal techniques as an alternative method to the industrially-adopted processes are also found in the literature to alter the physical properties of the "as-received" extruded Nafion®.[43,44] In both approaches, (1) *solution-processing* and (2) *melt-processing*, the first step is to eliminate the crystalline components (which prevent chain mobility) by dissolving PFSIs using an alcohol/water mixture at elevated temperature (ca. 250 $^{o}$C) in a Parr high pressure reactor. A procedure for dissolving Nafion® membranes was detailed in the early 1980's by Grot and Martin.[45,46] Moore and Martin recognized that a material, which is very different from as-

received extruded Nafion®, is obtained when the solvent is removed from alcohol/water solution of Nafion® at room temperature (Figure I-9).[12,44,47] This material was essentially brittle and showed poor mechanical stability. Solution-processing at an elevated temperature (ca. 180 °C) using a high boiling point, good solvent such as dimethylsulfoxide (DMSO), however, restored the crystalline character and thus improved the mechanical properties (Figure I-9).

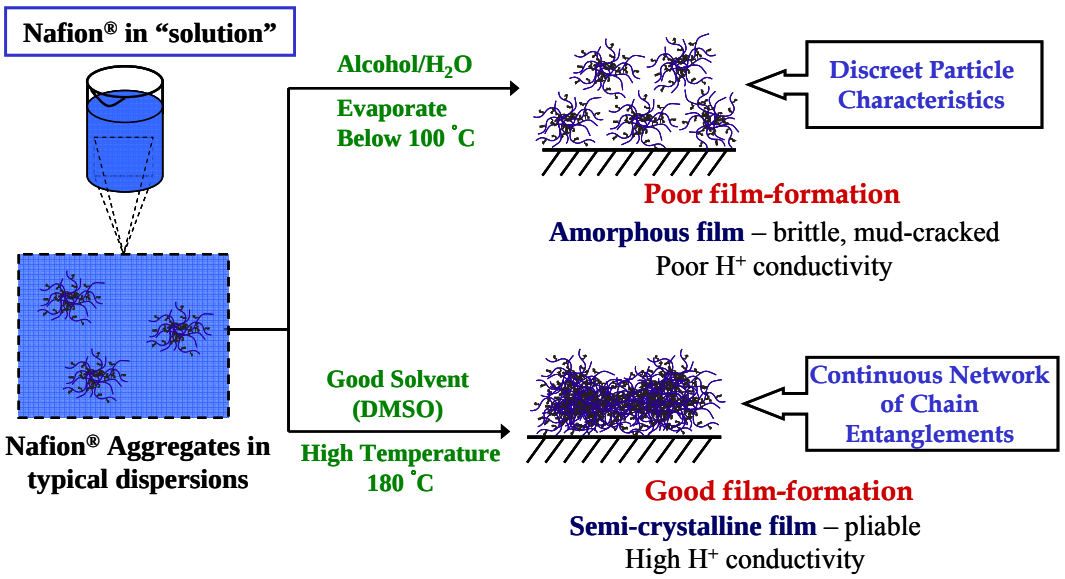


**Figure I-9.** Effect of solution-processing temperature and solvent on film formation of Nafion® membrane

Cable and Moore recognized that existence of PTFE-like crystals and an electrostatic network are the principle barriers to melt-processing the Nafion®. To manipulate the electrostatic interaction, the authors chose to neutralize $H^+$-form Nafion® with bulky, organic tetrabutylammonium ($TBA^+$) counterions which have been shown to effectively reduce the strength of electrostatic interaction in a sulfonated polystyrene ionomer system by forming weak dipole-dipole pairs. $TBA^+$-form Nafion® was then dissolved in methanol (30 % by volume) / propanol (30 % by volume) / DI water (40 % by volume) mixture at elevated pressure and temperature. By performing a "steam-stripping" process, the PTFE-like crystallites were

completely eliminated (which is verified by wide-angle X-ray diffraction, WAXD) and thus obtained amorphous $TBA^+$-form Nafion® powder was melt-processed at 190 °C and 200 psi to reintroduce crystalline component into the PFSI (which is again verified by WAXD). Moore et al. observed the overall dynamic mechanical relaxation characteristics of the melt-processed $TBA^+$-form Nafion® was quite comparable to those of as-received $TBA^+$-form Nafion®. It was further noticed that after re-acidification, water uptake content (%) of melt-processed Nafion® was almost identical to the as-received membranes, meaning the regeneration of the hydrophilic character of the melt-processed membranes.

It is significant to realize that the properties and performance of Nafion® membranes are directly related to their complex morphology, and the supermolecular organization of ionic and crystalline domains may be altered by the processing history. It has been shown that the morphologies, physical properties, and chemical characteristics of the solution-processed PFSI membranes were not identical to those of the as-received membranes prepared by high temperature extrusion. However there is limited information about solution-processed and melt-processed membranes to establish a processing-structure-property relationship in Nafion® because a majority of the previous work was limited to the as-received extruded membrane. Figure I-10 shows SAXS profiles from this thesis work comparing as-received, melt-processed, and solution-processed Nafion® membranes. Of profound importance to the field from this SAXS result is that the power law dependence at low $q$ is subject to processing history and $q^{-1}$ (attributed to rod-like aggregate structure), typically observed in "as-received" extruded Nafion® membranes and also in Nafion® solution of alcohol/water mixtures appears to be no longer present in membranes prepared by solution-processing with high boiling point solvents and melt-processing method.

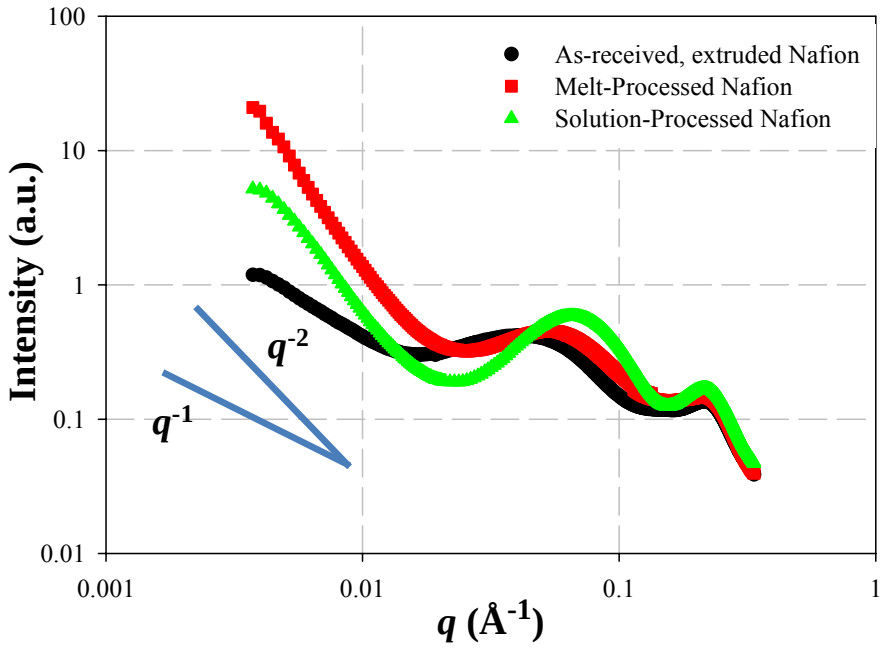


**Figure I-10.** SAXS profiles of as-received (●), melt-processed (■) and solution-processed (▲) Nafion® membranes

## E. Morphological Manipulation via Orientation

Despite the rich information accumulated from various SAXS/SANS studies on "as-received" extruded Nafion® membranes, establishing detailed morphology-property relationships in proton conducting membranes is not an easy task based on the previously proposed structural models that are often over-simplified to allow a refined analysis of the transport properties. Orientation of the nanostructure has been often employed to control material properties and also to impart novelty.[6] Furthermore, valuable structural/morphological information can be derived by subjecting polymeric materials to a simple mechanical deformation. Several mechanical deformations such as uniaxial orientation have been employed previously to explore the complex nature of the morphology of Nafion®.[17,19,23,24,27,30,32,35,48-54] Gierke et al. first investigated the effects of mechanical deformation on the SAXS profiles of both hydrolyzed and unhydrolyzed

Nafion®. While it was not specified in detail regarding the sample preparation, the authors presented two SAXS profiles, one from a moderately stretched sample (with a draw ratio of 2.0) and the other from a spun fiber (expected to have higher draw ratio). After moderate drawing, the intensity and the *q*-position of the scattering maximum at ca. 0.05 $Å^{-1}$ attributed to inter-crystalline domain scattering (often referred to as the long period) were observed to decrease in the machine direction and increase in the transverse direction as compared with an undrawn sample. At higher extension, on the contrary, this reflection peak was observed only in the meridional direction, which implied a periodicity of the crystallite along the fiber axis. In the case of the hydrolyzed ionomer (in $Na^+$-form, and swollen with water), the ionomer peak was only observed in the equatorial direction, which implied a periodicity of the ionic domains perpendicular to the orientation direction.

Fujimura et al. also conducted SAXS studies on cesium-neutralized Nafion® in which the draw ratio (i.e., the ratio of the final, extended length to the initial, undrawn length) was systematically varied from 1 to 1.5.[25] In an agreement with Gierke et al., the intensity and the *q*-position of the ionomer peak decreased with the deformation in the direction parallel to the stretching direction and increased with the deformation in the equatorial direction. Based on the Bragg's law to calculate inter-domain spacings from the peak maxima, the microscopic draw ratios ($\lambda_d = d / d_0$, where $d$ and $d_0$ are the spacings under the deformed and undeformed states, respectively) were calculated and compared to the macroscopic draw ratios ($\lambda_B = l / l_0$, where $l$ and $l_0$ are the dimensions of the membrane under the deformed and undeformed states, respectively). From this comparison, the authors noticed a nonaffine deformation behavior between the microscopic dimensions and the macroscopic deformation. Thus, it was concluded that nonaffine behavior was inconsistent with a model attributing ionomer peak to interparticle

interference origin but supported a model in which ionomer peak arose from intraparticle interference (i.e., a core-shell type particle).

Cable and coworkers have shown that large, hydrophobic counterions such as tetrabutylammoniumions ($TBA^+$) can effectively diminish the strength of Coloumbic interactions within the ionic domains.[23,43] This approach profoundly increased the ability to uniaxially orient Nafion® membranes up to high draw ratios ($\lambda_b = L/L_o$). As the Nafion® membrane was stretched ($\lambda_b = 5.4$), two-dimensional SAXS and WAXD patterns showed a strong anisotropy. While the anisotropic SAXS pattern was attributed to an elongation of the ionic domains in the direction of uniaxial extension, the anisotropic WAXD patterns showed that the amorphous and crystalline domains are "locked" into an orientation aligned with the direction of extension. Scanning electron microscopy (SEM) was also utilized to evidence the chain orientation (Figure I-11). It revealed a fibrillar-like texture in the stretching direction which is consistent with the nature of poly(tetrafluoroethylene) (PTFE) which tends to form fibrils upon stretching.[55] The consequence of this strong orientation has been further characterized in terms of anisotropic ionic conductivities, which showed the ionic conductivity in the direction parallel to the stretching direction was 40 % greater than the conductivity in the perpendicular direction.

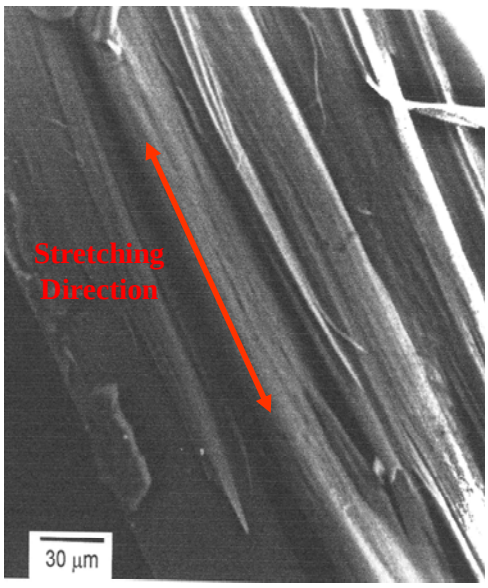


**Figure I-11.** Scanning electron micrograph (SEM) of a freeze-fractured surface of oriented, $TBA^+$-form Nafion® membrane ($\lambda_b$ = ca. 6). (Reprinted with permission from ref[23] *Chemistry of Materials*, **7**, 1601(1995). Copyright 1995, American Chemical Society)

Elliot and coworkers also performed SAXS studies on $H^+$-form extruded Nafion® membranes that were subjected to uniaxial and biaxial orientation. It should be pointed out that the as-received extruded unoriented samples displayed a slight arcing at the equatorial direction. Upon uniaxial deformation along the extrusion direction, the ionomer peak was shown to exhibit a significant degree of anisotropy, which agrees very well with earlier studies. On the basis of an inter-particle scattering model, the authors attributed the arcing behavior to an increase in coherence of the inter-cluster spacings perpendicular to the extrusion direction and a simultaneous decrease in the parallel direction. In a subsequent publication [54], Elliot et al. explored the microscopic and bulk swelling of Nafion® membranes in mixtures of ethanol and water using SAXS and optical microscopy. The authors noticed that the microscopic swelling from SAXS analysis decreased with increasing ethanol content, in contrast to the bulk swelling which increased dramatically, interestingly reaching a maximum at a 75/25 volume percent

mixture of ethanol/water. More interestingly, it was found that subjecting uniaxially oriented Nafion® to the 75/25 ethanol/water mixture led to a morphological relaxation of both the ionomer and crystalline peaks back to an almost isotropic state, which could not be achieved by using water alone. While no direct evidence of ethanol interacting with the fluorocarbon matrix in Nafion® was provided, the authors concluded that the ethanol acts as plasticizer to the fluorocarbon matrix, thus inducing ultimate reorganization of the ionic domains into smaller, more numerous clusters.

Londono et al. conducted synchrotron SAXS experiments on oriented Nafion® membranes and presented two-dimensional SAXS patterns as a function of elongation ranging from 0 % to 150 %.[56] These data indicated that an increase in elongation up to 150 % essentially led to a disappearance of the ionomer peak in the meridional direction and the peak narrowing azimuthally about the equator. Furthermore, an equatorial streaking, which is typically observed in SAXS of draw fibers containing microfibrils, appeared at this elongation level. Two-dimensional SAXS patterns along orthogonal orientations of the film were also acquired and showed isotropic scattering in the direction of orientation, which further confirms the fibrillar morphology of the Nafion® films. Based on additional experiments including SAXS/WAXS of in-situ deformed Nafion®, the authors suggested that the morphology of uniaxially oriented Nafion® may consist of oriented cylindrical or lamellar domains, as opposed to spherical clusters.

Van der Heijden et al. have performed a very detailed simultaneous synchrotron SAXS/WAXD experiment to investigate anisotropic morphology of uniaxially oriented Nafion® at various length scales. While the analysis of SAXS data was focused on the ionomer peak ($q$ = 0.15 Å$^{-1}$), the analysis of WAXD data was focused on (1) the amorphous peak ($q$ = 1.1 Å$^{-1}$), (2) the crystalline peak ($q$ = 1.24 Å$^{-1}$), and (3) a broad peak labeled as "Peak 3" ($q$ = 2.75 Å$^{-1}$),

which was attributed to several diffraction peaks resulting from intramolecular correlations. Upon uniaxial orientation, it was noticed that the crystalline peak positions in the meridional and equatorial direction did not change. On the contrary, the *q*-position of the ionomer peak, the amorphous peak and Peak 3 showed a decrease in the meridional direction with increasing draw ratio. Examination of the scattering intensity as a function of the azimuthal angle from $0^o$ (meridional) to $90^o$ (equatorial) revealed an increase in the scattering intensity with increasing azimuthal angle for the ionomer, crystalline and amorphous peaks, whereas Peak 3 showed a decrease in the scattering intensity. The authors attributed the higher intensity at the equator of the ionomer, amorphous and crystalline peaks to more chains being aligned along the stretching direction. The degree of orientation as a function of a draw ratio was quantified by calculating the Herman's orientation parameter (*f*) from the azimuthal plots where the *f* is defined as

$$f = \frac{3\left\langle \cos^2 \chi \right\rangle - 1}{2} \qquad \textbf{Eq I-1}$$

where $\chi$ is the azimuthal angle and $\langle \cos^2\chi \rangle$ (the average square of the cosine) is an expression of the orientation. The average square of the cosine was calculated from the integral

$$\left\langle \cos^2 \chi \right\rangle = \frac{\int_{\chi_1}^{\chi_2} I(\chi) \cos^2 \chi \sin \chi d\chi}{\int_{\chi_1}^{\chi_2} I(\chi) \sin \chi d\chi} \qquad \textbf{Eq I-2}$$

where I ($\chi$) is the scattering intensity as a function of $\chi$ and the limits of integration are between $\chi_1$ and $\chi_2$. The Herman's orientation function (*f*) will be 1 for a system with complete orientation of the scattering entities parallel to the director and -1/2 for the system with a perfect orientation of the scattering entities perpendicular to the director. For unoriented isotropic samples, the

value of *f* is zero. In the case of oriented Nafion® it is necessary to clarify that the director is the momentum transfer vector (or scattering vector), *q*. If the orientation direction of the films is established as the primary axis, then the director, *q*, will be perpendicular to the orientation plane, resulting in values of *f* near -1/2. A plot of the Herman's orientation parameter (*f*) versus draw ratio (%) indicated that the ionomer peak reached maximum orientation at lower draw ratios than the crystalline peak, whereas at higher draw ratio, two peaks began to correlate with respect to elongation. From this observation, the authors noticed that the orientation is different at the scale of several ionomer distances in comparison with the scale of several chains distances. Based on the previously proposed elongated polymeric aggregates model of Nafion®, the authors proposed a two-step mechanism of Nafion® orientation process. (Figure I-12) At the smaller draw ratios, the large bundles undergo rotations (which is the dominate mechanism) and simultaneously the elongated aggregates within the bundle are better aligned along the stretching direction. At higher draw ratios, however, individual elongated aggregates become more refined in the draw direction due to sliding or disentanglement of the aggregates from each other.

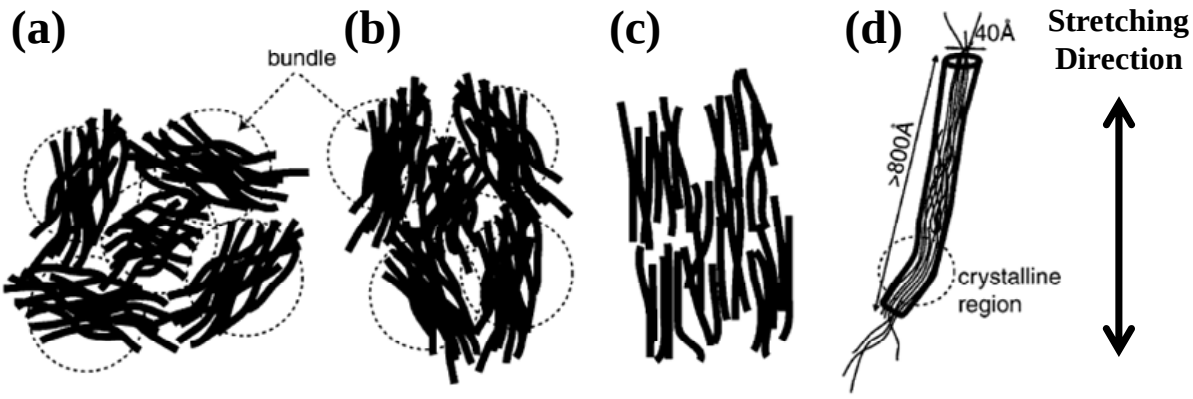


**Figure I-12**. Two-step orientation mechanisms proposed for Nafion®: (a) Organization of bundles of elongated aggregates. (b) Under uniaxial orientation, the bundles are rotating. (c) At higher draw ratio, the aggregates within the bundle are oriented along the stretching direction. (d) A magnification of an aggregate which is made of more or less aligned and ordered polymeric chains surrounded with ionic groups. (Reprinted with permission from ref[32] *Macromolecules*, **37**, 5327 (2004). Copyright 2004, American Chemical Society)

Recently, Page and coworkers performed variable temperature, SAXS experiments to investigate the thermal relaxation behavior of uniaxially oriented Nafion® membranes in an effort to evaluate the morphological stability of this ionomer at elevated temperatures.[35] The authors first neutralized Nafion® membranes with various alkylammonium counterions ($TMA^+$, $TEA^+$, $TPA^+$, and $TBA^+$) as a means to manipulate the strength of electrostatic interactions and then uniaxially oriented these samples to a draw ratio of 3. Figure I-13 shows the variable temperature azimuthal plots for (a) $TMA^+$, (b) $TEA^+$, (c) $TPA^+$, and (d) $TBA^+$-form Nafion®. Each figure in Figure I-13 is characterized by strong equatorial peaks located at the azimuthal angle approximately $90^o$ and $270^o$ ($\chi$) with respect to the orientation direction, indicating a strong alignment of ionic domains along the stretching direction. It is noticed that with increasing temperature, established strong anisotropic morphologies transform into isotropic morphologies as indicated by uniform intensity distribution throughout the range of azimuthal angles. However, the temperatures at which these sudden transformations occur are found to be dependent on the size of counterions used to neutralize the Nafion® membrane and decrease with increasing counterion size. Interestingly the temperature at which rapid decrease in the intensity of the equatorial peaks was observed was quite well correlated with the α-relaxation temperature (which is linked with the onset of long-range mobility of both the main and side chain) of dynamic mechanical analysis (DMA).[33]

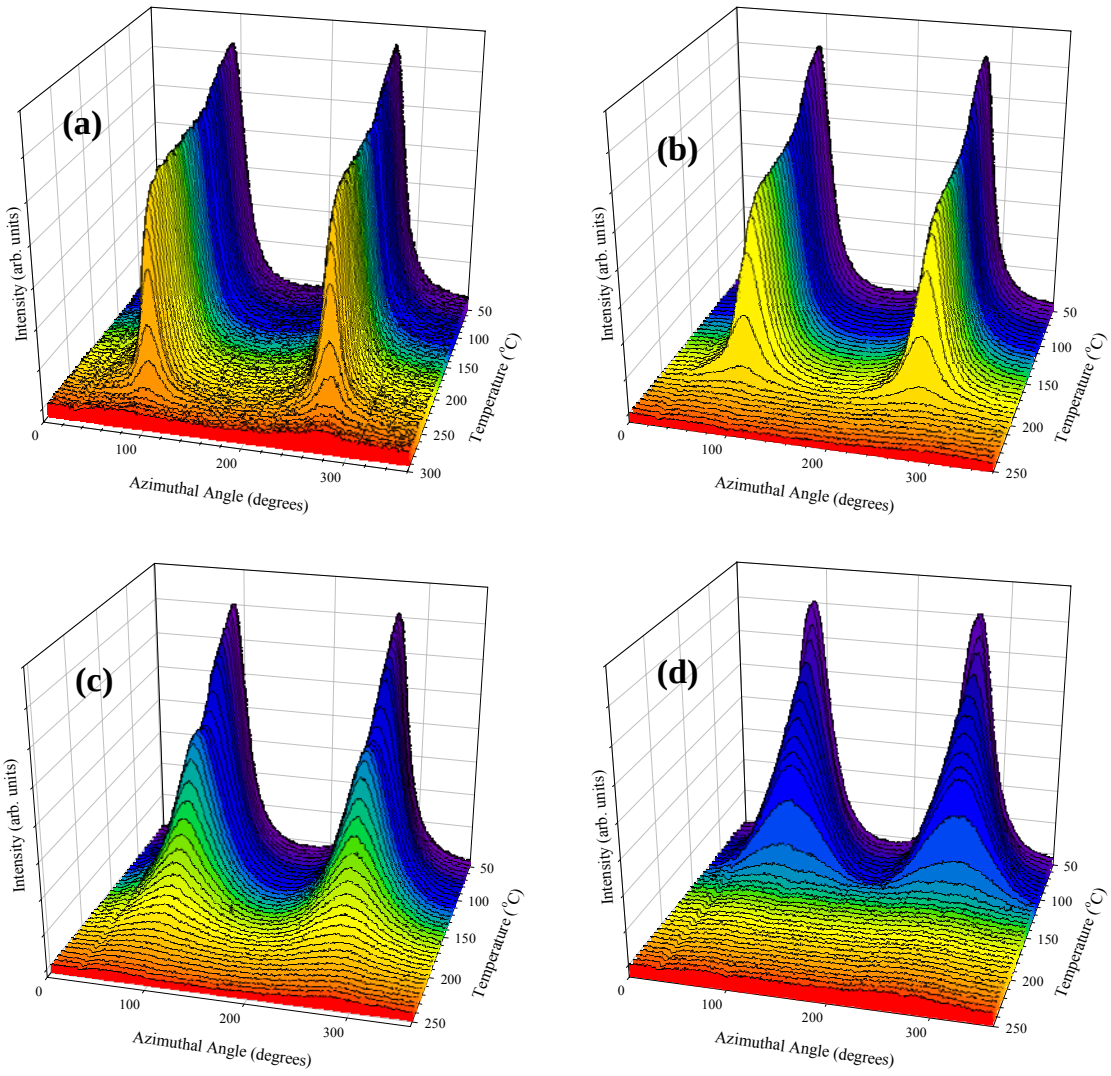


**Figure I-13.** Variable temperature SAXS for scattering in the azimuthal direction ($\chi$) (a) $TMA^+$, (b) $TEA^+$, (c) $TPA^+$, and (d) $TBA^+$-form Nafion®. (Reprinted with permission from ref[35] *Macromolecules*, **39**, 3939 (2006). Copyright 2006, American Chemical Society)

In a series of recent publications, Lin et al. have investigated the effects of uniaxially orienting recast Nafion® on the properties of water in the membrane, proton conductivity and direct methanol fuel cell (DMFC) performance.[51,57] To prepare uniaxially stretched membranes with draw ratios ranging from 1 to 7, dimethylacetamide (DMAc)-swollen recast Nafion® membranes were mounted onto the stretching frame and heated to 125 $^oC$, and then uniaxially to

stretched. After stretching, oriented samples were kept at 125 $^{o}$C for 1 hr in the stretching frame to fully evaporate DMAc, followed by an additional annealing step at 150 $^{o}$C for 2 hrs. It should be pointed out that stretched recast Nafion® membranes prepared according to the procedure described above showed no sign of any relaxation even after soaking for 12 hrs in a hot (60 $^{o}$C) 75/25 methanol/water mixture. The authors attributed persistence of the morphology in stretched recast Nafion® to the inclusion of the annealing step after stretching. It was suggested that the annealing step induced crystalline domains which helped to fix the stretched polymer morphology permanently. While no two-dimensional WAXS or SAXS patterns were presented throughout the series of these studies to convince the existence of anisotropic morphology, comparison of WAXD profiles of stretched and unstretched samples showed no significant difference, which was interpreted as no change in the degree of crystallinity or the size of crystallites. It is interesting to note that stretched recast Nafion® membranes showed a slight increase in through-plane proton conductivity and a gradual decrease in methanol permeability as a function of draw ratios, which are highly desirable properties for DMFC applications. Low temperature DSC thermograms of stretched, recast Nafion® membranes showed a monotonic decrease in the size of water melting peak with increasing draw ratios, which means there is less freezable water in Nafion® upon stretching. Furthermore, the authors noticed a systematic depression in the temperature at which the freezable water melted in the stretched recast samples. The intriguing observation of (1) the increase in non-freezable water and (2) the depression in the water melting temperature as a function of draw ratios have led the authors to hypothesize that there was a redistribution of ionic domains, which subsequently creates ionic domains with a smaller size but a greater number. To confirm this hypothesis, transmission electron micrographs (TEM) of stretched recast Nafion® membrane were collected. Figure I-14 displays

the membrane cross sections and clearly shows that the size of the ionic domains (darkened regions) was smaller and the number of such domains increased with increasing draw ratios.[51]

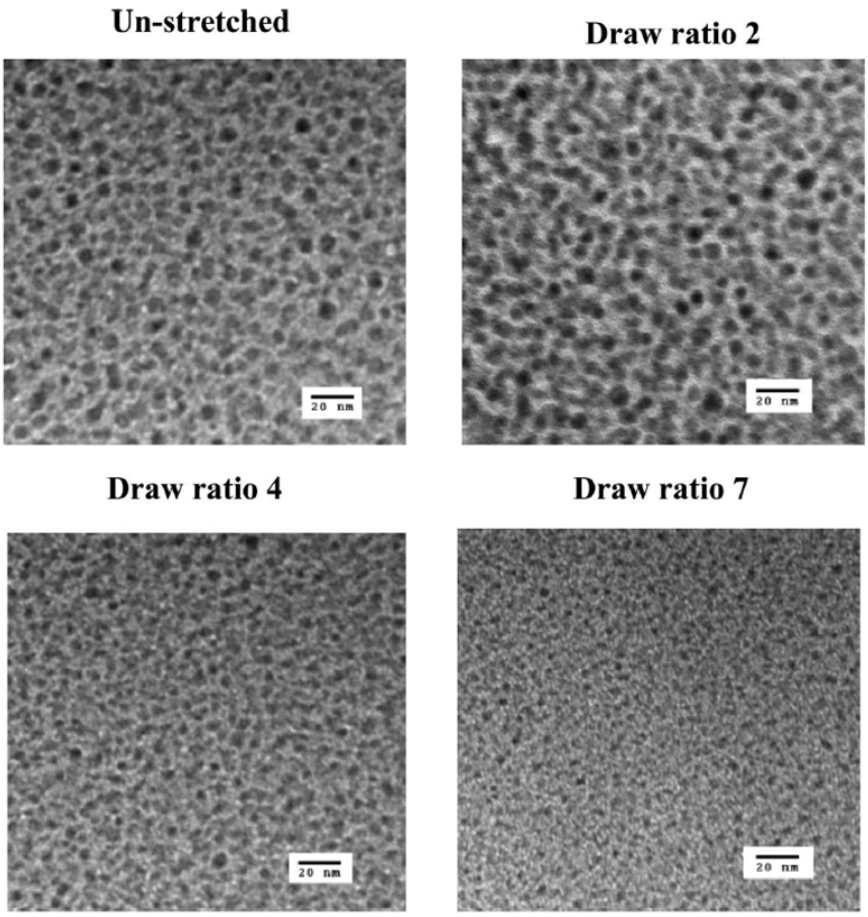


**Figure I-14**. Transmission electron micrographs of unstretched and prestretched recast Nafion® membrane across section. Dark regions are the hydrophilic domains. Strethcing direction was perpendicular to the x-y plane of the page. (Reprinted with permission from ref[51] *Macromolecules*, **41**, 4284 (2008). Copyright 2008, American Chemical Society)

Chourdakis and Voyiatzis employed polarized UV-Raman spectroscopy to study uniaxially oriented Teflon® and Nafion®.[49] To prepare oriented samples with high draw ratios, Nafion® membrane was drawn at 130 $^{o}$C, which is above the α-relaxation temperature, whereas Teflon® was drawn at 180 $^{o}$C above their Tg. It was noticed that uniaxial stretching induced a

significant change in molecular orientations both in Teflon® and Nafion®. For oriented Teflon® samples, a dramatic increase in the intensity of the C-C stretch band at 1377 $cm^{-1}$ was observed along the stretching direction. On the contrary, the intensity of the $CF_2$ stretch band at 731 $cm^{-1}$ was shown to increase perpendicular to the stretching direction. The band located at 1297 was essentially insensitive to the drawing process and thus it was assigned as C-C and C-F degenerate stretch. UV-Raman spectra were then recorded on Nafion® membranes that were uniaxially oriented to a different draw ratio ranging from 1.0 to 4.5. For the as-received extruded Nafion® membranes, the intensity of the C-C stretching band at 1377 $cm^{-1}$ was higher along the machine direction while the intensity of the $CF_2$ stretching band at 731 $cm^{-1}$ was lower along the machine direction. This result is in a good agreement with previous X-ray scattering studies and indicates an initial molecular orientation of the Nafion® membrane parallel to the extrusion (or machine) direction. As the Nafion® membranes were further stretched to higher draw ratios, the scattering intensity of the C-C symmetrical stretch at 1377 $cm^{-1}$ was further enhanced parallel to the draw axis. These authors also noted that two Nafion® side chain peaks of C-S stretch at 805 $cm^{-1}$ and C-O-C stretch at 971 $cm^{-1}$ were preferentially oriented perpendicular to the draw direction.

Rubatat and Diat have performed SAXS and SANS experiments to further characterize the fibrillar nature of Nafion® membranes.[36] For SAXS and SANS experiments, the two-dimensional scattering patterns were acquired by eradiating the beam onto the membrane surface to probe the polymeric structure in the meridional plane, $MP_1$ as depicted in Figure I-15a. Similar to the study by Londono et al., micro-SAXS patterns were also acquired along the two different planes, $MP_2$, and EP as shown in Figure 1-15a. The two-dimensional micro-SAXS patterns in the meridional plane, $MP_2$ through the thickness shown in Figure 1-15b displays

strong anisotropic scattering, similar to those typically observed through the membrane plane, $MP_1$ for uniaxially oriented Nafion® membranes. On the other hand, the two-dimensional micro-SAXS patterns in the equatorial plane, EP shown in Figure 1-15c remained isotropic after deformation and verified the results of Londono and coworkers. This observation was interpreted as a strong evidence of the uniaxiality of the deformation process of the Nafion® membrane.

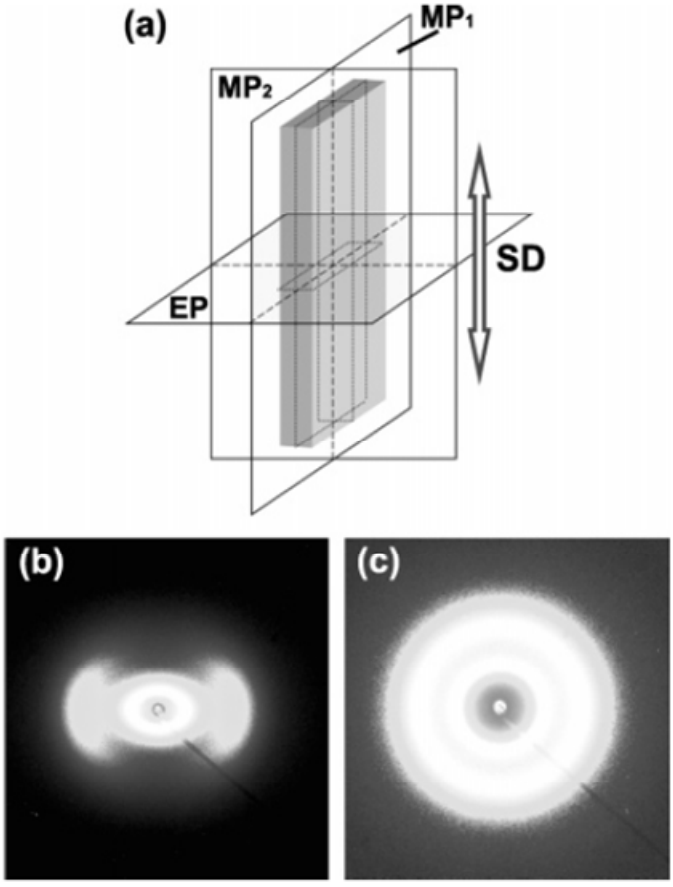


**Figure I-15**. (a) Configuration of geometrical planes examined during SAXS experiments, SD is the stretching direction. EP is the equatorial plane relative to the SD. $MP_1$ and $MP_2$ are meridian planes. Micro-SAXS images acquired in the meridian plane $MP_2$ (b) and SD (c). (Reprinted with permission from ref[36] *Macromolecules*, **40**, 9455 (2007). Copyright 2007, American Chemical Society)

Rubatat and Diat performed SANS and contrast variation experiments in an effort to determine the shape of the scattering entities in uniaxially oriented, swollen Nafion® membranes.[36] To achieve this goal, the authors assumed that in a narrow *q*-range near the ionomer peak, the scattering intensity can be depicted by a product of a structure factor and a form factor. Based on this assumption, the authors divided the spectra measured on a membrane swollen with $D_2O$ by the one measured on the same membrane swollen with $H_2O$ and consequently canceled the structure factor to give a ratio of two form factors. Examination of the experimental division curves determined perpendicular to the SD showed the minimum at 0.14 $Å^{-1}$ for both the undrawn and oriented samples, indicating the scattering length density profile of the scattering objects (i.e., the size of those objects) remained the same before and after drawing. On the other hand, the division curve determined parallel to the SD after drawing showed no longer the minimum 0.14 $Å^{-1}$, which means loss of the variation of the scattering length density along the stretching direction. The authors also presented the theoretical division curves which were calculated based on a core-shell cylinder form factor. Examination of the theoretical division curves showed the same trend as the experimental data. While the division curves calculated perpendicular to the SD and also for randomly oriented cylinders showed the same minimum, the division curve calculated parallel to the SD were essentially flat, indicating the loss of the correlation along the SD. From this observation, the authors concluded that the cylindrical scattering objects are simply oriented without significant deformation under uniaxial orientation, and ruled out the deformation of spherical ionic domains into an ellipsoidal shape.

While the majority of the previous orientation studies of Nafion® membranes involved a simple uniaxial or biaxial deformation, Lin and coworkers demonstrated an interesting approach to align the ionic aggregates along the membrane thickness direction (i.e., through-plane as

opposed to in-plane) by applying an electric field during solution-casting.[58] Before electric poling experiments, the 10 wt % Nafion® solution in DMAc solvent was prepared and cast in a glass vessel by evaporating the solvent under vacuum at 50 $^{o}$C for 30 min and then 60 $^{o}$C for 1hr. These membranes were then placed between the two electrodes (2 cm spaced out from each other) and a voltage of 15 kV was applied across the two electrodes. During the electric poling experiments, the temperature was controlled by a flowing heated nitrogen gas and was set at 120 $^{o}$C. The authors investigated two electric field alignment experiments, one with the Nafion® membrane surface parallel to the electric field (i.e., the electric field is vertical to the membrane thickness direction) and the other with the Nafion® membrane surface vertical to the electric field (i.e., the electric field is along the membrane thickness direction.) The consequence of the electric field application during the film formation was investigated using transmission electron microscopy (TEM), ionic conductivity, atomic force microscopy (AFM), and fuel cell performance test. The authors noticed that through-plane conductivity of the membrane prepared by applying an electric field vertical to the membrane surface was higher than those of other membranes prepared by applying electric field parallel to the membrane surface and by applying no electric field at all. The nano-structures of the prepared Nafion® membranes were characterized by both TEM and AFM. For example, Figure I-16 illustrates distinct morphology of Nafion® depending on the direction of the applied electric field during film formation. Figure I-16a shows AFM micrograph of the surface of the Nafion® membrane prepared by applying electric field parallel to the membrane surface and demonstrates the ionic aggregates (or fibril bundles) aligned along the direction of applied electric field. However, AFM micrograph (Figure I-16b) of the surface of Nafion® membrane prepared by applying electric field vertical to the membrane surface is quite different and does not show clearly the packing of bundles due to

their alignment which is normal to the membrane surface. Lastly, the authors conducted fuel cell performance tests (i.e., voltage and power density versus current density) on MEAs prepared from (1) commercial Nafion 117, (2) solution-cast membranes prepared by applying no electric field at all, and (3) solution-cast membranes prepared by applying electric field vertical to the membrane surface. It showed that the MEA prepared from the membrane after applying an electric field vertically to the surface of the membrane had a much better PEMFC performance than the MEAs prepared from the others. This study clearly demonstrated that higher proton conductivities and greater PEMFC performance can be achieved by the alignment of ionic aggregates along the membrane thickness direction to induce linear and less curved proton percolation pathways.

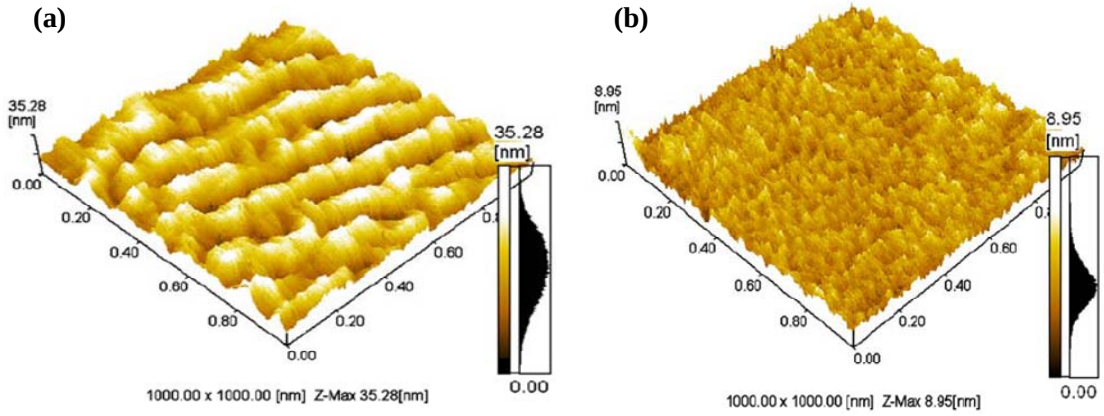


**Figure I-16**. AFM image of the surface of Nafion® membrane prepared by solution-casting after treatment with an electric field (a) parallel to the surface of membrane and (b) vertical to the surface of membrane. (Reprinted with permission from ref[58] *Journal of Polymer Research*, **13**, 379 (2006). Copyright 2006, Springer)

Very recently, Allahyarov and Taylor investigated the effect of stretching-induced structure orientation on the proton conductivity of Nafion® membranes using a coarse-grained simulation method.[24] In this simulation, the continuous backbone polymer was considered as a

set of connected segments and a weak force $\mathbf{f}_{\pm}$ was applied to the end monomer of each segment to construct the uniaxially stretched samples. It should be pointed out that the magnitude of $\mathbf{f}_{\pm}$ was limited to values much smaller than the forces arising from the bond, angle and dihedral potentials and were in the range of 190 pN on each chain segment. The results are quite interesting and indicate in general, clusterlike ionic aggregations of different sizes and shapes for unstreched Nafion® membranes. Upon backbone stretching, it was suggested that the rearrangement of ionic clusters occurs via elongation in one direction and shrinking in the other direction, which leads to anisotropic morphology as shown in Figure I-17. In this figure, the water molecules assembled in elongated clusters in association with the distribution of side-chain head groups and are clearly oriented in the direction of the applied stress. Detailed analysis of induced backbone ordering ($S_b$) and sidechain ordering ($S_s$) was also performed by calculating the order parameters. It turned out that the backbone ordering ($S_b$) increased with increasing stretching force, but decreased in the solvated case as the water content increased for a fixed force, **f**. In the case of sidechains, the sign of order parameters ($S_s$) indicated that the side chains tended to orient themselves perpendicular to the stretching direction, which is in a good agreement with the previous experimental study.[49] The longitudinal and transverse proton conductivity ($\chi_0$) values were also evaluated as a function of backbone order parameter and water content. It was observed that backbone ordering and water content in the membrane increased the conductivity ($\chi_0$) along the stretching direction. However, the transverse proton conductivity ($\chi_0$) across the stretched membrane decreases with increasing backbone ordering due to lack of continuous pathways for protons to travel across the stretched direction.

.

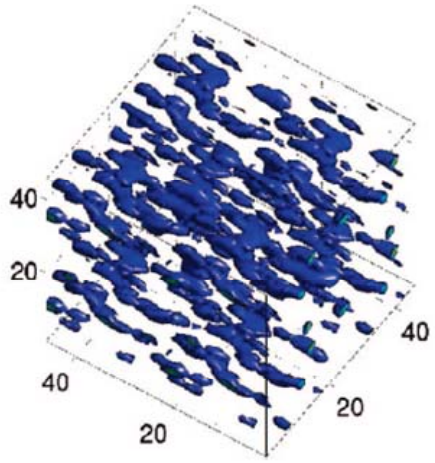


**Figure I-17.** Instantaneous distribution of water clusters in a stretched, solvated membrane for stretched force f=1, and water content λ=5 water molecules per sulfonate. (Reprinted with permission from ref[24] *Journal of Physical Chemistry B*, **113**, 610 (2009). Copyright 2009, American Chemical Society)

Recent publications by Li et al. have used $^2$H NMR spectroscopy to characterize anisotropy in Nafion®.[50,59] The use of deuterium NMR quadrupole coupling allowed to characterize DuPont extruded Nafion® 112 and the latest dispersion-cast Nafion® 212 membranes. Figure I-18 shows $^2$H NMR spectra as a function of membrane orientation with respect to $B_0$. For extruded samples (Figure I-18a), the degree of peak splitting ($\Delta\nu_Q$) is greatest in the extrusion direction, which means hydrophilic channel alignment along the extrusion direction, as expected due to extrusion and shear forces. Quite interestingly, however, dispersion-cast samples (Figure I-18b) showed greatest peak splitting across the membrane thickness, which indicates through-plane alignment of ionic channels. The authors attributed the through-plane alignment of hydrophilic channels to the casting solvent flow during evaporation. Further examination of the peak splitting using Eq I-3 indicated that "as-received" extruded Nafion® was biaxially aligned with asymmetry parameter ($\eta$) =0.12, while solution-cast membranes showed uniaxial symmetry ($\eta$) =0.

$$\eta = \left| \Delta\nu_Q^{\,y} - \Delta\nu_Q^{\,z} \right| / \Delta\nu_Q^{\,x} \qquad \textbf{Eq I-3}$$

The authors pointed out that biaxiality may be caused by the presence of either ellipsoidal channels or cylindrical channel (with zigzag characters) aligned along the extrusion direction in the membrane, and thus it was difficult to determine where Nafion® morphology exhibits a cluster-network model or cylindrical channel model. Correlation of hydrophilic channel alignment to transport property was made by measuring water self-diffusion coefficient using pulsed field gradient spin echo NMR along three different directions. It turned out that water self-diffusion coefficient in extruded Nafion® 112 along the extrusion direction was 18% faster than in the through-plane direction and 14% faster than in the perpendicular in-plane direction. However, diffusion anisotropy was minimal in solution-cast membranes, mostly likely due to weak alignment of hydrophilic channels.

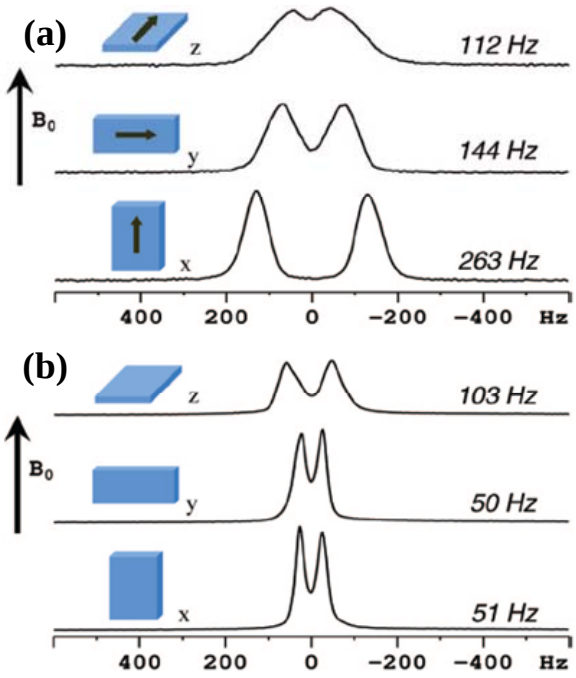


**Figure I-18.** $^2$H NMR spectra of (a) Extruded Nafion® 112 and (b) dispersion-cast Nafion® NRE212. The rectangular blocks are used to indicate the sample direction relative to the $B_0$. For the extruded samples, the arrows are used to indicate the extrusion direction. (Reprinted with permission from ref[59] *Macromolecules*, **41**, 4555 (2008). Copyright 2008, American Chemical Society)

## F. Transport Properties

While it requires further investigation to precisely determine the shape and size of ionic domains in PFSIs, it is now widely accepted that hydrophilic continuous pathways must exist in order for proton conduction and ion-water diffusions to occur.[5] Furthermore, the efficiency of the ion-water transport through the membrane should directly be related to how ionic percolation pathways are developed three-dimensionally within an hydrophobic PTFE matrix.[50] Of course, the proton transport properties of Nafion® membranes are largely influenced by the water content of the membrane. In the dry state, the Nafion® membrane behaves like an insulator. However the membrane is no longer an insulator once it becomes hydrated to a certain point. Early studies by Yeo suggested this minimum threshold was about six water molecules per sulfonic acid site, while Pourcelly et al. estimated about seven molecules.[60,61] Proton conductivity and water diffusion coefficient in PFSIs will be reviewed below because these two parameters have been the principle transport properties of interest to a PEMFC community.

### (1) Proton conductivity

Proton conduction in Nafion® membranes has been proposed to occur by three distinct mechanisms, (1) the vehicular mechanism, (2) the Grotthuss mechanism and (3) the surface mechanism.[62] In the vehicular mechanism, proton diffusion is proposed to occur through the assistance of a carrier species. While the proton diffuses with the carrier, a counter-flow of unprotonated carriers is established to sustain the net proton transport.[13] Using this basic model one can see that the rate determining factor for proton conduction is the rate of diffusion of the carrier species. Temperature dependence studies have shown that for many cases as temperature increases the vehicle mechanism begins to dominate conduction.[63] In the Grotthuss mechanism,

protons are conducted through "hopping" from one water molecule to another by the successive formation and breakage of hydrogen bonds. It should be noticed that this "hopping" process is much faster than the diffusion of hydronium ions in water. Lastly, in the surface mechanism, the protons are proposed to conduct along the array of sulfonic acid groups, basically "hopping" from one anion moiety to another.[62]

It should be emphasized that proton conductivity has been measured under a variety of environmental conditions such as water[64,65], water vapor[64,66,67], and humidified gases[68,69] at various temperatures.[63] With such a broad range of critical parameters affecting the conductivity of the Nafion® membranes, a wealth of conductivity information has been accumulated.[63,70] Regardless of a detailed conduction mechanism, the measured proton conductivity is a strong function of water content within the membrane due to the need for either uninterrupted hydrogen bond channels or proton carrier vehicles.[63,64,71] Kreuer has shown that with increasing degree of hydration, the proton mobility as well as water self-diffusion coefficient approaches the values for bulk water.[71] In addition to hydration effects, research was focused on the influence of temperature on conductivity, which showed, in general, an increase of membrane conductivity with increasing temperature. [63,72,73] Lee et al. measured the proton conductivities of Nafion® membranes at 95% RH and in liquid water using the four-probe and the two-probe methods.[63] It was noticed that the proton conductivities at 95% RH increased continuously up to about 0.11 S/cm at 80 $^{o}$C and then decreased at 90 $^{o}$C, regardless of the cell configurations. The authors attributed this decrease in conductivity at 90 $^{o}$C to the high vaporization rate of water from the Nafion® membrane under the water-vapor condition. Unlike the water-vapor state, proton conductivities in liquid water increased monotonically as a function of temperatures up to 90 $^{o}$C.

**(2) Water Diffusion:**

Along with proton conductivity, water diffusion coefficient is another crucial parameter in artificial muscle and PEMFC considering that the proton conduction is closely linked to the diffusion of water within the membrane. To determine water diffusion coefficient in Nafion® membrane, pulsed-field gradient spin-echo (PFGSE) $^1$H NMR has been the most widely employed technique in the literature.[50,52,73-76] In PFGSE NMR, application of two identical gradient pulses of amplitude (g), and width (δ), allows measurement of diffusion based on attenuation of the spin-echo signal during a diffusion time (Δ) within the pulse sequence. [74]

It can be shown that in the case of diffusion following the Fick's second law, the spin echo intensity, A(δ) can be given by

$$A(\delta) = A(0)\exp[-\gamma^2 g^2 D\delta^2(\Delta - \frac{\delta}{3})] \qquad \textbf{Eq I-4}$$

where A(0) is the intensity at time t = 2τ without the field gradient, D the diffusion coefficient and γ the gyromagnetic ratio. Arrangement of the Eq I-4 gives

$$\ln(\frac{A(\delta)}{A(0)}) = -\gamma^2 g^2 D\delta^2(\Delta - \frac{\delta}{3}) \qquad \textbf{Eq I-5}$$

with D extracted as the slope of the ln[A(δ)/ A(0)] versus $\gamma^2g^2\delta^2(\Delta - \delta/3)$ plot.

Zawodzinski et al. first used PFGSE NMR to measure water diffusion coefficients in hydrated Nafion® membranes at 30 $^o$C and showed water diffusion coefficients increased in a linear fashion at low water contents, yet began to plateau at higher water contents.[74] In contrast, diffusion coefficients taken from conductivity measurements using the Nernst-Einstein equation showed continual increase with water content, suggesting the Grotthuss mechanism for proton

transport dominates at high water content, and negligible at low water contents. Gong et al. have also applied PFGSE NMR to measure diffusion coefficients of water, ethanol and decafluoropentane in Nafion® membranes as a function of concentration and temperature.[77] Results showed that the diffusion coefficient increased with volume fraction of solvent in the membrane and with temperature, which agrees very well with data regarding the effects of hydration and temperature on proton conductivity measurements. Several authors demonstrated that the PFGSE NMR technique can provide information on the tortuosity of the percolation pathway by measuring diffusion coefficients at various diffusion times (Δ). Zhang and coworkers measured water diffusion coefficients as a function of time (ranging from 4 ms to 1s) over which diffusion is observed.[78] It was found that in "as-received" extruded Nafion® 117 membrane, diffusion coefficients did not depend strongly on diffusion times (Δ). On the contrary, the diffusion of water in solution-cast Nafion® 112 had a greater dependence on diffusion times (Δ), which is indicative of a tortuous pathway for diffusion. Recently, Ohkubo and coworkers investigated the micron-scale porous structure in Nafion® 117 membrane by measuring also the time-dependant self-diffusion coefficients at different water contents with temperatures ranging from 233 to 323 K.[75] The results revealed that the $^{1}H$ self-diffusion coefficients were dependant on diffusion times (Δ) less than 2 ms due to a micron-scale restricted structure and were constant beyond 3 ms.

## G. Mechanical Properties

A review of the open literature reveals that the vast majority of the previous investigations regarding mechanical properties of Nafion® membranes were focused on dynamic mechanical analysis (DMA) where loss tangent (tan δ), storage tensile modulus (E') and loss tensile modulus (E") were acquired as a function of temperature. The acquired DMA data was

used to primarily assign the thermomechanical transitions to morphological features. [5,33,35,79,80] The earliest DMA study on $H^+$-form Nafion® (EW = 1365 g $mol^{-1}$) by Yeo and Eisenberg observed three different transitions ($\alpha > \beta > \gamma$).[80] A transition, labeled α, in the tan δ curve was observed at 110 °C and this relaxation was initially assigned to the glass transition of the nonionic component because, in this preliminary study, the magnitude or position of this transition showed only a minor dependence on water. A β-relaxation for the same $H^+$-form membrane was observed at 20 °C, and shifted to lower temperatures with increasing water content, and thus subsequently was assigned to the glass transition of the ionic phase. A γ-relaxation at around -100 °C was attributed to short range molecular motions in the PTFE phase, the same origin as in pure PTFE. A few years later, Kyu and Eisenberg reversed the assignment of the α and β relaxations, while retaining the assignment for the low temperature γ-relaxation based on studies involving partially ionized and neutralized Nafion® membranes.[81]

A systematic DMA study was performed by Cable and Moore by neutralizing Nafion® membranes to incorporate a variety of counterions.[82,83] In this study, the α-relaxation was attributed to chain motions within and/or near ionic domains and the β-relaxation to chain motions of amorphous fluorocarbon far removed from ionic aggregates, i.e. within the PTFE matrix.[83] It is important to recognize from this study that researchers referred to chain motions within an electrostatic network instead of polar and fluorocarbon components being discrete, isolated domains, which is in a good agreement with Kyu and Eisenberg who showed that behaviors of one phase strongly affect the other phases as the two are in intimate contact and are of small size.

It has been shown that ionic aggregates in PFSIs can act as multifunctional physical cross-links that significantly restrict chain mobility.[33,43] However, the motional constraint

imposed by ionic clustering in PFSIs may be weakened by controlling electrostatic interactions. Page et al. showed that the strength of Columbic interactions within the ionic domain can effectively be manipulated by varying the size of neutralizing counterions, such as tetramethylammonium ($TMA^+$), tetraethylammonium ($TEA^+$), tetrapropylammonium ($TPA^+$), and tetrabutylammonium ($TBA^+$) ions.[33] Dynamic mechanical analysis (DMA), and small angle X-ray scattering (SAXS) analysis have revealed that tetraalkylammonium ion neutralized Nafion® membranes exhibited two distinct thermo-mechanical relaxations in the range of 70 – 300 ˚C that have been assigned as the α- and β-relaxations. The α-relaxation temperatures of $TMA^+$–, $TEA^+$–, $TPA^+$– and $TBA^+$–PFSIs are 240 ˚C, 160 ˚C, 130 ˚C, and 100 ˚C, respectively. On the other hand, the β-relaxation temperatures of $TMA^+$–, $TEA^+$–, $TPA^+$–, and $TBA^+$–PFSI membranes are 130 ˚C, 111 ˚C, 100 ˚C, and 73 ˚C, respectively. Compared to the $H^+$-form of the polymer, small $TMA^+$ ions caused dramatic increases in both the α and β relaxation temperatures due to the great strength of the electrostatic interactions between the ion-pairs, while larger $TPA^+$ or $TBA^+$ counterions caused the α- and β-relaxations to systematically shift to significantly lower temperatures. As the size of the counterion increases, the larger counterions significantly weaken the strength of the electrostatic interactions and the bulky, organic counterions can effectively plasticize the ionomer, which in turn yields lower α- and β-relaxation temperatures. As a result of this study, the low temperature β-relaxation was assigned to the onset of chain motions, primarily within the backbone, within the concept of a static, physically crosslinked network of chains, similar to the traditional concept of a polymer glass transition ($T_g$).[33] Furthermore, the α-relaxation was attributed to the onset of long-range mobility of both main and side chains through destabilization of the electrostatic network.[33] Network destabilization was

thought to occur through ion-hopping, the process of ion pairs transferring between ionic clusters to balance electrostatic and elastic forces.

Based on a correlation of dynamic mechanical analysis and dielectric spectroscopy, Osborn et al. undoubtedly assigned the glass transition temperature of $H^+$-form Nafion® 117 to the weak β-relaxation centered at -20 °C.[84] In DMA experiments on Nafion® membranes that were partially neutralized to contain $TBA^+$-ions, a strong and uniform compositional dependence was observed for the β-relaxation (Figure I-19). In contrast, the α-relaxation remained relatively independent of composition because both $H^+$ and $TBA^+$-form Nafion® membranes possess the α-relaxation at around 110 °C (Figure I-19).

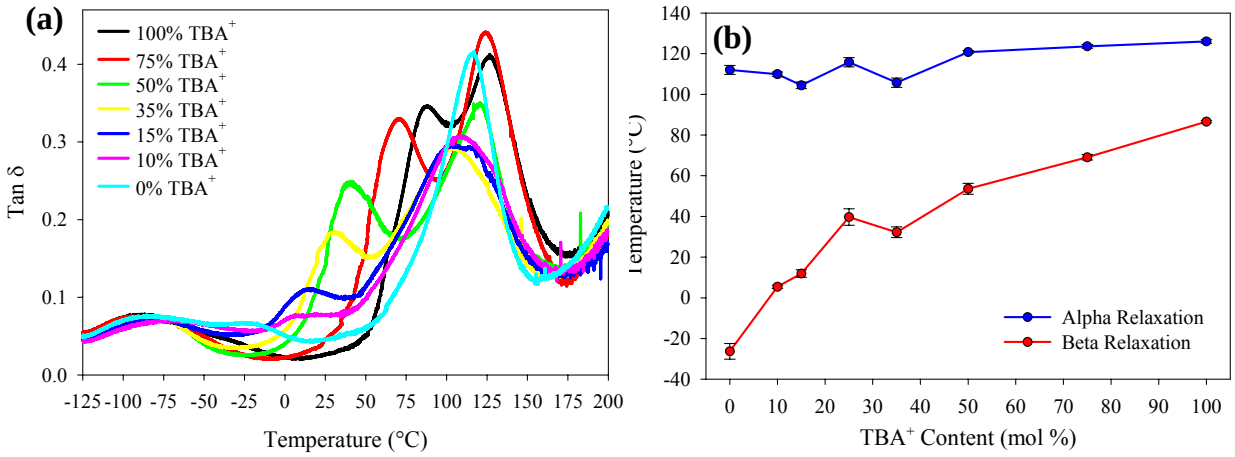


**Figure I-19.** (a) Dynamic mechanical tan δ versus temperature of partially neutralized Nafion® 117 for 100, 75, 50, 35, 15, 10, and 0% $TBA^+$ counterion compositions. (b) α and β-relaxation temperatures as a function of $TBA^+$ content. (Reprinted with permission from ref[84] *Macromolecules*, **40**, 3886 (2007). Copyright 2007, American Chemical Society)

## H. Applications

While various interesting and important practical uses of Nafion® membranes can be found in the literature[6], the primary applications have been in electrochemical cells such as (1)

chlor-alkali cells[1] and (2) proton exchange membrane fuel cells (PEMFCs)[4,5]. In all cases, the Nafion® membrane functions as a separator where it allows a flow of specific ionic charges and at the same time prevent the transfer of chemical species which remain located in the cathodic or anodic compartment. In chlor-alkali cells, the PFSI membrane separates two half-cells that produce $Cl_2$ gas in the anode and $H_2$ gas and NaOH in the cathode. Aqueous sodium chloride (NaCl) is fed into the anodic compartment of the cell and a DC current passing through the cell causes NaCl to split into $Na^+$ and $Cl^-$. Then chloride ions become oxidized at the anode to give off chlorine gas:

$2Cl^- \rightarrow Cl_2 + 2e^-$ (Anode Half-cell) **Eq I-6**

At the cathode, hydrogen in the water is reduced to hydrogen gas, releasing hydroxide ions into the solution:

$2H_2O + 2e^- \rightarrow H_2 + 2OH^-$ (Cathode Half-cell) **Eq I-7**

The PFSI membrane at the center of the cell transports the sodium ions ($Na^+$) to the cathode chamber where they react with the hydroxide ions to produce NaOH. A membrane cell is used to prevent the reaction between the chlorine and hydroxide ions. The overall reaction for the electrolysis of brine is thus:

$2NaCl + 2H_2O \rightarrow Cl_2 + H_2 + 2NaOH$ (Overall Cell Reaction) **Eq I-8**

With greater system efficiencies and environmental benefits, proton-exchange membrane fuel cells (PEMFCs) have become an attractive system as an alternative to nonrenewable, traditional energy sources.[3] Currently, perfluorosulfonate ionomers (PFSIs), particularly Nafion®, are the benchmark proton exchange membranes due to their unique morphology,

chemical stability, and excellent transport properties. In fuel cells, electrical energy is produced by conversion of chemical energy via redox reactions at the anode and cathode. Figure I-20 represents a basic hydrogen-oxygen fuel cell showing the continuous supply of reactant (hydrogen at the anode and oxygen at the cathode) and redox reactions in the cell. At the anode, hydrogen gas is first reduced to produce protons (Eq I-9), which travel to the cathode across the membrane, and electrons which are forced to travel through an external circuit driving some device. After crossing the membrane, the protons combine with oxygen at the cathode producing water (Eq I-10). An overall reaction is expressed in Eq I-11, which is the reverse hydrolysis of water.

$H_2 \rightarrow 2\ H^+ + 2e^-$ (Anode Half-cell) **Eq I-9**

$4\ H^+ + O_2 + 4e^- \rightarrow 2H_2O$ (Cathode Half-cell) **Eq I-10**

$2\ H_2 + O_2 \rightarrow 2H_2O$ (Overall Cell Reaction) **Eq I-11**

As can be observed from the overall cell reaction, water is produced as a byproduct and accumulated at the cathode as a function of time.[85] Additionally, water is transported within the cell by electro-osmotic drag.[86] While higher water content in the polymer electrolyte is beneficial for effective proton transport, an excess of water may be detrimental to the overall fuel cell performance because the existence of the liquid water prevents the access of reactants to the active electrochemical sites. Thus, the determination of the content and spatial distribution of water within a proton exchange membrane fuel cell (PEMFC) *under working conditions* is of fundamental importance in modern PEMFC technology.[85,87-89]

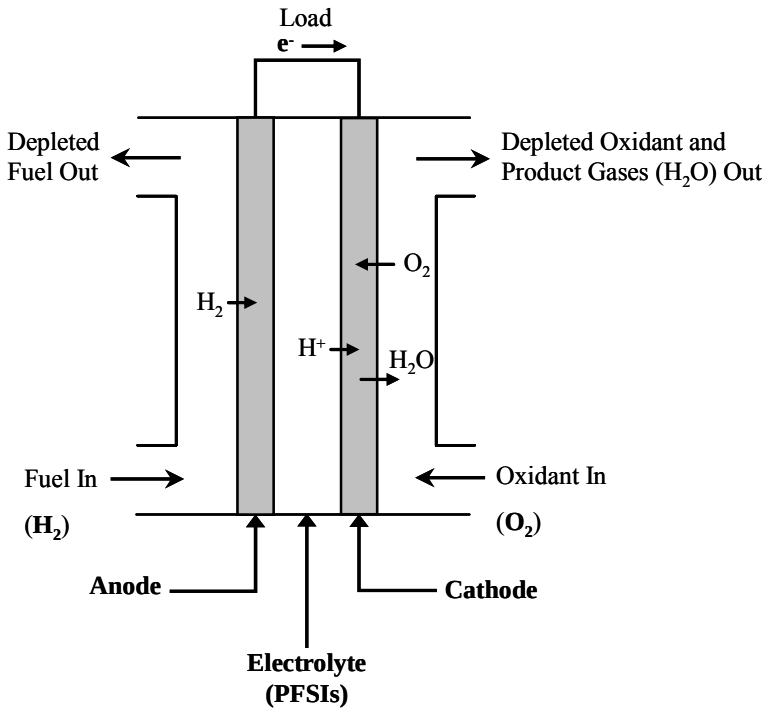


**Figure I-20.** Proton exchange membrane fuel cell (PEMFC)

## I. References


(1) Grot, W. *Chemie Ingenieur Technik* **1978**, *50*, 299-301.
(2) Yeo, R. S.; McBreen, J.; Kissel, G.; Kulesa, F.; Srinivasan, S. *J. Appl. Electrochem.* **1980**, *10*, 741-747.
(3) Winter, M.; Brodd, R. J. *Chem. Rev.* **2004**, *104*, 4245-4269.
(4) Doyle, M.; Rajendran, G. In *Handbook of Fuel Cells-Fundamentals, Technology and Applications*; Wielstich, W., Lamm, A., Gasteiger, H. A., Eds.; John Wiley & Sons: Chichester, 2003; Vol. 3; pp 351-395.
(5) Mauritz, K. A.; Moore, R. B. *Chem. Rev.* **2004**, *104*, 4535-4585.
(6) Park, J. K.; Moore, R. B. *ACS Appl. Mater. Interfaces* **2009**, *1*, 697-702.
(7) Connolly, D. J.; Gresham, W. F., 1966.
(8) Ezzell, B. R.; Carl, W. P.; Mod, W. A., 1982.
(9) Ezzell, B. R.; Carl, W. P.; Mod, W. A., 1982.
(10) Emery, M.; Frey, M.; Guerra, M.; Haugen, G. M.; Hintzer, K.; Lochhaas, K. H.; Pham, P.; Pierpont, D. M.; Schaberg, M.; Thaler, A.; Yandrasits, M. A.; Hamrock, S. J. *ECS Transactions* **2007**, *11*, 3-14.
(11) Gebel, G.; Moore, R. B. *Macromolecules* **2000**, *33*, 4850-4855.
(12) Moore, R. B.; Martin, C. B. *Macromolecules* **1989**, *22*, 3594-3599.
(13) Pourcelly, G.; Gavach, C. In *Proton Conductors: Solids, Membranes and Gels; Materials and Devices*; Colomban, P., Ed.; Cambridge University Press: Cambridge, 1992; pp 294-310.
(14) E. I. Dupont De Nemours & Co Inc., 2002; Vol. 2009.
(15) Curtin, D. E.; Lousenberg, R. D.; Henry, T. J.; Tangeman, P. C.; Tisack, M. E. *J. Power Sources* **2004**, *131*, 41-48.
(16) Osborn, S. J.; Mauritz, K. A.; Moore, R. B. *Polym. Prepr.* **2008**, *49*, 473-474.
(17) Fujimura, M.; Hashimoto, T.; Kawai, H. *Macromolecules* **1982**, *15*, 136-144.
(18) Starkweather, H. W. *Macromolecules* **1982**, *15*, 320-323.
(19) Gierke, T. D.; Munn, G. E.; Wilson, F. C. *J. Polym. Sci. Polym. Phys. Ed.* **1981**, *19*, 1687-1704.
(20) Schmidt-Rohr, K.; Chen, Q. *Nat. Mater.* **2008**, *7*, 75-83.
(21) Dreyfus, B.; Gebel, G.; Aldebert, P.; Pineri, M.; Escoubes, M.; Thomas, M. *J. Phys. France* **1990**, *51*, 1341-1354.
(22) Hsu, W. Y.; Gierke, T. D. *J. Membr. Sci.* **1983**, *13*, 307-326.
(23) Cable, K. M.; Mauritz, K. A.; Moore, R. B. *Chem. Mater.* **1995**, *7*, 1601-1603.
(24) Allahyarov, E.; Taylor, P. L. *J. Phys. Chem. B* **2009**, *113*, 610-617.
(25) Fujimura, M.; Hashimoto, T.; Kawai, H. *Macromolecules* **1982**, *15*, 136-144.
(26) Litt, M. H. *Polym. Prepr.* **1997**, *38*, 80-81.
(27) Elliott, J. A.; Hanna, S.; Elliott, A. M. S.; Cooley, G. E. *Macromolecules* **2000**, *33*, 4161-4171.
(28) Gebel, G. *Polymer* **2000**, *41*, 5829-5838.
(29) Haubold, H. G.; Vad, T.; Jungbluth, H.; Hiller, P. *Electrochim Acta* **2001**, *46*, 1559-1563.
(30) Londono, J. D.; Davidson, R. V.; Mazur, S. *Polym. Mater.: Sci. Eng.* **2001**, *85*, 23.
(31) Rubatat, L.; Rollet, A. L.; Gebel, G.; Diat, O. *Macromolecules* **2002**, *35*, 4050-4055.
(32) van der Heijden, P. C.; Rubatat, L.; Diat, O. *Macromolecules* **2004**, *37*, 5327-5336.
(33) Page, K. A.; Cable, K. M.; Moore, R. B. *Macromolecules* **2005**, *38*, 6472-6484.
(34) Kim, M.-H.; Glinka, C. J.; Grot, S. A.; Grot, W. G. *Macromolecules* **2006**, *39*, 4775-4787.
(35) Page, K. A.; Landis, F. A.; Phillips, A. K.; Moore, R. B. *Macromolecules* **2006**, *39*, 3939-3946.
(36) Rubatat, L.; Diat, O. *Macromolecules* **2007**, *40*, 9455-9462.
(37) Gebel, G.; Lambard, J. *Macromolecules* **1997**, *30*, 7914-7920.
(38) Chen, Q.; Schmidt-Rohr, K. *Macromol. Chem. Phys.* **2007**, *208*, 2189-2203.
(39) Loppinet, B.; Gebel, G.; Williams, C. E. *Journal of Physical Chemistry B* **1997**, *101*, 1884-1892.
(40) Loppinet, B.; Gebel, G. *Langmuir* **1998**, *14*, 1977-1983.
(41) Rubatat, L.; Gebel, G.; Diat, O. *Macromolecules* **2004**, *37*, 7772-7783.

(42) Roe, R.-J. *Methods of X-ray and neutron scattering in polymer science*; Oxford University Press: New York, 2000.
(43) Moore, R. B.; Cable, K. M.; Croley, T. L. *J. Membr. Sci.* **1992**, *75*, 7-14.
(44) Moore, R. B.; Martin, C. R. *Anal. Chem.* **1986**, *58*, 2569-2570.
(45) Grot, W. G., 1982.
(46) Martin, C. R.; Rhoades, T. A.; Ferguson, J. A. *Anal. Chem.* **1982**, *54*, 1639-1641.
(47) Moore, R. B.; Martin, C. R. *Macromolecules* **1988**, *88*, 1334-1339.
(48) Rubatat, L.; Diat, O. *Macromolecules* **2007**, *40*, 9455-9462.
(49) Chourdakis, N.; Voyiatzis, G. A. *J. Polym. Sci. Pol. Phys.* **2007**, *45*, 2509-2517.
(50) Li, J.; Wilmsmeyer, K. G.; Madsen, L. A. *Macromolecules* **2009**, *42*, 255-262.
(51) Lin, J.; Wu, P.-H.; Wycisk, R.; Pintauro, P. N.; Shi, Z. *Macromolecules* **2008**, *41*, 4284-4289.
(52) Kidena, K. *J. Membrane Sci.* **2008**, *323*, 201-206.
(53) Ma, S.; Siroma, Z.; Tanaka, H. *J. Electrochem. Soc.* **2006**, *153*, A2274-A2281.
(54) Elliott, J. A.; Hanna, S.; Elliott, A. M. S.; Cooley, G. E. *Polymer* **2001**, *42*, 2251-2253.
(55) Tosaka, M.; Tsuji, M.; Ogawa, T.; Kitano, H.; Nakano, K.; Kohjiya, S.; Danev, R.; Nagayama, K. *Polymer* **2006**, *47*, 951-955.
(56) Londono, J. D.; Davidson, R. V.; Mazur, S. *Polym. Mater.: Sci. Eng.* **2001**, *85*, 23-24.
(57) Lin, J.; Wu, P.-H.; Wycisk, R.; Trivisonno, A.; Pintauro, P. N. *J. Power Sources* **2008**, *183*, 491-497.
(58) Lin, H.-L.; Yu, T. L.; Han, F.-H. *J. Polym. Res.* **2006**, *13*, 379-385.
(59) Li, J.; Wilmsmeyer, K. G.; Madsen, L. A. *Macromolecules* **2008**, *41*, 4555-4557.
(60) Yeo, R. S. *J. Electrochem. Soc.* **1983**, *130*, 533-538.
(61) Pourcelly, G.; Oikonomou, A.; Gavach, C. *J. Electroanal. Chem.* **1990**, *287*, 43-59.
(62) Kreuer, K.-D. *Chem. Mater.* **1996**, *8*, 610-641.
(63) Lee, C. H.; Park, H. B.; Lee, Y. M.; Lee, R. D. *Ind. Eng. Chem. Res.* **2005**, *44*, 7617-7626.
(64) Thomas A. Zawodzinski Jr.; Neeman, M.; Sillerud, L. O.; Gottesfeld, S. *J. Phys. Chem.* **1991**, *95*, 6040-6044.
(65) Edmondson, C. A.; Stallworth, P. E.; Wintersgill, M. C.; Fontanella, J. J.; Dai, Y.; Greenbaum, S. G. *Electrochim Acta* **1998**, *43*, 1295-1299.
(66) Rieke, P. C.; Vanderborgh, N. E. *J. Membrane Sci.* **1987**, *32*, 313-328.
(67) Nouel, K. M.; Fedkiw, P. S. *Electrochim Acta* **1998**, *43*, 2381-2387.
(68) Wakizoe, M.; Velev, O. A.; Srinivasan, S. *Electrochim Acta* **1995**, *40*, 335-344.
(69) Buchi, F. N.; Scherer, G. G. *J. Electroanal. Chem.* **1996**, *404*, 37-43.
(70) Slade, S.; Campbell, S. A.; Ralph, T. R.; Walsh, F. C. *J. Electrochem. Soc.* **2002**, *149*, A1556-A1564.
(71) Kreuer, K. D. *Solid State Ionics* **2000**, *136-137*, 149-160.
(72) Thampan, T.; Malhotra, S.; Tang, H.; Datta, R. *J. Electrochem. Soc.* **2000**, *147*, 3242-3250.
(73) Zawodzinski, T. A.; Derouin, C.; Radzinski, S.; Sherman, R. J.; Smith, V. T.; Springer, T. E.; Gottesfeld, S. *J. Electrochem. Soc.* **1993**, *140*, 1041-1047.
(74) Zawodzinski, T. A.; Neeman, M.; Sillerud, L. O.; Gottesfeld, S. *J. Phys. Chem.* **1991**, *95*, 6040-6044.
(75) Ohkubo, T.; Kidena, K.; Ohira, A. *Macromolecules* **2008**, *41*, 8688-8693.
(76) Saito, M.; Arimura, N.; Hayamizu, K.; Okada, T. *J. PHys. Chem. B* **2004**, *108*, 16064-16070.
(77) Gong, X.; Bandis, A.; Tao, A.; Meresi, G.; Wang, Y.; Inglefield, P. T.; Jones, A. A.; Wen, W.-Y. *Polymer* **2001**, *42*, 6486-6492.
(78) Zhang, J.; Giotto, M. V.; Wen, W.-Y.; Jones, A. A. *J. Membrane Sci.* **2006**, *269*, 118-125.
(79) Page, K. A.; Park, J. K.; Moore, R. B.; Sakai, V. G. *Macromolecules* **2009**, *42*, 2729-2736.
(80) Yeo, S.; Eisenberg, A. *J. Appl. Polymer Sci.* **1977**, *21*, 875-898.
(81) Kyu, T.; Hashiyama, M.; Eisenberg, A. *Can. J. Chem.* **1983**, *61*, 680-687.
(82) Cable, K. M.; Gatlin, M. E.; Mauritz, K. A.; Moore, R. B. *Polym. Prepr.* **1995**, *36*, 374-375.
(83) Moore, R. B.; Cable, K. *Polym. Prepr.* **1997**, *38*, 272-273.

(84) Osborn, S.; Hassan, M.; Divoux, G.; Rhoades, D.; Mauritz, K.; Moore, R. B. *Macromolecules* **2007**, *40*, 3886-3890.
(85) Hickner, M. A.; Siegel, N. P.; Chen, K. S.; McBrayer, D. N.; Hussey, D. S.; Jacobson, D. L.; Arif, M. *J. Electrochem. Soc.* **2006**, *153*, A902-A908.
(86) Ren, X.; Gottesfeld, S. *J. Electrochem. Soc.* **2001**, *148*, A87-A93.
(87) Bellows, R. J.; Lin, M. Y.; Arif, M.; Thompson, A. K.; Jacobson, D. *J. Electrochem. Soc.* **1999**, *146*, 1099-1103.
(88) Satija, R.; Jacobson, D. L.; Arif, M.; Werner, S. A. *J. Power Sources* **2004**, *129*, 238-245.
(89) Feindel, K. W.; Bergens, S. H.; Wasylishen, R. E. *J. Am. Chem. Soc.* **2006**, *128*, 14192-14199.

# CHAPTER II

# DIRECT ANALYSIS OF THE ION-HOPPING PROCESS ASSOCIATED WITH THE α-RELAXATION IN PERFLUOROSULFONATE IONOMERS USING QUASIELASTIC NEUTRON SCATTERING

*This chapter is reformatted from [Page, Kirt A.; Park, Jong Keun; Moore, Robert B.; Garcia Sakai, Victoria, "Direct Analysis of the Ion-hopping Process Associated with the α-Relaxation in Perfluorosulfonate Ionomers using Quasielastic Neutron Scattering", *Macromolecules* **2009,** 42, 2729-2736].

## A. Introduction

Ionomers are an interesting class of polymeric materials that contain ionic comonomer units distributed along the polymer backbone and have been the focus of many studies over the last several decades.[1-17] The physical properties of these materials are dictated by the Coulombic interactions between the ion-pairs along the backbone. These electrostatic interactions lead to the formation of stable ionic associations that behave in many ways as cross-links. In particular, the relaxation behavior of these materials is greatly affected by these associations, and the resulting aggregates (multiplets), and has been the focus of several rheological studies.[11-14,16,17] Several studies have shown that the rheological behavior of these materials can be altered simply by changing the degree of neutralization or through choice of the counterion, factors that can be expected to influence the strength of the associations.[7] In particular, and pertinent to later discussion, early patent literature describes the neutralization of ionomers with alkylammonium ions and subsequent changes in the rheological properties.[18] In addition, Weiss et al.[15] observed a decrease in the viscosity of alkylamine neutralized polystyrene ionomers with an increase in

the bulkiness of the counterion and found that electrostatic interactions predominate for smaller counterions, while plasticization (increase in the segmental dynamics) is more important as the counterion becomes sufficiently bulky. These, and other studies, show that by changing the overall number and strength of the electrostatic interactions, a large degree of control can be exerted over the relaxation processes in these materials.

Although it is beyond the scope of this discussion, there have been several investigations of the relaxation behavior of ion containing polymers.[1,10] In short, two 'glass transition' temperatures ($T_g$) have been reported for ion-containing polymers: one attributed to the $T_g$ of the 'matrix' chains removed from the ionic aggregates and the other attributed to the $T_g$ of the 'cluster' domains, or chains in the vicinity of an ionic aggregate that have a restricted mobility due to decreased conformational entropy. The previous work by Page et al. has shown that for perfluorosulfonate ionomers (PFSIs) this description of the relaxation processes is not entirely accurate.[19,20] However, there are similarities of the description of the relaxations in PFSI's and the classical ionomer description.

The two predominant relaxation processes governing the melt rheological behavior of ionomers, in general, are (1) the terminal relaxation time of the polymer chains and (2) the average lifetime of the ionic associations.[13] Ultimately, the terminal relaxation time is dictated by the time that an ionic group resides in an aggregate before "hopping" to another aggregation site. This process has been termed "ion-hopping" and $\tau$ is the ion-hopping time.[2,4,9,11-14,21] The relative time scale of these two processes has been studied using rheology and cation diffusion measurements. The onset of this ion hopping process has been experimentally observed for both styrenecarboxylates and styrenesulfonates.[9,21,22] Ion-hopping has been identified as the mechanism for the cluster 'glass transition', or $\alpha$-relaxation process, for these materials.

Essentially, the presence of appreciable ion-hopping means the ionic aggregates are dynamic and the rigidity of the system is reduced because of the labile nature of these associations.[1] The concept of a temperature at which the electrostatic crosslinks (i.e., multiplets) become thermodynamically unstable was proposed by Eisenberg in a theoretical description of clustering in ionomers in 1970.[3] The 'ion-hopping temperature', of Eisenberg's, is defined as the temperature at which the multiplet becomes thermodynamically unstable and the elastic forces of the chain are balanced with the electrostatic forces of the aggregates.[3] The previous work by Page et al. has drawn upon the concept of ion-hopping to explain the molecular origins of the relaxation processes in PFSI's.[19,20] It should be clarified that we are careful not to definitively assign the $\alpha$-relaxation to a pure glass transition temperature, but rather to a transition from a state exhibiting static electrostatic cross-links to a state exhibiting dynamic electrostatic cross-links brought about by the onset of ion-hopping.

Recent simulations of ionomer self-assembly by Kumar and coworkers[23] provide some basic insights into the nature of these fluids. Upon cooling, there is first a transition where the counterions pair with the ions on the chain backbone to form small ion-multiplet structures that remain quite mobile. The character of these ion pairs in 'primitive model' ionic fluids has been shown to depend on ion valence and ion size asymmetry,[24,25] forming dipolar, or multiple, low energy structures depending on these asymmetry factors. The long range interactions of the small ion-multiplet structures lead to the supermolecular assembly of the small ion-multiplets (ribbon-like structures in the simulations of Kumar and coworkers) in a well-defined order-disorder transition upon further cooling characterized by a maximum in the specific heat and a sharp drop in the mobility of counterions that have been incorporated into the self-assembled structures. Kumar and coworkers suggest that this self-assembly transition can be identified with

the 'cluster $T_g$' of Eisenberg.[3,4,23] The second, lower $T_g$, is naturally attributed to the conventional $T_g$ of the polymeric structures with the large-scale supermolecularly assembled ionomer multiplet structures. The description put forth by the simulations of Kumar *et al.*[23] is congruent with earlier descriptions of the relaxation processes for PFSI's. It is apparent that the 'self-assembly' of the ion pairs into supermolecular structures that they observe upon cooling corresponds to the same process involved in destabilization of the electrostatic network upon heating described in earlier work.

Nafion® is a widely examined PFSI and the focus of our work.[26]

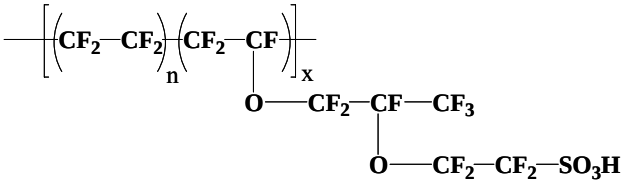

The perfluoroether side-chains containing the ionic, sulfonate groups have been shown to organize into aggregates, thus leading to a nanophase-separated morphology where the ionic domains, termed clusters, are distributed throughout the non-polar polytetrafluoroethylene (PTFE) matrix. This morphology gives a characteristic scattering peak in small angle x-ray and neutron scattering centered at Q = 0.20 $Å^{-1}$.[26] The membranes used in this study have been neutralized with tetramethyl-($TMA^+$) and tetrabutyl-($TBA^+$) ammonium counterions according to previously published methods.[19,20] The size, or polarizability, of the counter-ion influences the strength of the electrostatic network, thus changing the chain dynamics and, in turn, the mechanical properties.[19,20]

Our earlier studies of these materials correlating dynamic mechanical analysis (DMA) with a variety of other techniques show that the α-relaxation of these materials is due to the onset

of long-range mobility of both the main- and side-chains, which is facilitated by a profound weakening of the electrostatic interactions within the ionic aggregates. At temperatures in the vicinity of the α-relaxation ($T_\alpha$), a significant destabilization of the electrostatic network may be observed, which results in the activation of a *dynamic* network facilitated through the ion-hopping process described above. In contrast, the β-relaxation ($T_\beta$) was associated with the onset of segmental motions (principally backbone motions) within the framework of a *static* physically cross-linked network of chains.[19,20]

The present work uses quasielastic neutron scattering (QENS) to investigate the correlations between counter-ion dynamics and the bulk mechanical relaxations in alkyl ammonium neutralized PFSIs in order to obtain a better understanding of the physical basis of the relaxation processes in these materials. QENS provides a direct measure of counterion dynamics, making it possible to calculate time-scales associated with the motions of the ions and ion diffusion coefficients for temperatures above the α-relaxation. QENS measures the dynamic structure factor in the frequency domain, thus providing information about the motions of atoms, or molecules, on the time scale of $10^{-8}$ seconds to $10^{-13}$ seconds. QENS is sensitive to the motion of hydrogen atoms, which have a significantly larger incoherent scattering length than other atoms. In the systems presented here, only the counterions contain hydrogen, thus allowing us to isolate the dynamics of the counterions. We use QENS to study the counter-ion dynamics, and thus directly confirm and characterize the ion-hopping process.

## B. Experimental

***Materials.*** Nafion® 117 (1100 EW, sulfonic acid form) films were obtained from E. I. DuPont de Nemours & Co. The tetra-methyl ($TMA^+$), ethyl ($TEA^+$) and butylammonium

($TBA^+$) counterions were obtained from Aldrich in the form of hydroxides dissolved in either water or methanol. All other reagents were obtained from Aldrich and used without further purification.

***PFSI Sample Preparation.*** The PFSI membranes were cleaned by refluxing in 4 mol/L methanolic $H_2SO_4$ for ca. 12 h. These $H^+$-form membranes were then washed with deionized (DI) water to remove excess acid. The $TMA^+$, $TEA^+$ and $TBA^+$ form samples were prepared by soaking the $H^+$-form membranes in a 5 molar excess of solutions of the appropriate alkylammonium hydroxide. The neutralized membranes were then thoroughly rinsed of excess alkylammonium hydroxide and dried in a vacuum oven at 70 °C for 12 hr.

***Quasielastic Neutron Scattering.*** The QENS experiments were performed on the High-Flux Back-scattering Spectrometer (HFBS)[27] at the National Institute of Standards and Technology (NIST) Center for Neutron Research (NCNR). Films of 145 μm thickness (5.5 cm x 8 cm), to achieve ~ 90 % neutron transmission through the sample and avoid multiple scattering, were loaded into annular, thin-walled (500 μm) aluminum cells and mounted to closed-cycle refrigerator unit. Initial temperature scans with the instrument in the so-called fixed window mode, where only the elastic scattering is measured, over a temperature range from -223 $^oC$ to 277 °C, at a heating rate of 1 °C/min and over a momentum transfer (or scattering vector, Q) range from 0.25 $Å^{-1}$ to 1.75 $Å^{-1}$. The raw data were normalized to the beam monitor. In general, such scans are comparable to thermal techniques such as differential scanning calorimetry (DSC) scans and clearly show relaxations in the system. Further information regarding the dynamics of the counter-ions was obtained from measuring the dynamic structure factor, $S(Q,\omega)$, at different temperatures using an energy range of ± 17 μeV (resolution of 0.85 μeV) and over a Q range of 0.25 $Å^{-1}$ to 1.75 $Å^{-1}$. The data was reduced by taking into consideration contributions from

absorption and detector efficiency. The instrument resolution function was measured by performing a dynamic scan on the sample at -233 °C. At this temperature we assume that all motions are "frozen" and that the scattering is purely elastic. The data reduction and the analysis, including peak deconvolution were carried out using DAVE [Data Analysis and Visualization Environment], a software package developed at the NCNR.[28]

***Small-angle X-ray and Neutron Scattering (SAXS/SANS).*** Variable temperature (VT), time-resolved small-angle X-ray scattering was performed at the Brookhaven National Laboratory on the Advanced Polymer Beamline (X27C) at the National Synchrotron Light Source. The incident x-ray beam was tuned to a wavelength of 0.1366 nm and the sample to detector distance was 85 cm. The two dimensional scattering images were recorded using a Mar CCD camera with an intensity uncertainty on the order of 2 %. The Nafion® samples were heated in a sample chamber in the X-ray beam at a heating rate of 5°C/min with an uncertainty of ± 1 °C while acquisition times were kept to 1 min and data were recorded from 50 °C to 300 °C. Intensity versus pixel data was obtained from the integration of the 2-D images using the POLAR software developed by Stonybrook Technology and Applied Research, Inc. The relationship between pixel and the momentum transfer vector Q was determined by calibrating the scattering data with a silver behenate standard. All scattering intensities were corrected for transmission, incident beam flux, and background scatter due to air and Kapton windows.

The SANS measurements were carried out on the NG7 beamline at the NCNR. The NG7 beamline includes a high-resolution 2D neutron detector (65 x 65) $cm^2$ and focusing refractive lenses. The instrument employs a mechanical velocity selector as a monochromator and a circular pinhole collimator. The SANS intensity, $I$, was recorded as a function of the magnitude of the scattering vector Q ($Q = 4\pi \sin(\theta/2)/\lambda$, where $\theta$ is the scattering angle and $\lambda$ is the neutron

wavelength, equal to 6 Å) and corrected for film thickness and background. The detector angle was set at $0^o$, and the sample-to-detector distance was set to 1 m, 4.5 m, and 13 m to cover the Q range of 0.003 $Å^{-1}$ to 0.6 $Å^{-1}$. These settings enable one to probe structural features in materials ranging from approximately 10 Å to 2000 Å. The intensity was corrected for background scatter, sample thickness, and detector dark current using software developed at the NCNR.[29]

***Wide-angle X-ray Diffraction (WAXD).*** Synchrotron wide-angle X-ray diffraction (WAXD) was performed at the Argonne National Laboratory on the DND-CAT (5-ID) beamline at the Advanced Photon Source. The wavelength of the incident x-ray was 0.82656 Å and the sample-to-detector distance was 236 mm. The samples were heated from 50 °C to 300 °C using a Linkam heating stage (THMS600) at a heating rate of 5 °C/min (temperature stability < 0.1 °C) and two-dimensional scattering patterns were recorded every 10 °C using a Roper Scientific detector. All scattering intensities were corrected for incident beam flux, background scatter due to air, and thickness of each sample. The scattering profiles are displayed as absolute intensity ($cm^{-1}$) as a function of the scattering vector, Q.

## C. Results and Discussion

### SAXS/WAXD/SANS

***Variable Temperature SAXS/WAXD.*** To ensure that we can eliminate potential contributions from melting of PFSI crystallites on the α-relaxation, we have investigated the effect of counterion on the melting behavior and, thus the α-relaxation in these systems. In order to determine whether changes in the α-relaxation temperature as a function of counterion are related to melting of the Nafion® crystallites, VT-SAXS and VT-WAXD experiments were performed. The VT-SAXS patterns for $TMA^+$ and $TBA^+$ Nafion® can be seen in Figure II-1a

and b. The peak at approximately 0.045 $Å^{-1}$ arises from the long-range correlations between the Nafion® crystallites. One can see that the long-period peak, due to the crystallites, begins to decrease in intensity at temperatures between 243 °C and 248 °C for $TMA^+$ and between 237 °C and 248 °C for $TBA^+$ Nafion®. This demonstrates that melting is only slightly affected by the choice of the counterion. Further confirmation of this can be found in the VT-WAXD. Figure II-2a and b show the WAXD patterns for $TMA^+$ and $TBA^+$ Nafion® over the temperature range of 220 °C to 300 °C. There are many features in the WAXD, however, discussion will be limited to the peak at approximately 1.2 $Å^{-1}$, which is due to the (100) plane of the Nafion® crystallites. Again, these data show that the crystalline peak decreases (due to melting) in an identical fashion for both counterion types. However, unlike the counterion independent melting, it has been demonstrated[19,20,30] that the α-relaxation temperature can be changed by as much as 137 °C just by changing the counterion from $TMA^+$ to $TBA^+$. This is clear evidence that the presence of crystallinity has little, if any, effect of the α-relaxation for these materials.

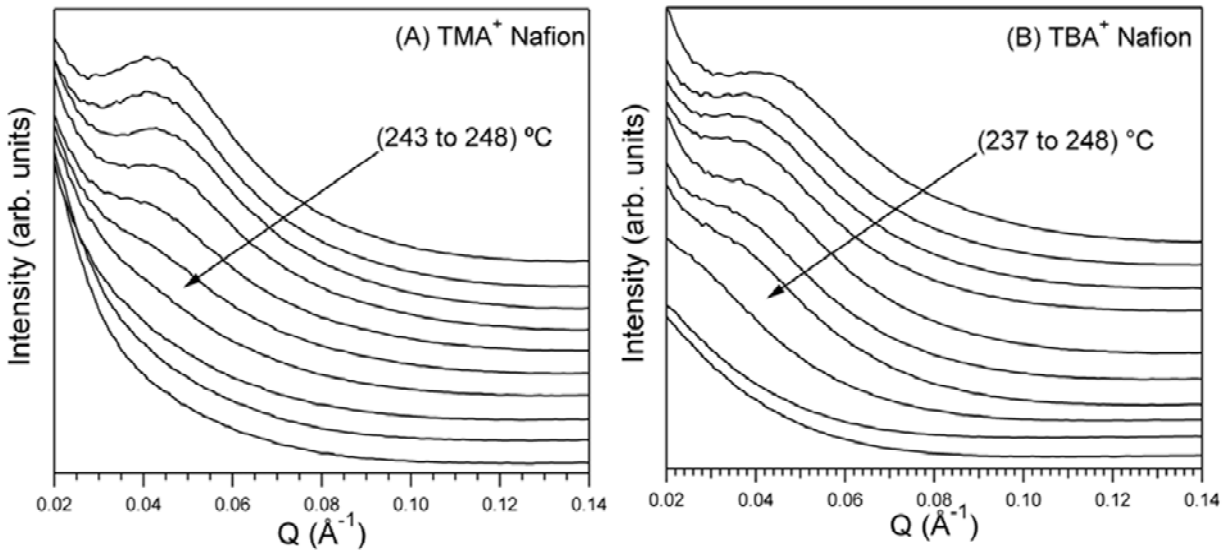


**Figure II-1**. Variable temperature SAXS profiles for (a) $TMA^+$ and (b) $TBA^+$ Nafion®.

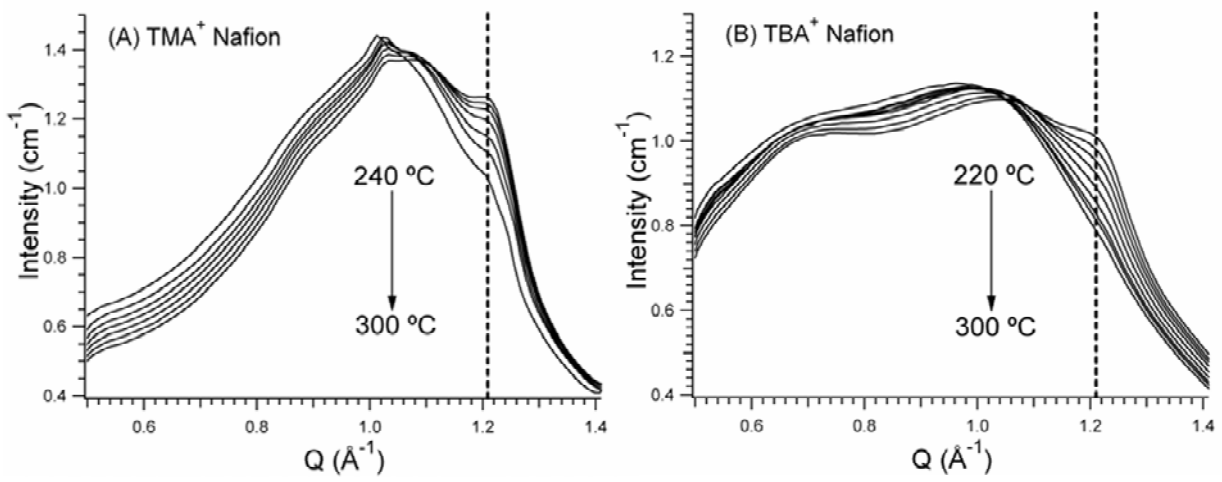


**Figure II-2**. Variable temperature WAXD profiles for (a) $TMA^+$ and (b) $TBA^+$ Nafion®.

***SANS.*** In order to gain insight into the dynamics as measured by QENS, it is necessary to measure the neutron scattering behavior of these materials. The SANS data for both $TMA^+$ and $TBA^+$ Nafion® are shown in Figure II-3. As discussed earlier, the peak at approximately 0.2 $Å^{-1}$ is due to the inter-aggregate spacing. Although there is still much debate over the exact morphological structures giving rise to this peak, this discussion is not in the scope of this publication and it is important only that this peak is, indeed, due to correlations between domains containing the counterions in the system. The line at 0.25 $Å^{-1}$ shows the lowest Q value accessible by HFBS at NIST. While this Q value is not sufficiently low enough to match the exact length scale associated with the aggregates, there is still enough intensity due to scattering from the ionomer structure to describe the dynamics of the counterions on a length scale close to that of the inter-aggregate spacing.

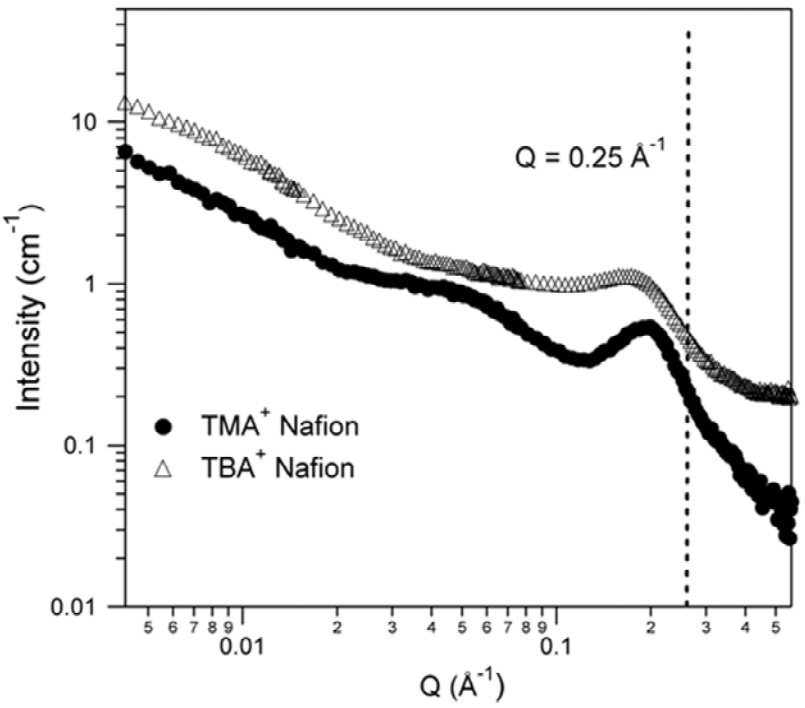


**Figure II-3.** SANS profiles for (○)$TMA^+$ and (□)$TBA^+$ Nafion®. The peak at ca. 0.2 $Å^{-1}$ is the ionomer peak. The dotted line represents the Q value, 0.25 $Å^{-1}$, at which the QENS fixed-window scans were taken.

## QUASIELASTIC NEUTRON SCATTERING (QENS).

***Variable Temperature Elastic Scattering.*** The temperature-dependent elastic scattering at wavevectors of Q=0.25 $Å^{-1}$ and Q=0.99 $Å^{-1}$ (Q=2π/d, where d is the length scale of motion) for $TMA^+$, $TEA^+$, and $TBA^+$ Nafion® can be seen in Figure II-4a and b. For Q=0.25 $Å^{-1}$, Figure II-4a, the elastic scattering from each sample exhibits a distinct drop in intensity, which is attributed to the onset of mobility of the counter-ions having motions on a length scale of approximately 25 Å. The transition observed from the fixed-window data was determined from the intersection of two lines taken on each side of the transition. The results of this estimation

are shown in Table II-1 along with data from dynamic mechanical analysis (DMA) adopted from the previous work.[19,20] The most striking feature of this data is the excellent correlation between the transition temperature in the elastic scattering intensity and the α-relaxation temperature ($T_\alpha$) obtained by DMA. These data give unequivocal evidence that the α-relaxation is linked with the onset of "long-range" mobility of the counter-ions, thus lending support to our previous assignment of the molecular origins of the α-relaxation to an ion-hopping transition.[19,20]

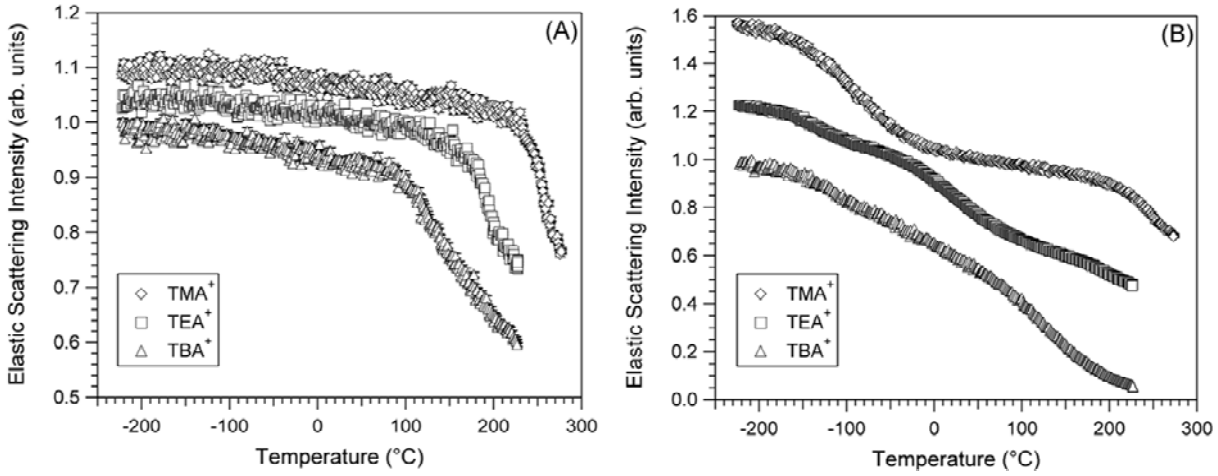


**Figure II-4**. Fixed-window, elastic scans for (◇)$TMA^+$, (□)$TEA^+$, and (△)$TBA^+$ Nafion® at (A) Q = 0.25 $Å^{-1}$ and (B) Q = 0.99 $Å^{-1}$.

**Table II-1**. Comparison of mechanical data from references 19 and 20 with the QENS measurements.

| **Counterion form** | **DMA** | | **QENS** |
|---|---|---|---|
| | $T_\alpha$ | $T_\beta$ | |
| $TMA^+$ | 237 °C | 133 °C | 234 °C |
| $TEA^+$ | 160 °C | 111 °C | 167 °C |
| $TBA^+$ | 100 °C | 72 °C | 97 °C |

It is interesting that the fast relaxations (ca. $10^8$ Hz) measured by QENS are comparable to relaxations measured by other techniques such as DMA, differential scanning calorimetry (DSC) and dielectric measurements, which probe relaxations on a much longer time scale. However, there is sufficient precedence in the literature for comparing QENS measurements to other more "macroscopic" techniques, such as DSC, when studying the nature of transitions in polymer systems, especially the glass transition.[31-35] The reader is directed toward a discussion for this comparison by Ngai and coworkers in the context of glass-forming liquids.[35] In general, the transitions observed in the elastic scattering, measured by QENS, are sensitive to changes in the mean square displacement, $\langle u^2 \rangle$ (i.e. the Debye-Waller factor), of the scattering particles. For glass forming liquids, it has been demonstrated that $\langle u^2 \rangle$ shows a sharp increase at the calorimetrically defined glass transition temperature, $T_g$.[32-35] This is curious considering that the $T_g$ measured at typical laboratory time-scales, say by DSC, is on the order of seconds to minutes.[33] Transitions observed in DSC and DMA are also manifested as a result of changes in the amplitude of motion (i.e., mean square displacement) of the molecules in the system. While these techniques probe longer time scales, they also probe larger length scales. Fixed window scans are probing fast relaxations at very short length scales on the order of Angstroms. Therefore, any transitions in the amplitude of motion should be comparable to transitions observed with other techniques which are also sensitive to changes in the amplitude of molecular motions. In addition, as Angell[33] has pointed out, relaxation times can change by eight orders of magnitude over a very narrow temperature range for typical fragile liquids. This argument was presented to explain why transitions in $\langle u^2 \rangle$ measured by QENS correspond closely with transitions determined by methods such as DSC. The elastic scattering intensity is related to the Debye-Waller factor and, therefore, is also subject to the same interpretation.[33]

By examining the elastic scattering intensity at higher Q values (Q=0.99 $Å^{-1}$) as a function of temperature, Figure II-4b, one observes an additional drop in the intensity at very low temperatures (approximately -150 °C). This transition is common among all three samples. It is useful to explain the origin of this transition considering the tetramethyl ammonium ($TMA^+$) counterion because the hydrogens present are associated only with the methyl groups on this counterion. The origin for this decrease in the elastic scattering intensity can be attributed to methyl group rotations on the counterion. This type of transition has been observed for polymers and small molecules containing methyl groups and is well understood.[36-38] The larger counterions also show a similar, broader transition in this temperature regime. The deviation from the simple case of methyl rotors is due to the increasing level of complexity as the alkyl group becomes longer and includes -$CH_2$- groups. The molecular origin of the transition is likely due to complex rotational and librational motions of the alkyl "chain" of the counterion. This insight into the counterion dynamics will be discussed in detail below in context with the results obtained from dynamic scans and analysis of the elastic incoherent structure factor (EISF).

***Variable Temperature Dynamic Scans.*** Further information regarding the dynamics of the counterions was obtained from measuring the quasi-elastic scattering in the energy range of ± 17 μeV and over a Q range of 0.25 $Å^{-1}$ to 1.75 $Å^{-1}$. A typical dynamic structure factor (S(Q,ω)) is shown in Figure II-5 for $TBA^+$ Nafion® at Q = 0.99 $Å^{-1}$. The measured S(Q,ω) was fit with a delta function convoluted with the instrument resolution function, a Lorentzian function, and a flat background. The Lorentzian function serves to account for the incoherent quasi-elastic component of the scattering and is given by

$$S_{inc}(Q,\omega) = \frac{1}{\pi} \cdot \frac{\Delta\omega(Q)}{\omega^2 + \left[\Delta\omega(Q)\right]^2} \qquad \textbf{Eq II-1}$$

where the half-width at half-maximum of the Lorentzian, $\Delta\omega(Q)$ (also represented as $\Gamma(\mu eV)$) , is related to the diffusion of the hydrogen atoms in the sample.[39] These data have been analyzed by considering the diffusion of the hydrogen atoms within a sphere and a jump diffusion model. The continuous diffusion within a sphere model was developed by Volino and Dianoux[40] and has been used to describe the diffusion of water in Nafion® membranes.[39,41] The scattering law for this model describes the diffusion of the scattering particle within a characteristic sphere of radius, R, and has been described in the literature.[39-41] While this model takes into consideration the Lorentzian component of the QENS data and a single Lorentzian is enough to describe the scattering, it is likely that it is not sufficient to describe the intricacies of the counterion dynamics including methyl and methylene group rotations and the rotational motion of the entire counterion. In particular, it has been shown from the fixed-window data that at low temperatures the methyl and methylene group motions result in a decrease in the elastic intensity, which can lead to a broadening of the dynamic structure factor. However, the dynamic scans have been performed at high temperatures. The broadening observed can be attributed to different aspects of the counterion motion as it moves through the ion-hopping temperature. Therefore, when analyzing the diffusion of the hydrogen atoms within in a sphere, it is important to consider that this sphere may describe mobile portions of the counterion, or the entire counterion.

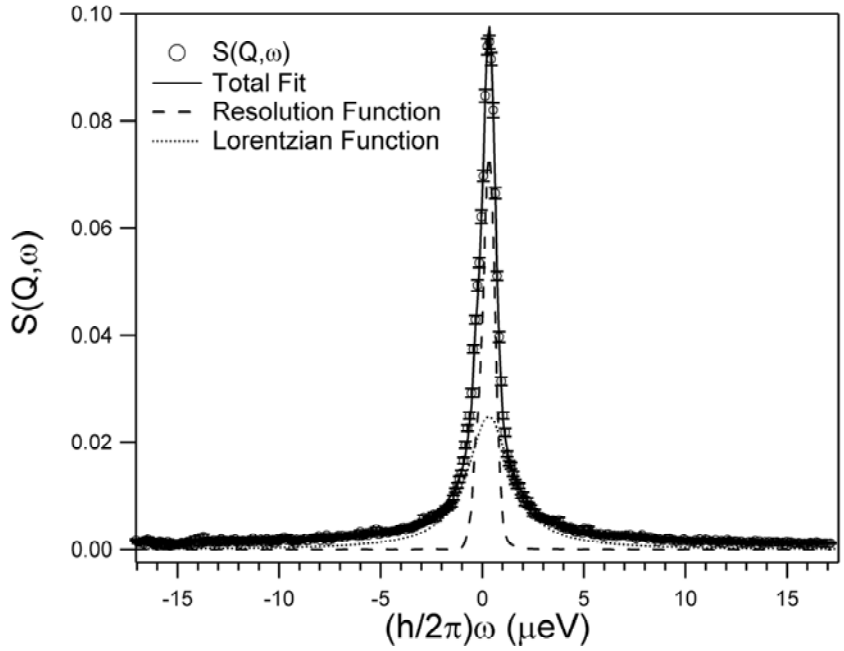


**Figure II-5.** Example fitting of the dynamic structure factor, S(Q,ω).

In order to characterize the dynamic length scales and geometry of the counter-ion motions and to more specifically describe the motions occurring around the ion-hopping temperature, the elastic incoherent structure factor (EISF) was determined for each sample over a range of temperatures. The value of the EISF is defined as the ratio of the integrated intensity of the elastic peak to the total integrated intensity (i.e. quasi-elastic and elastic). In order to determine the spatial distribution of the diffusing hydrogen atoms, and indirectly the counterions; the spherical diffusion model was applied to the EISF using the following relationship

$$EISF(Q) = \phi + (1-\phi)\left(\frac{3j_1(QR)}{(QR)}\right)^2 \qquad \textbf{Eq II-2}$$

where ϕ accounts for the fraction of hydrogen atoms that are immobile within the time window of the experiment and $j_1(QR)$ is the first order Bessel function given by

$$j_1(QR) = \frac{\sin(QR)}{(QR)^2} - \frac{\cos(QR)}{(QR)} \qquad \textbf{Eq II-3}$$

where Q is the scattering vector and R is the radius of the sphere within which the dynamics occur.

The EISF for $TMA^+$ and $TBA^+$ at temperatures above and below their respective $T_\alpha$'s are shown in Figure II-6a and b. These data have been fit with Eq II-2 and the fits are represented by lines in Figure II-6a and b. From these data we can conclude that approximately 60 °C to 70 °C below their respective α-relaxation temperatures, the counterion motion is very local and most of the scattering is elastic (i.e., the counterions do not have long-range mobility). This is confirmed by the values of ϕ determined for each counterion below $T_\alpha$. For $TMA^+$ at 177 °C the fraction of immobile hydrogens, ϕ, is approximately 0.71, while for $TBA^+$ at 27 °C ϕ is approximately 0.85. As the temperature is raised above the α-relaxation temperature, the scattering becomes dominated by the quasielastic component and the rapid decay in the EISF at low Q values is consistent with motions occurring over longer length scales than at lower temperatures. It should also be noted that when compared at the same temperature (177 °C) the fraction of immobile hydrogens is higher in the $TMA^+$ (ϕ~0.71) than for $TBA^+$ (ϕ~0.27), as indicated by the lower value of the EISF.

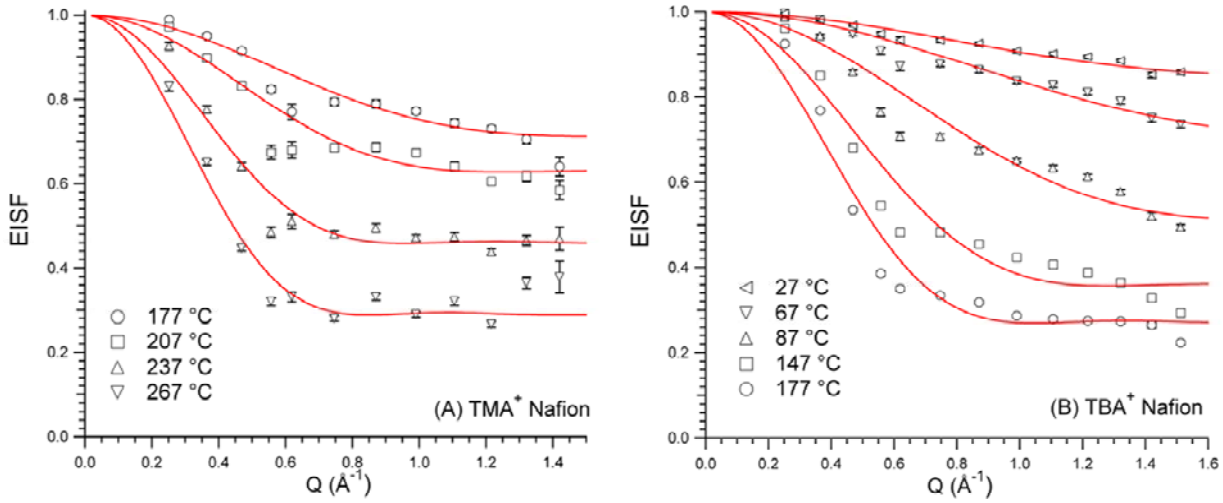


**Figure II-6.** The Elastic Incoherent Structure Factor (EISF) for (A) $TMA^+$ Nafion® at temperatures of (○)177 °C, (□)207 °C, (△)237 °C, and (▽)267 °C and for (B) $TBA^+$ Nafion® at temperature of (◁)27 °C, (▽)67 °C, (△)107 °C, (□)147 °C, and (○)177 °C. Solid lines are fits of Equation 2 to the data.

A fit of the EISF for $TMA^+$ Nafion® at 177 °C (Figure II-6a) results in a radius of 2.92 Å ± 0.3 Å, which correlates well with the reported crystallographic radius of the $TMA^+$ counterion (3.20 Å, 3.47 Å).[42-44] Given the relative simplicity of the $TMA^+$ counterion it is important to consider these results together with the elastic scans described in Figure II-4b. As discussed earlier, the decrease in the elastic scattering at low temperatures can be attributed to methyl group rotations. As the temperature is increased, the elastic scattering reaches a plateau before the second transition that has been attributed to ion-hopping. This plateau is indicates that the quasi-elastic broadening due to methyl rotations has moved outside the resolution of the instrument. This, along with the excellent agreement between the characteristic radius determined from the EISF at 177 °C and the reported radius of the $TMA^+$ counterion, seem to indicate that the motions at this temperature are due to counterion rotations. However, as the temperature increases the radius increases to a value of 5.32 Å ± 0.2 Å at 267 °C. Atomistic simulations of Nafion® by Devanathan and coworkers have shown that at low water

concentrations the distance between sulfur atoms is, on average, approximately 5 Å and is comparable to other values reported in the literature for similar systems.[45,46] This length scale is in excellent agreement with the characteristic radius of the sphere in which the dynamics occur as determined by modeling of the EISF for $TMA^+$ Nafion® at temperatures above the ion-hopping temperature. From these data and the results obtained from modeling a clear picture of the ion dynamics begins to immerge. At temperatures just below the ion-hopping temperature the $TMA^+$ counterion is rotating in place, but no long-range diffusion takes place. The absence of long-range diffusion is also supported by the earlier studies, in which no structural reorganization of oriented ion domains was observed below $T_\alpha$.[19,20] At temperatures above the α-relaxation temperature, the hydrogen dynamics are occurring within a sphere that has a comparable radius to the distance between sulfur atoms. It can be concluded that at these temperatures the counterions can then effectively move between adjacent sulfonate groups, thus facilitating long-range diffusion. While these results have led to a general picture of the counterion dynamics, further high resolution QENS experiments must be carried out to refine our description of the dynamics.

A fit of the EISF for $TBA^+$ Nafion® at 27 °C (Figure II-6b) results in a radius of 2.12 Å ± 0.2 Å, which is much smaller than the reported crystallographic radius of the $TBA^+$ counterion (4.94 Å[47]). This suggests that at temperatures below the α-relaxation temperature the Lorentzian broadening is likely due to local motions of the butyl "arms" of the counterion. Due to the increased level of complexity in the $TBA^+$ counterion, this qualitative conclusion must be investigated further by performing high resolution QENS experiments and a much more sophisticated modeling. However, these results do give an indication that the motions are local and cannot facilitate long range diffusion (i.e., hopping). The sphere increases to a size of 4.31

Å ± 0.2 Å at 177 °C, which is now comparable to the inter-sulfur distance determined by atomistic simulations, as discussed earlier. The counterions can then make the move to an adjacent sulfonate group. It should be noted that this radius is also comparable to the reported radius of the $TBA^+$ counterion. Therefore, it is likely that at temperatures above $T_\alpha$ the counterion is rotating and translating as it undergoes its long-range motion. This must be confirmed with further high-resolution experimentation.

By plotting the half-width at half-maximum ($\Gamma(\mu eV)$) versus $Q^2$ of the quasi-elastic component (Lorentzian) of $S(Q,\omega)$, the diffusive nature of the counter-ions has been ascertained. The data for both $TMA^+$ and $TBA^+$ Nafion® at 267 °C and 177 °C, respectively, can be seen in Figure II-7. The non-zero intercept of $\Gamma$ at low Q values is indicative of spatially confined diffusion of the counter-ions[41,48] whereas the rise in $\Gamma$ to an asymptotic value at high $Q^2$ values is consistent with random jump-diffusion within the confined spatial region.[39,41,48] These data have been analyzed using the following expression:

$$\Gamma(\mu eV) = \frac{\hbar}{\tau}\left(1 - \exp(-D_{jump} \cdot \tau \cdot Q^2)\right) + \frac{\hbar}{\tau_o} \qquad \textbf{Eq II-4}$$

where ħ = 6.582x10-16 eV·s, $\tau$ is the residence time between jumps measured in picoseconds (ps), $D_{jump}$ is the jump diffusion coefficient, and Q is the scattering vector. The term $\frac{\hbar}{\tau_o}$ accounts for the non-zero intercept and is the residence time of the local confinement and can be used to determine the local diffusion coefficient, $D_{local}$, using the following relationship

$$\Gamma_{Q\to 0} = 4.33 \cdot \frac{D_{local}}{R^2} \qquad \textbf{Eq II-5}$$

where $\Gamma_{Q\to 0} = 1/\tau_o$, as determined by Eq II-4, and R is the characteristic radius of confinement determined by fitting the EISF with Eq II-2. The parameters for ion-hopping for $TMA^+$ at 267

°C and $TBA^+$ at 177 °C were determined from the data in Figure II-7. The residence times between jumps for $TMA^+$ and $TBA^+$ are (411 ± 14) ps and (341 ± 29) ps, respectively and the jump diffusion coefficients, $D_{jump}$, were determined to be $(4.39 \pm 0.37)*10^{-7}$ $cm^2s^{-1}$ for $TMA^+$ and $(1.59 \pm 0.1)*10^{-7}$ $cm^2s^{-1}$ for $TBA^+$. The residence times and jump diffusion coefficients for the two counterions are comparable. It is important to note, however, that a direct comparison cannot be made because the results for each counterion were determined at different temperatures simply due to the dynamical behavior of the different systems. Also, it is likely that the dynamic components contributing to the broadening are somewhat different for the two coutnerions. According to Eq II-5 the local diffusion coefficients, $D_{local}$, for the counterions are estimated to be $4.4x10^{-7}$ $cm^2s^{-1}$ and $4.8x10^{-7}$ $cm^2s^{-1}$ for $TMA^+$ and $TBA^+$, respectively. Work by Tierney and Register[11-13] has shown that the diffusion coefficients for the $Na^+$ and $Li^+$ cations in ethylene-methacrylate ionomer melts are on the order of $10^{-11}$ $cm^2s^{-1}$ to $10^{-10}$ $cm^2s^{-1}$, while Colby and co-workers[2] have shown that for polystyrene ionomers the diffusion coefficients for $Na^+$ and $Rb^+$ are on the order of $10^{-14}$ $cm^2s^{-1}$. Both of these studies show considerably lower diffusion coefficients than those we have measured, however, it should be noted that the counterions used in these studies lead to very strong electrostatic interactions and over-all lower chain mobilities. Rollet et al.[49,50] have studied the dynamics of $TMA^+$ ions in hydrated Nafion® membranes. They found that the diffusion coefficients are on the order of $10^{-5}$ $cm^2s^{-1}$, which is closer to the value measured in the work presented here. Of course, the dynamics measured in this study are slower since the membranes in this study are (1) dry and (2) in the melt.

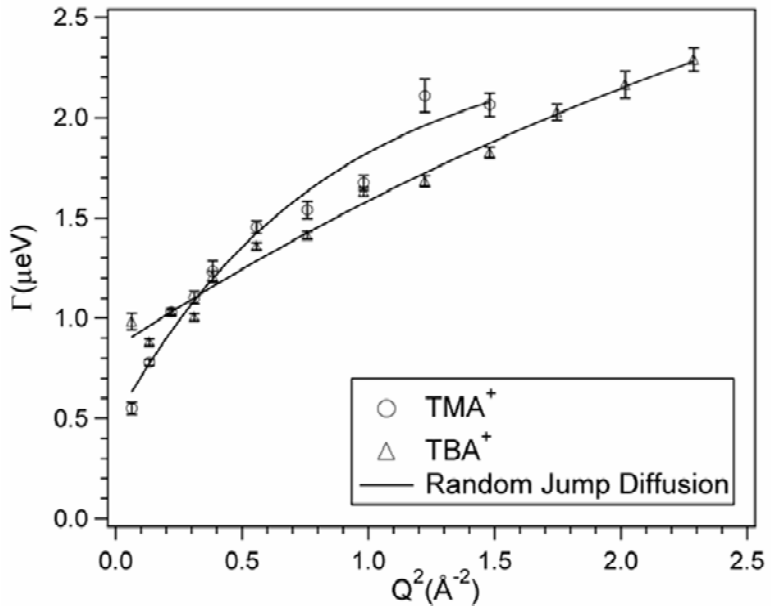


**Figure II-7**. Half-width at half-maximum, Γ(μeV), of the Lorentzian component of S(Q,ω) versus $Q^2$. The solid line represents the fit of the random jump diffusion model (**Eq II-4**) to the data.

As stated earlier, using QENS techniques for these particular systems allow one the unique advantage of probing the dynamics of the counterions themselves. However, it must be understood that while QENS probes the counterion dynamics, the polymer chains are also undergoing dynamical processes and transitions. These motions include the main-chain of the polymer as well as the side-chain. Therefore, it is of fundamental importance that the results obtained and described above be interpreted in the context of earlier studies and what has already been demonstrated about the chain dynamics in these systems.[19,20,51,52] By correlating several techniques, a consistent and more detailed description of the dynamics begins to form. The data in this study show that at temperatures below the α-relaxation the counterion motions are local and that there is no long-range diffusion taking place. In earlier studies, it has also been shown that at temperatures below $T_\alpha$, there is no relaxation of the ionic aggregates in oriented systems.[20] In order for large-scale morphological rearrangements to occur, the chains must be mobile enough to facilitate long-range motion. At temperatures in the vicinity of $T_\alpha$, the 'ionomer peak'

in SAXS has been shown to undergo transitions that correlate very well with bulk relaxations measured by DMA. The current data, both from fixed-window and dynamic scans, show explicitly that long-range diffusion of the counterions begins to occur in the temperature range of $T_\alpha$. Therefore, it can be concluded that the long-range diffusion of the counterions in this temperature range facilitate large-scale morphological rearranges not possible at temperatures well below $T_\alpha$. In addition, transitions measured in the side-chain dynamics from solid-state $^{19}F$ nuclear magnetic resonance (NMR) spectroscopy[19] clearly correlate with the transitions in the counterion dynamics measured here. Therefore, we can conclude that the motions of the counterions are dynamically coupled with the Nafion® chains through the side-chains. These conclusions are consistent with earlier descriptions of the ion-hopping process for these materials.

## D. Conclusions

The variable temperature small- and wide-angle x-ray scattering data show that the melting behavior of the PTFE-like crystallites are relatively unaffected by the choice of neutralizing counterion. In contrast, both the $\alpha-$ and $\beta$-relaxation temperatures are greatly affected by the choice of counterion. Therefore, it is readily apparent that the influence of the strength of the electrostatic interactions is the most important factor determining the segmental dynamics associated with the $\alpha$-relaxation in such systems. Moreover, the use of QENS has proven to be a useful tool in studying the counter-ion dynamics in PFSI membranes. Through this study, we have been able to explicitly show that the $\alpha$-relaxation in these materials is indeed linked to the onset of mobility of the counter-ions on the length-scale of 20 Å to 30 Å. To our knowledge, these data are the first direct *in-situ* measure of the dynamics associated with the ion-

hopping process in these ion-containing polymers. In addition, we have demonstrated that at temperatures below the α-relaxation the counterion motions are very local and that as the temperature is increased the amplitude of the motions approaches length scales that facilitate ion-hopping between sulfonate groups. When considered together, the variable temperature X-ray scattering and the QENS studies not only serve to show that the α-relaxation is not related to the melting of PTFE-like crystallites in this material, but provide further fundamental understanding of the link between electrostatic interactions and the dynamics in perfluorosulfonate ionomers.

## E. Acknowledgements

Kirt A. Page (the co-author of the manuscript) gratefully acknowledges support from the National Research Council-NIST Associateship program. Additional support for this work has been provided by the National Science Foundation CMMI-0707364 and the NSF MRSEC program at The University of Southern Mississippi. This work utilized facilities supported in part by the National Science Foundation under Agreement No. DMR-0454672. Use of the Advanced Photon Source was supported by the U. S. Department of Energy, Office of Science, Office of Basic Energy Sciences, under Contract No. DE-AC02-06CH11357. SAXS data was collected at the National Synchrotron Light Source, Brookhaven National Laboratory (supported in part by the U. S. Department of Energy, Division of Materials Sciences and Division of Chemical Sciences, under contract No. DE-AC02-98CCCCH10886).

## F. References


(1) Adi Eisenberg; Kim, J.-S.; John Wiley & Sons, Inc.: New York, 1998; pp 59-85.
(2) Colby, R. H.; Zheng, X.; Rafailovich, M. H.; Sokolov, J.; Peiffer, D. G.; Schwarz, S. A.; Strzhemechny, Y.; Nguyen, D. *Physical Reveiw Letters* **1998**, *81*, 3876-3879.
(3) Eisenberg, A. *Macromolecules* **1970**, *3*, 147-154.
(4) Eisenberg, A.; Hird, B.; Moore, R. B. *Macromolecules* **1990**, *23*, 4098-4107.
(5) Greener, J.; Gillmor, J. R.; Daly, R. C. *Macromolecules* **1993**, *26*, 6416-6424.
(6) Han, S.-I.; Im, S. S.; Kim, D. K. *Polymer* **2003**, *44*, 7165-7173.
(7) Kim, J.-S.; Eisenberg, A. *Journal of Polymer Science: Part B: Polymer Physics* **1995**, *33*, 197-209.
(8) Kim, J.-S.; Jackman, R. J.; Eisenberg, A. *Macromolecules* **1994**, *27*, 2789-2803.
(9) Kim, J.-S.; Yoshikawa, K.; Eisenberg, A. *Macromolecules* **1994**, *27*, 6347-6356.
(10) *Ionomers: Synthesis, Structure, Properties and Applications* Tant, M. R.; Mauritz, K. A.; Wilke, G. L., Eds.; Springer, 1997, pp 528.
(11) Tierney, N. K.; Register, R. A. *Macromolecules* **2002**, *35*, 6284-6290.
(12) Tierney, N. K.; Register, R. A. *Macromolecules* **2002**, *35*, 2358-2364.
(13) Tierney, N. K.; Register, R. A. *Macromolecules* **2003**, *36*, 1170-1177.
(14) Vanhoorne, P.; Register, R. A. *Macromolecules* **1996**, *29*, 598-604.
(15) Weiss, R. A.; Agarwai, P. K.; Lundberg, R. D. *Journal of Applied Polymer Science* **1984**, *29*, 2719-2734.
(16) Weiss, R. A.; Fitzgerald, J. J.; Kim, D. *Macromolecules* **1991**, *24*, 1071-1076.
(17) Weiss, R. A.; Fitzgerald, J. J.; Kim, D. *Macromolecules* **1991**, *24*, 1064-1070.
(18) Brenner, D.; Oswald, A. A.; Exxon Research & Engineering Co.: United States, 1978; Vol. 4102876.
(19) Page, K. A.; Cable, K. M.; Moore, R. B. *Macromolecules* **2005**, *38*, 6472-6484.
(20) Page, K. A.; Landis, F. A.; Phillips, A. K.; Moore, R. B. *Macromolecules* **2006**, *39*, 3939-3946.
(21) Hird, B.; Eisenberg, A. *Macromolecules* **1992**, *25*, 6466-6474.
(22) Kim, J.-S.; Wu, G.; Eisenberg, A. *Macromolecules* **1994**, *27*, 814-824.
(23) Goswami, M.; Kumar, S. K.; Bhattacharya, A.; Douglas, J. F. *Macromolecules* **2007**, *40*, 4113-4118.
(24) Panagiotopoulos, A. Z. *Fluid Phase Equilibria* **1992**, *76*, 97-112.
(25) Yan, Q.; Pablo, J. J. d. *Physical Reveiw Letters* **2002**, *88*, 095504-1-4.
(26) Mauritz, K. A.; Moore, R. B. *Chem. Rev.* **2004**, *104*, 4535-4585.
(27) Meyer, A.; Dimeo, R. D.; Gehring, P. M.; Neumann, D. A. *Rev. Sci. Instrum.* **2003**, *74*, 2759-2777.
(28) http://www.ncnr.nist.gov/dave.
(29) Kline, S. R. *J. Appl. Cryst.* **2006**, *39*, 895-900.
(30) Cable, K. M.; Mauritz, K. A.; Moore, R. B. *Journal of Polymer Science: Part B: Polymer Physics* **1995**, *33*, 1065-1072.
(31) Colmenero, J.; Arbe, A. *Physical Review B* **1998**, *57*, 13508-13513.
(32) Soles, C. L.; Douglas, J. F.; Wu, W.; Dimeo, R. M. *Macromolecules* **2003**, *36*, 373-379.
(33) Angell, C. A. *Science* **1995**, *267*, 1924-9135.
(34) Frick, B.; Richter, D. *Science* **1995**, *267*, 1939-1945.
(35) Ngai, K. L.; Bao, L.-R.; Yee, A. F.; Soles, C. L. *Physical Reveiw Letters* **2001**, *87*, 215901-1-4.
(36) Arrighi, V.; Ferguson, R.; Lechner, R. E.; Telling, M.; Triolo, A. *Physica B* **2001**, *301*, 35-43.
(37) Arrighi, V.; Higgins, J. S. *J. Chem. Soc., Faraday Trans.* **1997**, *93*, 1605-1612.
(38) Frick, B.; Fetters, L. J. *Macromolecules* **1994**, *27*, 974-980.
(39) Bee, M. *Quasielastic Neutron Scattering: Principles and Applications in Solid State Chemistry, Biology and Materials Science*; Adam Hilger: Philadelphia, 1988.
(40) Volino, F.; Dianoux, A. J. *Mol. Phys.* **1980**, *41*, 271-279.

(41) Pivovar, A. M.; Pivovar, B. S. *J. Phys. Chem. B* **2005**, *109*, 785-793.
(42) Coetzee, J. F.; Cunningham, G. P. *Journal of the American Chemical Society* **1965**, *87*, 2529-2534.
(43) Gill, D. S. *Electrochimica Acta* **1979**, *24*, 701-703.
(44) Robinson, R. A.; Stokes, R. H. In *Electrolyte Solutions*; Butterworths Scientific Publications: London, 1955; pp 113-127.
(45) Devanathan, R.; Venkatnathan, A.; Dupuis, M. *J. Phys. Chem. B* **2007**, *111*, 8069-8079.
(46) Hristov, I. H.; Paddison, S. J.; Paul, R. *J. Phys. Chem. B* **2008**, *112*, 2937-2949.
(47) Barthel, J.; Gores, H.-J.; Schmeer, G.; Wachter, R. *Topics in Current Chemistry* **1983**, *111*, 33-144.
(48) Bellissent-Funal, M.-C.; Chen, S. H.; Zanotti, J.-M. *Physical Review E* **1995**, *51*, 4558-4569.
(49) Rollet, A.-L.; Jardat, M.; Dufreche, J.-F.; Turq, P.; Canet, D. *Journal of Molecular Liquids* **2001**, *92*, 53-65.
(50) Rollet, A.-L.; Simonin, J.-P.; Turq, P.; Gebel, G.; Kahn, R.; Vandais, A.; Noel, J.-P.; Malveau, C.; Canet, D. *J. Phys. Chem. B* **2001**, *105*, 4503-4509.
(51) Osborn, S. J.; Hassan, M. K.; Divoux, G. M.; Rhoades, D. W.; Mauritz, K. A.; Moore, R. B. *Macromolecules* **2007**, *40*, 3886-3890.
(52) Page, K. A.; Jarrett, W.; Moore, R. B. *Journal of Polymer Science: Part B: Polymer Physics* **2007**, *45*, 2177-2186.

# CHAPTER III

# ANISOTROPIC MORPHOLOGY AND TRANSPORT PROPERTIES IN UNIAXIALLY STRETCHED PERFLUOROSULFONATE IONOMER

## A. Introduction

Perfluorosulfonate ionomers (PFSIs) have been shown to be of great importance in fuel cells[1], water electrolyzers[2], chlor-alkali cells[3] and soft actuators/sensors[4]. Their wide applicability in electrochemical/mechanical processes originates from their unique nanophase-separated morphology and excellent transport properties. The most extensively studied PFSI and the focus of the present investigation is Nafion® which is commercially available from E.I. Dupont de Nemours and Co. and has the following structure:

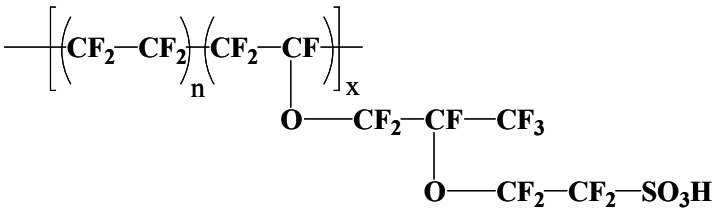


Nafion® is a copolymer of tetrafluoroethylene and generally less than 15 mol % of perfluorovinylether units terminated with sulfonic acid functionalities.[1] With a sufficient length of polytetrafluoroethylene (PTFE) segments between side chains, Nafion® can organize into crystalline domains generally less than ca. 10 wt % in 1100 equivalent weight (EW, the grams of dry polymer per equivalent of sulfonic acid units). While the existence of crystalline component in PFSI membranes is now well-known, the true crystallite organization (stacked lamellae vs. fringed micelles), the proximity of the crystallites to the ionic domains, and the ultimate roles of

crystallinity in affecting key membrane characteristics such as water uptake, proton conductivity and mechanical stability in this benchmark perfluorosulfonate ionomers have not been fully resolved. Greater efforts, however, have been given to the unique nanophase-separated morphology observed upon aggregation of the polar, ionic side chains within the matrix of hydrophobic PTFE because these ionic clusters, and specifically their shape, spatial distribution and connectivity define the supramolecular organization and function of this technologically important material as an ionic conductor.

Numerous small angle X-ray scattering (SAXS) investigations have focused on characterizing the complex, phases-separated morphology which includes crystalline, amorphous and ionic domains.[5-12] Specifically, there is a scattering maximum (often called the ionomer peak) appearing in SAXS profile of this material at ca. $q = 0.2$ Å$^{-1}$ which corresponds to a Bragg spacing of ca. 50Å.[1,5,9,13] This SAXS maximum has been attributed to an inter-particle scattering between the ionic aggregates dispersed in PTFE matrix.[1] Numerous structural models have been proposed to account for the origin of the ionomer peak. The oldest but still most referenced cluster-network model of Gierke et al. suggested swollen inverse micelles of roughly spherical geometry that are located on a paracrystalline cubic lattice.[5] These micelles are interconnected by narrow channels that are ca. 10 Å in size, so that it can account for ion and water transport ability exhibited by PFSIs.

While it requires a further investigation to determine the detailed shape and size of ionic domains, it is widely accepted that hydrophilic continuous pathways must exist in order for proton conduction and water diffusion to occur and recent studies have suggested elongated, locally parallel water channels.[1,14] Transport properties of PFSIs have been widely explored by various methods, such as quasi-elastic neutron scattering (QENS)[15,16], NMR[17-20], radio tracer[21],

and impedance analyser[17,18,22]. The primary transport properties of interest are water diffusion and proton conductivity, each crucial to the performance of the perfluorosuflonate ionomer membrane processes. Water diffusion coefficients were often measured using pulsed-field-gradient (PFG) NMR experiments.[18,20,23,24] For example, Zawodzinski et al. showed water self-diffusion coefficients increased in a linear fashion at low water contents, yet began to plateau at higher water contents.[18] Several authors demonstrated that PFG NMR technique can also provide information on the tortuosity of the percolation pathway by measuring diffusion coefficients at various diffusion times (Δ). Zhang and coworkers measured water diffusion coefficients as a function of time (ranging from 4 ms to 1s) over which diffusion is observed.[25] It was found that in "as-received" extruded Nafion® 117 membrane, diffusion coefficients did not depend strongly on diffusion times (Δ). On the contrary, the diffusion of water in solution-cast Nafion® 112 had a greater dependence on diffusion times (Δ), which is indicative of a tortuous pathway for diffusion. Recently, Ohkubo and coworkers investigated the micron-scale porous structure in Nafion® 117 membrane by measuring also the time-dependant self-diffusion coefficients at different water contents with temperatures ranging from 233 to 323 K.[23] The results revealed that the $^{1}H$ self-diffusion coefficients were dependant on diffusion times (Δ) less than 2 ms due to a micron-scale restricted structure and were constant beyond 3 ms.

Proton transport properties of Nafion® membranes are strongly influenced by the water content of the membrane. In the dry state, the Nafion® membrane behaves essentially like an insulator. However the membrane is no longer an insulator once it becomes hydrated to a certain point. Early studies by Yeo suggested this minimum threshold was about six water molecules per sulfonic acid site, while Pourcelly et al. estimated about seven water molecules.[26,27] It should be emphasized that proton conductivity has been measured under a variety of environmental

conditions such as water[18,28], water vapor[18,29,30], and humidified gases[31,32] at various temperatures.[22] With such a broad range of critical parameters affecting the conductivity of the Nafion® membranes, a wealth of conductivity information has been accumulated.[22,33]

Despite the rich information accumulated from the above studies, the impact of polymer morphology on transport properties in proton conducting membranes has not been fully explored. It is important to point out that the efficiency of the water/proton transport through the membrane should directly be related to how ionic percolation pathways are developed three-dimensionally within hydrophobic PTFE matrix. Based on the previously proposed structural models that are often over-simplified to allow a refined analysis of the transport properties, establishing a detailed morphology-transport relationship is a challenging task. In an attempt to elucidate and/or verify the complex PFSI morphology and to explore a detailed link between morphology and transport, current investigation involves uniaxially oriented $H^+$-form Nafion®. Orientation of the nanostructure has been often employed to control material properties and also to impart novelty. For example, we have previously demonstrated that artificial muscles based on the perfluorinated ionomer nanostructure altered by uniaxial orientation yielded a new anisotropic actuation response.[4] Furthermore, valuable structural/morphological information can be derived by subjecting polymeric materials to a simple mechanical deformation. Several mechanical deformations such as uniaxial orientation have been employed previously to explore the complex nature of the morphology of Nafion®.[8,34,35] To our knowledge, there have been no systematic studies evaluating water/proton transport behaviors in uniaxially oriented $H^+$-Nafion®. In this study, we utilized SAXS to characterize the anisotropic morphology. The influence of ordered morphology on the consequent transport properties was investigated by measuring water diffusion coefficients at three different directions (i.e., two in-plane and one through-plane

directions) and in-plane proton conductivities at two different directions, respect to uniaxial orientation direction. Established transport-morphology relationships are expected to provide valuable insights for predicting the performance of a membrane in a particular application and for designing new membranes.

## B. Experimental

***Materials.*** Extruded Nafion® 117CS from E.I. DuPont de Nemours & Co. (1100 g/equivalent, sulfonic acid form) was precleaned by refluxing in aqueous 8M nitric acid for 2 hr, and then in deionized (DI) water for 1 hr. These cleaned membranes were dried at 70 $^{o}$C in a vacuum oven for 12 hr.

***Uniaxial Orientation of As-Received $H^+$-Nafion®.*** Uniaxially oriented samples were prepared by cutting the vacuum-dried $H^+$-Nafion® membranes into dog-bone shapes and mounting them on a specially designed drawing apparatus. This drawing apparatus allowed $H^+$-Nafion® membranes to be drawn at 150 °C (above the α-relaxation temperature of $H^+$-form[36]) to draw ratios ($\lambda_b$ = final length (L) / initial length ($L_0$)) ranging from 1 to 4 as determined by the displacement of ink marks on the samples. Stretching rate was 10 mm/min and temperature was increased from room temperature to 150 $^{o}$C at a rate of 6 $^{o}$C/min. As soon as the desired draw ratio was reached, the membranes were rapidly quenched to room temperature to prevent thermal relaxation.[35] To prepare water-swollen samples, uniaxially oriented $H^+$-form membranes were then mounted in Kel-F clamps and soaked in DI water for 24 hr.

***Synchrotron Small-angle X-ray Scattering (SAXS).*** Small angle X-ray scattering (SAXS) was performed at the Brookhaven National Laboratory on the Advanced Polymer

Beamline (X27C) at the National Synchrotron Light Source. The wavelength of X-ray beam was 1.366Å and the sample-to-detector distances were 1890 mm and 867 mm for low and medium *q* ranges, respectively. Two-dimensional SAXS images were recorded using a Mar CCD camera with an intensity uncertainty on the order of 2% and analyzed using the POLAR software developed by Stonybrook Technology and Applied Research, Inc. The relationship between pixel and the momentum transfer vector *q* was determined by calibrating the scattering data with a silver behenate standard. All scattering intensities were corrected for transmission and background scatter due to air and Kapton windows and represented in arbitrary, relative intensity units as a function of the scattering vector, *q*, which is a function of the scattering angle through the following relationship

$$q = (\frac{4\pi}{\lambda})\sin\theta \qquad \textbf{Eq III-1}$$

where λ is the wavelength of X-ray beam (1.366 Å) and $\theta$ is half of the scattering angle ($2\theta$).

***$^1$H Pulsed Field Gradient NMR (PFG NMR):*** $H_2O$ diffusion experiments were performed at 25 °C on a Bruker 9.4 T Wide bore spectrometer corresponding to $^1$H frequency of 400.13 MHz. A Micro5 imaging probe with triple axis gradient at maximum 298 G/cm was used. $^1$H PFG diffusion was performed using PGSTE sequence[37] with δ = 2ms, Δ = 7- 50 ms. The NMR signal attenuation is described by the following equation: [37]

$$I = I_0 e^{-D\gamma^2 g^2 \delta^2 (\Delta - \delta/3)} = I_0 e^{-Db} \qquad \textbf{Eq III-2}$$

where $I$ is the spin-echo signal intensity, $I_0$ is the signal intensity at zero gradient, $\gamma$ is the gyromagnetic ratio of the probe nucleus (rad $s^{-1}$ $T^{-1}$), $\delta$ (s) is the duration of the field gradient

pulse with magnitude $g$ (T $m^{-1}$), D is the self-diffusion coefficient of water in the membranes, $\Delta$ is the duration between the leading edges of the two gradient pulses. $b$ is commonly known as the Stejskal–Tanner parameter[37]. An average value of diffusion coefficient (D) was obtained from 5 experiments with a standard deviation of 2%. An in-house built sample cell made of Teflon and glass is depicted in Figure III-1. The sample cell is pressure sealed with low dead volume (< 20%) to allow membrane equilibration and minimize water evaporation. The sample cell with 8mm OD can fit tightly into NMR probe insert with the aid of additional Teflon tape wrapped outside the glass tube. Diffusion anisotropy was obtained by measuring $^1H_2O$ diffusion along 3 orthogonal membrane axes by applying pulsed field gradient in respective directions without repositioning the sample. We use axis definition consistent with membrane convention, i.e. $x$ as the in-plane extrusion or draw direction, $y$ as the in-plane perpendicular direction, and $z$ as the through-plane direction. Nafion® membranes were cut into 4.5mm x4.5mm pieces with one edge along the extrusion or draw direction. 6-14 pieces were stacked in exactly the same orientation to enhance NMR signal. The stack of membranes were loosely wrapped with Teflon tape and soaked in $^1H_2O$ for at least one week to obtain maximum water uptake. Water uptake expressed in wt %, were determined by the measuring weight gain versus the weight of the vacuum dried membranes. The wt % of unsaturated membranes was measured by the partially swollen membrane weight and confirmed with relative NMR signal intensity. Water uptake $\lambda$ is defined as moles of water molecules per mole of sulfonate group. Partially swollen membranes were prepared by allowing $^1H_2O$ to evaporate from the membrane stack before sealing with extra Teflon tape and LDPE plastic wrap. The sealed membrane stacks were placed into the cavity of the sample cells and pressure sealed with a piston cap. An equilibration time of 3 hours was given to allow membranes to reach steady state.

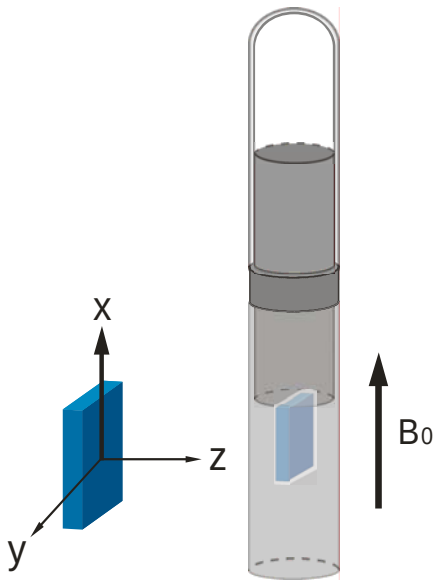


**Figure III-1**. Sample cells used to measure $H_2O$ self-diffusion coefficients. Diffusion coefficients can be measured in three principle directions with either in-plane x,y directions or through plane z direction along NMR magnetic field $B_0$

***Proton Conductivity Analysis.*** Measurement of in-plane proton conductivity was conducted on oriented Nafion® membranes using a 4-point conductivity cell developed by Bekktech. To evaluate anisotropic proton conductivity, the probe was positioned onto the hydrated membranes (with a constant pressure) such that the gaps between the Pt electrodes were aligned in directions either parallel or perpendicular to the direction of uniaxial deformation. Then, the conductivity cell loaded with fully hydrated membrane was stored in a humidity chamber and equilibrated at 95% RH and 80 $^{o}$C for 12 hr. Measurements were taken from 0.1 to 500,000 Hz using a 1255 HF frequency analyzer coupled with a 1286 electrochemical interface, both from Solatron. Data analysis was carried out using both Zplot and Zview software purchased from Scribner and Associates, Inc. The in-plane conductivity was then calculated using the definition of the resistance in terms of the bulk resistivity and the cell geometry, shown in Eq III-3 where $\rho$ is the membrane resistivity ($\Omega \cdot$cm), A is the cross-sectional area

perpendicular to the current flow, W is the width of the sample, L is the distance between the two reference electrodes and T is the thickness of the film.

$$R = \frac{\rho \times L}{A} = \frac{\rho \times L}{W \times T} \qquad \textbf{Eq III-3}$$

Since conductivity is the inverse of resistivity, Eq III-3 can be rewritten in terms of conductivity as shown in Eq III-4 where σ is the conductivity (S/cm), ρ is the membrane resistivity (Ω.cm), and R is the membrane resistance (Ω).

$$\sigma = \frac{1}{\rho} = \frac{L}{R \times W \times T} \qquad \textbf{Eq III-4}$$

The membrane resistance is determined by taking the real Z-axis intercept of the complex impedance plot or the real Z value for which the phase, Φ, is equal to zero. To investigate the effects of different water content, proton conductivities were recorded at various % RH values.

## C. Results and Discussion

### SAXS

The effects of uniaxial deformation on the morphology of $H^+$-form Nafion® have been characterized by two-dimensional SAXS. For the as-received state (Figure III-2a), the isotropic SAXS data show a diffuse outer ring of maximum intensity at ca. $q$ = 0.2 $Å^{-1}$, which has been attributed to scattering from the ionic aggregates dispersed in the PTFE matrix. The intense scattering near the beam stop is associated with typical ionomer long-range heterogeneities and a contribution from PTFE-like crystalline domains. The initially isotropic intercrystalline domain peak is observed at ca. $q$ = 0.05 $Å^{-1}$ and also shown to be sensitive to uniaxial deformation. Although it is beyond the scope of this investigation, it is important to point out that three recent models for the morphology of PFSIs have focused on the existence of crystallites dispersed

between[38] or within[9] rod-like ionic domains or as lamellae[39] separating the ionic regions. Clearly, the proximity of the crystallites to the ionic domains differs significantly in the proposed structures, and thus fundamental research is needed to provide definitive evidence for the true semi-crystalline structure in these technologically important ionomers. As the membrane is increasingly stretched up to $\lambda_b = 4.0$, the initially isotropic scattering pattern for the ionomer peak transforms into a strongly anisotropic scattering pattern (i.e., equatorial spots) as is clearly observed in Figure III-2h. The scattering maximum in the meridional direction no longer exists, which indicates the loss of liquid-like order in this direction. With further extension, equatorial streaking in the SAXS pattern is observed, consistent with the formation of fibrillar-like morphologies. Van der Heijden and coworkers attributed this anisotropic scattering to the alignment of elongated polymeric aggregates in the direction of uniaxial extension.[34] Recently, Rubatat and Diat suggested that the cylindrical scattering objects are simply aligned (or tilted) preferably toward the stretching direction without undergoing any significant shape change during uniaxial orientation, and thus ruled out the deformation of spherical ionic domains into an ellipsoidal shape.[11]

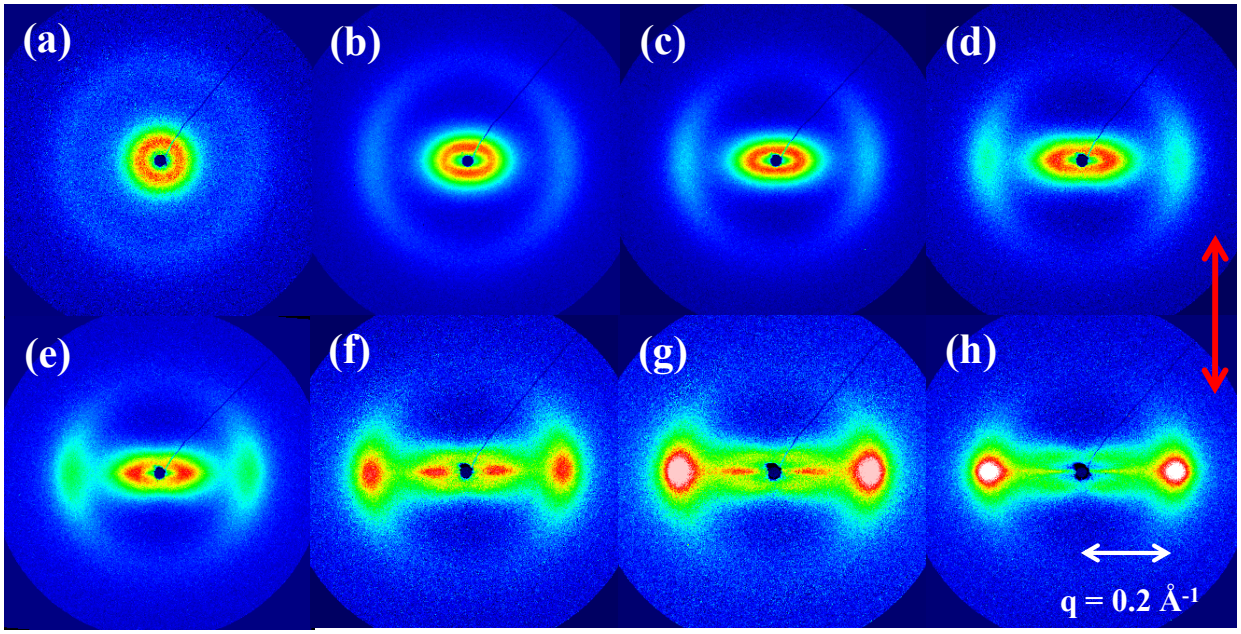


**Figure III-2.** Two-dimensional SAXS patterns of dried $H^+$-form Nafion® elongated to various extensional ratios, $\lambda_b = L$ (final length) / $L_o$ (initial length). (a) $\lambda_b = 1.0$, (b) $\lambda_b = 1.25$, (c) $\lambda_b = 1.5$, (d) $\lambda_b = 1.75$, (e) $\lambda_b = 2.0$, (f) $\lambda_b = 2.5$, (g) $\lambda_b = 3.0$, and (h) $\lambda_b = 4.0$, Stretching direction is indicated with a red arrow. Samples were uniaxially stretched at 150 °C with a strain rate of 10 mm/min.

Because the ionomer peak is observed only at the equatorial direction for oriented samples, 1-dimensional analysis of oriented SAXS patterns can be performed at the azimuthal angle 90° (Data not shown). The peak maximum slightly shifts from $q \approx 0.20$ Å$^{-1}$ to $q \approx 0.22$ Å$^{-1}$ as the draw ratio increases from $\lambda_b = 1.0$ to $\lambda_b = 1.5$. For $\lambda_b \geq 1.5$, the $q_{max}$ remains fairly constant at a value of $q \approx 0.22$ Å$^{-1}$ and this is consistent with the previous orientation studies involving Nafion® membranes deformed at the room temperature.[34] This indicates a decreased correlation distance at the equator direction because of cylindrical ionic aggregates getting closer to each other.[11]

Once a dry Nafion® membrane is uniaxially stretched, solvent swelling was achieved by first mounting the dry, oriented membrane onto Kel-F clamp and then soaking in DI water for 24

hr at room temperature (RT). After removal from the clamp, no changes in the dimensions of the hydrated membranes (e.g., retraction) were observed. Without the use of Kel-F clamp, however, oriented Nafion® showed a relaxation during the swelling process. Two dimensional SAXS patterns of oriented, fully hydrated Nafion® membranes shown in Figure III-3, reveal that the anisotropic patterns are persisted even after hydration process indicating that no significant relaxation of the ionic aggregates is taking place. It should be pointed that established anisotropic morphology was held stable without any notable relaxation (confirmed by SAXS) even after 6 months. It is also apparent that the scattering maximum shifts to lower scattering angles with solvent swelling; the $q_{max}$ shifts from 0.2 $Å^{-1}$ (dry) to 0.15 $Å^{-1}$ (hydrated) for $\lambda_b = 4.0$. This shifting to lower scattering angle with solvent swelling is due to the presence of water, essentially enlarging the hydrophilic channels.

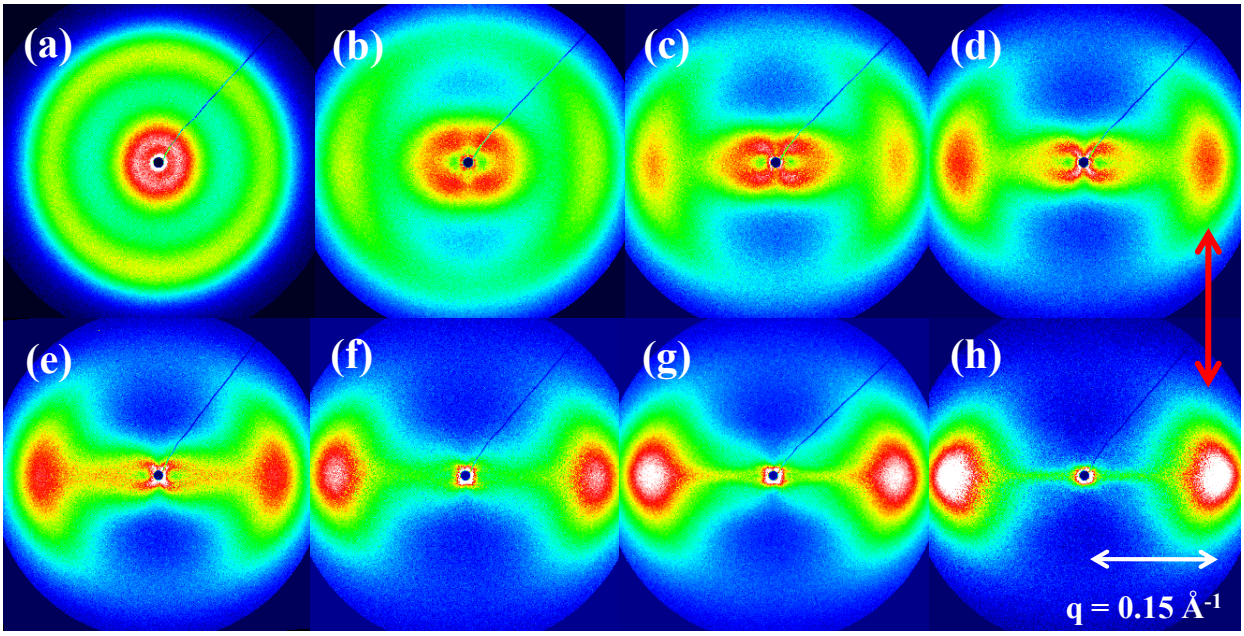


**Figure III-3.** Two-dimensional SAXS patterns of $H^+$-form Nafion® elongated to various extensional ratios, $\lambda_b$ = L (final length) / $L_o$ (initial length). (a) $\lambda_b = 1.0$, (b) $\lambda_b = 1.25$, (c) $\lambda_b = 1.5$, (d) $\lambda_b = 1.75$, (e) $\lambda_b = 2.0$, (f) $\lambda_b = 2.5$, (g) $\lambda_b = 3.0$, and (h) $\lambda_b = 4.0$, Stretching direction is indicated with a red arrow. Samples are hydrated after uniaxial deformation.

Figure III-2 and 3 clearly indicate that the scattering intensity of the ionomer peak grows at the equatorial direction as a function of extenional ratio ($\lambda_b$). To quantify the degree of orientation as a function of $\lambda_b$, we have calculated Herman's orientation order parameter (*f*) from the azimuthal plots using the equation, Eq III-5:[40,41]

$$f = \frac{3\left\langle \cos^2 \chi \right\rangle - 1}{2} \qquad \textbf{Eq III-5}$$

where $\chi$ is the azimuthal angle and $\langle \cos^2 \chi \rangle$ denotes the average of $\cos^2 \chi$. The average square of the cosine was calculated from the equation:

$$\left\langle \cos^2 \chi \right\rangle = \frac{\int_{\chi_1}^{\chi_2} I(\chi) \cos^2 \chi \sin \chi d\chi}{\int_{\chi_1}^{\chi_2} I(\chi) \sin \chi d\chi} \qquad \textbf{Eq III-6}$$

where I ($\chi$) is the scattering intensity as a function of $\chi$ and the limits of integration are between $\chi_1$ and $\chi_2$. According to the Eq III-5, the Herman's orientation parameter (*f*) assumes a value of 1 for a system with complete orientation of the scattering entities parallel to the director and -1/2 for the case where perfect orientation of the scattering entities is perpendicular to the director. For unoriented isotropic systems, the value of *f* assumes zero. In the case of oriented Nafion®, the director corresponds to the momentum transfer vector, *q*. The results of the Herman's orientation parameters as a function of draw ratios ($\lambda_b$) are tabulated in Table III-1 for both dried and hydrated Nafion® membranes. It is interesting to note that there is no significant differences in the calculated Herman's order parameters between dry and hydrated samples. This observation simply indicates that there is no major structural reorganization during swelling process. Table III-1 shows that slight uniaxial deformation greatly affects the Herman's order parameter which changes from almost 0 to -0.26 for $\lambda_b$=1.25. As the draw ratio increases up to

4.0, the order parameter seems to plateau at around -0.4. This indicates considerable orientation of ionic domains along the stretching direction.[34,35] Recently, Stasiak et al. investigated the strain response of styrene-isoprene-styrene (SIS) block copolymers with cylindrical (18 wt % PS) and spherical (16 wt % PS) morphologies using SAXS. Comparison of changes in orientation order parameters as a function of elongation for cylinder– and sphere-forming materials provide some basic insights into how microstructures respond to uniaxial deformation. The authors observed that the cylinder-forming morphology can form a very well-ordered structure following extensional flow in the channel die and its order parameters are responsive to uniaxial deformation.[41] Interestingly the sphere-forming material, however, did not exhibit well-ordered anisotropic morphology and its order parameter remained almost constant during stretching up to 200 % of strain.[41] Therefore, this observation strongly indicates that the shape of ionic domains in Nafion® is more like cylindrical rather than spherical.

**Table III-1**. Herman's orientation order parameters

| $\lambda_b$ | **1.0** | **1.25** | **1.5** | **1.75** | **2.0** | **2.5** | **3.0** | **4.0** |
|---|---|---|---|---|---|---|---|---|
| **Dried samples** | -0.04 | -0.26 | -0.28 | -0.31 | -0.32 | -0.35 | -0.36 | -0.38 |
| **Hydrated samples** | -0.03 | -0.23 | -0.26 | 0.28 | -0.30 | -0.32 | -0.34 | -0.37 |

In addition to changes in spatial distribution/order of the ionic aggregates, the overall degree of phase separation or the extent of ionic aggregation may be changing as well upon uniaxial deformation. The scattering invariant (Q), which is a good representation of the overall degree of phase separation present in the polymer, can be calculated by the following equation (Eq III-7)

$$Q = 2\pi^2(\Delta\rho)^2 V = \int_0^\infty I(q)q^2 dq \qquad \textbf{Eq III-7}$$

where $V$ is the volume of the scattering particles, $\Delta\rho$ is the electron density difference between scattering particles and matrix, $I(q)$ is the scattered intensity and $q$ is the scattering vector. Previously Lin et al. calculated the scattering invariant Q of Nafion® membranes cast from various alcohol:water solutions.[42] The authors noticed that the Q values decreased as the aliphatic alcohol chains increased (methanol < ethanol < 2-propanol), indicating a decrease in the phase separation between the hydrophobic and hydrophilic regions in the membranes. To calculate the scattering invariant (Q) of dry, oriented Nafion® membranes, the scattering profile extracted from Figure III-2 was integrated between $q$ = 0.1 Å$^{-1}$ and $q$ = 0.31 Å$^{-1}$ and a plot of the invariant (Q) versus the extensional ratio is shown in the Figure III-4. It seems that uniaxial orientation does not induce a major change in the scattering invariant (Q), which means the degree of overall phase separation was not affected during uniaxial deformation.

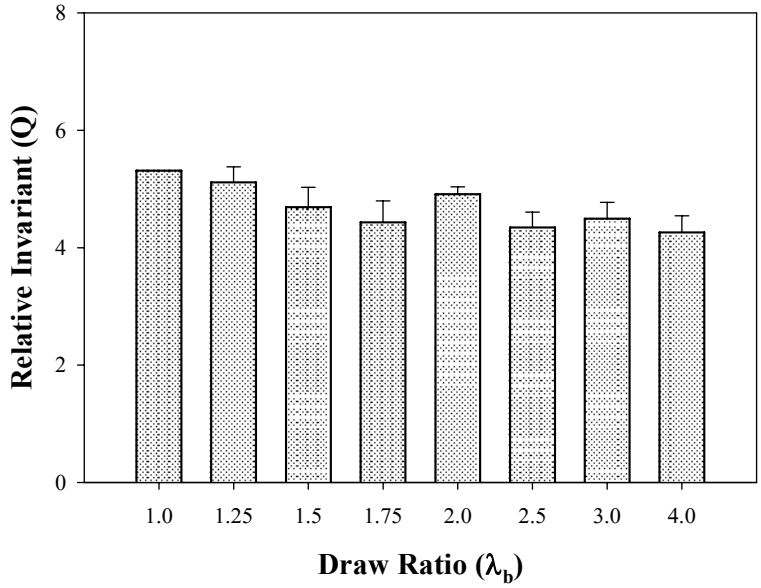


**Figure III-4.** A plot of the scattering invariant (Q) versus extensional ratio ($\lambda_b$) for dry, elongated $H^+$-form Nafion®

**PFG NMR**

To evaluate the effect of induced anisotropic morphology on transport properties, apparent self-diffusion coefficients of the penetrant, $H_2O$, were probed at three different directions (*x*, *y* and *z*) relative to uniaxial orientation direction. Anisotropic water transport behaviors in PFSIs were previously reported by several authors.[20,24] Due to the weak anisotropy induced during membrane processing (i.e., melt-extrusion through a die), anisotropy in transport behavior was also minimal. To our knowledge, there have been no systematic studies evaluating water transport behavior in uniaxially oriented $H^+$-Nafion®. Figure III-5 shows determined self-diffusion constants for $H_2O$ in oriented Nafion® ($\lambda_b = 4$) as a function of the time over which self-diffusion occurs in the stimulated echo pulse sequence. Diffusion time ($\Delta$) was varied from 7 ms to 50 ms to look for any structural restriction that may lead to tortuous diffusion behavior in highly oriented Nafion®. No significant tortuosity was observed previously in the range of the diffusion times employed in this study for as-received, unoriented Nafion® 117.[20] However, it is important to point out that Ohkubo *et al*. clearly showed the dependence of self-diffusion coefficient on diffusion time ($\Delta$) between 1 and 2 ms.[23] Although our study does not include the same range of diffusion times, any structural changes such as merging or elongating ionic domains during uniaxial orientation, could cause the diffusion restriction to be observed at greater $\Delta$. In Figure III-5, it is obvious that diffusion coefficients at all directions (x, y, and z) are found not to depend strongly on diffusion time ($\Delta$). This information would simply indicate that no significant structural changes were induced during uniaxial orientation. The impact of uniaxial orientation on transport properties is well demonstrated by comparing diffusion coefficients measured at three orthogonal membrane axes. In Figure III-5, diffusion coefficients ($D_{eff}$) for parallel to the draw direction (*x*) are always higher than those for perpendicular to draw

($y$) and through-plane ($z$) directions regardless of diffusion time ($\Delta$). In fact, perpendicular to draw and through-plane directions showed almost the same diffusion coefficients at any given diffusion times ($\Delta$).

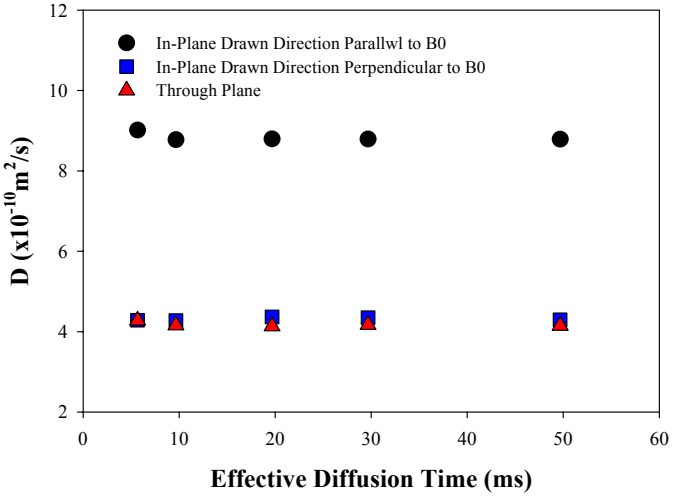


**Figure III-5.** Water self-diffusion coefficients in oriented Nafion® membranes ($\lambda_b = 4$) as a function of effective diffusion time (These data were acquired in collaboration with Prof. Louis A. Madsen.)

To characterize systematically how induced anisotropic morphology influences transport properties in Nafion®, water self-diffusion coefficients ($D_{eff}$) were evaluated at three different directions ($D_{xx}$, $D_{yy}$, and $D_{zz}$) in drawn Nafion® with a $\lambda_b$ of 1.0 (a), 1.5 (b), 2.0 (c), 3.0 (d), and 4.0 (e) and are presented in Figure III-6. In each sample, we gradually decreased water contents to investigate the effect of degree of swelling on anisotropic transport. Firstly, regardless of membrane orientation directions, higher water diffusion coefficients are observed as the degree of swelling is increased within Nafion®. This is not surprising considering that an increase in water content obviously affects ionic domains, which presumably swell the hydrophilic ionic channels, and facilitates connectivity between the adjacent ionic domains, making long range water/proton transport easier. In Figure III-6, we also find that for a given extensional ratio ($\lambda_b$), $D_{xx}$ is always greater than $D_{yy}$ and $D_{zz}$ at all water contents regardless of the degree of orientation.

Comparison to the diffusion coefficients for unoriented samples reveals that uniaxial deformation of Nafion® membranes essentially enhances transport ability in one direction (i.e., the parallel to draw direction) and suppresses in the other two directions (i.e., two orthogonal directions relative to the stretching direction). Greater transport ability along the stretching direction should directly be related to the preferential alignment of hydrophilic channels along the draw direction as evidenced by SAXS results. Very interestingly, water transport behaviors are observed to be exactly the same at the in-plane, perpendicular to draw direction and through-plane direction. This observation is a strong evidence of the uniaxiality of the deformation process of the Nafion® membrane and further supports the presence of elongated hydrophilic channels that are tilted preferentially toward the stretching direction. It is important to note that this is the first effort to show uniaxial ionic domain order in mechanically deformed Nafion® membranes.

Figure III-6 also plots the ratio of $D_{xx}$ to $D_{yy}$, named the degree of anisotropy ($R_d$), to clarify the differences in water diffusion coefficients as a function of water contents. The degree of anisotropy is equal to unity ($R_d = 1$) for isotropic or unoriented samples, and increases up to almost 3 as the membrane is highly elongated (i.e., $\lambda_b = 4$). As can be seen in Figure III-6, the degree of anisotropy is also found to be a function of water content within the membrane and this behavior becomes more evident with increasing draw ratios. Interestingly, the transport anisotropy is most pronounced in the drier states, which was also observed by Allahyarov and Taylor in their recent coarse-grained simulation efforts.[43] A decrease in the degree of anisotropy may be attributed to relaxation of oriented morphology in the presence of higher water content. However this idea should be ruled out if we consider the Herman's order parameters for hydrated and dried samples presented in Table III-1 which showed essentially no significant difference.

Rather, this phenomenon is likely linked to an anisotropic swelling mechanism (i.e., water swelling perpendicular to the cylinder orientation axis) observed in oriented Nafion® membranes. To examine the effect of uniaxial deformation on the swelling behaviors, we measured dimensional changes at three different membrane axes before and after hydration (Figure III-7). While unoriented Nafion® undergoes essentially isotropic dimensional changes, elongated membranes show a strong anisotropic swelling behavior. Swelling in the through-plane (i.e., along the thickness, *z*) direction and in-plane perpendicular to draw direction (*y*) was much larger than that in the in-plane parallel to draw (*x*). This anisotropic swelling behavior may be a macroscopic indication of ordered microstructures of Nafion® membranes. Given the preferential swelling in *z* and *y* directions, it is reasonable to conclude that water transport in the directions perpendicular to the cylinder orientation axis may take precedence, which will lead to a decrease in the diffusion anisotropy.

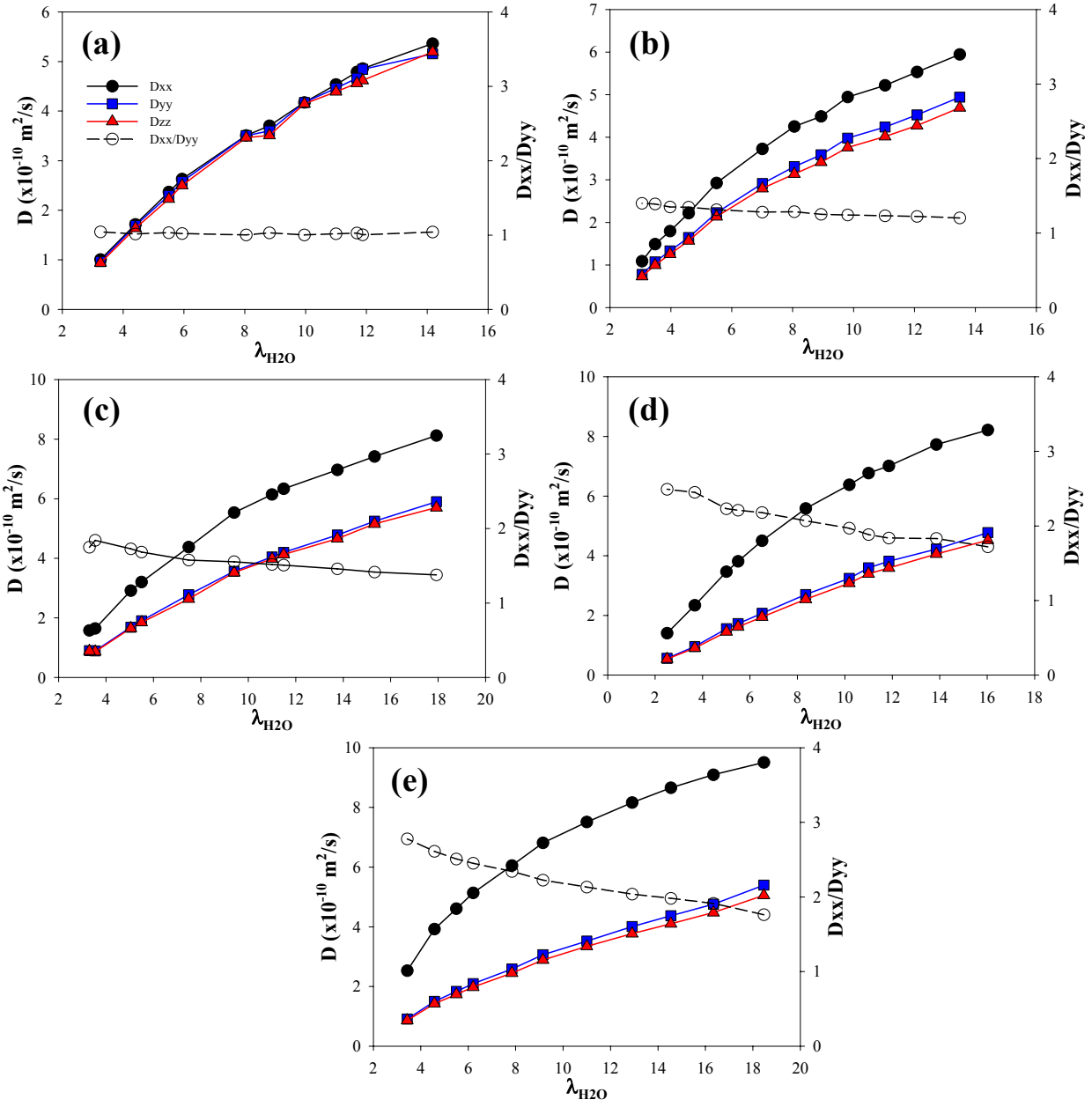


**Figure III-6**. Water diffusion coefficients as a function of water contents in drawn Nafion® with a $\lambda_b$ of 1.0 (a), 1.5 (b), 2.0 (d), 3.0 (d), and 4.0 (e) (These data were acquired in collaboration with Prof. Louis A. Madsen.)

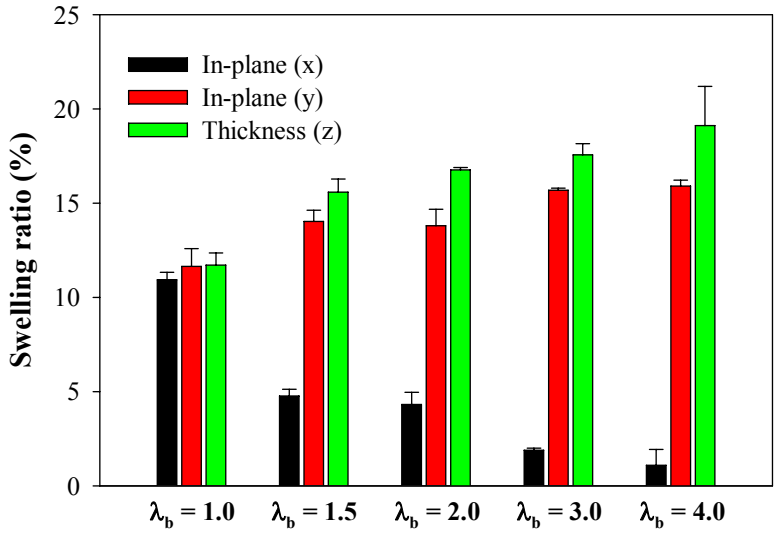


**Figure III-7**. Anisotropic swelling behavior of uniaxially oriented Nafion® membranes

**Proton Conductivity Analysis**

Proton conductivities often play a role of a gauge of a successful ionic conductor and are measured to evaluate the viability of newly developed materials. Proton conduction in Nafion® membranes has been proposed to occur by three distinct mechanisms, (1) the vehicular mechanism, (2) the Grotthuss mechanism and (3) the surface mechanism.[44] In the vehicular mechanism, proton conduction is proposed to occur through the assistance of a carrier species. Thus, the rate of diffusion of the carrier species becomes the rate determining factor in this mechanism. In the Grotthuss mechanism, protons are conducted through "hopping" from one water molecule to another by the successive formation and breakage of hydrogen bonds. It should be pointed out that this "hopping" process is much faster than the diffusion of hydronium ions in water. Lastly, in the surface mechanism, the protons are proposed to conduct along the array of sulfonic acid groups, basically "hopping" from one anion moiety to another.[44]

Regardless of the detailed mechanism, proton conduction within ionomeric materials should be intimately related to thier morphology, specifically hydrophilic channel

order/alignment. In order to understand the relationship between the Nafion® microstructure and proton conductivity, we measured in-plane proton conductivity on oriented Nafion® membranes using a 4-point conductivity cell. Figure III-8 plots proton conductivities evaluated at two different directions, parallel to draw ($\rho_x$) and perpendicular to draw ($\rho_y$) in drawn Nafion® with a $\lambda_b$ of 1.0 (a), 2.0 (b), 3.0 (c), and 4.0 (d). Regardless of the degree of orientation and membrane orientation direction, proton conductivity increases as a function of relative humidity (% RH), indicating a strong dependence of proton conductivity on the water content within the membrane. While unoriented Nafion® membranes show essentially isotropic proton conductivities, uniaxially drawn samples show a strong anisotropy in proton conductivities with $\rho_x$ being greater than $\rho_y$ at all water contents. Comparison of proton conductivities of drawn Nafion® membranes along the stretching direction as a function of the draw ratio ($\lambda_b$) reveals that ordering in the hydrophilic channels essentially increases the proton conduction. Conversely, the transverse proton conductivities examined across the stretched membrane decreases as a function of draw ratio ($\lambda_b$). These results are in good agreement with SAXS and water diffusion results which indicated a strong alignment of hydrophilic channels along the stretching direction. Figure III-8 also plots the ratio of $\rho_x$ to $\rho_y$, named the degree of anisotropy ($R_p$), to clarify the differences in proton conductivities as a function of membrane orientation direction. The degree of anisotropy is equal to unity ($R_p = 1$) for isotropic or unoriented samples, and increases as the degree of orientation becomes greater. As observed for water diffusion results, the degree of anisotropy is also found to be a function of water content although the magnitude is minimal (most likely due to a narrow range of water contents that can be achieved between 0 and 95 % RH). It is of interest to note that, for a given draw ratio ($\lambda_b$), the degree of anisotropy observed in proton conductivity is quite comparable to that of water diffusion coefficients at relatively low water

contents. This information evidently indicates a close link between these two transport parameters which are strongly influenced by the order/alignment of hydrophilic channels within Nafion® membranes.

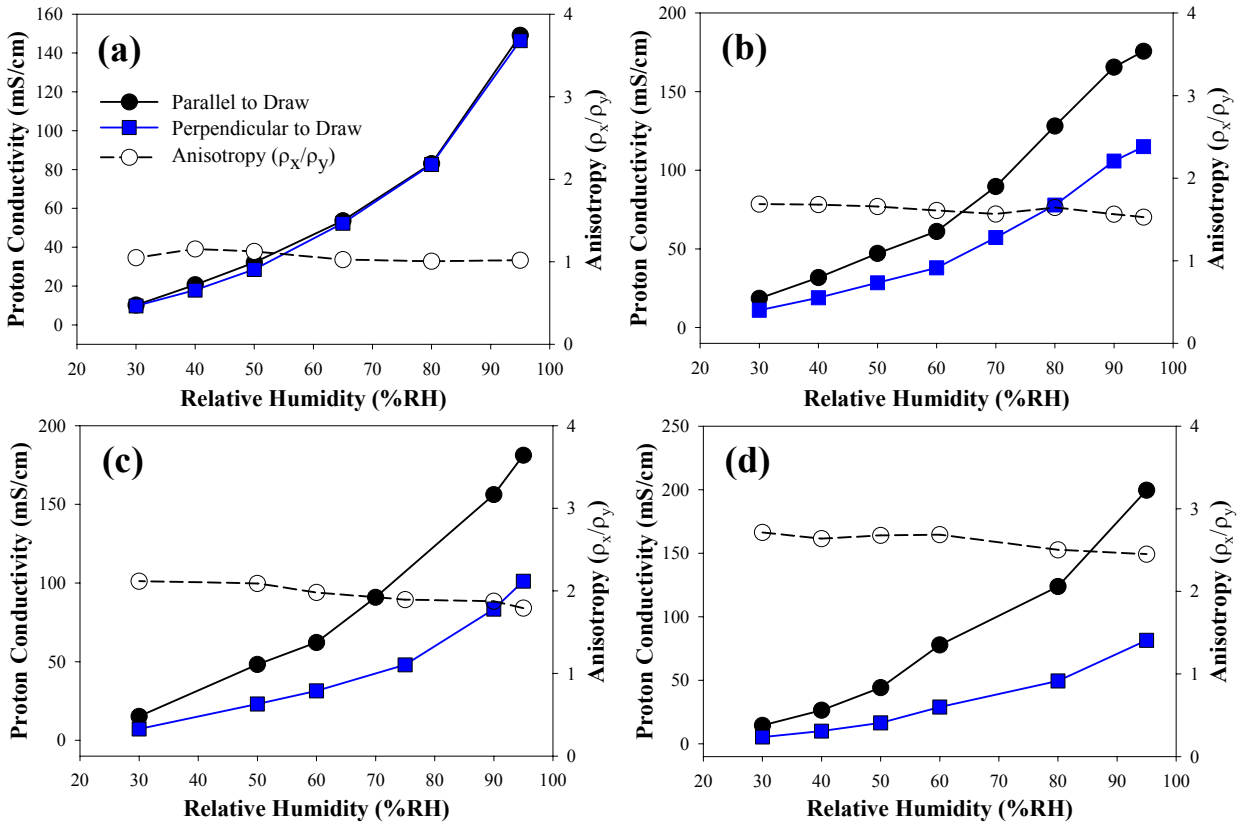


**Figure III-8**. Proton conductivities in drawn Nafion® with a $\lambda_b$ of 1.0 (a), 2.0 (b), 3.0 (d), and 4.0 (e)

## D. Conclusions

The effect of uniaxial orientation on the structure and transport properties of Nafion® membranes was examined. SAXS experiments on dry membranes that were uniaxially elongated above the α-relaxation temperatures showed a strong anisotropic morphology. Established anisotropic morphology was shown to be persisted over the swelling process without a significant relaxation. Herman's order parameters for the ionomer peak were strongly

influenced by uniaxial deformation, which supports a presence of cylindrical rather than spherical morphology for ionic domains. Comparison of the water diffusion coefficients between unoriented and oriented samples reveals that uniaxial deformation of Nafion® membranes essentially enhances transport ability in one direction (i.e., the parallel to draw direction) and suppresses in the other two directions (i.e., two orthogonal directions relative to the stretching direction). In an agreement with the water diffusion experiment and SAXS results, proton conductivities evaluated at two different directions, parallel to draw ($\rho_x$) and perpendicular to draw ($\rho_y$) in drawn Nafion® showed ordering in the hydrophilic channels essentially increases the proton conduction.

## E. Acknowledgements

Support for this work was provided by the National Science Foundation CMMI-0707364 and CBET-0756439. Use of the National Synchrotron Light Source, Brookhaven National Laboratory, was supported by the U.S. Department of Energy, Office of Science, Office of Basic Energy Sciences, under Contract No. DE-AC02-98CH10886. Authors also would like to sincerely thank Prof. Louis A. Madsen and Dr. Jing Li for their collaboration, discussion and for running the $^1$H Pulsed Field Gradient (PFG) NMR experiments.

## E. References


(1) Mauritz, K. A.; Moore, R. B. *Chem. Rev.* **2004**, *104*, 4535-4585.
(2) Yeo, R. S.; McBreen, J.; Kissel, G.; Kulesa, F.; Srinivasan, S. *J. Appl. Electrochem.* **1980**, *10*, 741-747.
(3) Grot, W. *Chemie Ingenieur Technik* **1978**, *50*, 299-301.
(4) Park, J. K.; Moore, R. B. *ACS Appl. Mater. Interfaces* **2009**, *1*, 697-702.
(5) Gierke, T. D.; Munn, G. E.; Wilson, F. C. *J. Polym. Sci. Polym. Phys. Ed.* **1981**, *19*, 1687-1704.
(6) Fujimura, M.; Hashimoto, T.; Kawai, H. *Macromolecules* **1982**, *15*, 136-144.
(7) Elliott, J. A.; Hanna, S.; Elliott, A. M. S.; Cooley, G. E. *Macromolecules* **2000**, *33*, 4161-4171.
(8) Londono, J. D.; Davidson, R. V.; Mazur, S. *Polym. Mater.: Sci. Eng.* **2001**, *85*, 23.
(9) Rubatat, L.; Rollet, A. L.; Gebel, G.; Diat, O. *Macromolecules* **2002**, *35*, 4050-4055.
(10) Page, K. A.; Cable, K. M.; Moore, R. B. *Macromolecules* **2005**, *38*, 6472-6484.
(11) Rubatat, L.; Diat, O. *Macromolecules* **2007**, *40*, 9455-9462.
(12) Haubold, H.-G.; Vad, T.; Jungbluth, H.; Hiller, P. *Electrochim. Acta* **2001**, *46*, 1559-1563.
(13) Page, K. A.; Park, J. K.; Moore, R. B.; Sakai, V. G. *Macromolecules* **2009**, *42*, 2729-2736.
(14) Schmidt-Rohr, K.; Chen, Q. *Nat. Mater.* **2008**, *7*, 75-83.
(15) Pivovar, A. M.; Pivova, B. S. *J. Phys. Chem. B.* **2005**, *109*, 785-793.
(16) Perrin, J.-C.; Lyonnard, S.; Volino, F. *J. Phys. Chem. C* **2007**, *111*, 3393-3404.
(17) Saito, M.; Arimura, N.; Hayamizu, K.; Okada, T. *J. Phys. Chem. B* **2004**, *108*, 16064-16070.
(18) Thomas A. Zawodzinski Jr.; Neeman, M.; Sillerud, L. O.; Gottesfeld, S. *J. Phys. Chem.* **1991**, *95*, 6040-6044.
(19) Ma, S.; Siroma, Z.; Tanaka, H. *J. Electrochem. Soc.* **2006**, *153*, A2274-A2281.
(20) Li, J.; Wilmsmeyer, K. G.; Madsen, L. A. *Macromolecules* **2009**, *42*, 255-262.
(21) Rollet, A.-L.; Jardat, M.; Dufreche, J.-F.; Turq, P.; Canet, D. *J. Mol. Liq.* **2001**, *92*, 53-65.
(22) Lee, C. H.; Park, H. B.; Lee, Y. M.; Lee, R. D. *Ind. Eng. Chem. Res.* **2005**, *44*, 7617-7626.
(23) Ohkubo, T.; Kidena, K.; Ohira, A. *Macromolecules* **2008**, *41*, 8688-8693.
(24) Kidena, K. *J. Membrane Sci.* **2008**, *323*, 201-206.
(25) Zhang, J.; Giotto, M. V.; Wen, W.-Y.; Jones, A. A. *J. Membrane Sci.* **2006**, *269*, 118-125.
(26) Yeo, R. S. *J. Electrochem. Soc.* **1983**, *130*, 533-538.
(27) Pourcelly, G.; Oikonomou, A.; Gavach, C. *J. Electroanal. Chem.* **1990**, *287*, 43-59.
(28) Edmondson, C. A.; Stallworth, P. E.; Wintersgill, M. C.; Fontanella, J. J.; Dai, Y.; Greenbaum, S. G. *Electrochim Acta* **1998**, *43*, 1295-1299.
(29) Rieke, P. C.; Vanderborgh, N. E. *J. Membrane Sci.* **1987**, *32*, 313-328.
(30) Nouel, K. M.; Fedkiw, P. S. *Electrochim Acta* **1998**, *43*, 2381-2387.
(31) Wakizoe, M.; Velev, O. A.; Srinivasan, S. *Electrochim Acta* **1995**, *40*, 335-344.
(32) Buchi, F. N.; Scherer, G. G. *J. Electroanal. Chem.* **1996**, *404*, 37-43.
(33) Slade, S.; Campbell, S. A.; Ralph, T. R.; Walsh, F. C. *J. Electrochem. Soc.* **2002**, *149*, A1556-A1564.
(34) Van der Heijden, P. C.; Rubatat, L.; Diat, O. *Macromolecules* **2004**, *37*, 5327-5336.
(35) Page, K. A.; Landis, F. A.; Phillips, A. K.; Moore, R. B. *Macromolecules* **2006**, *39*, 3939-3946.
(36) Osborn, S. J.; Hassan, M. K.; Divoux, G. M.; Rhoades, D. W.; Mauritz, K. A.; Moore, R. B. *Macromolecules* **2007**, *40*, 3886-3890.
(37) Stejskal, E. O.; Tanner, J. E. *Journal of Chemical Physics* **1965**, *42*, 288-292.
(38) Kim, M.-H.; Glinka, C. J.; Grot, S. A.; Grot, W. G. *Macromolecules* **2006**, *39*, 4775-4787.
(39) Litt, M. H. *Polym. Prepr.* **1997**, *38*, 80-81.
(40) Wilkes, G. L.; Stein, R. S. In *Structure and Properties of Oriented Polymers*; Ward, I. M., Ed.; Chapman & Hall, 1997; pp 44-135.
(41) Stasiak, J.; Squires, A. M.; Castelletto, V.; Hamley, I. W.; Moggridge, G. D. *Macromolecules* **2009**, *42*, 5256-5265.
(42) Lin, H.-L.; Yu, T. L.; Huang, C.-H.; Lin, T.-L. *J. Polym. Sci. Pol. Phys.* **2005**, *43*, 3044-3057.

(43) Allahyarov, E.; Taylor, P. L. *J. Phys. Chem. B* **2009**, *113*, 610-617.
(44) Kreuer, K.-D. *Chem. Mater.* **1996**, *8*, 610-641.

# CHAPTER IV

# MORPHOLOGICAL INVESTIGATION OF NAFION® MEMBRANES PREPARED BY SOLUTION-PROCESSING AT VARIOUS TEMPERATURES

## A. Introduction

Perfluorosulfonate ionomers (PFSIs) have become an extremely versatile class of semicrystalline ionomers with their wide applications ranging from chlor-alkali cell[1], water electrolyzers[2], batteries[3], fuel cells[3,4] to artificial muscles[5]. The most widely explored PFSI, and the focus of the current investigation, is Nafion®, which is developed and produced by E. I. Dupont Chemical Company.[4] Nafion® is composed of a polytetrafluoroethylene (PTFE) segment and perfluoroether side chains terminated with sulfonic acid groups as shown in Figure III-1.

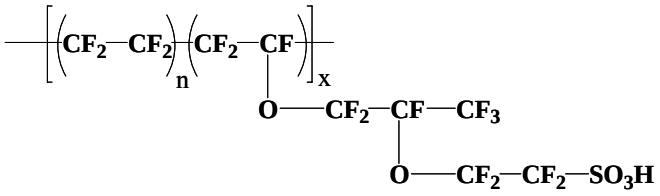

**Figure IV-1.** Chemical structure of Nafion®

It has been shown that the polar, perfluoroether side chains containing the sulfonic acid groups aggregate into ionic clusters which are dispersed throughout the non-polar PTFE matrix.[4,6] These ionic clusters, and specifically their shape, size, order, spatial distribution, and connectivity, precisely define the supramolecular organization and function of this

technologically important material as an ionic conductor.[4,6-8] In addition, PTFE segments of sufficient length are capable of organizing into crystalline domains having unit cell dimensions virtually identical to that of pure PTFE.[9] The complex, phase-separated morphology, consisting of crystalline and ionic domains, of PFSIs has been the focus of numerous investigations aimed at characterizing the morphology and thermomechanical behaviors of these materials.[6,10-15]

Nafion® is generally produced by melt-extrusion of the precursor form containing the pendant sulfonyl fluoride $-SO_2F$ moiety and then implementing a solid-state hydrolysis to convert the non-ionic precursor into the ionomer form containing a sulfonate group, $-SO_3^-$.[16] More recently, due to the necessity for thin membranes in modern proton exchange membrane fuel cell (PEMFC) applications, the current industrial membrane processing procedures have shifted from high-temperature melt extrusion to relatively low-temperature dispersion-casting method.[17] While the new dispersion-casting method allows several crucial advantages such as (1) less contamination, (2) increased overall production rates and (3) improved thickness control and uniformity, it has been reported that these new membranes exhibit physical properties that are significantly different from the extruded counterparts.[17] For example, new, dispersion-cast Nafion® NRE212CS undergoes disintegration in boiling methanol, however as-received, extruded Nafion® membranes remain intack in boiling methanol even after several hours.[18]

Alternative methods to the industrially-adopted melt-extrusion and dispersion-casting processes are also found in the literatures.[19-22] Cable and Moore recognized that existence of PTFE-like crystals and an electrostatic network are the principle barriers to melt-processing the Nafion®.[19] In an effort to manipulate the electrostatic interaction, the authors chose to neutralize $H^+$-form Nafion® with bulky, organic tetrabutylammonium ($TBA^+$) counterions which have been shown to effectively reduce the strength of electrostatic interaction in a sulfonated polystyrene

ionomer system by forming weak dipole-dipole pairs.[23] $TBA^+$-form Nafion® was then dissolved in alcohol/water mixture at elevated pressure and temperature. By performing a "steam-stripping" process, the PTFE-like crystallites were completely eliminated (which is verified by WAXD) and thus obtained amorphous $TBA^+$-form Nafion® powder was melt-processed at 190 $^oC$ and 200 psi to a thickness of ca. 200 μm.[19]

Another alternative method to morphological manipulation has been demonstrated through solution casting.[20-22,24-26] Martin first detailed a procedure for dissolving PFSIs using an alcohol/water mixture at elevated temperatures and pressures.[25] Moore and Martin recognized that a material, which is very different from as-received extruded Nafion®, is obtained when the solvent is removed from alcohol/water solution of Nafion® at room temperature (Figure IV-2). This material was essentially brittle and showed a poor mechanical stability. Solution-processing at an elevated temperature using an appropriate solvent, however, restored the crystalline character and thus improved the mechanical properties (Figure IV-2).[20,21] Recently, Luan and coworkers investigated structural evolution of Nafion® ionomer from concentrated *N*,*N*-dimethyl formamide (DMF)-based solution to a membrane state.[24] It was suggested that increasing casting temperature induced greater interdigitation of ionic aggregates, which subsequently led to improved insolubility, higher membrane density and greater tensile stress at break of the PFSI membranes.[24]

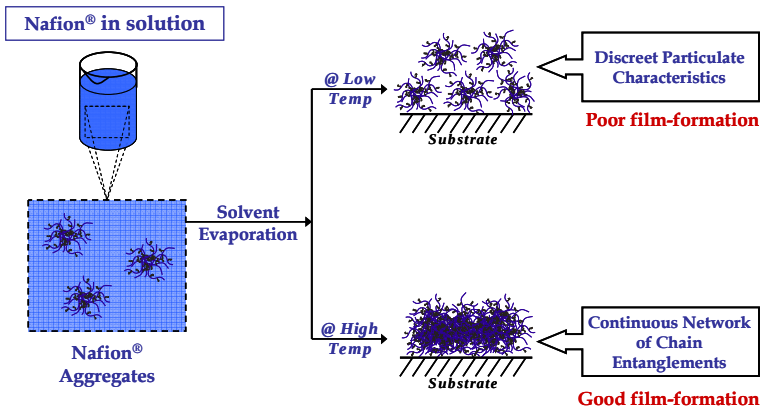


**Figure IV-2.** Effect of solution-processing temperature and solvent on Nafion® membrane formation

While the existence of crystallinity in the PFSI membranes is well known[6,9], this important morphological feature has received little attention in comparison to the proton-conducting, ionic domains. Our preliminary investigation and the previous study by Page et al. indicated the slow crystallization behavior of PFSIs from a melt state.[12] To explore the ultimate roles of crystallinity in affecting key fuel cell membrane characteristics such as water uptake, ionic domain structure and dimensions, proton conductivity and mechanical stability in this benchmark perfluorosulfonate ionomers, the current investigation employs a solution-processing method to manipulate the crystalline component in PFSIs. More specifically, as-received extruded $H^+$-form Nafion® 117CS membranes are dissolved in alcohol/water mixture and then solution processed using a high boiling point solvent (dimethylsulfoxide, DMSO) at elevated temperatures ranging from 130 $^oC$ to 190 $^oC$ to explore the effects of casting temperature on the overall crystallization behavior. Furthermore, fundamental understanding of the formation and function of this essential morphological feature will be elucidated.

## B. Experimental

***Materials***. The PFSI membrane, Nafion® 117CS (1100 EW, sulfonic acid form) was obtained from E.I. Dupont de Nemours & Company. Ethanol and dimethylsulfoxide (DMSO) were all reagent grade and used as received. All other reagents were used without further purification.

***Preparation of PFSI Solution***. Nafion® membranes were cleaned by refluxing in aqueous 8M $HNO_3$ for 2hr. The $H^+$-form membrane was then boiled in deionized (DI) water for 1 hr to remove excess acid and then dried under vacuum oven at 70 $^oC$ for 12 hr. The $H^+$-form PFSI solution was prepared by dissolving the cleaned membrane in a solvent mixture of DI water (50 % by volume) and ethanol (50 % by volume). The PFSI dissolution was performed using a Parr reactor at 250 $^oC$ under pressure with constant stirring, for 2hr. After cooling to room temperature, the solution was filtered to remove residual, undissolved polymer.

***Preparation of Solution-Processed Membranes***. In a 25 mL glass vial, 5 mL of DMSO was added to 20 mL of a 0.5 % (w/v) PFSI solution. The majority of ethanol and water was removed by heating on a hot plate at ca. 80 $^oC$. Finally, the solution-processed membranes were formed by evaporating the resulting solution of the Nafion®/DMSO to dryness at various temperatures ranging from 130, 135, 142, 151, 160, 180, to 190 $^oC$ for 20 min. To remove any residual DMSO after casting, all membranes were cleaned by refluxing in aqueous 8M $HNO_3/H_2O$ for 2 hr and then in DI water for 1 hr.

***Thermogravimetric Analysis (TGA)***. Hi-Res TGA 2950 Thermogravimetric Analysizer (TA Instruments) was used to determine the total drying time at various solution-processing temperatures. The isothermal weight loss was monitored at the same temperatures incorporated in the current study to form membranes.

***Differential Scanning Calorimetry (DSC)***. DSC data were collected using a TA differential scanning calorimeter (DSC 2000). First, solution-processed $H^+$-form membranes were neutralized to contain $Na^+$ ions. These samples were then dried at 70 $^oC$ under vacuum for 12 h prior to thermal analysis. The samples (ca. 10 mg) were scanned from 50 $^oC$ to 350 $^oC$ at a rate of 20 $^oC$/min under $N_2$ purge.

***Wide-angle X-ray Diffraction (WAXD)***. WAXD experiment was performed on the Gemini diffractometer system from Oxford Diffraction equipped with a two-dimensional position sensitive area detector. A sealed tube source was used to produce the Cu Kα radiation ($\lambda$ = 1.54 Å ) and the sample-to-detector distance was 55 cm. Scattering patterns (collected for 10 min) were corrected for background scattering and integrated using the GADDS software package.

***Small-angle X-ray Scattering (SAXS)***. To characterize the morphology of solution-processed membranes, synchrotron SAXS was carried out at the Brookhaven National Laboratory (BNL) on the Advanced Polymer Beamline (X27C) at the National Synchrotron Light Source (NSLS). The incident X-ray beam was tuned to a wavelength of 0.1366 nm, and the sample-to-detector distance was 85 cm. The two-dimensional scattering patterns were recorded on a high resolution Mar CCD camera. The relationship between pixel position and the momentum transfer vector $q$ was determined by calibrating the scattering data using a silicon wafer standard. All data analysis was carried out using the polar software developed by Stonybrook Technology and Applied Research, Inc. The scattering intensities were corrected for transmission, incident beam flux, and background scattering due to air and Kapton windows. The scattering profiles are displayed as intensity (arbitrary unit) versus the scattering vector, $q$, which is a function of the scattering angle ($\theta$) through the following relationship:

$$q = \frac{4\pi}{\lambda}\sin(\theta) \qquad \textbf{Eq IV-1}$$

where λ is the wavelength of radiation (0.1366 nm) and $\theta$ is half of the scattering angle ($2\theta$).

***Water Uptake Measurement***. The water content in the solution-processed membranes was determined gravimetrically and presented in terms of the lamda (λ) value which is defined as the number of water molecules per sulfonic acid site and calculated using Eq IV-2.

$$\lambda = \frac{(M_{hyd} - M_{dry})/18}{M_{dry}/1100} \qquad \textbf{Eq IV-2}$$

The membrane was first boiled in deionized water for 1 hr, the surface blotted dry and weighed ($M_{hyd}$) and the membrane was then dried at 70 $^{o}$C under vacuum for 12 hr ($M_{dry}$). 18 is the molar mass (g/mol) of water and 1100 is the equivalent weight of the Nafion® used in this study.

***Dynamic Mechanical Analysis (DMA)***. Dynamic mechanical analysis of Nafion® membranes prepared by solution-processing at various temperatures was performed using a TA Instruments DMA Q800 analyzer in tensile mode. Vacuum-dried membranes with a width of 5.3 mm were run in triplicate to verify results and reduce experimental error. The membranes were analyzed at a frequency of 1Hz from -120 $^{o}$C to 160 $^{o}$C with a heating ramp of 2 $^{o}$C /min.

***Tensile Analysis***. To investigate the tensile properties of the solution-processed membranes, the stress versus strain curves were recorded using a Linkam tensile testing system, TST 350 at with a crosshead speed of 10 mm/min. In order to reduce experimental error, more than 5 samples were prepared for each processing temperature.

## C. Results and Discussion

To evaluate how rapidly a casting solvent (DMSO) will evaporate at various processing temperatures and thus to determine appropriate casting time (solvent evaporation time), TGA

was used to simulate the overall solution processing. Figure IV-3a shows a plot of the % weight loss as a function of the elapsed time at various isothermal temperatures. TGA data shows that the % weight loss reached a plateau, 20 wt % after a certain amount of time at all processing temperatures. As expected, the amount of time to reach this plateau decreases as the processing temperature increases. The time required to reach the 20 wt % as a function of the processing temperature is plotted and shown in Figure IV-3b. The plot of *solvent evaporation time* versus *processing temperature* was also fitted with a second order polynomial; the equation is as follows ($r^2$ is linear least-squares correlation coefficient):

Evaporation time (min) = 50.9895 + 0.379 × (processing temperature) + 8.875 × (processing temperature)$^2$, ($r^2$ =0.99158)

For the current investigation, solvent evaporation time of 20 min was used for all solution processing temperatures to ensure a majority of solvent evaporated during this time period.

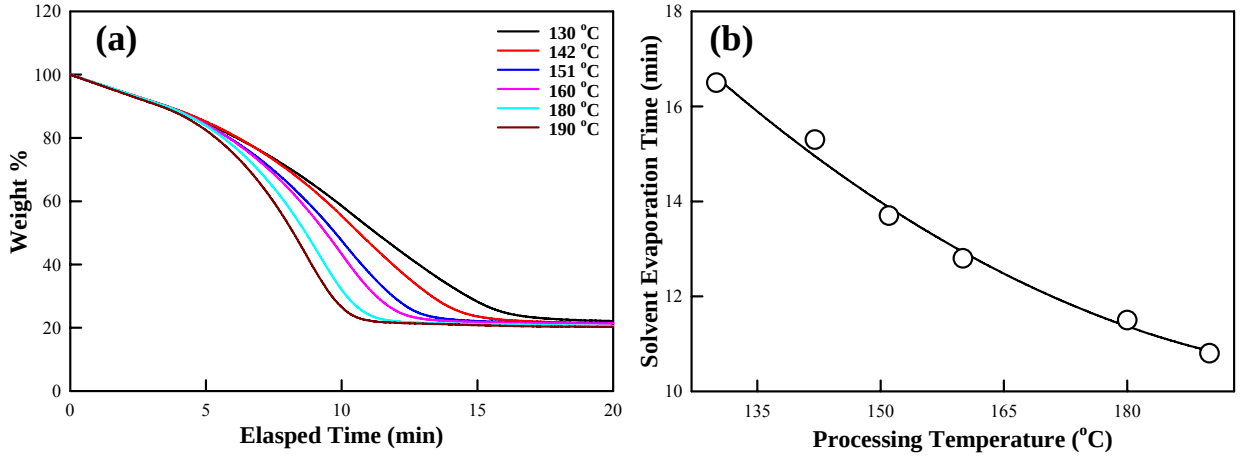


**Figure IV-3.** Consideration of solvent evaporation time while solution-processing $H^+$-form Nafion® at various temperatures (solvent = DMSO). % weight loss vs. elapsed time during isothermal process (a) and solvent evaporation time vs. solution-processing temperature (b)

Figure IV-4 shows the DSC results obtained for the Nafion® membranes that are prepared by solution processing at various temperatures. DSC thermograms of these membranes do not show the previously observed two endothermic peaks below 300 $^{o}$C in the initial heating scan of as-received extruded materials.[12] The observed single endotherm is sensitive to the processing temperature and it systematically shifts to higher temperature as the processing temperature increases. In an agreement with the thermal behavior of semicrystalline polymers and the previous studies on PFSIs, we attribute this endotherm to the melting of solvent-induced PTFE-like crystallites due to their sensitivity on the thermal history.[12] The heat of fusion ($\Delta H$) value for each solution-processing temperature was also analyzed by integrating the area under the endothermic peak. Figure IV-5 plots both $T_m$ and $\Delta H$ values as a function of solution-processing temperature. It turns out that both parameters ($T_m$ and $\Delta H$) are strongly influenced by solution-processing temperatures. Unlike $T_m$, which continuously increases with solution-processing temperatures, $\Delta H$ shows a slight decrease at higher solution-processing temperature. The trend of $T_m$ and $\Delta H$ may be rationalized by considering the number and size of crystals induced during the solution-processing. At lower processing temperatures, it can be assumed that relatively small-sized crystals are formed and thus they melt at lower temperatures. However the population of these crystals is high and thus overall crystallinity is also high. At higher processing temperatures, it is possible to form large and thick crystals that will subsequently melt at higher temperatures. However the population of these big crystals is low and thus overall crystallinity is also low.

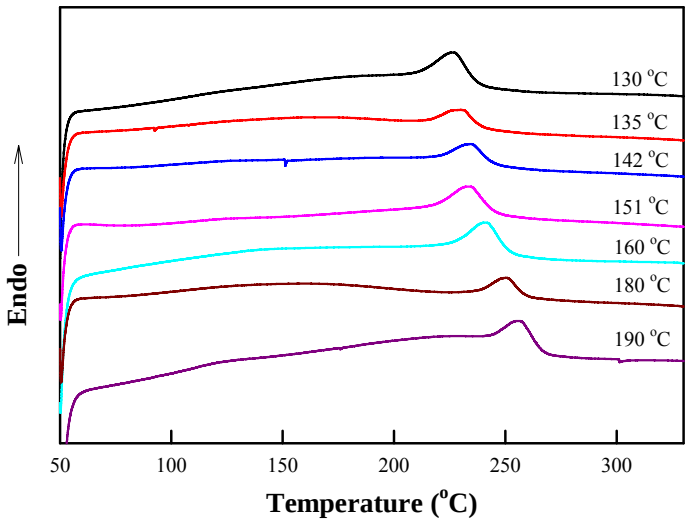


**Figure IV-4.** DSC thermograms of solution-processed membranes prepared at various temperatures. (All samples were neutralized to contain $Na^+$ ions after casting. Data acquired with the initial heating scan, 20 °C / min)

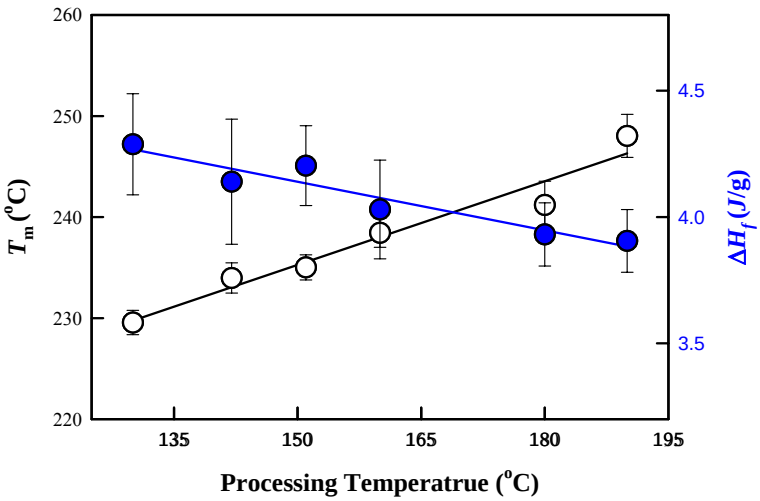


**Figure IV-5.** Plot of melting point temperature ($T_m$, left) and the heat of fusion (ΔH, right) as a function of the solution-processing temperature.

Structural characterization by wide-angle X-ray diffraction (WAXD) was performed on dry membranes to gain information regarding the degree of crystallinity and the perfection of the crystalline lattice. Figure IV-6a shows the integrated WAXD profiles (plotting relative intensity vs. the scattering angle, $2\theta$) of the solution-processed membranes prepared at various

temperatures. These profiles display characteristic diffraction peaks at $2\theta$ = 8 – 30 °. The peak at ca. $2\theta$ = 18 ° is attributed to the weak reflection of PTFE-like crystallites, hkl = 100, which is superimposed as a shoulder on a broad amorphous halo. To calculate the % crystallinity, peak devolution was performed using PeakFit® software (SPSS, Inc.). Figure IV-6b shows an illustration of the deconvolution into the amorphous and crystalline peaks using Lorentzian area and Gaussian area, respectively. Thus calculated % crystallinity and full-width at half maximum (FWHM) value of the crystalline peak are provided in Table IV-1 for each membrane. Although there is a small disparity in the behavior of how the amount of crystallinity determined by DSC and WAXS progress as a function of the processing temperature, the general trend of determined crystallinity indices from DSC and WAXS methods reveals a decrease in the degree of crystallinity with increasing solution processing temperatures. Furthermore, the FWHM value of the crystalline peak monotonically decreases (Table IV-1) with increasing processing temperatures, which indicates that the perfection of the crystalline lattice becomes greater in membranes prepared at higher temperatures.

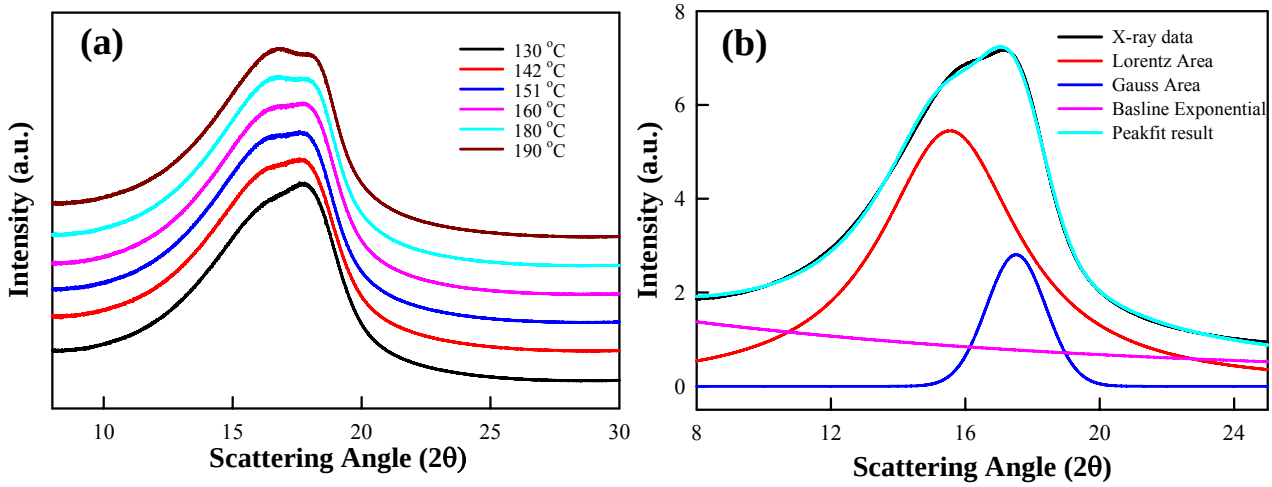


**Figure IV-6.** WAXD profiles of Nafion® membranes prepared by solution-processing at various temperatures (a) and an illustration of peak devolution method employed to calculate % crystallinity (b).

**Table IV-1. Determined % crystallinity and FWHM of crystalline peak**

| | Casting temperature ($^{o}$C) | | | | | |
|---|---|---|---|---|---|---|
| | 130 | 142 | 151 | 160 | 180 | 190 |
| Calculated crystallinity (%) | 24.3 | 21.7 | 20.7 | 20 | 19.1 | 17.7 |
| FWHM of crystalline peak | 2.42 | 2.35 | 2.28 | 2.25 | 2.12 | 1.92 |

Both DSC and WAXS results definitely showed that the fraction of crystalline component (the degree of crystallinity) decreases as processing temperature is increased from 130 to 190 $^{o}$C, but within the crystalline domain, the perfection of chain packing into a crystalline lattice is greatly improved. Small-angle X-ray scattering (SAXS) was also used to access information regarding the developing morphological features of both the crystalline and ionic domains as a function of processing temperature. For the as-received extruded Nafion® 117CS, a scattering maximum (often referred to as ionomer peak) appear typically at ca. $q$ = 0.2 Å$^{-1}$, which has been attributed to scattering from the ionic aggregates dispersed in the PTFE matrix.[4] Another relatively broad scattering maximum appearing at ca. $q$ = 0.05 Å$^{-1}$ in SAXS profiles from the as-received extruded Nafion® membrane has been attributed to the electron density difference between PTFE-like crystalline and amorphous domains of the polymer.[4] In an agreement with the previous studies, these solution-processed membranes also show two scattering maxima as shown in Figure IV-7. It clearly shows that SAXS profiles of solution-processed membranes are strongly affected by the temperature used during film formation. While the ionic domain peak remained relatively constant over the temperature range used for this study, the shape, amplitude and $q$-position of the crystalline peak are strongly influenced by

the casting temperature. The crystalline scattering maximum shifts systematically to smaller scattering angles with an increase in the solution processing temperature. Furthermore, it is evident that the maximum intensity of the crystalline peak is increasing consistently as the casting temperature increases while that of the ionomer peak remains fairly constant. Detailed analysis of the SAXS profiles was performed through peak de-convolutions using the PeakFit® software (SPSS, Inc.) and presented in Figure IV-8. The best fitting results were achieved by using an exponential function as a background and fitting crystalline and ionic SAXS peaks with Gaussian area functions. It is obvious that the FWHM value of the crystalline peak is much more responsive to the casting temperature than the ionomer peak. While the FWHM value of the ionomer peak marginally increases with the casting temperature, the FWHM value of the crystalline peak systematically decreases. A decrease in FWHM values suggest a narrowing of the distribution of the correlation distances between the scattering particles, which indicates a significantly improved spatial crystalline domain order at higher processing temperatures.

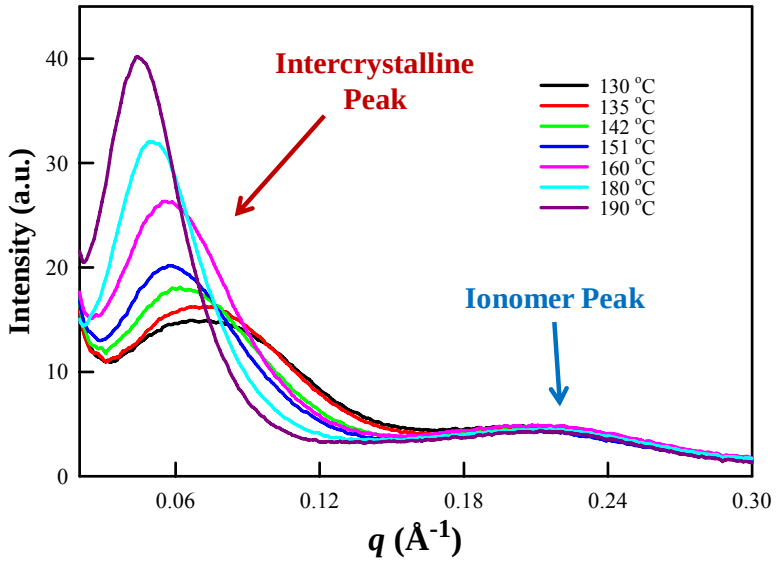


**Figure IV-7.** SAXS profiles of solution-processed membranes as a function of different processing temperature

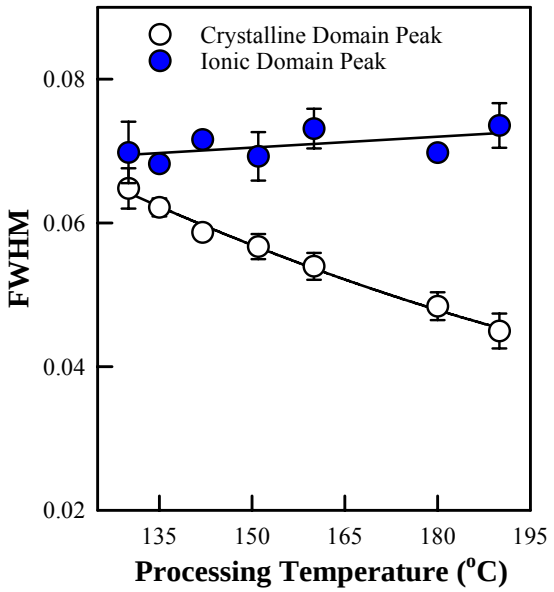


**Figure IV-8.** Plots of FWHM as a function of solution-processing temperature for the ionomer and crystalline peaks.

It was observed from the DSC, WAXD and SAXS results that the crystalline domains are profoundly affected by the temperature used during membrane processing. Furthermore, these data indicated that higher processing temperatures induced bigger/thicker crystallites in the solution-processed membranes. Figure IV-9 schematically illustrates the proposed crystal formation behavior that might occur at lower temperatures and higher temperatures, respectively. At lower processing temperatures, there are a higher number of crystallites with a broad size distribution and their relative distances are closer as proved by the crystalline domain peak in SAXS profiles. These are relatively small-sized crystals which undergo melting at lower temperatures (Figure IV-4). At higher processing temperatures, there are a lower number of crystallites, but with more uniform sizes. And their relative distances are larger as evidenced by the crystalline domain peak in SAXS profiles. However, these are big/thick crystals that melt at higher temperatures (Figure IV-4).

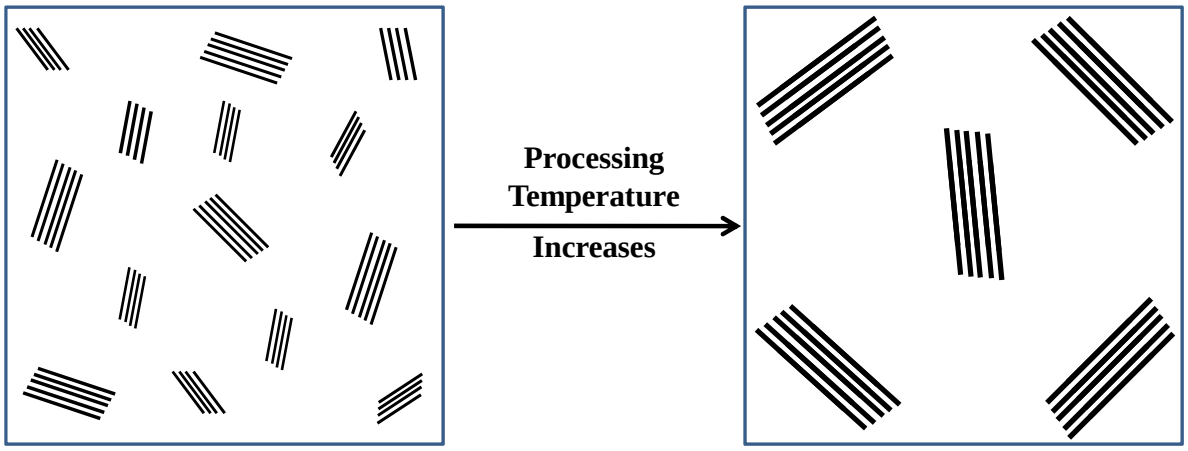


**Figure IV-9**. A schematic drawing (not to be scaled) showing the proposed crystal formation behavior at low (left) and high temperatures (right)

To examine tensile properties of the solution-processed membranes, the stress versus strain curves were recorded using a Linkam tensile testing system, TST 350. From the data shown in Figure IV-10, various important tensile properties can be immediately extracted to reveal the impact of casting temperature on the mechanical properties of solution-processed membranes. A stress-strain curve for as-received extruded Nafion® 117CS is also presented as a means of comparison to that of solution-processed membranes. While the elastic modulus or the slope of the stress-strain curve at small strains remains relatively constant regardless of the processing temperature, the plastic modulus, or the slope of the stress-strain curve beyond the yield point is observed to be sensitive to the processing temperature and increases gradually as a function of processing temperature. A positive slope in the tensile curve beyond the yield point has been commonly referred to as experimental strain hardening and was previously observed in Nafion®-related materials and also other ionomeric systems.[27-29] In solution-processed membranes, both the stress at break and the strain at break are strongly influenced by the casting temperature and systematically increase as a function of processing temperature (Figure IV-11).

Furthermore, experimental strain hardening becomes more pronounced with increasing processing temperatures. This information can likely be linked to the different crystalline structure (i.e., crystallite size and crystalline order) established during solution-processing at various temperatures. For example, large-sized crystals (with an improved crystalline order) formed at elevated temperatures may act as a barrier to tensile loading. It is interesting to note that Gilbert and coworkers also observed an increase in experimental strain hardening of the Nafion® precursor containing the pendant sulfonyl fluoride $-SO_2F$ moiety after annealing at 70 °C.[29] The authors also noticed an increase in tensile strength along with a decrease in elongation at break of annealed materials, which was attributed to improvement of the crystalline structure.

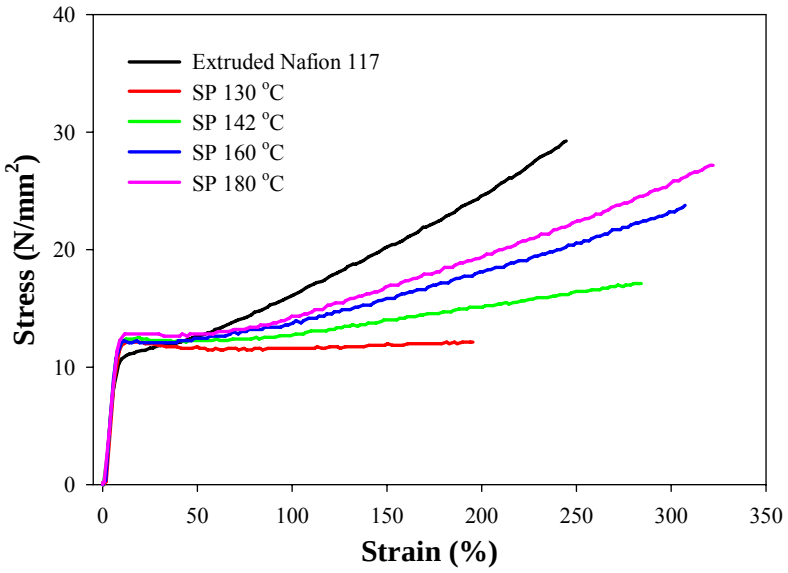


**Figure IV-10.** Mechanical tensile stress vs. strain plots of solution-processed (SP) $H^+$-form Nafion® membranes prepared at various temperatures.

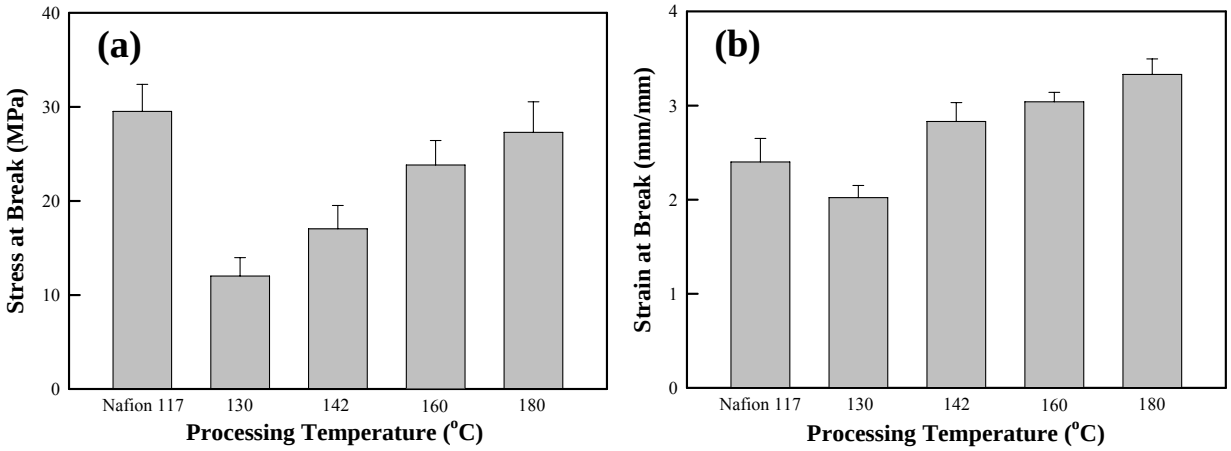


**Figure IV-11.** Plot of stress at break vs. processing temperature (a) and strain at break vs. processing temperature (b)

Dynamic mechanical analysis (DMA) was also performed to investigate thermomechanical properties of solution-processed $H^+$-form membranes. Previous DMA studies on $H^+$-form Nafion® membranes (EW = 1100 g $mol^{-1}$) observed three different transitions ($\alpha > \beta > \gamma$).[30,31] A transition, labeled α, in the tan δ curve was observed at ca. 110 °C and this relaxation was attributed to the onset of long-range mobility of both main and side chains through destabilization of the electrostatic network.[12] Network destabilization was thought to occur through ion-hopping, the process of ion pairs transferring between ionic clusters to balance electrostatic and elastic forces. The weak β-relaxation ($T_\beta$) centered at -20 °C was associated with the onset of segmental motions (principally backbone motions) within the framework of a *static* physically cross-linked network of chains.[32,33] A γ-relaxation at around -100 °C was attributed to short range molecular motions in the PTFE phase, the same origin as in pure PTFE.[31] Figure V-12 shows the storage modulus (top) and loss tangent (bottom) curves of solution-processed membranes as a function of temperature. With increasing temperature, the storage modulus changes from a glassy state, through an ionic plateau, to a rubbery flow. Loss

tangent vs. temperature curve shows the previously observed three transitions (α > β > γ). While α-relaxation seems to be slightly changed by solution-processing temperatures, essentially β and γ-relaxation temperatures remained unaffected. Even though DSC, WAXD, and SAXS results indicated a considerable difference in crystallization behavior under different processing temperatures, no significant change in thermomechanical transition temperatures is probably due to a narrow window of crystallinity (ca. 10 wt %) that can be manipulated in 1100 EW Nafion®.[4,9]

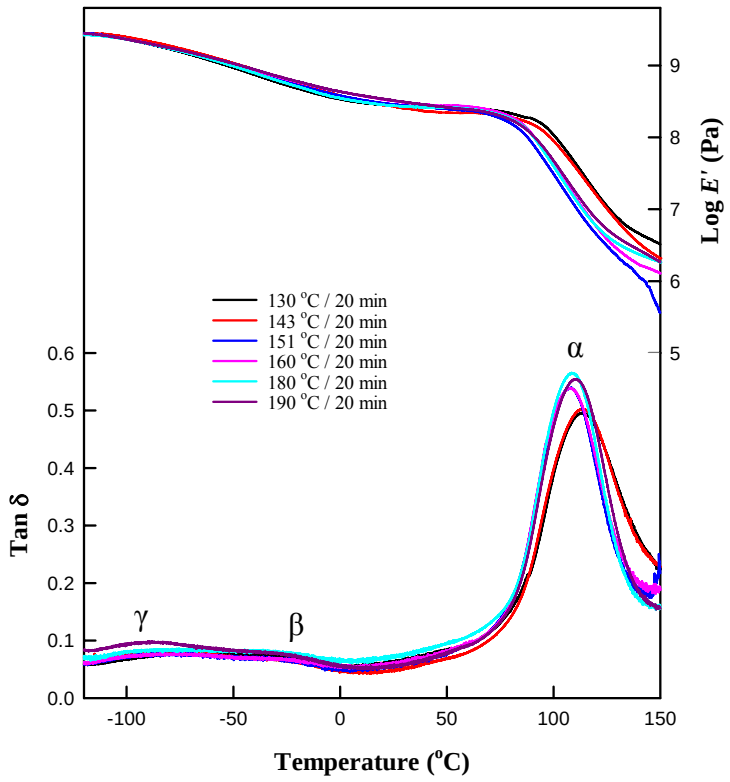


**Figure IV-12.** Dynamic mechanical analysis (DMA) of solution-processed membranes at different temperatures (top: Storage modulus, bottom: tan δ )

Water uptake of membranes is intimately related to the critical membrane properties and play an essential role in the membrane behavior.[34] While the exact shape, size, order and connectivity of ionic domains are still under debate, it is widely accepted that water imbibed in PFSI membranes increases the size of ionic domain and perhaps improve the connectivity as well, to subsequently increase the proton conductivity.[15,35,36] Figure IV-13 shows water uptake values determined gravimetrically for the solution-processed membranes. It is observed that the water content is strongly influenced by the solution-processing temperature and it decreases from $\lambda$ = 35 to 25 as the processing temperature increases from 130 $^{o}$C to 190 $^{o}$C. It should be noted that water uptake values reported here is still higher than that of as-received Nafion® 117CS produced by extrusion process (ca. $\lambda$ = 23). A dry Nafion® membrane will absorb water until the resulting pressure within the ionic domain is balanced by the elastic stresses that are developed within the polymer backbones. Thus, it is quite reasonable to assume that the amount and/or size of crystallites will strongly influence the water uptake values. Based on the DSC and WAXD results, decreases in water content at higher processing temperature may be attributed to formation of uniform-sized big/thick crystals that may act as barrier to solvent swelling. Although the current investigation did not discuss the structural model of Nafion® in detail, consideration of, such as a rod-like model where crystallites are within the ionic aggregates may be simply rejected based on the information from the membranes prepared by solution-processing at various temperatures, and thus manipulating the degree of crystallinity.[13,15,37] Strong dependence of water content with varying amount of crystallinity is a strong indication that crystallites cannot be within the ionic aggregates.

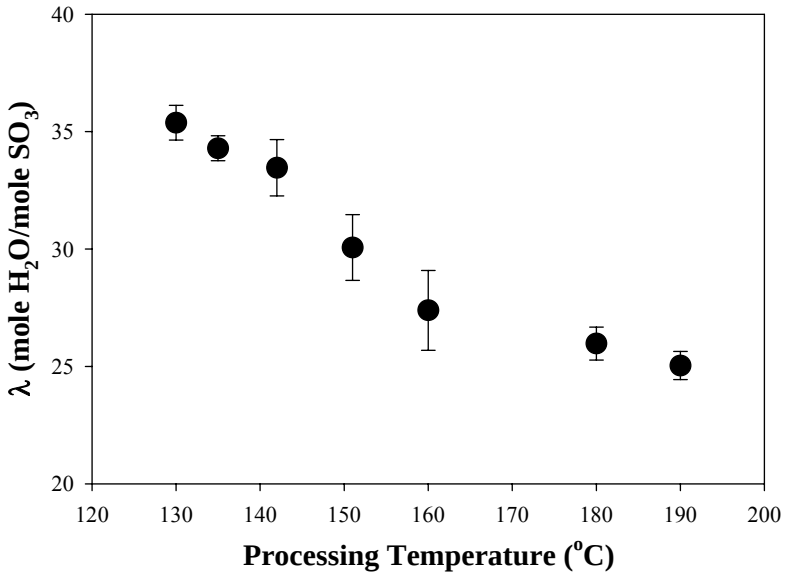


**Figure IV-13.** Water uptake of $H^+$-form solution-processed Nafion® membranes

## D. Conclusions

With the commercial development of much thinner fuel cell membranes, we are faced with challenges associated with its premature mechanical integrity failures and pin-hole formation in the membranes, which would eventually lead to fuel cell failure. To explore the role of crystallinity on mechanical stability in proton exchange membrane (PEM) fuel cell applications, we have prepared solution-processed membranes at various temperatures in an effort to manipulate the crystalline component. SAXS profiles of solution-processed membranes showed that the ionic domain peak remained relatively constant over the temperature range used for this study, but the shape, amplitude and *q*-position of the crystalline peak are strongly influenced by the casting temperature. The degree of overall crystallinity (or the fraction of crystalline component) determined by both DSC and WAXD decreased as processing temperature was increased from 130 to 190 $^oC$. With elevated processing temperatures, however,

bigger/thicker crystallites were formed and within the crystalline domain, the perfection of chain packing into a crystalline lattice was greatly improved. It turns out that the water content was strongly influenced by the solution-processing temperature, which indicates strong dependence of water content with the crystalline component within Nafion® membranes. Measurements of proton conductivity and water diffusion are under way and will be used to better define the role of crystallinity on membrane properties.

## E. Acknowledgements

Support for this work was provided by the National Science Foundation CMMI-0707364 and CBET-0756439. Use of the National Synchrotron Light Source, Brookhaven National Laboratory, was supported by the U.S. Department of Energy, Office of Science, Office of Basic Energy Sciences, under Contract No. DE-AC02-98CH10886.

## F. References

(1) Grot, W. *Chemie Ingenieur Technik* **1978**, *50*, 299-301.
(2) Yeo, R. S.; McBreen, J.; Kissel, G.; Kulesa, F.; Srinivasan, S. *J. Appl. Electrochem.* **1980**, *10*, 741-747.
(3) Winter, M.; Brodd, R. J. *Chem. Rev.* **2004**, *104*, 4245-4269.
(4) Mauritz, K. A.; Moore, R. B. *Chem. Rev.* **2004**, *104*, 4535-4585.
(5) Park, J. K.; Moore, R. B. *ACS Appl. Mater. Interfaces* **2009**, *1*, 697-702.
(6) Gierke, T. D.; Munn, G. E.; Wilson, F. C. *J. Polym. Sci. Polym. Phys. Ed.* **1981**, *19*, 1687-1704.
(7) Li, J.; Wilmsmeyer, K. G.; Madsen, L. A. *Macromolecules* **2008**, *41*, 4555-4557.
(8) Doyle, M.; Rajendran, G. In *Handbook of Fuel Cells-Fundamentals, Technology and Applications*; Wielstich, W., Lamm, A., Gasteiger, H. A., Eds.; John Wiley & Sons: Chichester, 2003; Vol. 3; pp 351-395.
(9) Starkweather, H. W. *Macromolecules* **1982**, *15*, 320-323.
(10) Page, K. A.; Park, J. K.; Moore, R. B.; Sakai, V. G. *Macromolecules* **2009**, *42*, 2729-2736.
(11) Schmidt-Rohr, K.; Chen, Q. *Nat. Mater.* **2008**, *7*, 75-83.
(12) Page, K. A.; Cable, K. M.; Moore, R. B. *Macromolecules* **2005**, *38*, 6472-6484.
(13) Rubatat, L.; Rollet, A. L.; Gebel, G.; Diat, O. *Macromolecules* **2002**, *35*, 4050-4055.

(14) Kim, M.-H.; Glinka, C. J.; Grot, S. A.; Grot, W. G. *Macromolecules* **2006**, *39*, 4775-4787.
(15) Gebel, G. *Polymer* **2000**, *41*, 5829-5838.
(16) E. I. Dupont De Nemours & Co Inc., 2002; Vol. 2009.
(17) Curtin, D. E.; Lousenberg, R. D.; Henry, T. J.; Tangeman, P. C.; Tisack, M. E. *J. Power Sources* **2004**, *131*, 41-48.
(18) Osborn, S. J.; Mauritz, K. A.; Moore, R. B. *Polym. Prepr.* **2008**, *49*, 473-474.
(19) Moore, R. B.; Cable, K. M.; Croley, T. L. *J. Membr. Sci.* **1992**, *75*, 7-14.
(20) Moore, R. B.; Martin, C. R. *Macromolecules* **1988**, *88*, 1334-1339.
(21) Moore, R. B.; Martin, C. R. *Anal. Chem.* **1986**, *58*, 2569-2570.
(22) Grot, W. G., 1982.
(23) Weiss, R. A.; Agarwai, P. K.; Lundberg, R. D. *J. Appl. Polym. Sci* **1984**, *29*, 2719-2734.
(24) Luan, Y.; Zhang, H.; Zhang, Y.; Li, L.; Li, H.; Liu, Y. *J. Membrane Sci.* **2008**, *319*, 91-101.
(25) Martin, C. R.; Rhoades, T. A.; Ferguson, J. A. *Anal. Chem.* **1982**, *54*, 1639-1641.
(26) Gebel, G.; Aldebert, P.; Pineri, M. *Macromolecules* **1987**, *20*, 1425-1428.
(27) Shah, R. K.; Hunter, D. L.; Paul, D. R. *Polymer* **2005**, *46*, 2646-2662.
(28) Satterfield, M. B.; Majsztrik, P. W.; Ota, H.; Benziger, J. B.; Bocarsly, A. B. *J Polym Sci Pol Phys* **2006**, *44*, 2327-2345.
(29) Gilbert, M.; Haworth, B.; Myers, D. J. B. *Polym. Eng. Sci.* **2004**, *44*, 272-282.
(30) Osborn, S.; Hassan, M.; Divoux, G.; Rhoades, D.; Mauritz, K.; Moore, R. B. *Macromolecules* **2007**, *40*, 3886-3890.
(31) Yeo, S.; Eisenberg, A. *J. Appl. Polymer Sci.* **1977**, *21*, 875-898.
(32) Page, K. A.; Cable, K. M.; Moore, R. B. *Macromolecules* **2005**, *38*, 6472-6484.
(33) Page, K. A.; Landis, F. A.; Phillips, A. K.; Moore, R. B. *Macromolecules* **2006**, *39*, 3939-3946.
(34) Dimitrova, P.; Friedrich, K. A.; Vogt, B.; Stimming, U. *J. Electroanal. Chem.* **2002**, *532*, 75-83.
(35) Lee, C. H.; Park, H. B.; Lee, Y. M.; Lee, R. D. *Ind. Eng. Chem. Res.* **2005**, *44*, 7617-7626.
(36) Zawodzinski, T. A.; Neeman, M.; Sillerud, L. O.; Gottesfeld, S. *J. Phys. Chem.* **1991**, *95*, 6040-6044.
(37) van der Heijden, P. C.; Rubatat, L.; Diat, O. *Macromolecules* **2004**, *37*, 5327-5336.

# CHAPTER V

# UNIAXIAL ORIENTATION AS A MEANS TO ELUCIDATE THE CRYSTALLINE/IONIC DOMAIN ORDER IN PERFLUOROSULFONATE IONOMERS

## A. Introduction

With greater system efficiencies and environmental benefits as well, proton-exchange membrane fuel cells (PEMFCs) have become an attractive system as an alternative to nonrenewable, traditional energy sources.[1] Currently, perfluorosulfonate ionomers (PFSIs), particularly Nafion®, are the benchmark proton exchange membranes due to their unique morphology and excellent transport properties.[2] Nafion®, whose structure is shown in Figure V-1, is a copolymer of tetrafluoroethylene and generally less than 15 mol % of perfluorovinylether units terminated with sulfonic acid functionalities. A significant research efforts have been given to the unique nanophase-separated morphology observed upon aggregation of the polar, ionic side chains within the matrix of hydrophobic PTFE.[2] These ionic clusters, and specifically their shape, spatial distribution and connectivity, precisely define the supramolecular organization and function of this technologically important material as an ionic conductor. With a sufficient length of polytetrafluoroethylene (PTFE) segments between side chains, Nafion® is capable of organizing into crystalline domains that generally comprise less than ca. 10 wt % in an 1100 equivalent weight (EW, the grams of dry polymer per equivalent of sulfonic acid units).[2]

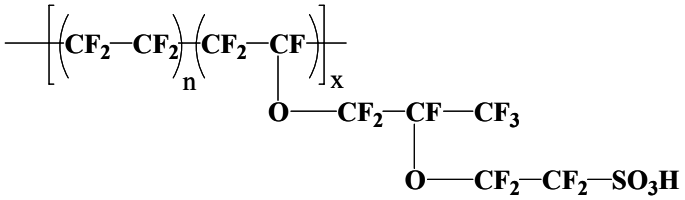

**Figure V-1.** Chemical structure of Nafion®

With electron density differences between the PTFE matrix and ionic clusters, a single scattering maximum appears in small-angle X-ray scattering (SAXS) profiles at ca. $q$ = 0.2 Å$^{-1}$, which has been termed as the "ionomer peak".[2-13] Furthermore, there is another low angle scattering peak or shoulder at ca. $q$ = 0.05 Å$^{-1}$, which has been attributed to scattering from the locally ordered crystallites composed of relatively long runs of PTFE segments between side chains.[2,5] It should be pointed out that it has been difficult to access quantitative morphological information of this unique ionomer because of a random chemical structure which leads to an organization into the complex formation of ionic and crystalline domains with a significant distribution in dimensions/sizes over a wide range of length scales. [2,14]

Numerous structural models have been proposed in order to explain the origins of the ionomer peak in Nafion®. Hsu and Gierke suggested a model with swollen inverse micelles of roughly spherical geometry that are connected by nano-scale hydrophilic channels.[4] In addition to the early work of Hsu and Gierke, the most common ones include the core-shell model by Fujimura et al.,[7] the local order model by Dreyfus et al.[15], lamellar model by Litt et al.[11], and the fringed-micelle model by Kim et al.[3]. More recently, the Grenoble group have pointed out that unoriented Nafion® samples show an I($q$) ~ $q^{-1}$ power law behavior between $q$ = $10^{-3}$ Å$^{-1}$ and $q$ = $5\times10^{-1}$ Å$^{-1}$ which is typically observed from elongated scattering objects.[9,10] Based on this

observation, Rubatat and coworkers suggested that Nafion® membrane is composed of rod-like aggregates with the core containing fluorocarbon backbones and the exterior decorating with ionic functionality.[9,16] Schmidt-Rohr and Chen also recognized the presence of an elongated object as a scattering entity in the Nafion® membrane, but they modeled the structure of Nafion® as cylindrical and parallel water channels surrounded by partially hydrophilic side branches, forming inverted-micelle cylinders.[14,17] Although each model differs significantly in the shape/order of ionic domains, they all recognize the presence of ionic aggregates that are dispersed throughout the PTFE matrix.

A careful review of these models, however, reveals that only a few studies have considered the existence or role of a crystalline component. For example, three recent models for the morphology of PFSIs have focused on the existence of crystallites dispersed between[3] or within rod-like ionic domains[9] or as lamellae separating the ionic regions[11]. Clearly, the true crystallite organization (stacked lamellae vs. fringed micelles) and the proximity of the crystallites to the ionic domains differs significantly in the proposed structures, and thus fundamental research is needed to provide definitive evidence for the true semi-crystalline structure in these technologically important ionomers.

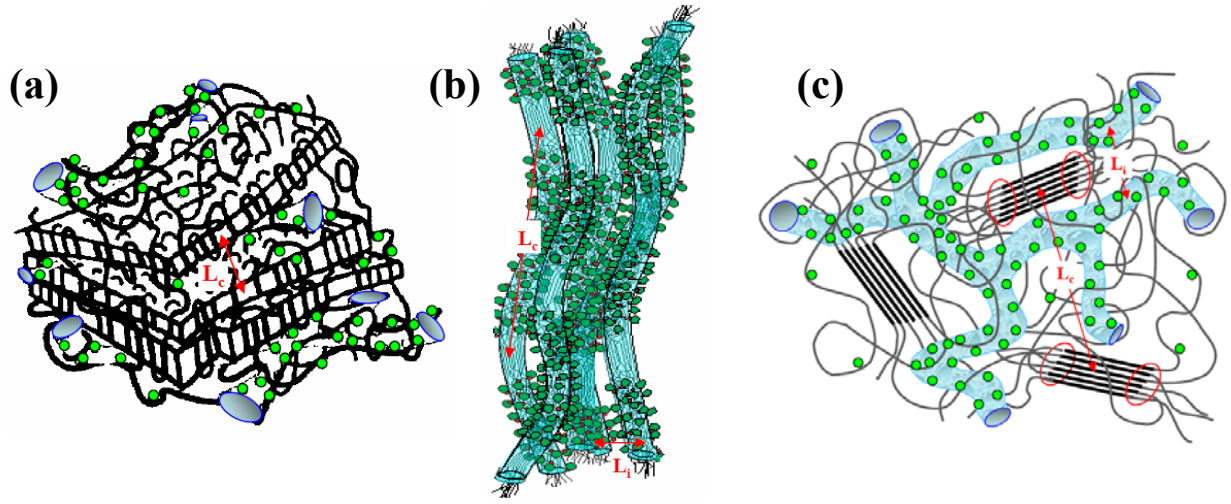


**Figure V-2**. Current morphological models for the semi-crystalline structure of perfluorosulfonate ionomers. (a) lamellar model (Reprinted with permission from ref[18] *Macromolecules*, **39**, 4775 (2006). Copyright 2006 American Chemical Society), (b) rod-like aggregate model (Reprinted with permission from ref[19] *Macromolecules*, **37**, 7772 (2004). Copyright 2004, American Chemical Society) and (c) fringed-micelle model (Reprinted with permission from ref[18] *Macromolecules*, **39**, 4775 (2006). Copyright 2006 American Chemical Society)

While the existence of the crystalline component in PFSI membranes is well-known[4,20,21], this important morphological feature has received very little attention in comparison to the proton-conducting ionic domains. Since key fuel cell membrane characteristics such as water uptake, ionic domain structure and dimensions, proton transport, and mechanical stability are intimately linked to the presence and organization of the crystalline domains in PFSIs[2,14], it is of profound importance that we develop a fundamental understanding of crystalline order and its proximity to the ionic domains in Nafion®. In this study, we employ uniaxial orientation as a means to elucidate the crystalline/ionic domain order in Nafion®. Several mechanical deformation studies were performed previously and resulted in valuable information.[4,6,7,12,22] To briefly summarize, SAXS of oriented Nafion® samples exhibits anisotropic scattering patterns showing the ionomer peak exclusively in the equatorial directions.[12,23,24] However, only a limited $q$ range was considered and again the crystalline component was not discussed. While

uniaxial extension can yield an anisotropic morphology in Nafion® that is stable and persistent at room temperature, there have been few SAXS studies to date exploring large length-scale morphological features. Furthermore, the majority of previous modeling efforts are based on SAXS studies which have principally involved PFSIs in a single morphological state (i.e., as-received extruded Nafion® supplied by DuPont). Based on the SAXS results, the Chapter IV showed that solution-processing significantly affects both the position and shape of the crystalline peak. More importantly, the $I(q) \sim q^{-1}$ power law behavior exhibited by the as-received materials was not observed in the membranes prepared by the solution-processing method involving a high boiling point solvent. In this paper, small- and wide-angle X-ray scatterings (SAXS and WAXS) are used to investigate the orientation of the crystalline and ionic components to elucidate the spatial arrangements of the key morphological features that are generally applicable to all PFSIs. Recognizing that solution-processing at elevated temperatures can lead to significantly improved spatial crystalline domain order in PFSIs, the focus of the current investigation will be solution-processed membranes.

## B. Experimental

***Materials.*** As-received, extruded $H^+$-form Nafion® 117CS (1100 g/equivalent, 7 mil thickness) and Dispersion-cast $H^+$-form Nafion® NRE212CS (1100 g/equivalent, 2 mil thickness) were obtained from E.I. DuPont de Nemours & Company. As-received $H^+$-form Nafion® 117CS was precleaned by refluxing in 8M $NHO_3/H_2O$ for 2 h, and then in deionized (DI) water for 1 h. These cleaned membranes were dried at 70 $^oC$ in a vacuum oven for 12 hr.

***Preparation of Solution-Processed $H^+$-Nafion®.*** Solution-processed PFSI membranes were prepared by casting from dimethyl sulfoxide (DMSO) at 180 °C by following a standard procedure.[25,26] Solutions of PFSIs were prepared by dissolving 7 g of as-received $H^+$-Nafion® 117CS into a solvent system consisting of 100 g of ethanol and 100 g of DI water by heating the mixture to 250 $^oC$ in a pressure vessel for 2 hr. In a 25 mL glass vial, 5 mL of DMSO were added to 20 mL of a ca. 0.5 % PFSI solution. The majority of the ethanol and DI water was removed by heating on a hotplate at 80 $^oC$. Finally, solution-processed membranes were formed by evaporating the remaining DMSO solution of the PFSI to dryness at 180 $^oC$. To remove any residual DMSO after solvent casting, all samples were cleaned by refluxing in 8M $NHO_3/H_2O$ for 2 hr and then in DI water for 1 hr. These cleaned membranes were dried at 70 $^oC$ for 12 hr in a vacuum oven.

***Uniaxial Orientation of Solution-Processed $H^+$-Nafion®.*** Uniaxially elongated samples were prepared by cutting the vacuum-dried $H^+$-Nafion® membranes into dog-bone shapes and mounting them on a specially designed drawing apparatus. This drawing apparatus allowed $H^+$-Nafion® membranes to be drawn at 150 °C (above the α-relaxation temperature of $H^+$-form[27]) to draw ratios ($\lambda_b$ = final length (L) / initial length ($L_0$)) ranging from 1 to 4 as determined by the displacement of ink marks on the samples. Stretching rate was 10 mm/min and temperature was increased from room temperature to 150 $^oC$ at a rate of 6 $^oC$/min. As soon as the desired draw ratio was reached, the membranes were rapidly quenched to room temperature to prevent thermal relaxation.[12] To prepare water-swollen samples, uniaxially oriented $H^+$-form membranes were then mounted in Kel-F clamps and soaked in DI water for 24 hr at room temperature.

***Synchrotron Small-angle X-ray Scattering (SAXS).*** Small-angle X-ray scattering (SAXS) was performed at the Brookhaven National Laboratory on the Advanced Polymer Beamline (X27C) at the National Synchrotron Light Source. The wavelength of X-ray beam was 1.366 Å and the sample-to-detector distances (SDD) were 1890 mm and 867 mm for low and medium $q$ ranges, respectively. Two-dimensional SAXS images were recorded using a Mar CCD camera with an intensity uncertainty on the order of 2 % and analyzed using the POLAR software developed by Stonybrook Technology and Applied Research, Inc. The relationship between pixel and the momentum transfer vector $q$ was determined by calibrating the scattering data with a silver behenate standard. All scattering intensities were corrected for transmission and background scatter due to air and Kapton windows and represented in arbitrary, relative intensity units as a function of the scattering vector, $q$, which is a function of the scattering angle through the following relationship (Eq V-1),

$$q = (\frac{4\pi}{\lambda})\sin\theta \qquad \textbf{Eq V-1}$$

where λ is the wavelength of X-ray beam (1.366 Å) and $\theta$ is half of the scattering angle ($2\theta$).

***Wide-Angle X-ray Diffraction (WAXD)***. WAXD experiment was performed on the Gemini diffractometer system from Oxford Diffraction equipped with a two-dimensional position sensitive area detector. A sealed tube source was used to produce the Cu Kα radiation (λ=1.54 Å) with sample-to-detector distance of 55 cm. Scattering patterns were corrected for background scattering and integrated using the GADDS software package.

## C. Results and Discussion

While rich morphological information of Nafion® has been accumulated from numerous scattering and diffraction studies in an attempt to precisely define the molecular/supermolecular organization of perfluorosulfonate ionomers in various physical states, a universally accepted morphological model as the structure of Nafion® has yet to be defined.[2,14] It should be pointed out that recent morphological models featuring an elongated cylindrical object have been motivated by the observation of the I($q$) ~ $q^{-1}$ power law behavior in unoriented Nafion® membranes. Thus it is significant for us to check if the I($q$) ~ $q^{-1}$ power law behavior observed in as-received, extruded Nafion® membranes are general in all perfluorosulfonate ionomers.

A SAXS profile from the as-received, dried Nafion® 117CS produced by melt-extrusion, is shown in Figure V-3 and displays two scattering maxima at ca. $q$ = 0.2 and 0.05 Å$^{-1}$ attributed to the ionomer peak and intercrystalline domain peak, respectively. In an agreement with the previous observation by the Grenoble group[9] and Kim et al.[18], the averaged intensity decays between 3 $\times 10^{-3}$ and 2 $\times$ $10^{-2}$ Å$^{-1}$ following a $q^{-1}$ power law, which is typical for elongated scattering objects such as cylindrical morphologies. Figure V-3 also shows SAXS profiles of membranes prepared by Moore and Martin's solution-processing method (which involves the use of a high boiling point solvent, DMSO) and DuPont's new dispersion-cast method (NRE212CS).[25,28] It is important to recognize that AR 117CS, solution-processed and NRE212CS membranes have almost the same shape and position of the ionomer peak. However, the power law dependence for the solution-processed membrane (I ($q$) ~ $q^{-2.23}$) and DuPont's dispersion-cast NRE212CS membrane (I ($q$) ~ $q^{-1.93}$) are significantly different from that for AR 117CS. While the different power law dependence observed in this study can likely be linked to a different processing/thermal history, Figure V-3 clearly shows that I ($q$) ~ $q^{-1}$ power law

behavior applies only to as-received extruded Nafion® membrane and is not a general feature for all perfluorosulfonate ionomers. More interestingly, SAXS profiles of the sulfonyl fluoride form –$SO_2F$), precursor to Nafion®, with various equivalent weights (EW) ranging from 1000 to 1500 also show I ($q$) ~ $q^{-1}$ power law dependence even though there is no ionic character (and thus no ionic aggregation) in the Nafion® precursor (Figure V-4a). Furthermore, I ($q$) ~ $q^{-1}$ power law dependence is no longer persisted after the AR Nafion® 117 CS membrane is heated up to 330 °C (i.e., above $T_m$) and then rapidly quenched to room temperature to remove the crystalline component (Figure V-4b). Thus the recent approach in the literatures to propose a morphological model based on the slope in the log ($I$) vs log ($q$) plot needs to be critically checked.

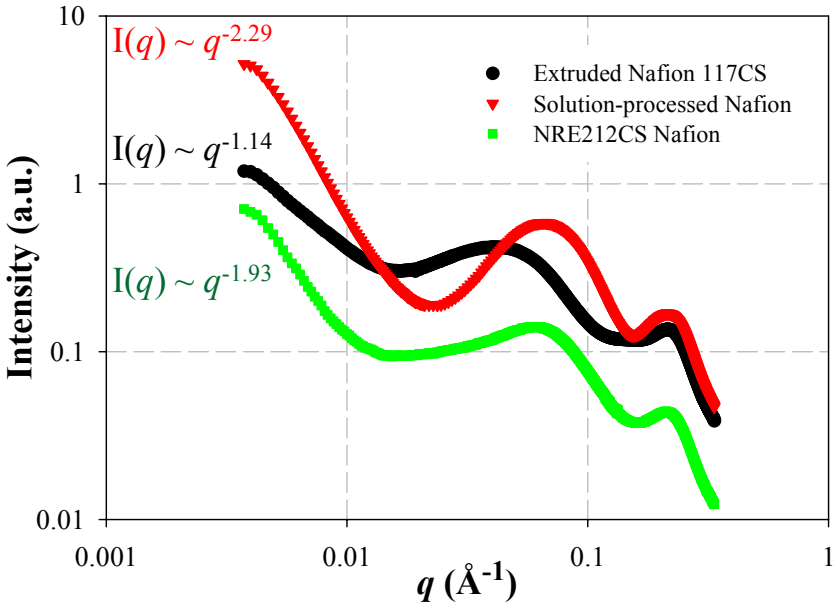


**Figure V-3**. SAXS profiles of as-received (AR) dried Nafion® 117CS (●), solution-processed membrane (▲), and dispersion-cast NRE212CS (■). Drying condition was under vacuum at 70 °C for 12hr.

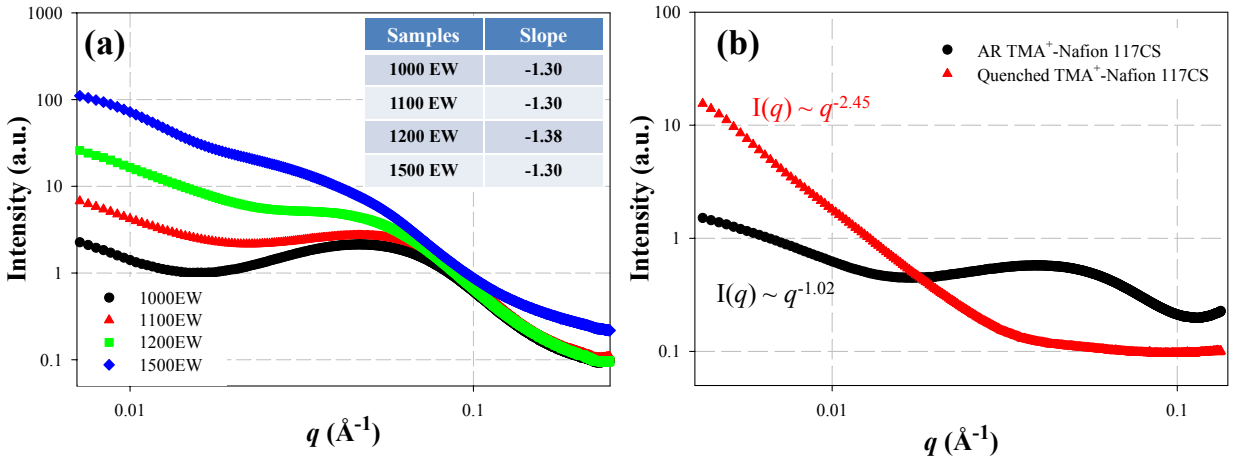


**Figure V-4**. SAXS profiles of Nafion® precursors with various equivalent weight (EW) (a) and tetramethylammonium ($TMA^+$)-form Nafion® before and after melt-quenching from 330 °C (b)

Figure V-5 shows real-time SAXS profiles of a solution-processed membrane during dehydration process at ambient environment (24 °C, 45 % RH). Upon dehydration, it is observed that the intensities of both intercrystalline and ionomer peaks are decreasing due to decreased electron density differences among crystalline, amorphous, and ionic domains and the both peaks are shifted to higher $q$ indicating decreased correlation distances. Considering that water molecules imbibed within the Nafion® membrane remains in the ionic domains, a change in crystallites correlation distance as a function of water content is a strong indication that the correlation of crystals span across the ionic domain. This observation is clearly not in tune with the rod-like ionic aggregate model by the Grenoble group where the authors attributed the intercrystalline peak to the correlation between the crystalline parts along the polymeric aggregates (see Figure V-2).[9] By plotting Bragg distances ($D_{Bragg}$, defined as $D_{Bragg} = 2/q_{max}$ where $q_{max}$ is the peak position) for both crystalline and ionomer peaks as a function of the elapsed time during membrane dehydration, comparison of how two characteristic peaks are shifted simultaneously with water content can be made (Figure V-5b). While two $D_{Bragg}$ values

related to the distribution of crystallinity ($L_c$) and the ionic domains ($L_i$) reaches an asymptotic values after ca.15 min under ambient environment (25 $^oC$, 45 % RH), the intercrystalline spacing ($L_c$) shifts in a manner significantly different from that of the ionomer peak ($L_i$) as water content decreases. Quite surprisingly, intercrystalline peak ($L_c$) shifts ca. 39.17 Å and ionomer peak ($L_i$) 17.63 Å. While it needs a detailed research regarding the intercrystalline peak being more responsive to water content than the ionomer peak, a dissimilar shift of the peak position indicates that the crystalline component in PFSIs is not necessarily located within a common morphological feature. [2,11]

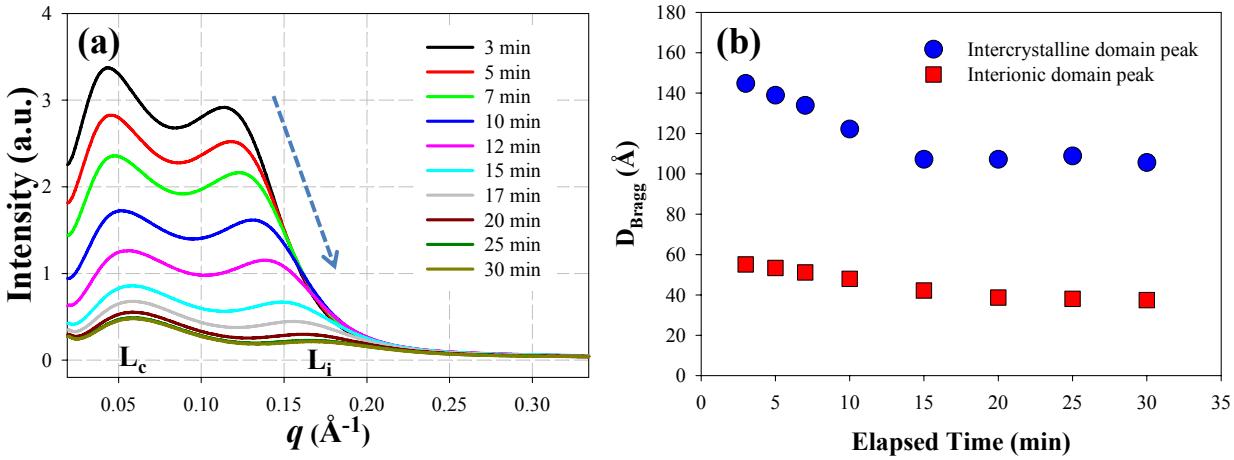


**Figure V-5**. Real-time SAXS of solution-processed membrane during dehydration process at ambient environment (25 $^oC$, 45 % RH) (a), a plot of Bragg distance ($D_{Bragg}$) as a function of an elapsed time (b)

The effects of uniaxial deformation on the morphology of $H^+$-form solution-processed Nafion® have been characterized by two-dimensional SAXS. Valuable mechanical deformation studies were performed previously on as-received extruded Nafion® 117.[6,12,24] To briefly summarize, SAXS of oriented as-received (AR) Nafion® samples exhibited anisotropic scattering patterns showing the ionomer peak exclusively in the equatorial directions. However, only a limited *q* range was considered and the crystalline component was not incorporated mostly due

to the fact that the diffraction reflections of the PTFE-like crystallites are broad and relatively weak. Based on the results presented in the previous chapter (Chapter IV), the solution-processing method significantly improves crystalline order and thus allows us to conduct a detailed analysis of both ionic and crystalline component simultaneously. In Figure V-6a (unoriented and dried state), the isotropic SAXS data show a diffuse outer ring of maximum intensity at ca. $q$ = 0.2 $Å^{-1}$, which has been attributed to scattering from the ionic aggregates dispersed in the PTFE matrix. The intense scattering near the beam stop is associated with typical ionomer long-range heterogeneities and a contribution from PTFE-like crystalline domains. Consistent with the previous orientation studies, as the film is stretched to various draw ratios ($\lambda_b$ defined as L (final length) divided by $L_o$ (initial length)), from 1.25 up to 4.0, the initial isotropic scattering profile for the ionomer peak transforms into a strongly anisotropic scattering pattern (i.e., equatorial spots in Figure V-6h).[12,23,24] Van der Heijden and coworkers attributed this anisotropic scattering to the alignment of elongated polymeric aggregates in the direction of uniaxial extension based on the observation of $q^{-1}$ dependence in the SAXS profiles for the unoriented samples.[24] Recently, Rubatat and Diat suggested that the cylindrical scattering objects are simply aligned (or tilted) preferably toward the stretching direction without undergoing any significant shape change during uniaxial orientation, and thus ruled out the deformation of spherical ionic domains into an ellipsoidal shape.[29] For the intercrystalline peak, the initially isotropic scattering pattern transforms into an ellipse, and scattering intensities grow at the equatorial direction as membranes are elongated to higher draw ratios. This is better demonstrated in Figure V-7 with hydrated samples. In the presence of water, scattering contrasts among ionic, crystalline and amorphous domains are significantly enhanced to allow us to distinctively elucidate the spatial arrangements of the key morphological features. Initially

isotropic outer (the ionomer peak) and inner (the intercrystalline peak) rings in Figure V-7a are almost instantaneously transformed into equatorial arcs at lower draw ratios (Figure V-7b and c) and then equatorial dots at higher draw ratios (Figure V-7g and h).

It should be pointed out that SAXS profiles of oriented solution-processed (SP) Nafion® membranes, both in dried and hydrated states do not show any hint of horizontal streaking. An equatorial streak perpendicular to the stretching direction which passes through $q = 0$ has been observed in SAXS patterns of highly oriented Nafion®[2] and as-received Nafion® 117CS (Chapter III). This type of scattering has been interpreted as a characteristic of intraparticle interference by an elongated object. To quantify the degree of orientation in solution-processed membranes, we have calculated Herman's orientation order parameter (*f*) from the azimuthal plots using Eq V-2

$$f = \frac{3\left\langle \cos^2 \chi \right\rangle - 1}{2} \qquad \textbf{Eq V-2}$$

where $\chi$ is the azimuthal angle and $\langle \cos^2 \chi \rangle$ (the average square of the cosine) is an expression of the orientation. The average square of the cosine was calculated from the integral (Eq V-3)

$$\left\langle \cos^2 \chi \right\rangle = \frac{\int_{\chi_1}^{\chi_2} I(\chi) \cos^2 \chi \sin \chi d\chi}{\int_{\chi_1}^{\chi_2} I(\chi) \sin \chi d\chi} \qquad \textbf{Eq V-3}$$

where I ($\chi$) is the scattering intensity as a function of $\chi$ and the limits of integration are between $\chi_1$ and $\chi_2$. The Herman's orientation function (*f*) assumes a value of 1 for a system with complete orientation of the scattering entities parallel to the director and -1/2 for the case where complete

orientation of the scattering entities is perpendicular to the director. For unoriented samples, the value of *f* is zero. In the case of oriented Nafion® it is necessary to clarify that the director is the momentum transfer vector (or scattering vector), *q*. If the orientation direction of the films is established as the primary axis, then the director, *q*, will be perpendicular to the orientation plane, resulting in values of *f* near -1/2. The results of the Herman's orientation parameters as a function of draw ratios are tabulated in Table V-1 for both as-received (from Chapter III) and solution-processed membranes. Just as observed for oriented as-received Nafion® 117CS, the Herman's order parameter is greatly affected by uniaxial deformation and reaches almost -0.4 for $\lambda_b = 4$, which indicates considerable orientation of ionic aggregates along the stretching direction as previously stated and is in agreement with the literature. It is important to recognize that there is no significant difference between the Herman's order parameters for as-received and solution-processed membranes, meaning the same degree of orientation of ionic aggregates have been achieved. Thus it is not clearly understood why similar equatorial streaking is not observed from oriented solution-processed Nafion®.

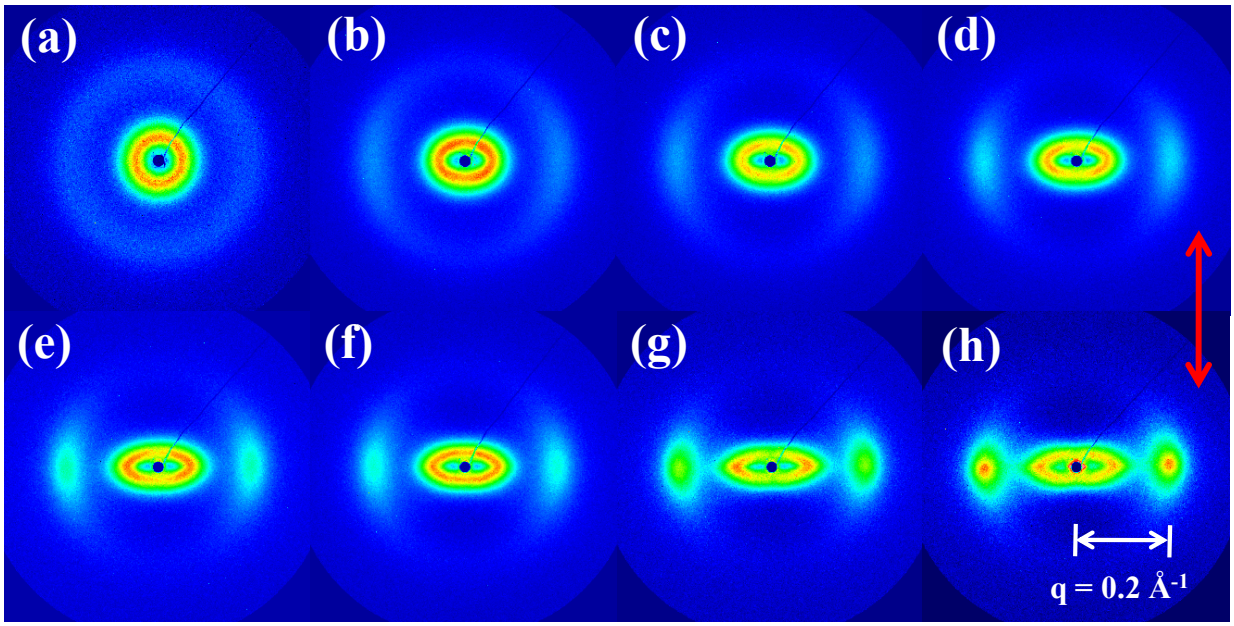


**Figure V-6.** Two-dimensional SAXS patterns of uniaxially oriented, solution-processed $H^+$-form Nafion® (a) $\lambda_b$=1.0, (b) $\lambda_b$ =1.25, (c) $\lambda_b$ =1.5, (d) $\lambda_b$ =1.75, (e) $\lambda_b$=2.0, (f) $\lambda_b$=2.5, (d) $\lambda_b$=3.0, and (h) $\lambda_b$=4.0, Stretching direction is indicated with a red arrow. Samples are in a dried state. Draw ratio ($\lambda_b$) is defined as L divided by $L_o$.

**Table V-1**. Calculated Herman's orientation order parameters (For the purpose of comparison, Herman's order parameter (from Chapter III) for as-received membranes are tabulated together.)

| $\lambda_b$ | 1.0 | 1.25 | 1.5 | 1.75 | 2.0 | 2.5 | 3.0 | 4.0 |
|---|---|---|---|---|---|---|---|---|
| **As-received** | -0.04 | -0.26 | -0.28 | -0.31 | -0.32 | -0.35 | -0.36 | -0.38 |
| **Solution-processed** | 0 | -0.27 | -0.29 | 0.30 | -0.32 | -0.34 | -0.36 | -0.38 |

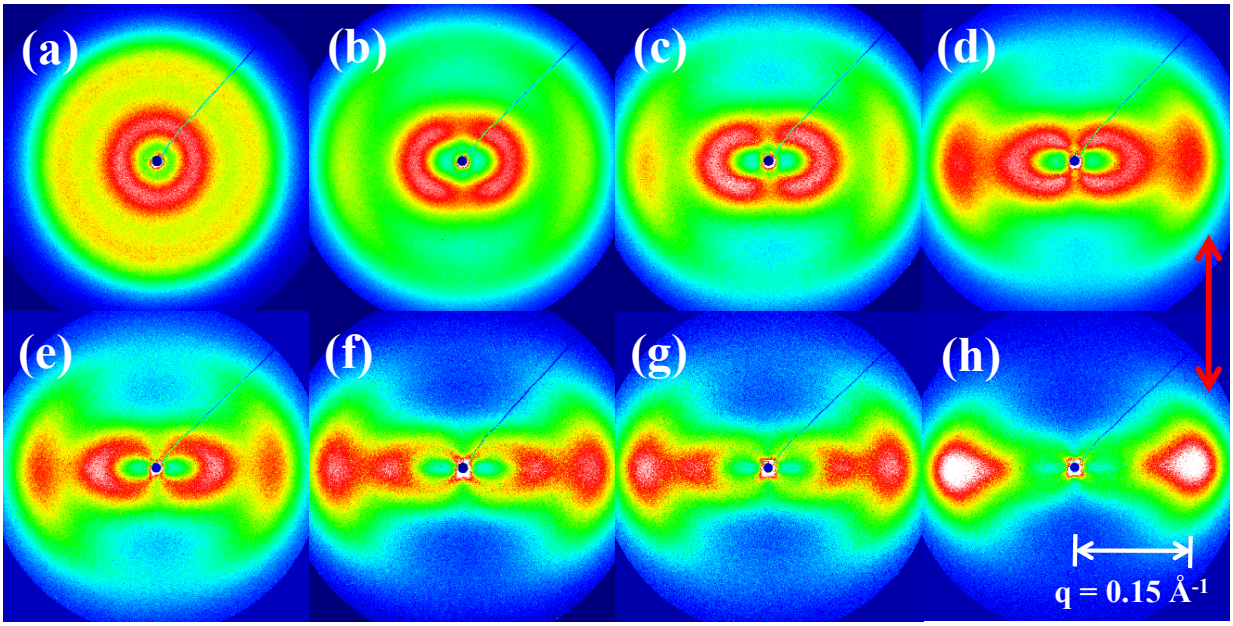


**Figure V-7.** Two-dimensional SAXS patterns of uniaxially oriented, solution-processed $H^+$-form Nafion® (a) $\lambda_b$=1.0, (b) $\lambda_b$ =1.25, (c) $\lambda_b$ =1.5, (d) $\lambda_b$ =1.75, (e) $\lambda_b$=2.0, (f) $\lambda_b$=2.5, (d) $\lambda_b$=3.0, and (h) $\lambda_b$=4.0,, Stretching direction is indicated with a red arrow. Samples are in a hydrated state. Draw ratio ($\lambda_b$) is defined as L divided by $L_o$.

Because both the intercrystalline and ionomer peaks are observed at the equatorial direction after uniaxial orientation, 1-dimensional analyses of oriented SAXS patterns were performed at the azimuthal angle 90°. Figure V-8 shows that the *q* positions of both peaks systematically shift to higher *q* values as a function of draw ratios which indicates decreased correlation distances at the equator. Detailed analysis of change in both $q_{max}$ and $D_{Bragg}$ is shown in Figure V-9a and b, respectively. It should be noticed that the intercrystalline spacings shift as a function of draw ratios in a manner significantly different from that of the interionic cluster spacings. The *q*-positions of ionomer peaks shifted from 0.2254 to 0.2374 $Å^{-1}$ as the Nafion® membrane was elongated to the draw ratio of 4. The Bragg spacing ($D_{Bragg}$) changed from 27.87 to 26.46 Å. On the contrary, the *q*-positions of the intercrystalline peaks underwent a shift from 0.056 to 0.0962 $Å^{-1}$ and $D_{Bragg}$ changed from 112.19 to 65 Å. The observation of dissimilar

shifts strongly indicates that these two important morphological features are dissociated from each other and once again the crystalline component in PFSIs cannot be located within a common morphological feature. It is important to point out that the magnitude of the shift of $D_{Bragg}$ for the ionomer peak is marginal and thus this further supports the concept of ionic channel tilting or rotating without a significant deformation under uniaxial elongation. On the contrary, the intercrystalline domain spacing undergoes a considerable narrowing during uniaxial orientation. We attribute this change in intercrystalline domain spacing to the thinning of the amorphous domains between the crystallites.

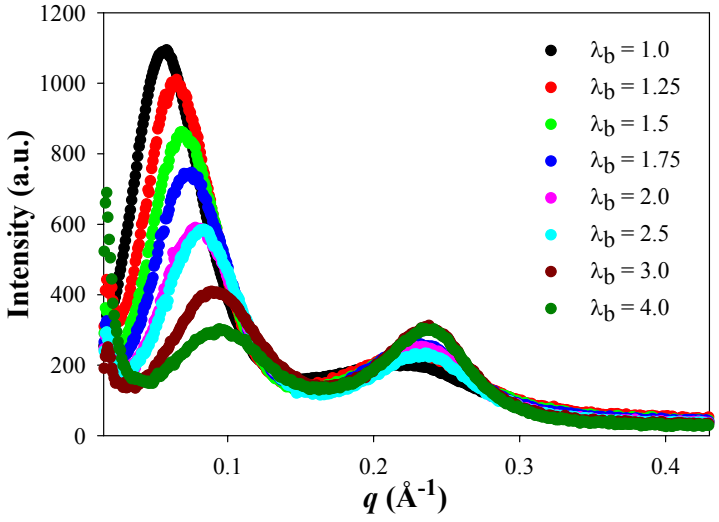


**Figure V-8**. 1-dimensional analysis of oriented SAXS patterns at the equatorial direction as a function of draw ratio ($\lambda_b$)

The effects of uniaxial orientation on the WAXD patterns are shown in Figure V-10. The diffuse inner ring from the unoriented sample in Figure V-10a is attributed to a weak crystalline reflection of PTFE-like crystallites, *hkl* = 100, at $2\theta = 18^o$, which is superimposed as a shoulder on a broad amorphous halo (ca. $2\theta = 12^o$ - $22^o$). The outer ring in Figure V-10a is attributed to the PTFE crystalline reflection *hkl* = 101 at $2\theta = 40^o$. As the sample is uniaxially elongated to a

draw ratio of 4, anisotropic scattering patterns (i.e., equatorial arcs) are developed, which indicates that both the amorphous and crystalline chain segments are aligned along the direction of extension.

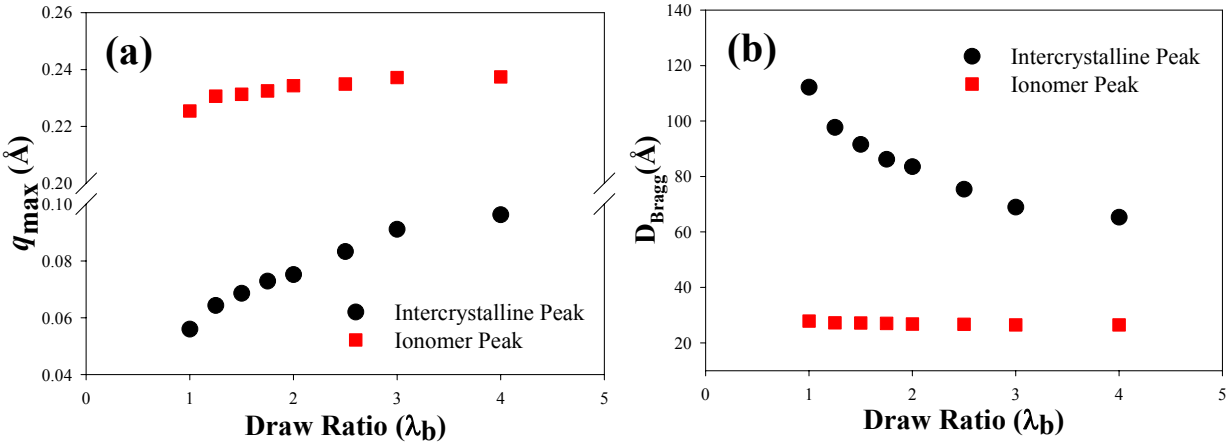


**Figure V-9**. Plots of $q_{peak}$ (a) and $D_{Bragg}$ (b) as a function of draw ratio ($\lambda_b$) for the ionomer peak (■) and intercrystalline peak (●)

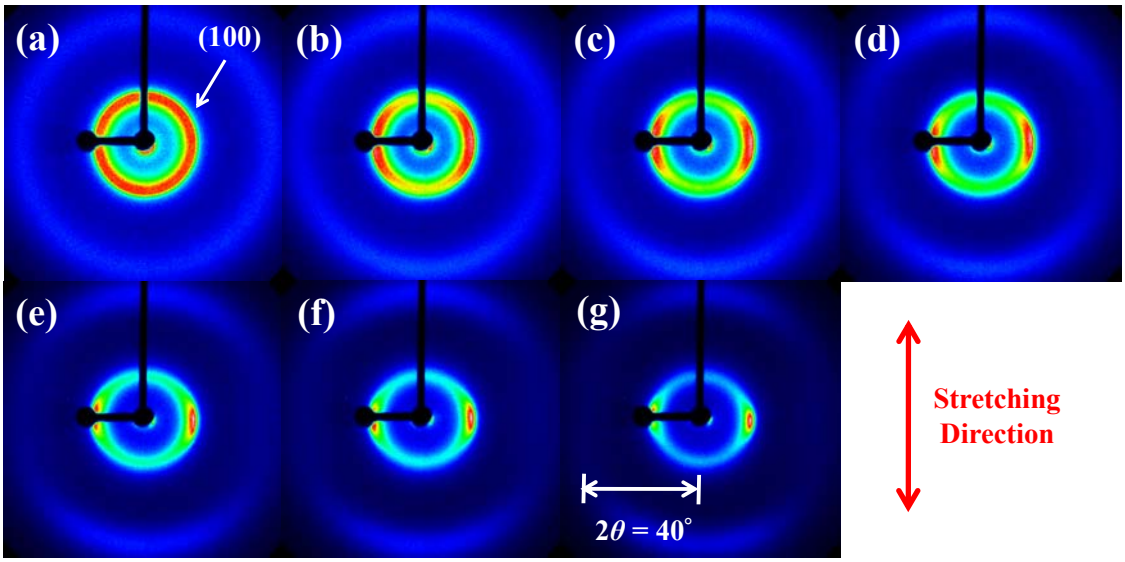


**Figure V-10.** Two-dimensional WAXD patterns of uniaxially oriented, solution-processed $H^+$-form Nafion® (a) $\lambda_b$ =1.0, (b) $\lambda_b$ =1.25, (c) $\lambda_b$ =1.5, (d) $\lambda_b$ =1.75, (e) $\lambda_b$ =2.0, (f) $\lambda_b$ =3.0 and (g) $\lambda_b$ = 4.0 Stretching direction is indicated with a red arrow. Samples are in a dried state.

Three recent models for the morphology of PFSIs have focused on the existence of crystallites dispersed between[18] or within[9] rod-like ionic domains or as lamellae[11] separating the ionic regions (Figure V-2). A lamellar model by Litt[11] provides a convenient and simple explanation for the swelling behavior of Nafion®. It also explains correlation of the intercrystalline peak being across the ionic domain. Furthermore, this model can explain the anisotropic equatorial WAXD patterns after uniaxial deformation (Figure V-11). However, it faces difficulty in explaining the anisotropic SAXS patterns of intercrystalline and ionomer peaks because lamellar-type morphology should have meridional rather than equatorial scatterings after uniaxial deformation (Figure V-11). In Figure V-9, it was shown that the intercrystalline spacings shift as a function of draw ratios in a manner significantly different from those of the interionic cluster spacings. Since the lamellar model essentially stipulates a parallel shift for the two maxima attributed to a lamellar structure of the ionic domains imposed by the semicrystalline character of the polymer, the observation of dissimilar shifts indicates that the lamellar model is an over-simplication in the global description of the morphology of Nafion®.

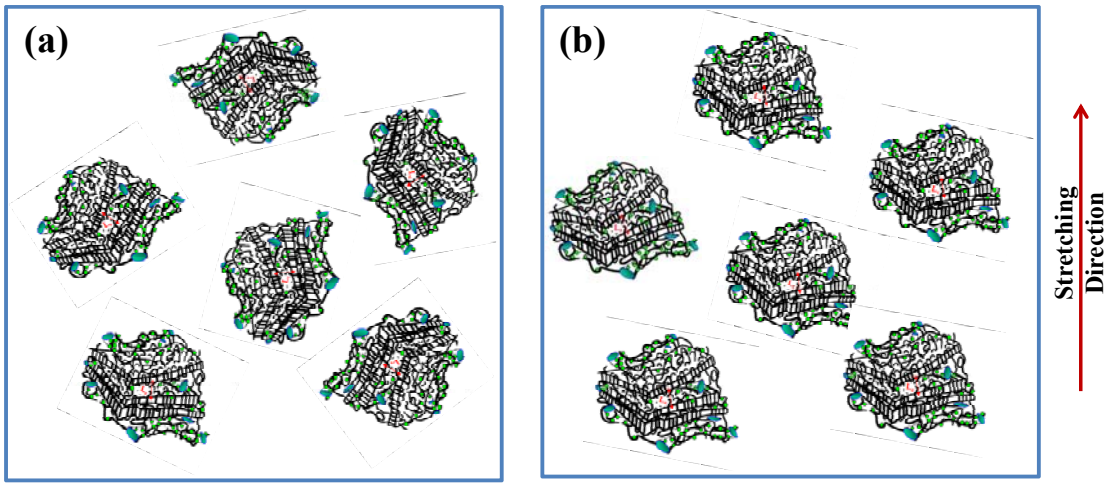


**Figure V-11**. Proposed lamella model for Nafion® morphology before (a) and after (b) uniaxial deformation

Unlike the lamellar model, the elongated rod-like model suggests that crystallites remain within the rod-like ionic domains and thus correlation of the intercrystalline peaks does not lie across the ionic domains (Figure V-2b). This model is simply based on I ($q$) ~ $q^{-1}$ power law typical of long cylinders as a scattering particle at small $q$. However, dehydration experiments clearly indicated that the intercrystalline peak correlation lies across the ionic domains, rejecting this type of morphological configuration. Furthermore, it does not explain the dissimilar shifts of the intercrystalline and interionic cluster spacing as a function of water content. Even more importantly, the I ($q$) ~ $q^{-2}$ rather than I ($q$) ~ $q^{-1}$ power law dependence was observed in our solution-processed membranes and dispersion-cast NRE212CS. In the model of Kim *et al.*[18] (Figure V-2c), the hydrated clusters are worm-like channels that merge freely and thus form a network. This model suggests that crystallites are dispersed between worm-like ionic domains and thus correlation of the intercrystalline peak lies across the ionic domains. Furthermore, by assuming fringed-micelle crystal morphology rather than lamellar crystals, it is possible to explain both the anisotropic equatorial SAXS and WAXS patterns. The choice of a fringed-micelle type crystal is also quite reasonable given the inherent stiffness of the PTFE segments of the Nafion® backbone. [23] Closer examination of the worm-like model by Kim et al., however, reveals that crystallites exist the very next to the ionic channels and thus it does not allow any room for amorphous chains that would undergo a thinning during uniaxial deformation. Furthermore, two crystallites are separated by only one ionic channel. While it needs a detailed research, dehydration study clearly indicated that the intercrystalline peak was much more responsive to water content than this ionomer peak (almost twice in a linear scale), which indicates more than a single ionic channel must exist between the two neighboring crystallites.

## D. Conclusions

We prepared PFSI membranes by solution-processing method and investigated the effects of uniaxial deformation on the morphology by two-dimensional SAXS/WAXD. It was obvious that the processing method significantly affected both the position and shape of the intercrystalline peak. More importantly, the previously observed I ($q$) ~ $q^{-1}$ power law at low $q$ was no longer observed in this study. Furthermore, the peak position is shifted to lower q upon hydration which is a strong indication that the correlation of crystals is across the ionic domain. Under uniaxial deformation, initially isotropic outer (the ionomer peak) and inner (the intercrystalline peak) rings in SAXS patterns were almost instantaneously transformed into equatorial arcs at lower draw ratios and then equatorial dots at higher draw ratios. Interestingly, SAXS profiles of oriented SP Nafion® membranes, both in dried and hydrated states did not show any hint of horizontal streaking. Based on 1-dimensional analyses of oriented SAXS patterns at the azimuthal angle 90°, three recent models (lamellar model, semicrystalline rod-like model and fringed-micelle model) for the morphology of PFSIs were critically checked. The loss of meridonal scattering, different orientation behavior of the crystalline and ionic domains, and inherent chain stiffness precludes the possibility of a chain-folded lamellar morphology. While the interaggregate dimensions remain constant at high draw ratios, the inter-crystalline spacings decrease significantly. Coupled with the distinctly different orientation behavior, these observations preclude the existence of crystallites solely within the rod-like aggregates. While worm-like ionic channel model was able to explain the behavior of SAXS and WAXD relatively well, this model also had limitations such as (1) crystalline domain directly linked to the ionic domain (and thus a lack of amorphous chains) and (2) a presence of only a single ionic channel between the two neighboring crystallites.

## E. Acknowledgements

Support for this work has been provided by the National Science Foundation CMMI-0707364 and CBET-0756439. Use of the National Synchrotron Light Source, Brookhaven National Laboratory, was upported by the U.S. Department of Energy, Office of Science, Office of Basic Energy Sciences, under Contract No. DE-AC02-98CH10886.

## F. References


(1) Doyle, M.; Rajendran, G. In *Handbook of Fuel Cells-Fundamentals, Technology and Applications*; Wielstich, W., Lamm, A., Gasteiger, H. A., Eds.; John Wiley & Sons: Chichester, 2003; Vol. 3; pp 351-395.
(2) Mauritz, K. A.; Moore, R. B. *Chem. Rev.* **2004**, *104*, 4535-4585.
(3) Kim, M.-H.; Glinka, C. J.; Grot, S. A.; G., G. W. *Macromolecules* **2006**, *39*, 4775-4787.
(4) Gierke, T. D.; Munn, G. E.; Wilson, F. C. *J. Polym. Sci. Polym. Phys. Ed.* **1981**, *19*, 1687-1704.
(5) Page, K. A.; Cable, K. M.; Moore, R. B. *Macromolecules* **2005**, *38*, 6472-6484.
(6) Londono, J. D.; Davidson, R. V.; Mazur, S. *Polym. Mater.: Sci. Eng.* **2001**, *85*, 23.
(7) Fujimura, M.; Hashimoto, T.; Kawai, H. *Macromolecules* **1982**, *15*, 136-144.
(8) Elliott, J. A.; Hanna, S.; Elliott, A. M. S.; Cooley, G. E. *Macromolecules* **2000**, *33*, 4161-4171.
(9) Rubatat, L.; Rollet, A. L.; Gebel, G.; Diat, O. *Macromolecules* **2002**, *35*, 4050-4055.
(10) Heijden, P. C. v. d.; Rubatat, L.; Diat, O. *Macromolecules* **2004**, *37*, 5327-5336.
(11) Litt, M. H. *Polym. Prepr.* **1997**, *38*, 80-81.
(12) Page, K. A.; Landis, F. A.; Phillips, A. K.; Moore, R. B. *Macromolecules* **2006**, *39*, 3939-3946.
(13) Gebel, G.; Lambard, J. *Macromolecules* **1997**, *30*, 7914-7920.
(14) Schmidt-Rohr, K.; Chen, Q. *Nat. Mater.* **2008**, *7*, 75-83.
(15) Dreyfus, B.; Gebel, G.; Aldebert, P.; Pineri, M.; Escoubes, M.; Thomas, M. *J. Phys. France* **1990**, *51*, 1341-1354.
(16) Loppinet, B.; Gebel, G. *Langmuir* **1998**, *14*, 1977-1983.
(17) Schmidt-Rohr, K. *J. Appl. Cryst.* **2007**, *40*, 16-25.
(18) Kim, M.-H.; Glinka, C. J.; Grot, S. A.; Grot, W. G. *Macromolecules* **2006**, *39*, 4775-4787.
(19) Rubatat, L.; Gebel, G.; Diat, O. *Macromolecules* **2004**, *37*, 7772-7783.
(20) Moore, R. B.; Cable, K. M.; Croley, T. L. *J. Membrane Sci.* **1992**, *75*, 7.
(21) Starkweather, H. W. J. *Macromolecules* **1982**, *15*, 320-323.
(22) Rubatat, L.; Diat, O. *Macromolecules* **2007**, *40*, 9455-9462.
(23) Park, J. K.; Moore, R. B. *ACS Appl. Mater. Interfaces* **2009**, *1*, 697-702.
(24) van der Heijden, P. C.; Rubatat, L.; Diat, O. *Macromolecules* **2004**, *37*, 5327-5336.
(25) Moore, R. B.; Martin, C. R. *Anal. Chem.* **1986**, *58*, 2569-2570.
(26) Moore, R. B.; Martin, C. R. *Macromolecules* **1988**, *88*, 1334-1339.
(27) Osborn, S. J.; Hassan, M. K.; Divoux, G. M.; Rhoades, D. W.; Mauritz, K. A.; Moore, R. B. *Macromolecules* **2007**, *40*, 3886-3890.
(28) Curtin, D. E.; Lousenberg, R. D.; Henry, T. J.; Tangeman, P. C.; Tisack, M. E. *J. Power Sources* **2004**, *131*, 41-48.
(29) Rubatat, L.; Diat, O. *Macromolecules* **2007**, *40*, 9455-9462.

# CHAPTER VI

# SCIENTIFIC BACKGROUND: ELECTROACTIVE POLYMERS — IONIC POLYMER METAL COMPOSITES

## A. Introduction

For ages, human beings have tried to mimic Mother Nature's behavior. An attempt to emulate biological muscles which are a complex but highly optimized system was made using electro-active ceramics (EACs) and shape memory alloys (SMAs).[1,2] Much attention has recently been focused on polymer systems, known as electro-active polymers (EAPs) that respond to electrical stimulation with a significant change in shape and size.[1-10] Generally, EAPs can induce strains that are as high as two orders of magnitude greater than the rigid and fragile EACs. EAP materials are superior to SMAs due to their lower density, higher response speed, and less power consumption.[11] The current limitations of EAP materials include low actuation force, mechanical energy density and robustness limiting the scope of their practical applications.[1] In this chapter, fundamental aspects of biological muscles will be first presented, followed by discussion of various EAP materials with an emphasis on the specific class of EAPs, ionic polymer metal composites (IPMCs).

## B. Biological Muscle

For proper emulation, it is evidently necessary to understand the basic structural features of biological muscles which are driven by complex mechanisms and are capable of lifting large loads with short response times (i.e., milliseconds).[12] The overall arrangement of biological muscle is hierarchical. A whole skeletal muscle is a bundle of parallel muscle fibers held

together by connective tissue. The connective tissue at the ends of each muscle fiber joins together to form the whole muscle tendon which, in turn, attaches to bone or fascia.[13] Muscle fibers contain hundreds of myofibrils, each of which span the length of the fiber and are about 1 to 2 μm in diameter.[13] Myofibrils are linear arrays of cylindrical sarcomeres, the basic structural units of muscle contraction. The myofibrillar sarcomere comprises three types of polymeric filament, (a) the thick filament, (b) the connecting filament and (c) the thin filament.[12,13] The thick filaments, which are built of multiple repeats of the protein myosin, are connected linearly by connecting filaments and flanked by thin filaments.[12] In vertebrate muscle the connecting filament is built largely of the protein titin. The thin filament is also polymeric and consists mainly of multiple repeats of the protein actin. Structural regularity within the sarcomere is maintained by crosslinks between adjacent filaments, forming essentially a highly crosslinked, water-swollen polymer gel.

The actual mechanism of contraction, and thus actuation, in muscle tissue has been the focus of research over the past century.[14] Prior to the 1950's researchers believed contraction occurred through a process of protein folding; however, this idea fell out of favor with the discovery of parallel filament geometries in the 1950's. At this time, theories involving the thin actin filaments and the thick myosin filaments sliding past one another became prominent. A widely accepted theory to explain this sliding process is the cross-bridge theory of muscle contraction.[14] This theory proposes that the filament sliding process is driven by cross-bridges that extend from the myosin filament and periodically interact with the actin filament as adenosine triphosphate (ATP) is hydrolyzed.[13] It was suggested that each cross-bridge probably generates a force of about 1 pN and after a power stroke of about 12 nm (during which 1 ATP molecule is hydrolyzed) the drag distance was estimated to be at least 28 nm.[15,16] The rate of this

cross-bridge cycling appeared to be more or less dependent on the type of muscle and highly temperature-dependant.

Due to conflicting experimental results and the lack of direct evidence of sufficient cross-bridge rotation, recent research was driven to focus on the gel-like character of muscle tissue.[12] In this context, contraction is proposed to be driven by a phase transition within the gel. Interestingly, the idea of phase transitions within a gel structure is very similar to the pre-1950's theory of protein folding. The water-swollen gel of muscle tissue is proposed to contract through phase transitions and alteration of the molecular dimensions of each filament making up the sarcomere.[12] All three filaments (i.e., the thick filament, the connecting filament and the thin filament) shorten through phase transitions of the proteins and the hierarchal organization of the sarcomere transforms this nano-scale transition into a macroscopic change in length. The connecting filaments, which provide restorative tension to the structure, have been shown to undergo dimensional changes through unfolding of immunoglobulin-like domains within the chain.[12,17] Thick filaments contract through a helix-coil transition, the extended conformation of the helix relaxing to a collapsed chain structure thereby shortening the filament.[12] Shortening of the thick filament is thus conceptually similar to the entropically-driven contraction of highly extended polymer chains into a lower energy coil conformation. Contraction of the thin filaments occurs through a more complex step-wise inching movement driven by local changes in molecular structure, thereby driving the filament much like the motion of an inchworm.[12] Complex and precise organization of the individual components of muscle tissue facilitates transformation of nanoscale molecular changes into macroscopic contraction or extension of the entity.

## C. Electroactive Polymers (EAPs)

### (1) Ferroelectric Polymer

Ferroelectric polymers are a special class of piezoelectrics, which exhibit, in general, a large piezoelectric response.[2,9,18] A piezoelectric material can be simply and broadly described as one that undergoes a change in electrical polarization in response to mechanical stress or vice versa.[9] The piezoelectric property of ferroelectric polymers was first reported by Kawai using poly(vinylidene fluoride) (PVDF) while poly(vinylidene fluoride-trifluoroethylene), P(VDF-TrFE) is the most commonly used polymer for actuation.[2,18] Spontaneous polarization in ferroelectric polymers is attributed to the electronegativity of fluorine which leads to highly polar bonds between fluorine and carbon, and thus creates local dipoles on the polymer backbone. These polar groups align to create polarized domains within a molecule and across the crystalline regions. In response to applied electric field, polarized domains align which remains even after removal of the electric field. The realignment produces reversible conformational changes which can be captured for useful actuation.[2]

In these materials, the electromechanical effect is linear such that strain (S) and stress (T) are coupled to the electric field (E) and displacement (or charge density D),

$S = d\,E$ (Inverse Piezoelectric Effect) **Eq VI-1**

$D = d\,T$ (Direct Piezoelectric Effect) **Eq VI-2**

where d is the piezoelectric effect.[19] Current limitations associated with the ferroelectric materials include a substantial hysteresis, low strain levels (~0.1 %) and high field requirement (~150 MV $m^{-1}$ and voltages > 1 kV).[20] Further studies recognized that disruption of the long

range correlations between polar groups may result in improved performance.[20] To introduce imperfection, Zhang and coworkers used electron-irradiation and observed a significant increase in strain levels (up to 4%) opening the window of application for ferroelectric polymers to include high strain applications.[21]

**(2) Conducting Polymer**

Conjugated polymers (e.g., polypyrrole and polyaniline) are attractive candidates for the potential application as artificial muscles due to their (a) large strain, (b) high strength, (c) low voltage requirement for actuation (typically 1 V or less), (d) ability to actuate at room or body temperature, (e) light weight, (f) ability to hold a fairly constant strain under DC voltage, (g) easy micro-fabricability and (h) ability to operate in liquid electrolytes, including body fluids.[4] Actuation of conjugated polymers are attributed to volume changes upon electrochemical oxidation and reduction.[22] These volume changes are based on the incorporation/expulsion of ions and solvent into/from the conjugated polymer during its oxidation/reduction process.[22,23] Commonly, conjugated polymer actuators are composed of a bilayer structure of a conductive polymer layer and a "no volume-change film" (e.g., polyethylene) layer. With the conductive polymer being the only electroactive component of the device, oxidation or reduction of the bilayer in the presence of an electrolyte ($C^+A^-$) solution leads to deflection of the actuator due to induced stress at the interface of the two layers. While Hara et al.[24] recently achieved a strain rate of 10.8 % $s^{-1}$ with polypyrrole systems, their relatively slow speed is considered as one of the limitations along with their inability to actuate in the absence of an electrolyte, and poor efficiency in converting electrical to mechanical energy.[4]

**(3) Carbon Nanotube (CNT)**

Carbon nanotubes (CNTs) are hollow, long and thin cylinders consisting solely of carbon.[25] CNTs have diameters of typically 1.2 nm or larger and these tubes aggregate into bundles of diameters of 10 nm being typical in samples used in actuation studies.[7,26] Among several proposed actuation mechanisms, double layer charge injection has been the dominant mechanism which proposes dimensional changes in the covalently bonded direction (Figure VI-1a and b).[27] If carbon nanotubes are immersed in an electrolyte and an electric potential is applied between the nanotubes and a counter electrode, ions are attracted to the CNTs, leading to the accumulation of ionic charges at their surfaces. This charge is balanced by electronic charges within the tubes. The charging leads to dimensional changes due to a rearrangement of the electronic structure of the nanotubes and Coulombic forces.[27] The first CNT-based actuators devised by Baughman et al. were composed of nanotube mats adhered to a Scotch tape substrate and immersed in a salt water electrolyte (Figure VI-1c).[7] Under electrical stimulation, the equality between the lengths of the two nanotube sheets was disrupted and subsequently actuators underwent displacement to the left or right. While CNT-based actuators can generate stresses higher than that of natural muscles and may be operated at very wide temperatures, low strains (between 0.1 % and approximately 1 %) and high cost (~$100/g) are considered as their key disadvantages.[2]

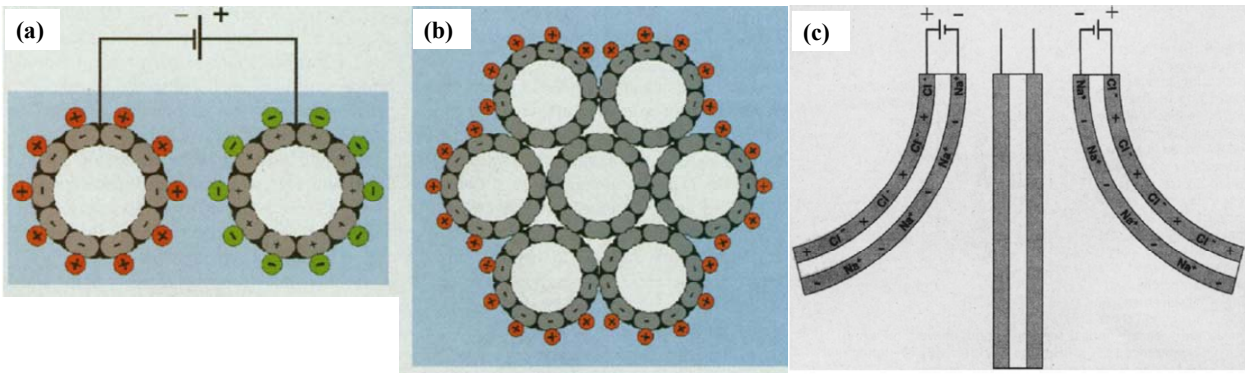


**Figure VI-1.** Schematic representation of charge injection in a carbon nanotube (a) and (b). In (a), an applied potential injects charge of opposite sign in the two pictured nanotube electrodes, which are in a electrolyte solution (blue background). In (b), charge injection at the surface of a nanotube bundle is illustrated. (c) Edge-view of a cantilever-based actuator operated in aqueous NaCl, which consists of two strips of single walled carbon nanotubes (shaded) that are laminated together with an intermediate layer of double-sided Scotch tape (white). (Reprinted with permission from ref[7] *Science*, **284**, 1340 (1999). Copyright 1999, AAAS.)

### (4) Polyelectrolyte Gels

While polyelectrolyte gels can be actuated by various stimuli, current discussion will be limited only to electrically actuated gel systems. Polymer gels have attracted considerable attention over the several decades.[28] Applications of polyelectrolyte gels in numerous devices were recently reviewed by Peppas et al.[5] and Calvert[6]. In the 1970s, Grodzinsky and Shoenfeld demonstrated actuation with collagen membranes being immersed in salt solution by an applied electric field.[10,29] The authors suggested that application of the electric field led to changes in intramembrane salt concentrations thereby causing repulsive forces between collagen fibrils leading to membrane strain and actuation. In early 1990s, Osada et al. demonstrated actuation based on electrokinetic molecular assembly reaction of surfactant molecules (n-dodecyl pyridinium chloride, $C_{12}$PyCl) on the hydrogel, which is made of weakly crosslinked poly (2-acrylamido-2-methyl propane) sulphonic acid (PAMPS) (Figure VI-2).[30] The observed actuation was attributed to the neutralization of negative charges of sulfonate moieties in the gel by forming complexes with surfactant cations decreasing the osmotic pressure different between the

inside of the gel and the surrounding solution.[30] It was further suggested that hydrophobic interactions between neighboring long alkyl chains stabilize the complex and allow effective contraction of the gel. Currently, a few key disadvantages associated with polyelectrolyte gel systems include immersion in electrolyte solutions, slow actuation (it takes minutes to electrically stimulate polyelectrolyte to cause the expansion and contraction) and lack of mechanical stability.[28]

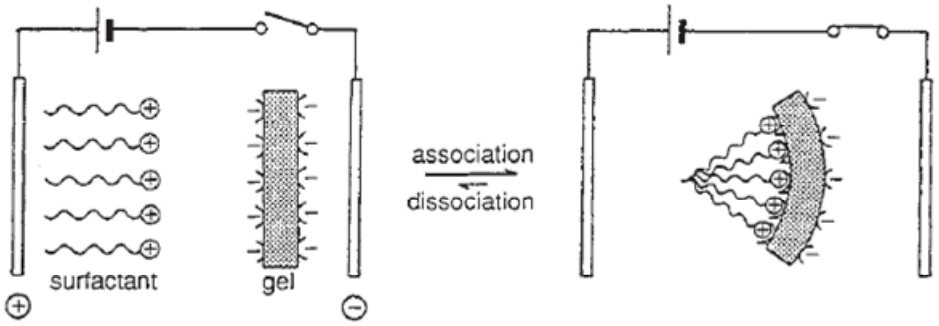


**Figure VI-2**. Schematic illustration of actuation mechanism by anisotropic association of surfactant molecules with gel in response to electric field. (Reprinted with permission from ref[30] *Nature*, **355**, 242 (1992). Copyright 1992, Nature Publishing Group.)

**(5) Ionic Polymer-Metal Composite (IPMC)**

To overcome difficulties with actuators based on polyelectrolyte gel, such as slow actuation and lack of mechanical stability, systems containing solid polymer electrolyte and conductive metal electrodes (often referred to as ionic polymer-metal composites, IPMCs) were considered.[31] IPMCs were first demonstrated in the early 1990s's by Shahinpoor[32], Sadeghipour[33] and Oguro[34]. To date, this field has been principally dominated by engineers demonstrating the versatility of IPMC systems for numerous actuator and sensor applications. Under an applied electric field across the IPMC, water and ions are believed to migrate through the percolation pathway within the nano-structured ionomer membrane (e.g., Nafion®) to create

differential swelling forces on the opposing surfaces, which will then induce an actuation. The converse property is a sensor application.[33] When a mechanical force is applied onto an IPMC sample, it is believed that macroscopic motion of IPMC induces microscopic motions of mobile counter-ions which can stimulate a detectable electrical response for a motion sensor application.

The rest of this chapter will be devoted to the discussion of (a) IPMC fabrication procedures, (b) the role of each constitutive component (i.e., ionomer membrane, counterions, metal electrodes, and swelling solvent) and (c) the proposed actuation mechanisms in detail.

**IPMC Fabrication**

Ionic polymer-metal composites are typically fabricated by electroless deposition of a conductive metal onto the surfaces of an ionomer membrane.[35] The standard procedure involves first surface-roughening by mechanically rubbing the surface with sand papers to increase surface area. Then, the $H^+$-form ionomer membrane (e.g., Nafion®) is allowed to equilibrate with the platinum salt solution ($[Pt(NH_3)_4]Cl_2$) overnight. After rinsing with deionized water to remove excess platinum salts, the membrane is immersed in DI water and the Pt (II) ions in the membrane are reduced to Pt metal particles using a strong reducing agent such as sodium borohydride ($NaBH_4$). Addition of $NaBH_4$ is typically carried out in seven steps at 30 min intervals over which the temperature is ramped from 40 °C to 60 °C. The electroded membrane is then rinsed in DI water before immersing in 0.1 M HCl to convert the material to the acid form. The whole reduction process above is carried out for three cycles to thicken platinum electrode layers. Finally, the $H^+$-form IPMC may be neutralized to contain various counterions. Diffusion of both the reducing agent and the metal salt results in selective deposition at the membrane faces creating surface electrode. As shown in Figure VI-3 (from this thesis work), the surface

electrodes actually consist of metal nanoparticles that facilitate application of an electric potential across the membrane through enhanced surface area. TEM micrographs also display very dense layers (ca. 5 um) of Pt particles at the film edge and less densely dispersed Pt particles at the film interior.

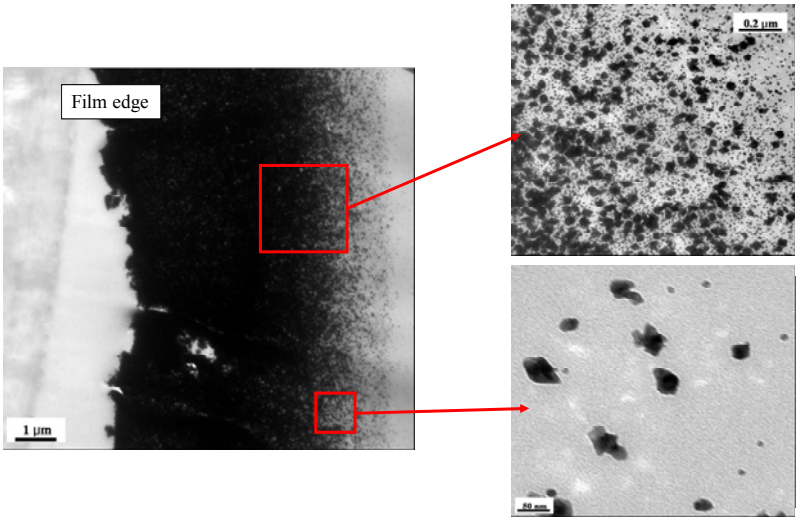


**Figure VI-3.** TEM micrographs of IPMCs at low (left) and high (right) magnification

## IPMC Performance

*Effect of ionomer type:* As pointed out by a recent review by Duncan et al.[36], the vast majority of previous IPMC studies have principally involved the class of perfluorosulfonate ionomers (PFSIs), Nafion® in a single morphological state (i.e., as-received membranes supplied by DuPont). Nafion® is a copolymer containing runs of tetrafluoroethylene and less than 15 mol % of perfluorovinyl ether units that are end capped with a sulfonic acid exchange site.[37] It has been shown that the polar, perfluoroether side chains containing the sulfonic acid groups aggregate

into ionic clusters which are dispersed throughout the non-polar PTFE matrix.[37] Thus, with this commercially available Nafion® platform, only one structure has been evaluated and consequently, only a limited set of actuation properties have been observed.[35]

As a new alternative matrix material for IPMC systems, Akle and coworkers used sulfonated poly(arylene ether sulfone) and a sulfonated poly(arylene thioether sulfone).[38] It was found that IPMCs based on sulfonated poly(arylene ether sulfone) produced 6 times greater force and 2 times greater displacement than Nafion®. The performance improvement observed was attributed to increased membrane stiffness and IPMC capacitance. Phillips and Moore fabricated ionic actuators based on novel sulfonated ethylene vinyl alcohol (EVOH) copolymer membranes.[39] The authors noticed that modified EVOH IPMCs behaved similar to Nafion®, yet actuation kinetics in the new ionomer-based IPMCs is significantly slower. Slower actuation kinetics was attributed to slower water diffusion caused by a disorganized morphology in the sulfonated ethylene vinyl alcohol.[39] Recently, Lu et al. fabricated IPMCs based on an ionic networking membrane of poly(styrene-alt-maleimide) (PSMI)-incorporated poly(vinylidene fluoride) (PVDF).[40] With an applied 0.5 volt DC excitation, the tip displacement of the actuator constructed with the ionic network membrane was several times higher than that of its Nafion® counterpart of similar thickness without significant back-relaxation. The authors attributed enhanced electromechanical properties of IPMCs based on PSMI-incorporated PVDF to the inherent large ionic-exchange capacity and the unique hydrophilic nanochannels of the ionic networking membrane. The studies discussed here evidently demonstrate that many opportunities for tailoring a new ionomer matrix exist to enhance IPMC performance.[36]

*Effect of counterion type:* A few studies compared actuation behaviors of IPMCs in various counterion forms.[31,41-43] It was noticed that with increasing counterion radius the speed of IPMC

actuation slowed, yet greater final displacement was often achieved.[41,43] Nemat-Nasser and Wu prepared Flemion®-based IPMCs neutralized with large hydrophobic tetrabutylammonium ($TBA^+$) counter-ions and observed large displacement though at much slower actuation speeds.[41] The authors attributed the slower actuation kinetics to lower mobility of bulky cations within the hydrophilic channels.[41] Onishi et al.[43] explained this large displacement observed with $TBA^+$-form IPMCs in terms of "ion-pumping" effect where the bulky hydrophobic $TBA^+$ ions could effectively pump solvent through the connecting hydrophilic channels proposed by Hsu and Gierke (Figure VI-4).[44] When exchanged with alkali metal ions (e.g., $Na^+$) as counter-ions, the fast actuation response was observed although the overall tip displacement was seen to decrease compared to that of $TBA^+$-form IPMCs.[41] Recently, Nam and Yoo comprehensively studied the bending behaviors of Nafion®-based IPMCs neutralized to contain various cationic species.[42] Under the applied 1 V DC, $Li^+$-form IPMCs showed an immediate and efficient deformation while at elevated electric potential (e.g., 3 V DC) divalent cuprous form IPMCs exhibited the greater tip displacement.

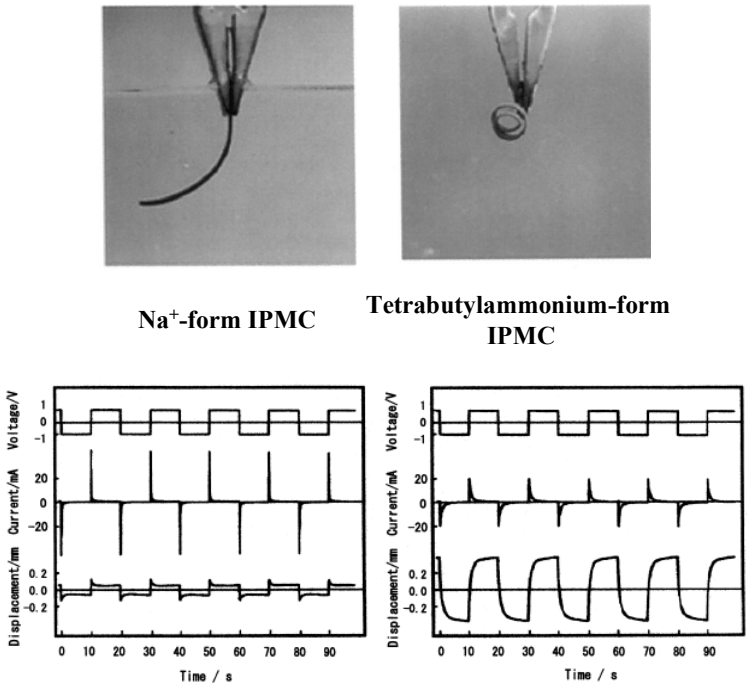


**Figure VI-4**. Comparison of Flemion®-based IPMC in sodium (left) and tetrabutylammonium (right) counterion forms under a 1V step potential at 0.1 Hz. The lower graphs show the excitation signal, current response and tip displacement of the IPMCs. (Reprinted with permission from ref[43] *Electrochimica Acta*, **46**, 1233 (2001). Copyright 2001, Elsevier.)

*Effect of solvent type*: Swelling solvent plays a critical role in determining the performance of IPMCs. For poorly-solvated membranes, Columbic interactions between sulfonate groups and cations are expected be strong and thus reduce or eliminate migration of cation species. So far, water has been the most widely employed solvent, but the water quickly evaporates in open air environments limiting the widespread use of IPMCs.[35,39] Furthermore, water-swollen IPMCs must adhere strictly to the 1.23 V electrolysis limits, otherwise water molecules will decompose into hydrogen and oxygen gas. To overcome the limitations imposed on water-swollen IPMCs, Bar-Cohen et al. employed a barrier coating and therefore were able to operate in air for 4 months.[45] Other studies were focused on searching for alternative solvent systems that will reduce or eliminate the problems associated with water. Nemat-Nasser and Zamani

demonstrated the use of ethylene glycol as a suitable solvent for IPMC actuation although they observed much slower actuation than those swollen in water.[46] Nam and Yoo tested bending behaviors of IPMCs in various organic solvents such as $D_2O$, DMSO, NMP, DMF and PEG 200.[42] Among these solvents, the heavy water, $D_2O$ and DMSO/water (1mole/L) mixture gave relatively good tip displacement with less solvent loss due to lower vapor pressures thereby extending the time window for actuation.[42] Bennett and Leo chose ionic liquids (1-ethyl-3-methylimidazolium trifluoromethanesulfonate or EMI-Tf) to replace water due to their great electrochemical stability, and non-volatility.[47] They demonstrated that IPMCs swollen with ionic liquids actuated for ca. $10^5$ cycles under 1.5 V input and 2 Hz sine wave while water-swollen IPMC stopped actuation after ca. $10^3$ cycles. Slower actuation speed was identified as the main limitation associated with the use of ionic liquids as diluents for IPMCs.

*Effect of conductive metal electrode*: To establish an electric field across the thickness of an ionomeric membrane, conductive metal electrodes must be plated on both faces of the membrane.[48] Multiple researchers have explored the effects of metal electrode on the performance of IPMCs.[31] A review of the open literature reveals that the vast majority of previous IPMC studies have principally involved gold (Ag) and plantinum (Pt). While these noble metals are highly conductive and resistant to oxidation and thus have been shown to function very well in this application, the use of expensive noble metals could limit the potential wide-spread applications for this technology. In an effort to decrease the amount of noble metal used, Bennett and Leo employed alloys of platinum and copper covered by a gold surface layer showing performance of these IPMCs to be of comparable to those of IPMCs based on Pt or Ag.[49] Work done by Shahinpoor and Kim demonstrated that electrochemical deposition of silver and copper above the initial platinum layer could be employed to increase actuation force in

IPMCs.[50] The authors proposed that improved performance resulted from the deposition of a continuous metal layer thereby increasing the surface conductivity and preventing large drops in voltage away from the contact electrode.[50]

**IPMC Actuation Mechanism**

One proposed mechanism for IPMC actuation has commonly been discussed in terms of electrophoresis-like counterion and water redistribution within the nanostructured ionomer membrane.[48,51,52] Since the ionic polymer is negatively charged typically with protons or alkali-metal cations as the counterions, these mobile cations in the hydrated membrane are readily redistributed in response to the applied electric field to create cation-rich and cation-poor boundary layers near the electrode/membrane interfacial regions**. (**Figure VI-5**)** As cations migrate toward the cathode, they are accompanied by water molecules (i.e., a hydraulic mechanism), which consequently causes swelling near the cathode and contraction (due to dehydration) near the anode. This swelling/contraction thus induces a bending force that curves the IPMC toward the anode.

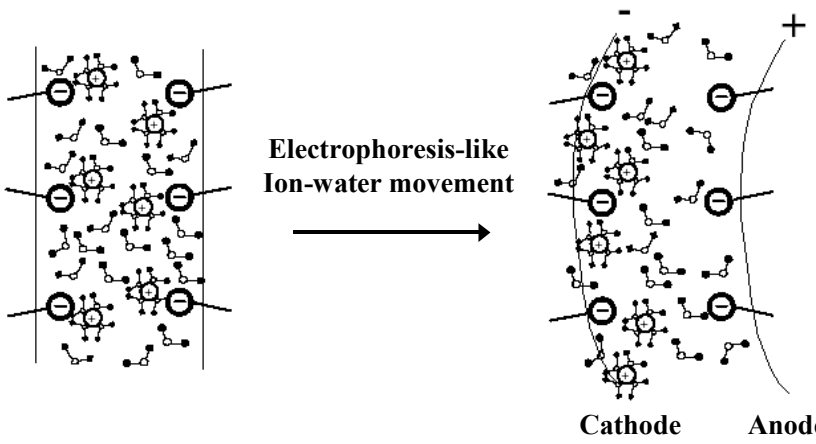


**Figure VI-5**. A schematic describing the electrophoretic migration of ions and water in a hydrated IPMC under an applied electrical potential. (Reprinted with permission from ref[3] *Electrochimica Acta*, **48**, 2343 (2003). Copyright 2003, Elsevier.)

In contrast to a hydraulic model, which attributes actuation to charge and solvent transport, electrostatic models are based on a redistribution of cations and anions both within and at the surface of ionic aggregates.[53] According to the electrostatic model by Nemat-Nasser and Li[54], fast bending actuation originates from local cation redistribution upon application of an electric field. The migration of cations results in relaxation of polymer chains in the anion-rich region and extension of polymer chains in the cation-rich region. Weiland and Leo proposed a slightly modified electrostatic actuation mechanism.[53] In constrast to the work of Nemat-Nasser, Weiland and Leo propose that the initial rapid actuation behavior is dominated by a polarization mechanism, leaving only the slow relaxation to result from liquid and ion transport processes. The forces acting on dipoles located at the aggregate surface include dipole-dipole interactions, pendant chain stiffness, cluster surface energy and externally applied forces. Application of an external electric field is believed to cause the dipoles, that are assumed to have an equal magnitude and meta-stable orientations (all dipoles directed toward the center of the spherical cluster), to undergo reorientation and elongate or contract depending on their initial directions relative to the

applied electric field. Macroscopic IPMC strain is then inferred from the distortion of the initially spherical aggregate into an ellipsoidal shape. The proposed model, however, relies on a number of simplifying assumptions which include very close contact between cation and anion in the hydrated state and primarily a spherical aggregate geometry not in tune with current Nafion® morphological models.[55,56]

## D. References


(1) Bar-Cohen, Y. In *Electroactive Polymer (EAP) Actuators as Artificial Muscles*; Bar-Cohen, Y., Ed.; SPIE, 2001; pp 3-44.
(2) Madden, J. D. W.; Vandesteeg, N. A.; Anquetil, P. A.; Madden, P. G. A.; Takshi, A.; Pytel, R. Z.; Lafontaine, S. R.; Wieringa, P. A.; Hunter, I. W. *IEEE Journal of Oceanoic Engineering* **2004**, *29*, 706-728.
(3) Shahinpoor, M. *Electrochim. Acta* **2003**, *48*, 2343-2353.
(4) Smela, E. *Adv. Mater.* **2003**, *15*, 481-494.
(5) Peppas, N. A.; Hilt, J. Z.; Khademhosseini, A.; Langer, R. *Adv. Mater.* **2006**, *18*, 1345-1360.
(6) Calvert, P. *Adv. Mater.* **2009**, *21*, 743-756.
(7) Baughman, R. H.; Cui, C.; Zakhidov, A. A.; Iqbal, Z.; Barisci, J. N.; Spinks, G. M.; Rinzler, G. G.; Jaschinski, O.; Roth, S.; Kertesz, M. *Science* **1999**, *284*, 1340-1344.
(8) Baughman, R. H. *Synth. Met.* **1996**, *78*, 339-353.
(9) Lovinger, A. J. *Science* **1983**, *220*, 1115-1121.
(10) Grodzinsky, A. J.; Shoenfeld, N. A. *Polymer* **1977**, *18*, 435-443.
(11) Bar-Cohen, Y. In *Electroactive Polymer (EAP) Actuators as Artificial Muscles*; Bar-Cohen, Y., Ed.; SPIE, 2001; pp 2-45.
(12) Pollack, G. H.; Blyakhman, F. A.; Reitz, F. B.; Yakovenko, O. V.; Dunaway, D. L. In *Electroactive Polymer (EAP) Actuators as Artificial Muscles*; Bar-Cohen, Y., Ed.; SPIE, 2001; pp 47-66.
(13) Garrett, R. H.; Grisham, C. M. In *Principles of Biochemistry with a Human Focus*; Brooks/Cole, 2002.
(14) Eisenberg, E.; Hill, T. L. *Science* **1985**, *227*, 999-1006.
(15) Ishijima, A.; Doi, T.; Sakurada, K.; T., Y. *Nature* **1991**, *352*, 301-306.
(16) Higuchi, H.; Goldman, Y. E. *Nature* **1991**, *352*, 352-354.
(17) Rief, M.; Gautel, M.; Oesterhelt, F.; Fernandez, J. M.; Gaub, H. E. *Science* **1997**, *276*, 1109-1112.
(18) Kawai, H. *Jpn. J. Appl. Phys.* **1969**, *8*, 975-976.
(19) Zhang, Q.; Scheinbein, J. In *Electroactive Polymer [EAP] Actuators as Artificial Muscles*; Bar-Cohen, Y., Ed.; SPIE: Bellingham, WA, 2001; pp 89-120.
(20) Zhang, Q.; Scheinbeim, J. In *Electroactive Polymer (EAP) Actuators as Artificial Muscles*; Bar-Cohen, Y., Ed.; SPIE, 2001; pp 89-120.
(21) Zhang, Q. M.; Bharti, V.; Zhao, X. *Science* **1998**, *280*, 2101-2104.
(22) Sansinena, J.-M.; Olazabal, V. In *Electroactive Polymer (EAP) Actuators as Artificial Muscles*; Bar-Cohen, Y., Ed.; SPIE, 2001; pp 193-221.
(23) Okabayashi, K.; Goto, F.; Abe, K.; Yoshida, T. *Synth. Met.* **1987**, *18*, 365-370.
(24) Hara, S.; Zama, T.; Takashima, W.; Kaneto, K. *Synthetic Met.* **2005**, *149*, 199-201.
(25) Iijima, S.; Ichihashi, T. *Nature* **1993**, *363*, 603-605.
(26) Affoune, A. M.; Yamada, A.; Umeda, M. *J. Power Sources* **2005**, *148*, 9-17.
(27) Spinks, G. M.; Wallace, G. G.; Baughman, R. H. In *Electroactive Polymer (EAP) Actuators as Artificial Muscles*; Bar-Cohen, Y., Ed.; SPIE, 2001; pp 223-246.
(28) Calvert, P. In *Electroactive Polymer (EAP) Actuators as Artificial Muscles*; Bar-Cohen, Y., Ed.; SPIE, 2001; pp 123-138.
(29) Shoenfeld, N. A.; Grodzinsky, A. J. *Biopolymers* **1980**, *19*, 241-262.
(30) Osada, Y.; Okuzaki, H.; Hori, H. *Nature* **1992**, *355*, 242-244.
(31) Nemat-Nasser, S.; Thomas, C. W. In *Electroactive Polymer (EAP) Actuators as Artificial Muscles*; Bar-Cohen, Y., Ed.; SPIE, 2001; pp 139-191.
(32) Shahinpoor, M. *Smart Mater. Struct.* **1992**, *1*, 91-95.
(33) Sadeghipour, K.; Salomon, R.; Neogi, S. *Smart Mater. Struct.* **1992**, *1*, 172-179.
(34) Asaka, K.; Oguro, K.; Nishimura, Y.; Mizuhata, M. *Polym. J.* **1995**, *27*, 436-440.

(35) Park, J. K.; Moore, R. B. *ACS Appl. Mater. Interfaces* **2009**, *1*, 697-702.
(36) Duncan, A. J.; Leo, D. J.; Long, T. E. *Macromolecules* **2008**, *41*, 7765-7775.
(37) Mauritz, K. A.; Moore, R. B. *Chem. Rev.* **2004**, *104*, 4535-4585.
(38) Akle, B. J.; Leo, D. J.; Hickner, M. A.; McGrath, J. E. In *AD (American Society of Mechanical Engineers)* Proceedings of the ASME Aerospace Division, 2003; Vol. 68; pp 445-452.
(39) Phillips, A. K.; Moore, R. B. *Polymer* **2005**, *46*, 7788-7802.
(40) Lu, J.; Kim, S.-G.; Lee, S.; Oh, I.-K. *Adv. Funct. Mater.* **2008**, *18*, 1290-1298.
(41) Nemat-Nasser, S.; Wu, Y. *J. Appl. Phys.* **2003**, *93*, 5255-5267.
(42) Nam, B. K.; Yoo, Y. In *Smart structures and materials 2005: Electroactive polymer actuators and devices (EAPAD)*; Bar-Cohen, Y., Ed.; SPIE: San Diego, CA, 2005; Vol. 5759; pp 525-533.
(43) Onishi, K.; Sewa, S.; Asaka, K.; Fujiwara, N.; Oguro, K. *Electrochim. Acta* **2001**, *46*, 1233-1241.
(44) Hsu, W. Y.; Gierke, T. D. *J. Membrane Sci.* **1983**, *13*, 307-326.
(45) Bar-Cohen, Y.; Leary, S. P.; Shahinpoor, M.; Harrison, H. S.; Smith, J. In *Smart Materials and Structures 1999: Electroactive Polymer Actuators and Devices (EAPAD)*; Bar-Cohen, Y., Ed.; SPIE-The International Society for Optical Engineering, 1999; Vol. 3669; pp 51-56.
(46) Zamani, S.; Nemat-Nasser, S. In *Smart Materials and Structures 2003: Electroactive Polymer Actuators and Devices (EAPAD)*; Bar-Cohen, Y., Ed.; SPIE-The International Society for Optical Engineering, 2003; Vol. 5051; pp 233-244.
(47) Bennett, M. D.; Leo, D. J. *Sensor Actuat. A-Phys* **2004**, *115*, 79-90.
(48) Shahinpoor, M.; Bar-Cohen, Y.; Simpson, J. O.; Smith, J. *Smart Mater. Struct.* **1998**, *7*, R15-R30.
(49) Bennett, M. D.; Leo, D. J. *Smart Mater. Struct.* **2003**, *12*, 424-436.
(50) Shahinpoor, M.; Kim, K. J. *Smart Mater. Struct.* **2000**, *9*, 543-551.
(51) De Gennes, P. G.; Okumura, K.; Shahinpoor, M.; Kim, K. J. *Europhys. Lett.* **2000**, *50*, 513.
(52) Shahinpoor, M. *Smart Mater. Struct.* **1994**, *3*, 367-372.
(53) Weiland, L. M.; Leo, D. J. *Smart Mater. Struct.* **2004**, *13*, 323-336.
(54) Nemat-Nasser, S.; Li, J. Y. *J. Appl. Phys.* **2000**, *87*, 3321-3331.
(55) Schmidt-Rohr, K.; Chen, Q. *Nat. Mater.* **2008**, *7*, 75.
(56) Kim, M.-H.; Glinka, C. J.; Grot, S. A.; Grot, W. G. *Macromolecules* **2006**, *39*, 4775.

# CHAPTER VII

# INFLUENCE OF ORDERED MORPHOLOGY ON THE ANISOTROPIC ACTUATION IN UNIAXIALLY-ORIENTED ELECTROACTIVE POLYMER SYSTEMS

*This chapter is reformatted from [Park, Jong Keun; Moore, Robert B., "Influence of Ordered Morphology on the Anisotropic Actuation in Uniaxially-Oriented Electroactive Polymer Systems", *ACS Appl. Mater. Interfaces* **2009,** 1 (3), 697-702].

## A. Introduction

Electroactive polymers (EAPs) respond to electrical stimulation with a significant change in size or shape and have therefore recently attracted increasing interest with potential for technologically important applications ranging from biologically-inspired artificial muscles to micro/nanofluidics and robotics.[1] Various types of polymers have been considered as electroactive materials, including conducting polymers[2, 3], dielectric elastomers[4], polymer gels[5], and ionic polymer-metal composites (IPMCs)[6-9].

Among EAPs, IPMCs are considered as one of the most promising candidates for artificial muscles due to their capability of significant mechanical motion with the stimulus of a relatively weak electric field (e.g., 1 to 5 volts).[8] Conversely, an external mechanical force applied to the surface of an IPMC can stimulate a detectable electrical response, and thus the system acts as a motion sensor. IPMCs are typically fabricated through electroless deposition of a conductive metal (e.g., platinum or gold) onto both surfaces of an ion-exchange membrane.[6] The standard electroding procedure involves neutralization of an ionomer with relatively bulky metal ions, such as Pt(II). Subsequently, the ionomer membrane is dipped into an aqueous

reducing agent (e.g., $NaBH_4$) to convert the Pt(II) ions to Pt metal. Due to the "outside-in" diffusion of the reducing agent and the inside-out diffusion of the Pt(II) ions, Pt nanoparticles are nucleated and grow near the surfaces of the membrane. With sufficient amounts of Pt metal, the surfaces become electrically conductive, thus forming the IPMC electrode layers.

A review of the open literature reveals that the vast majority of previous IPMC studies have principally involved a perfluorosulfonate ionomer (PFSI), Nafion®, in a single morphological state (i.e., as-received membranes supplied by DuPont). Nafion® is a copolymer of tetrafluoroethylene and generally less than 15 mol% of perfluorovinyl ether units terminated with sulfonic acid functionalities.[10] Thus, with this commercially-available Nafion® platform, only one structure has been evaluated and consequently, only a limited set of actuation properties has been observed. In order to expand these structure property relationships, we have previously demonstrated many ways to manipulate morphology in PFSIs.[11-13] By recognizing the existence of rod-like aggregates within Nafion®[10, 14, 15], we have subjected Nafion® films to uniaxial orientation to create an anisotropic fibrillar morphology. The resulting, hierarchical structure mimicks natural muscle tissue, which is also highly anisotropic in nature. By understanding the fundamental role of the nanoscale morphology of the ionomer membrane in affecting actuation behavior of IPMC systems, we hope to gain a unique insight into the molecular-level processes associated with the, as of yet, unexplained IPMC actuation mechanism. Moreover, this knowledge will foster the development of tailored processing procedures for ionic polymer membranes in the design of the next-generation platform for electroactive materials.

## B. Experimental

***Materials.*** Extruded Nafion® 117 from E.I. DuPont de Nemours & Co. (1100g/equivalent, sulfonic acid form) was precleaned by refluxing in 8M Nitric acid for 2 hr, then in deionized (DI) water for 1 hr. Tetrabutylammonium ($TBA^+$) neutralized membranes were prepared by soaking the cleaned $H^+$-form membranes in tetrabutylammonium hydroxide (TBAOH) (Aldrich) in methanol solutions (1 M) for 12 hr and then rinsing with methanol to remove the residual TBAOH. This rinse consisted of three wash cycles in 200 mL of methanol under ultrasonic agitation. These neutralized membranes were then dried at 70 $^oC$ overnight in a vacuum oven.

***Fabrication of Oriented IPMC.*** Uniaxially oriented samples of Nafion® were prepared by cutting the $TBA^+$ neutralized membranes into dog-bone shapes and mounting them on a specially designed drawing apparatus. This drawing apparatus allowed $TBA^+$ neutralized Nafion® membranes to be drawn at 90 °C to a draw ratio ($\lambda_b$ = final length (L) / initial length ($L_0$)) of 2 as determined by the displacement of ink marks on the samples. Uniaxially oriented $TBA^+$-form membranes were then mounted in Kel-F® clamps and converted to the $H^+$-form by boiling in 4M $H_2SO_4$/MeOH for 1 hour, in MeOH for 30 min, and in DI water for 30 min. These oriented $H^+$-form Nafion® samples were then used to fabricate oriented IPMCs following the standard multi-step electroding procedure after surface-roughening by mechanically rubbing the surface with 400 grain sand paper.[6] A platinum salt complex $[Pt(NH_3)_4]Cl_2$ (Aldrich) was used to make an aqueous solution with a concentration of 2 mg $mL^{-1}$ solution. The $H^+$-form Nafion® membrane was allowed to equilibrate with the platinum salt solution overnight. After rinsing with deionized water, the membrane was immersed in DI water and the Pt(II) ions in the membrane were reduced to Pt metal particles using 5 wt % aqueous sodium borohydride ($NaBH_4$, Aldrich). Addition of $NaBH_4$ was carried out in seven steps at 30 min intervals over which the temperature was ramped from 40 °C to 60 °C. After completing the initial series of

$NaBH_4$ additions, a final addition was performed and reduction was allowed to proceed for 1.5 hr. The electroded membrane was then rinsed in water before immersing in 0.1 M HCl to convert the material to the acid form. The whole reduction process above was carried out for three cycles to produce the final IPMCs used in the current study. Following the complete electroding procedure, the oriented IPMCs were removed from the Kel-F clamps and were observed to be dimensionally-stable, with a swollen thickness of 200 μm.

***Fabrication of Unoriented IPMC.*** $TBA^+$-form Nafion® was converted to $H^+$-form by boiling in 4M $H_2SO_4$/MeOH for 1 hr, in MeOH for 30 min, and in DI water for 30 min. Ion exchange processes from $H^+$ to $TBA^+$, and then back to $H^+$-form are necessary in terms of membrane initialization protocol to ensure that unoriented IPMCs entered experimentation in the same chemical state and experienced the same swelling and thermal histories as oriented IPMCs. These control $H^+$-form Nafion® membranes were used to fabricate the unoriented IPMCs following the standard multi-step electroding procedure described above. The swollen thickness of the unoriented IPMC was measured to be 230 μm.

***Small/Wide Angle X-ray Scattering (SAXS/WAXS).*** SAXS and WAXS images were acquired at the Advanced Photon Source, Argonne National Laboratory (Beamline 5-ID DND-CAT). The wavelength of X-ray beam was 0.8266 Å and the sample-to-detector distances for SAXS and WAXS were 1343 mm and 228 mm, respectively. SAXS and WAXS two-dimensional images were simultaneously obtained using a Mar CCD and Roper camera, respectively, with a 5 second exposure time.

***Measurement of Tip Displacement.*** Characterization of actuation performance was carried out using a LabView™ –based system devised in-house. Square waveform input signals were generated using a Function Generator VI (LabView™) and sent to an external amplifier

using a DAQ card (National Instruments PCI-6024E). All samples were cut to 2.0 cm in length and 0.5 cm in width and fully hydrated before any measurement. Displacement of the IPMCs under different electrical stimuli was captured by means of an Imaging Solutions Group camera (LightWise LW-1.3-R-1394) interfaced to LabView. Final image analysis was accomplished using Datapoint software (Xannah Applied Science and Engineering).

***Determination of Bending Modulus.*** The bending moduli of unoriented/oriented $TBA^+$-form Nafion® and hydrated $H^+$-form IPMCs were measured by dynamic mechanical analysis performed on a TA Intruments (DMA Q800 analyzer) in bending mode using a micro-3-point bending clamp. All the measurements were conducted at room temperature with the furnace open. An applied strain of 0.5 % and four different frequencies, 0.1, 0.5, 1.0, and 10 Hz were investigated.

***TEM Characterization of IPMC Cross-Section.*** Transmission electron microscopy (TEM) was used for the nano-scale characterization of IPMC morphology (including Pt nanoparticle size, shape, and spatial distribution) in unoriented and oriented IPMCs. TEM micrographs of IPMC cross-sections were obtained using a JEOL JEM-2100 LaB6 microscope operated at 200 KeV. IPMC samples were first embedded in an epoxy resin, and microtomed sections (thickness 100nm) were deposited on a carbon-coated copper grid.

## C. Results and Discussion

With a sufficient length of polytetrafluoroethylene (PTFE) segments between side chains, Nafion® is capable of organizing into crystalline domains (generally less than ca. 10 wt

% in 1100 equivalent weight Nafion®). Greater efforts, however, have been given to the unique nanophase-separated morphology observed upon aggregation of the polar, ionic sidechains within the matrix of hydrophobic polytetrafluoroethylene. These ionic clusters, and specifically their spatial distribution and connectivity, precisely define the supramolecular organization and function of this technologically important material as an ionic conductor. It has also been shown that these ionic aggregates act as multifunctional physical cross-links that significantly restrict chain mobility.[12, 16] In an effort to increase the melt-flow character of Nafion®, Moore and Cable utilized large, hydrophobic tetrabutylammonium ($TBA^+$) counterions to effectively diminish the strength of Columbic interactions within the ionic domains.[12, 13, 17, 18] This approach profoundly increased the ability to uniaxially-orient Nafion® up to draw ratios ($\lambda_b$ = final length (L) / initial length ($L_0$)) of about 6.[13, 19] The consequence of this orientation has been characterized in terms of anisotropic morphologies[13, 15, 19-24]and ionic conductivities[13], indicating a strong alignment of ionic domains along the stretching direction. However, no study has been reported that exploits the significance of this morphological orientation on actuation behavior in IPMCs.

The effects of uniaxial deformation on the morphology of $TBA^+$-form Nafion® have been characterized by two-dimensional small/wide-angle X-ray scattering. For the as-received state, Figure VII-1a, the relatively[25] isotropic SAXS data show a diffuse outer ring of maximum intensity at ca. $q$ = 0.1 - 0.2 $Å^{-1}$, which has been attributed to scattering from the ionic aggregates dispersed in the PTFE matrix.[10, 18-21] The intense scattering near the beam stop is associated with typical ionomer long-range heterogeneities,[16, 26] and a contribution from PTFE-like crystalline domains.[14, 18, 20, 21] As the film is stretched to a draw ratio, $\lambda_b$ = 2, the previously isotropic scattering profile transforms into a strongly anisotropic scattering pattern (i.e., equatorial spots) as clearly observed in Figure VII-1b. Heijden and co-workers attributed this anisotropic scattering to alignment of elongated polymeric aggregates in the direction of uniaxial

extension.[15] With further extension, equatorial streaking in the SAXS patterns is observed, consistent with the formation of fibrillar-like morphologies.[10, 13, 19]

In the unoriented WAXS image, Figure VII-1c, two rings can be observed where the inner ring is attributed to the weak reflection of PTFE-like crystallites, *hkl* = 100 at $q$ = 1.24 Å$^{-1}$ [27], which is superimposed as a shoulder on a broad amorphous halo. The outer ring in Figure VII-1c is attributed to the PTFE crystalline reflection *hkl* = 101 at $q$ = 2.72 Å$^{-1}$ [27]. For the oriented sample, anisotropic WAXS patterns (i.e., equatorial arcs) indicate that both the amorphous and crystalline chains are oriented parallel to the direction of stretching, as shown in Figure VII-1d.[15] These chain orientations are consistent with a fibrillar morphology and the alignment of rod-like ionic domains in the stretching direction.

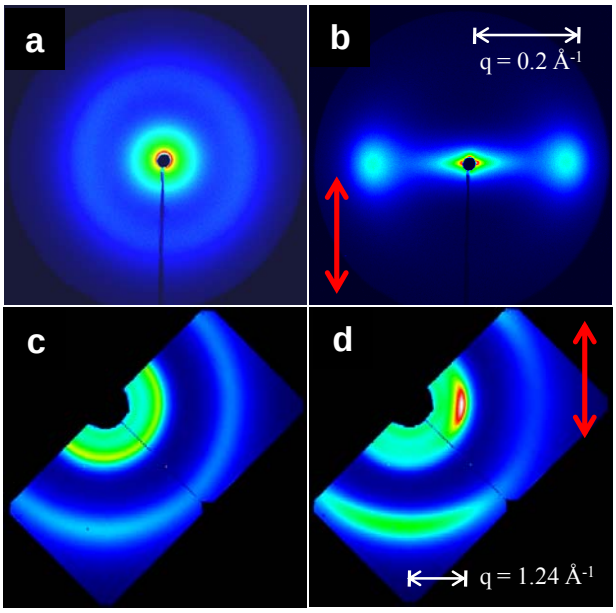


**Figure VII-1.** Two-dimensional X-ray scattering patterns of TBA$^+$-form Nafion® (a) SAXS of unoriented and (b) uniaxially-oriented ($\lambda_b$=2) samples. (c) WAXS of unoriented and (d) uniaxially-oriented samples. Stretching directions are indicated with red arrows.

Once Nafion® membranes are uniaxially oriented, electroless plating of platinum was performed following a multi-step procedure to prepare the nanostructured electrode layers (consisting of densely-packed Pt nanoparticles) of the IPMC.[6] With a 3V, square-waveform

stimulus (i.e., a field strength of ca. 15 V/mm), these IPMCs display significant bending actuation, as shown in the overlay images of Figure VII-2. For the oriented IPMCs, actuation behavior is clearly anisotropic and differs greatly in amplitude from that of the unoriented sample. It is evident that IPMCs cut from films oriented perpendicular to the draw direction (Figure VII-2d) yield tip-displacement values that are significantly greater than that of unoriented IPMCs (Figure VII-2a). In contrast, IPMCs cut from films oriented parallel to the draw direction (Figure VII-2c) appear to resist bending and yield tip-displacement values that are much less than that of the unoriented IPMC.

As a quantitative measure of this actuation performance, Figure VII-3 shows plots of tip-displacement versus field strength (applied voltage divided by IPMC thickness). At relatively low field strengths (below 6 V/mm), the electrically-stimulated driving force for actuation[7, 28, 29] is inadequate to cause significant bending motion. Upon the application of higher field-strengths, the tip-displacement for each IPMC increases significantly. Moreover, at field strengths above 10 V/mm, the anisotropic actuation in these oriented IPMCs is well resolved (i.e., perpendicular more responsive than parallel) and becomes much more evident with increasing field strength. At 15 V/mm, the perpendicular IPMC yields a tip-displacement that is 2 times that of the unoriented system and 4 times that of the parallel IPMC.

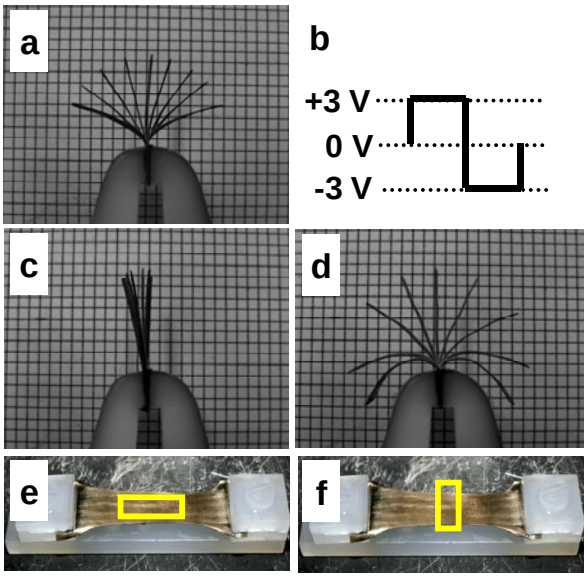


**Figure VII-2.** Composite overlay of images (square grid dimensions of 2 mm) captured during bending actuation of (a) unoriented IPMCs, oriented IPMCs cut (c) parallel and (d) perpendicular to draw direction under (b) 3V square waveform input with a frequency of 0.1 Hz. As-fabricated oriented IPMC with a rectangular box indicating the direction of sample orientation, (e) parallel and (f) perpendicular to draw direction

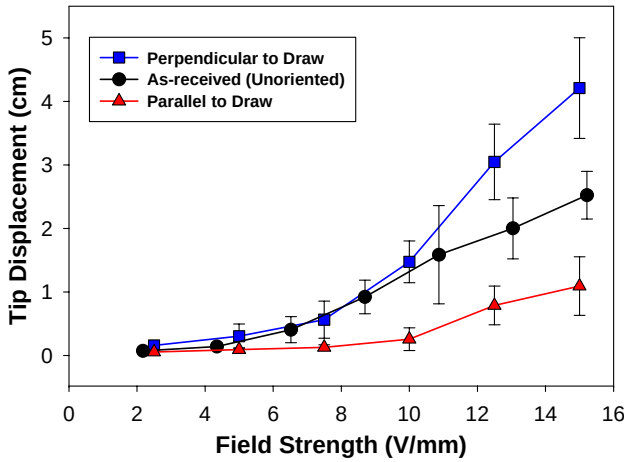


**Figure VII-3.** Plot of tip-displacement versus field strength (defined as applied voltage divided by IPMC thickness). All samples were 2 cm in length, and 5 mm in width. Error bars are the result of repetitive sample prepared under identical orientation and electroding conditions.

Due to the precise morphological control with uniaxial extension (shown above), we have also observed that samples cut 45$^{o}$ to the draw direction (Figure VII-4) yield a never before

seen twisting-mode of actuation for these "bending actuators." While this unique observation may open many new applications for these composite systems, it is of fundamental importance to recognize that these data show, for the first time, the impact of ionomer morphology on actuation behavior. Moreover, physical models developed to explain the actuation response of IPMCs must now consider the contribution of this structural parameter to the overall actuation mechanism.

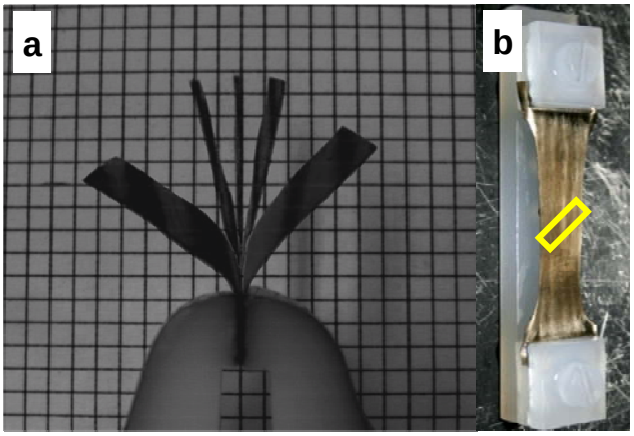


**Figure VII-4.** (a) Composite overlay of images (square grid dimensions of 2 mm) captured during twisting actuation of IPMCs cut 45 $^{o}$ to the draw direction under 2.5V square waveform input with a frequency of 0.1 Hz. (b) As-fabricated oriented IPMC with a rectangular box indicating the direction of sample orientation, 45 $^{o}$ to the draw direction.

Mechanisms for the bending actuation in IPMCs have been suggested to involve an electrically-stimulated differential swelling across the membrane thickness,[7] or changes in dimensional symmetry of the water-swollen clusters due to local electrostatic polarization.[29] In order to investigate the true mechanism of IPMC actuation, we have recently initiated neutron imaging studies to probe the existence and role of water and ion gradients during the actuation response.[30] Despite the lack of a precise, molecular-level understanding of the actuation mechanism, it is clear that the driving force for actuation must overcome the intrinsic stiffness of the bulk actuator. Specifically, the induced curvature in these bending actuators is inversely proportional to the bulk modulus of the IPMC.[28] To explore the effects of uniaxial orientation

on the bending stiffness of the ionic polymer matrix, we employed dynamic mechanical analysis using a 3-point bending clamp. Figure VII-5 shows the measured bending moduli of a dry, $TBA^+$-form Nafion® membrane (without electrode layers) and a hydrated, $H^+$-form IPMC (with electrode layers) at frequencies ranging from 0.1 to 10 Hz. The dry ionomer samples are observed to yield bending moduli that are an order of magnitude higher than that of the hydrated IPMC. This behavior is attributed to water acting as a softening (plasticizing) agent in the swollen IPMC. In complete agreement with the anisotropic actuation behavior, both samples demonstrate that bending ***along*** the draw direction (parallel orientation) yields a higher modulus value relative to the unoriented state. In contrast, bending ***across*** the draw direction (perpendicular orientation) yields a lower modulus value relative to the unoriented state. It is important to note from this comparison that the observed anisotropy in bending moduli is attributed to the oriented state of the ionic polymer and is not affected by the electroding process.

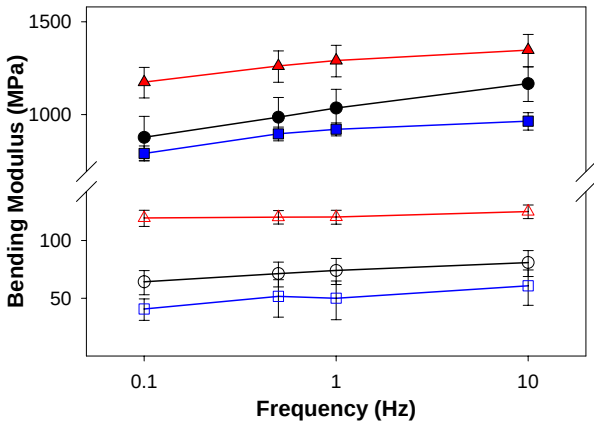


**Figure VII-5.** Effects of uniaxial orientation on the bending moduli of the ionic polymer matrix. Dry, $TBA^+$-form Nafion® bent along the draw direction (filled triangle), unoriented (filled circle), and bent across the draw direction (filled square); water-swollen, $H^+$-form IPMC bent along the draw direction (open triangle), unoriented (open circle) and bent across the draw direction (open square).

Based on our X-ray results (Figure VII-1), the increased moduli of the oriented films along the draw direction may be attributed to the oriented morphology of the ionic polymer

matrix, including the alignment of polymer chains, crystallites, and ionic domains. This is not surprising given the inherent stiffness of the PTFE segments of the Nafion® backbone.[31, 32] Furthermore, it is reasonable to expect that the water-swollen, rod-like ionic aggregates[24] act as nanoscale, anisotropic fillers in the matrix and resist folding along the aggregate axis. Consequently, this oriented morphology leads to anisotropic actuation. Since the oriented IPMCs are stiffer along the draw direction, actuation upon electrical stimulation is inhibited. Conversely, the lower bending modulus of IPMCs oriented perpendicular to the draw direction yields enhanced actuation.

It is of interest to note that anisotropy in actuation strain due to chain alignment has been observed recently in conducting polymer systems.[3] For these EAPs, anisotropy was attributed to the migration of counterions to locations between the oriented polymer chains, which yielded a higher degree of swelling perpendicular to the chain axis.[3] A similar swelling mechanism (i.e., water swelling perpendicular to the rod-like aggregate axis) may be envisioned for the oriented IPMC system studied here. For example, bulk water swelling of the unoriented ionomer shows an isotropic increase in dimensions of ca. 25%. In contrast, the oriented ionomer shows a negligible swelling along the draw direction, with an enhanced swelling of ca. 40% in the perpendicular directions. Since swelling along the aggregate length is inhibited due to morphological stability, preferential swelling in the perpendicular directions facilitates the observed anisotropy in actuation. However, the contribution of the stiff PTFE chains and oriented crystallites are also likely to be contributing factors. Therefore, the anisotropic actuation observed in these oriented IPMCs demonstrates, for the first time, the important contribution of the ionomer membrane morphology and chain conformation in the overall actuation phenomenon.

While the structural parameters of the ionic polymer matrix are now shown to be important contributions in the overall actuation mechanism, the effect of matrix orientation on the Pt nanoparticle formation and distribution within the electrode layers should also be considered as contributing factors. TEM micrographs of both unoriented (Figure VII-6a) and oriented (Figure VII-6b) IPMCs allow investigation of Pt particle distribution within these Nafion® membranes. Both images display very thin dense layers (ca. 0.5 μm) of Pt particles at the film edge and less densely dispersed Pt particles toward the film interior. While not shown in these images, the Pt particles in IPMCs are essentially absent at a depth beyond ca. 30 μm from the membrane surface. TEM micrographs of higher magnifications of both unoriented (Figure VII-6c) and oriented (Figure VII-6d) IPMCs show essentially no difference regarding spatial distribution, average size, and shape of the Pt particles, implying that uniaxial stretching has no significant effect on Pt particle formation. On the other hand, orientation yields a profound reorganization of the nanoscale morphology of the matrix as shown in the two-dimensional X-ray scattering patterns (Figure VII-1). From this information, it is evident that the Pt particle morphology/size or shape has no impact on the observed anisotropic actuation, thus supporting our argument that the actuation response is attributable to the oriented morphology of the ionic polymer matrix.

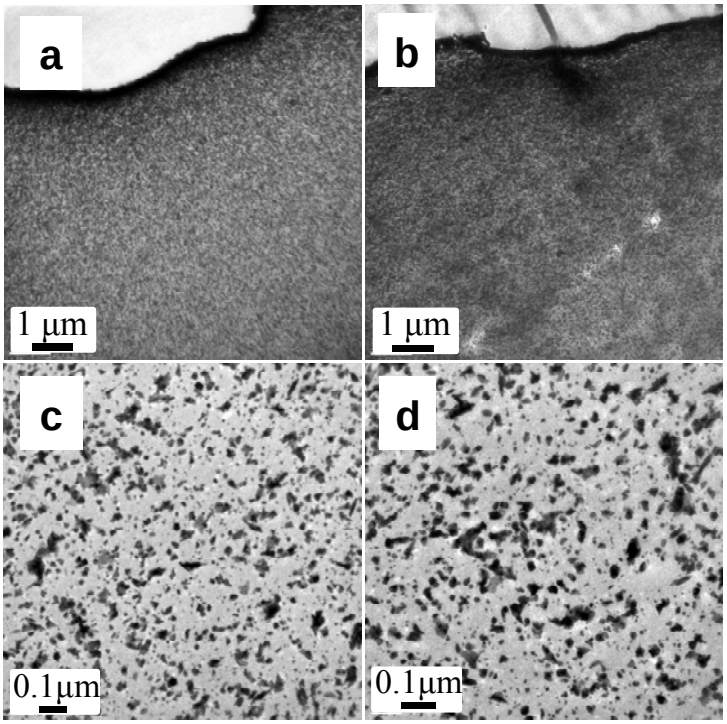


**Figure VII-6.** TEM micrographs of unoriented IPMCs at low (a) and high (c) magnifications and oriented IPMCs at low (b) and high (d) magnifications.

## D. Conclusion

Uniaxial orientation of Nafion® and the subsequent formation of electrode layers to create an IPMC were observed to yield anisotropic actuation behavior upon electrical stimulation. Relative to the unoriented state, polymer chains, crystallites, and rod-like aggregates oriented parallel to the draw direction inhibit actuation in the parallel orientation, while bending in the perpendicular orientation is significantly enhanced. In line with this unique anisotropic actuation behavior, dynamic mechanical analysis also showed that bending across the draw direction (perpendicular orientation) yields a lower modulus value relative to the unoriented state and a value much lower relative to bending along the draw direction (parallel orientation). Thus, the anisotropic actuation behavior of these oriented IPMCs is attributed, in part, to the contribution of the nanoscale morphology to the bulk bending modulus. As an

additional contribution, electrically-stimulated water swelling perpendicular to the rod-like aggregate axis facilitates bending in the perpendicular direction. Overall, this study clearly demonstrates (for the first time) the importance of the nanoscale morphology in affecting/controlling actuation behavior in IPMC electroactive systems. Further work is under way to investigate the effects of draw ratio, draw rate, and draw temperatures for the purpose of performance optimization.

## E. Acknowledgement

The authors wish to acknowledge support for this work provided by the National Science Foundation, (CMMI-0707364 and CBET-0756439), and the Materials Research Science and Engineering Center (MRSEC) program at the University of Southern Mississippi (DMR-0213883). Use of the Advanced Photon Source was supported by the U. S. Department of Energy, Office of Science, Office of Basic Energy Sciences, under Contract No. DE-AC02-06CH11357.

## F. References and Notes


(1) Bar-Cohen, Y., EAP History, Current Status, and Infrastructure. In *Electroactive Polymer (EAP) Actuators as Artificial Muscles*, Bar-Cohen, Y., Ed. SPIE: Bellingham, Washington, 2001; pp 3-44.
(2) Smela, E. *Adv. Mater.* **2003,** *15*, 481-494.
(3) Pytel, R.; Thomas, E.; Hunter, I. *Chem. Mater.* **2006,** *18*, 861-863.
(4) Pelrine, R.; Kornbluh, R.; Pei, Q.; Joseph, J. *Science* **2000,** *287*, 836-839.
(5) Liu, Z.; Calvert, P. "Multilayer Hydrogels as Muscle-Like Actuators," *Adv. Mater.* **2000,** *12*, 288-291.
(6) Shahinpoor, M.; Kim, K. J. *Smart Mater. Struct.* **2001,** *10*, 819-833.
(7) Shahinpoor, M. *Electrochim. Acta* **2003,** *48*, 2343-2353.
(8) Duncan, A. J.; Leo, D. J.; Long, T. E. *Macromolecules* **2008,** *41*, 7765-7775.
(9) Nemat-Nasser, S.; Wu, Y. *Smart Mater. Struct.* **2006,** *15*, 909-923.
(10) Mauritz, K. A.; Moore, R. B. *Chem. Rev.* **2004,** *104*, 4535-4585.
(11) Moore, R. B.; Martin, C. R. *Macromolecules* **1988,** *21*(5), 1334-1339.
(12) Moore, R. B.; Cable, K. M.; Croley, T. L. *J. Membrane Sci.* **1992,** *75*, 7-14.
(13) Cable, K. M.; Mauritz, K. A.; Moore, R. B. *Chem. Mater.* **1995,** *7*, 1601-1603.
(14) Rubatat, L.; Rollet, A. L.; Gebel, G.; Diat, O. *Macromolecules* **2002,** *35*, 4050-4055.
(15) van der Heijden, P. C.; Rubatat, L.; Diat, O. *Macromolecules* **2004,** *37*, 5327-5336.
(16) Eisenberg, A.; Hird, B.; Moore, R. B. *Macromolecules* **1990,** *23*, 4098-4107.
(17) Page, K. A.; Jarrett, W.; Moore, R. B. *J. Polym. Sci., Part B: Polym. Phys.* **2007,** *45*, 2177-2186.
(18) Page, K. A.; Cable, K. M.; Moore, R. B. *Macromolecules* **2005,** *38*, 6472-6484.
(19) Page, K. A.; Landis, F. A.; Phillips, A. K.; Moore, R. B. *Macromolecules* **2006,** *39*, 3939-3946.
(20) Gierke, T. D.; Munn, G. E.; Wilson, F. C. *J. Polym. Sci. Polym. Phys. Ed.* **1981,** *19*, 1687-1704.
(21) Fujimura, M.; Hashimoto, T.; Kawai, H. *Macromolecules* **1982,** *15*, 136-144.
(22) Elliott, J. A.; Hanna, S. *Macromolecules* **2000,** *33*, 4161-4171.
(23) Londono, J. D.; Davidson, R. V.; Mazur, S. *Polym. Mater.: Sci. Eng.* **2001,** *85*, 23-24.
(24) Schmidt-Rohr, K.; Chen, Q. *Nat. Mater.* **2008,** *7*, 75-83.
(25) Small intrinsic orientational anisotropy in the as-received state is attributed to the melt extrusion process through a die used to produce the membranes (i.e. machine direction).
(26) Moore, R. B.; Gauthier, M.; Williams, C. E.; Eisenberg, A. *Macromolecules* **1992,** *25*, 5769-5773.
(27) Starkweather, H. W. *Macromolecules* **1982,** *15*, 320-323.
(28) de Gennes, P. G.; Okumura, K.; Shahinpoor, M.; Kim, K. J. *Europhys. Lett.* **2000,** *50*, 513-518.
(29) Weiland, L. M.; Leo, D. J. *Smart Mater. Struct.* **2004,** *13*, 323-336.
(30) Park, J. K.; Page, K. A.; Hussey, D. S.; Jacobson, D. L.; Arif, M.; Moore, R. B. *Polym. Prepr.* **2008,** *49*, 1006-1007.
(31) Bunn, C. W.; Howells, E. R. *Nature* **1954,** *174*, 549-551.
(32) Chen, Q.; Schmidt-Rohr, K. *Macromol. Chem. Phys.* **2007,** *208*, 2189-2203.

# CHAPTER VIII

# ELECTRICALLY-STIMULATED GRADIENTS IN WATER AND COUNTERION CONCENTRATIONS WITHIN ELECTROACTIVE POLYMER ACTUATORS

## A. Introduction

Ionic polymer metal composites, or IPMCs, are a class of stimuli-responsive materials that exhibit actuation with similarities to biological muscles, and are often referred to as artificial muscles.[1-9] IPMCs were first demonstrated in the early 1990s's by Shahinpoor[7], Sadeghipour[8] and Oguro[9]. IPMCs are based on a solid polymer electrolyte which is plated on both surfaces by metal nanoparticles (e.g., platinum or gold) to serve as conductive electrodes. Under the stimulus of a relatively low electric field, IPMCs are capable of undergoing significant mechanical bending motion, while an external mechanical force applied to the surface of an IPMC can stimulate a detectable electrical response.[4]

A review of the open literature reveals that the perfluorosulfonate ionomer (PFSI) Nafion® remains the benchmark material for the vast majority of IPMC research and technology development.[1,2] Nafion®, having a chemical structure shown in Figure VIII-1, is a copolymer of tetrafluoroethylene and generally less than 15 mol % of perfluorovinylether units terminated with sulfonic acid functionalities.[10] Great attention has been given to the unique nanophase-separated morphology observed upon aggregation of the polar, ionic moeities within the matrix of hydrophobic PTFE.[10,11] The shape, spatial distribution and connectivity of polar ionic domains that are hydrophilic in nature precisely define the supramolecular organization. Numerous investigations have been focused on small angle X-

ray and neutron scattering to propose detailed models for this technologically important material as an ionic conductor. While it is beyond the scope of this study to discuss all the models in detail, and the studies of Nafion® morphology remain inconclusive, it is generally accepted that there are continuous pathways that allow transport of ions and water [10,12,13] and recent studies have suggested elongated, locally parallel water channels.[12,14]

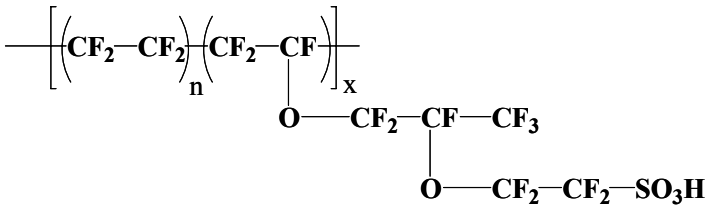

**Figure VIII-1.** Chemical structure of Nafion®

While IPMCs have received extensive attention for more than 10 years and have been well explored in regards to nature and type of solvent[15], electrode[16,17], counterions[18-20], and polymer electrolyte[1-3,19,21], fundamental research to understand the specific underlying actuation mechanism is lacking. One proposed mechanism for IPMC actuation has commonly been discussed in terms of electrophoresis-like counterion and water redistribution within the nanostructured ionomer membrane.[6,22,23] Since the ionic polymer is negatively charged with typically protons or alkali-metal cations as the counterions, these mobile cations in the hydrated membrane are readily redistributed in response to the applied electric field to create cation-rich and cation-poor boundary layers near the electrode/membrane interfacial regions**.** As cations migrate toward the cathode, they are accompanied by water molecules (i.e., a hydraulic mechanism), which consequently causes swelling near the cathode and contraction (due to dehydration) near the anode. This swelling/contraction thus induces a bending force that curves the IPMC toward the anode. In

contrast to a hydraulic model, which attributes actuation to charge and solvent transport, electrostatic models are based on a redistribution of cations and anions both within and at the surface of ionic aggregates.[24] According to the electrostatic model by Nemat-Nasser and Li[25], fast bending actuation originates from local cation redistribution upon application of an electric field. The migration of cations results in relaxation of polymer chains in the anion-rich region and extension of polymer chains in the cation-rich region. Weiland and Leo proposed a slightly modified electrostatic actuation mechanism.[24] In constrast to the work of Nemat-Nasser, Weiland and Leo propose that the initial rapid actuation behavior is dominated by a polarization mechanism, leaving only the slow relaxation to result from liquid and ion transport processes. The forces acting on dipoles located at the aggregate surface include dipole-dipole interactions, pendant chain stiffness, cluster surface energy and externally applied forces. Application of an external electric field is believed to cause the dipoles, that are assumed to have an equal magnitude and meta-stable orientations (all dipoles directed toward the center of the spherical cluster), to undergo reorientation and elongate or contract depending on their initial directions relative to the applied electric field. Macroscopic IPMC strain is then inferred from the distortion of the initially spherical aggregate into an ellipsoidal shape. The proposed model, however, relies on a number of simplifying assumptions which include very close contact between cation and anion in the hydrated state and primarily a spherical aggregate geometry not in tune with current Nafion® morphological models.[12,13]

In our recent investigation, the importance of the ionomer membrane morphology and chain conformation in the overall actuation phenomenon was clearly demonstrated for the first time.[2] Before full utilization of this unique electroactive material, a precise molecular-

level understanding of the actuation mechanism is a prerequisite. Previous efforts to characterize water redistriubtion within IPMC include MRI[26] and NMR[27] methods, which showed greater proton density (PD) and higher water diffusion coefficients near the cathode, respectively. The current study involves an alternative, novel characterization approach that provides more direct evidence of the water/counterion redistribution under electrical stimulation. In this research, neutron imaging and atomic force microscopy techniques are employed. Since the IPMC materials explored consist of Nafion® membranes and Pt electrode layers, these samples are essentially equivalent to the chemical composition of fuel cell membrane electrode assembly (MEA)-for which neutron imaging has proven to be of profound importance.[28-30] While the neutron imaging technique allows for direct imaging of electrically-induced water/counterion concentration profiles across the IPMC cross-section with a spatial resolution of 25 μm, AFM studies provide characterization of water/counterion transport and monitoring of changes in the morphological and surface characteristics that result from electrical stimulation. With the aid of these complimentary techniques, we have obtained direct experimental evidence supporting long-range water/counterion redistribution during electrical stimulation.

## B. Experimental

***Materials:*** The perfluorosulfonate ionomer, Nafion® 117CS membranes (1100g / equivalent, 7 mil thickness) were purchased from E.I. Dupont de Nemours & Co. and cleaned by refluxing in 8M aqueous nitric acid for 2 hr, and then in deionized (DI) water for 1 hr.

***Sample Preparation for Neutron Imaging:*** Tetrabutylammonium ($TBA^+$) neutralized membranes were prepared by soaking the previously cleaned $H^+$-form membranes in 1M

tetrabutylammonium hydroxide (TBAOH) (Aldrich) in methanol solutions for 12 hr and then rinsing with methanol to remove the residual TBAOH. $TBA^+$ neutralized membranes were dissolved in an alcohol-water mixture [methanol (30 % by volume) : Isopropanol (30 % by volume) : DI water (40 % by volume)] under high temperature (ca. 250 °C) and high-pressure conditions (ca. 7000 kPa).[31] The solution was filtered through a 200 μm inorganic membrane filter (Anotop 25, Whatman, Maidstone, UK) prior to membrane formation. Membranes with a thickness of 0.9 mm to 1.6 mm in thickness (in the hydrated state) were produced by casting at 180 °C from dimethylsulfoxide (DMSO), and then converted to the $H^+$ form by boiling in 4M $H_2SO_4$/methanol for 1 hr, in methanol for 30 min, and in DI water for 30 min. To fabricate the IPMCs[5], these solution-processed Nafion® surfaces were roughened by mechanically rubbing with 400-grain sandpaper to increase the surface area. Electroless plating of platinum was performed by following a multi-step procedure.[5] A platinum salt complex $[Pt(NH_3)_4]Cl_2$ (Aldrich) was used to make an aqueous solution with a concentration of 2 mg $mL^{-1}$ solution. The $H^+$-form Nafion® membrane was allowed to equilibrate with the platinum salt solution overnight. After rinsing with DI water, the membrane was immersed in DI water and the $Pt^{2+}$ ions in the membrane were reduced to Pt metal particles using 5 % by weight aqueous sodium borohydride ($NaBH_4$; Aldrich). The addition of $NaBH_4$ was carried out in seven steps at 30 min intervals, over which the temperature was ramped from 40 °C to 60 °C. After completion of the initial series of $NaBH_4$ additions, a final addition was carried out and reduction was allowed to proceed for 1.5 hr. The electroded membrane was then removed and rinsed in DI water before immersion in 0.1 M HCl to convert the material to the acid form. The whole reduction process above was carried out for three cycles to produce the final IPMCs used in the current

investigation. $H^+$-form IPMCs were further neutralized to contain tetramethylammonium ($TMA^+$) or sodium ($Na^+$) ions by soaking in excess (ca. 5 ×) aqueous solutions of the tetramethylammonium hydroxide (TMAOH, Aldrich) or sodium hydroxide (NaOH, Aldrich) respectively.

***Neutron Imaging*:** Direct imaging of an electrically-induced water/counterion concentration gradient profile across the IPMC cross-section was acquired using a neutron imaging method available at the National Institute of Standards and Technology (NIST) Center for Neutron Research (NCNR). At the NCNR, the neutron beam is processed through collimators, filters, an aperture, and an evacuated flight tube. Beam characteristics employed for the present experiment include the thermal neutron fluence rate of $1.9\times10^9$ $cm^{-2}s^{-1}$ with L/D ratio of 1200 where L (6 m) is the distance between the source and the detector and D (5 mm) is the source aperture diameter. In terms of neutron detection schemes, a micro-channel plate (MCP)-based counting detector was employed. The MCPs doped with high efficiency neutron conversion materials, such as $^{10}B$ or $^{157}Gd$ allows a high spatial resolution of 25 μm. The samples of IPMC prepared for neutron imaging were 2.0 cm in length, 0.5 cm in width and 0.9 mm to 1.6 mm in thickness (in the hydrated state). IPMC samples were equilibrated with DI water for 24 h before data acquisition. Hydrated IPMCs were then placed between copper electrodes sandwiched between Teflon spacers using the sample holder shown in Figure VIII-2, which inhibited the IPMC movement under electrical stimulation during the data acquisition.

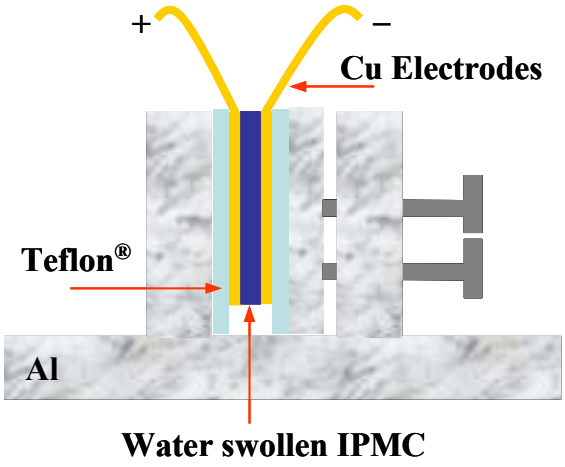


**Figure VIII-2**. Outline of the sample holder exposed in the neutron beam path

***Sample Preparation for Atomic Force Microscopy (AFM)*:** $H^+$-form Nafion® was dissolved into a solvent system consisting of 50 % (by volume) of ethanol and 50 % (by volume) of DI water by heating the mixture to 250 ˚C in a pressure vessel for 2 hr. The solution was filtered through a 200 μm inorganic membrane filter (Anotop 25, Whatman, Maidstone, UK) and deposited at room temperature onto the surface of a steel AFM stage puck to which a copper wire had been adhered using colloidal silver (Figure VIII-3). The Nafion® film was formed by evaporating the solvent in a vacuum oven at a pressure of 33 kPa and a temperature of 50 ˚C.

***Atomic Force Microscopy (AFM)*:** AFM measurements were made in an environmental chamber at room temperature where the relative humidity (RH) was controlled by a nitrogen purge and kept between 60 % and 70 %. The morphology and response to an applied electrical field were studied using an Agilent 5500 AFM (Agilent Technologies, Santa Clara, CA) in both tapping mode atomic force microscopy with an applied potential (APAFM) and current sensing atomic force microscopy (CSAFM) modes. The AFM has a variable voltage source attached to the copper wire (Figure VIII-3) that is capable of

applying a potential of –10 V to +10 V to the stage. APAFM was used to image both topography (height image) and domain behavior (phase image) of the cast films using a non-conductive silicon cantilever (RTESP, Veeco, Santa Barbara, CA) with a nominal resonant frequency of 300 kHz and a nominal force constant of 40 N/m. A bias ranging from 0 V to +3 V was applied to the metal stage puck through the attached copper wire and the topography and phase images were taken as a function of applied voltage using the same type of non-conductive cantilever (Figure VIII-3a, aplied potential). During APAFM, the ratio of the setpoint amplitude to the free amplitude ($A/A_0$) was maintained at a constant value.

CSAFM was used to probe the topography and local conductivity of the film with a bias ranging from –2 V to +2 V. A conductive platinum-coated silicon nitride cantilever (N9540-60002, Agilent Technologies, Santa Clara, CA) with a nominal force constant of 0.35 N/m was used for imaging (Figure VIII-3b). Topography and current images (detection of localized current) were obtained in contact mode. The voltage of the applied bias was verified by measuring the voltage between the metal stage puck and a ground on the AFM using a multimeter. During CSAFM the setpoint was maintained at a constant value. Data was processed using Gwyddion 2.10 software to improve image quality and remove artifacts. Images were leveled by mean plane subtraction, and scan lines were removed by matching the height median.

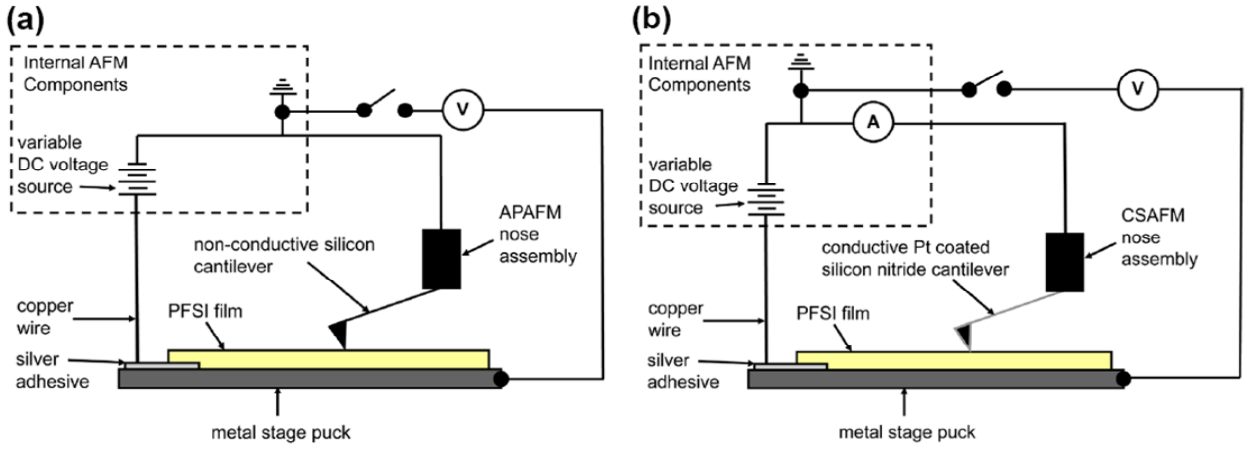


**Figure VIII-3**. Schematic drawings of (a) APAFM and (b) CSAFM. AFM voltage supply verified externally using multimeter. Non-conductive silicon cantilever in 3(a) acts as open switch. Conductive cantilever in 3(b) acts as closed switch.

## C. Results and Discussion

Typical actuation performance of Nafion®-based IPMC undergoing deformation in response to an applied electrical potential is shown in Figure VIII-4. Overlaid in each captured image is a schema showing the position on the electrical square wave excitation, denoted by an X, at which the image was acquired. In the initial image, Figure VIII-4a, the IPMC is clamped vertically between copper electrodes prior to application of the electrical stimulus. Without any electrical stimulation, the water/counterion distribution is expected to remain uniform across the IPMC thickness. Figure VIII-4b shows the maximum bending of the IPMC immediately prior to the polarity switch of the applied square wave, while Figure VIII-4c shows the maximum bending in the opposite direction. Assuming a hydraulic mechanism, the electrical stimulation is expected to attract counterions along with water molecules toward the cathode (Figure VIII-4b), which should yield a water/counterion concentration gradient across the IPMC thickness. With a reversed polarity (Figure VIII-4c), counterions and water molecules are expected to travel to the other side of the IPMC, which

will reverse the water/counterion concentration gradient.

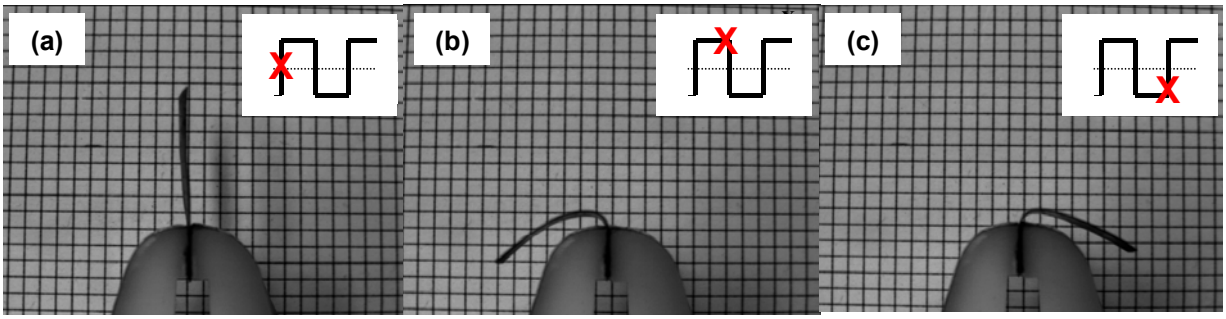


**Figure VIII-4**. IPMC actuation under applied electrical voltage. Each image was captured at the position of X on the excitation square wave (square-grid dimensions of 2 mm)

**Neutron Imaging of Hydrated IPMC Element**

Neutron radiography is an ideal tool to investigate the potential establishment of a water/counterion concentration gradient under electrical stimulation. Neutrons interact with materials differently than X-rays and hydrogen atoms have a uniquely high neutron scattering cross-section compared to other atoms including C, F, O, Na, S and Al (that are components of Nafion® and sample holders). Hydrogen atoms in the water molecules and the $TMA^+$ counterions will yield a strong attenuation of the impingent neutron beam according to Eq VIII-1:

$$I = I_0 \exp(-\sum_i \mu_i t_i) \qquad \textbf{Eq VIII-1}$$

where $I$ represents the neutron intensity attenuated while passing through the specimen, $I_0$ is the incident neutron intensity, $\mu_i$ is referred to as the neutron attenuation coefficient of the material $i$ and $t_i$ is the material thickness exposed in the beam path. By placing the working IPMC into the neutron beam path during electrical stimulation, it is possible to detect contrast variations in neutron transmission across the IPMC thickness with varying water/counterion concentrations. It is expected that any water/counterion concentration gradient created across the thickness of the Nafion® membrane will be detected as a neutron

intensity gradient in the outgoing neutron beam. The raw imaging data were acquired before and after application of the electrical stimulus (3 volts direct current, VDC) with an IPMC swollen with water and neutralized to contain tetramethylammonium ($TMA^+$) counterions. The neutron imaging data acquired before any electrical stimulation were used as the reference (i.e., with an equilibrium, isotropic water/counterion distribution across the film thickness). Figure VIII-5a shows one such processed image where all of the sample holder features and electrodes that do not change with electrical stimulation are normalized and not visible in the resulting image. In this image, water/counterion-depleted zones are represented by red color pixels, while water/counterion-rich zones are represented by blue color pixels. The sample thickness (ca. 950 μm) is represented by two vertical bars with a double-headed arrow and the direction of $H_2O/TMA^+$ migration indicated by a single-headed arrow. Figure VIII-5b shows a plot of the Change in Optical Density (ΔO.D.) across the IPMC thickness. ΔO.D. is defined as $-\ln (I_{after} / I_{before})$ where $I_{before}$ and $I_{after}$ represent the intensities of neutron beam attenuated while passing through the IPMC sample before and after electrical stimulation, respectively. These data clearly demonstrate that a water/counterion concentration gradient profile is established with the application of an electric field across the IPMC thickness, indicating that water/counterion molecules are redistributing away from the anode side of the IPMC.

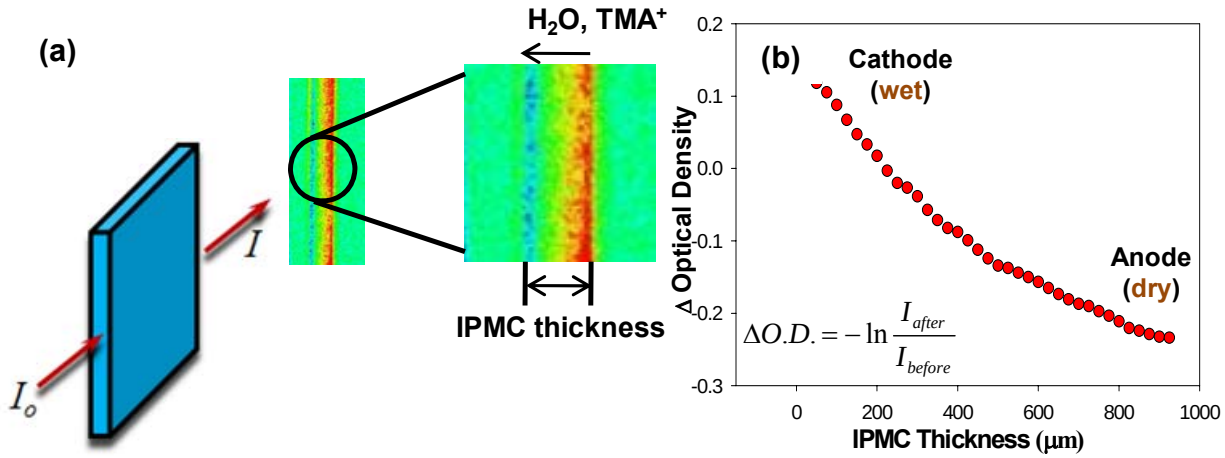


**Figure VIII-5**. (a) Colorized images showing water/tetramethylammonium ($TMA^+$)-depleted zones represented by red pixels and water/$TMA^+$-rich areas represented by blue pixels. IPMC was subjected to 3 VDC. (b) Water/counterion gradient profile across the IPMC thickness. Change in Optical Density ($\Delta O.D.$) is defined as $-\ln(I_{after}/I_{before})$ where $I_{after}$ and $I_{before}$ represent the neutron intensities attenuated while passing through the IPMC sample before and after electrical stimulation, respectively.

The neutron intensity gradient observed in Figure VIII-5 is attributed to both water and counterions due to the fact that water and $TMA^+$ both have an abundance of hydrogen atoms, in contrast to the perfluorinated ionomer matrix. To selectively characterize solvent migration, the IPMC is neutralized with $Na^+$ ions and swollen with $H_2O$. Because the H atom has almost 25 times larger scattering cross-section than the Na atom, the neutrons will only "*see*" the migration of $H_2O$, not $Na^+$, although both solvent and counterions are suggested to be redistributed under electrical stimulation in a hydraulic model.[6,22,23] Figure VIII-6 shows the time and space-resolved neutron attenuated raw intensity versus pixel location data along the $H_2O$ swollen, $Na^+$-form IPMC cross-section. Figure VIII-6a compares data acquired at 0 and 30 sec under 3 Volts and also identifies the position of IPMC along with other components of the sample holder. It should be noticed that the water-swollen IPMC significantly attenuates the neutron beam compared to the Cu electrode and PTFE spacer, leading to the U shape profile observed in the raw data. As expected, no water concentration gradient is observed prior to electrical stimulation, which indicates

uniform/random water distribution along the IPMC cross-section (i.e., a flat intensity profile across the IPMC). Electrical stimulation of 3 volts for 30 sec rapidly creates a distinct water concentration gradient (i.e., a non-flat intensity profile sloping from the anode to the cathode, across the IPMC thickness.

Figure VIII-6b shows data acquired over 300 sec before and after polarity reversal. The initially established water concentration gradient clearly remains over 300 sec and the slope of this gradient is quickly inverted as soon as the polarity is switched, which explains the rapid macroscopic bending movement of IPMCs with polarity switching. Previous IPMC studies often observed the back-relaxation in strain and bending force under DC electrical stimulation.[20,32] While not specifically investigated in our initial study, this persistent gradient suggests that back-relaxation may be related to a segmental relaxation of the polymer matrix as opposed to a back-diffusion of water and/or ions.

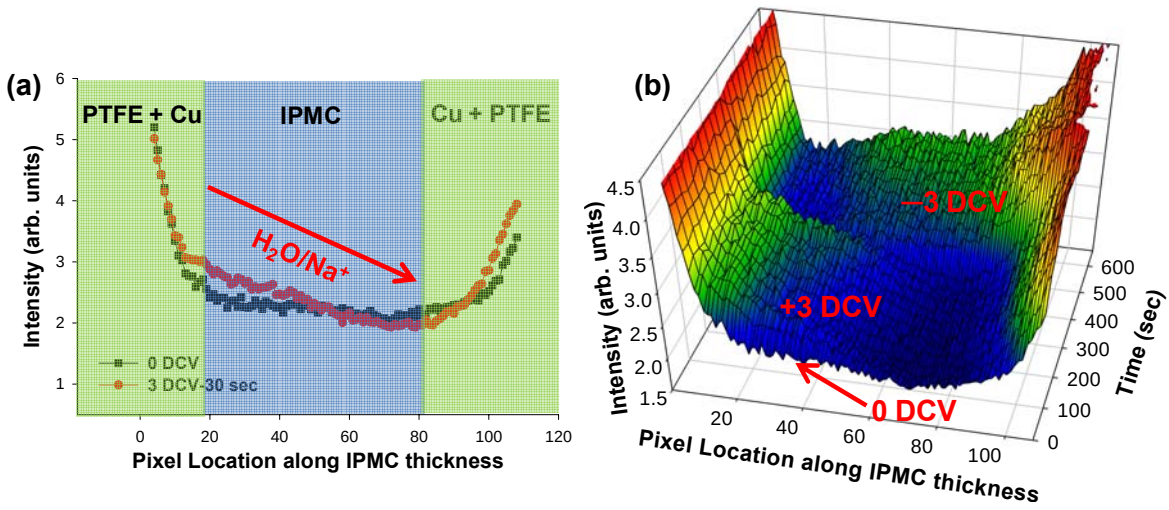


**Figure VIII-6**. Neutron attenuated raw intensity versus pixel location along $H_2O$ swollen, $Na^+$ form IPMC cross-section placed between copper electrodes sandwiched between Teflon spacers (a) Data taken at 0 sec and 30 sec under 3 V (b) Data acquired over 300 sec before and after polarity reversal (1 pixel represents 25 μm)

To selectively characterize counterion redistribution during electrical stimulation, two sets of IPMC samples were prepared. One sample was neutralized with $Na^+$ ions while the

other with $TMA^+$ ions. Both IPMC samples were then swollen with $D_2O$ as opposed to $H_2O$. It should be pointed out that, in our controlled experiment with Nafion® 117 based IPMCs, no noticeable difference in actuation performance was observed upon solvent switching from $H_2O$ to $D_2O$. However, the use of $D_2O$ as opposed to $H_2O$ will cause a significant decrease in an effective solvent scattering cross-section (defined as the products of cross-section and concentration for each element) and thus attenuation of the neutron intensity will be observed mostly by the counterions containing H atoms such as with $TMA^+$. Figure VIII-7a and 7b show ΔO.D. profiles obtained for IPMC samples neutralized with $Na^+$ and $TMA^+$ ions, respectively. For each counterion, the IPMC was subjected to electrical stimulation of 3 volts and the response of ΔO.D.was monitored for an extended time period, up to 20 min. As expected, for the $Na^+$-neutralized IPMC (Figure VIII-7a), the ΔO.D. profiles are essentially flat as a function of time, even though the $D_2O$ solvent and $Na^+$ ions are likely to be undergoing redistribution under electrical stimulation. However, the ΔO.D. profiles for $TMA^+$-neutralized IPMC (Figure VIII-7b), clearly shows that electrical stimulation yields a distinct counterion concentration gradient. Thus, this experiment demonstrates that the mobile ions in IPMCs are redistributed across the IPMC thickness along with water molecules in response to the applied electric field.

In Figure VIII-5b and 7b**,** the positive ΔO.D. near the cathode indicates an increased concentration of water and counterions under electrical stimulation compared to that observed without application of an electric field. On the contrary, the negative ΔO.D. near the anode indicates a decreased concentration of water and counterions under electrical stimulation compared to the uniform distribution in the absence of an applied field. This is indeed the first direct evidence of water and counterion redistribution during electrical

stimulation in these new stimuli-responsive materials, and evidently indicates that the hydraulic phenomenon is a strong contribution to the overall actuation mechanism. It should also be pointed out that the ΔO.D. profiles shown in Figure VIII-5b and 7b display a uniform gradient across the film as opposed to a step-like profile near the electrode layers. Thus, a more accurate description of this proposed hydraulic mechanism should involve the entire IPMC thickness, as oposed to simply a creation of cation-rich and cation-poor boundary layers near the electrode/membrane interfacial regions.

I

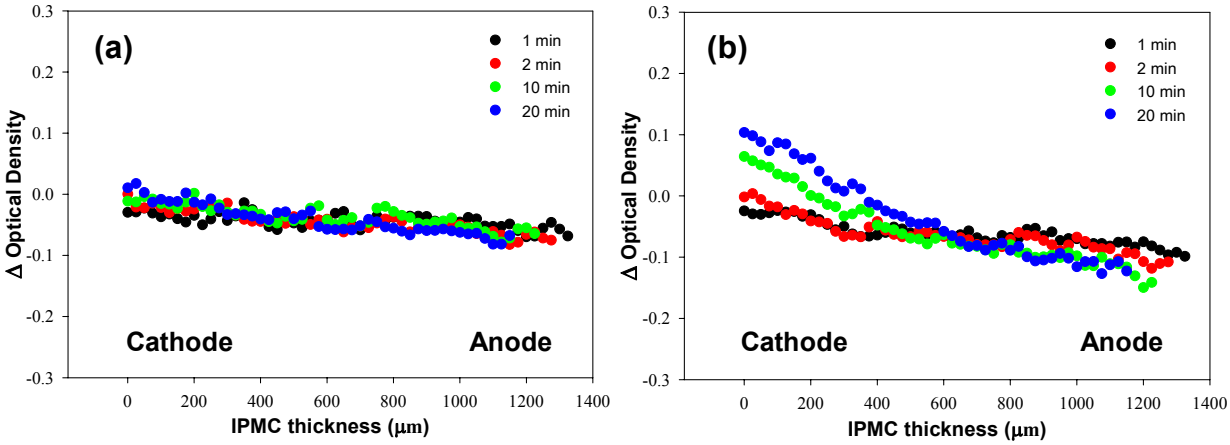


**Figure VIII-7**. Change in Optical Density (ΔO.D.) profiles across $D_2O$ swollen IPMCs neutralized to contain (a) $Na^+$ and (b) $TMA^+$ ions. IPMCs were electrically stimulated by 3 volts for an extended time period.

**AFM on PFSI Membranes under Electrical Stimulation**

The IPMC actuation mechanism was further characterized by atomic force microscopy (AFM). Various AFM studies on PFSIs have been performed previously with the goal of identifying the size and shape of hydrophilic domains distributed within the hydrophobic PTFE matrix.[33-35] More recent efforts have involved the use of a platinum-coated conductive AFM tip to determine the distribution of electrochemically active ionic domains.[36,37] However, there has been no detailed investigation regarding surface

characteristics of PFSIs that are under the influence of electrical stimulation, which is clearly needed to understand the mechanistic details of IPMC actuation. This work describes the use of a combination of APAFM and CSAFM to capture surface morphological response and local conductivities, respectively, as a function of an applied electric field.

Ion and water redistribution under electrical stimulation was probed by measuring the local mechanical energy dissipation on the surface of a PFSI membrane subjected to an applied bias voltage using APAFM (Figure VIII-8). In APAFM the cantilever was operated in the intermittent contact regime to minimize destructive lateral forces on the sample surface while both topographical and phase images were obtained. By measuring the phase shift with constant excitation force, differences in probe-tip sample interactions produce compositional contrast in a heterogeneous sample.[38] Contrast arises from differences in mechanical energy dissipation between the tip and the sample.[39,40] In the intermittent contact regime, softer, more viscous, energy dissipative components appear as darker features in the phase image, while harder, more elastic, components appear brighter.[41] In Figure VIII-8 topographical images are presented on the left, and the corresponding phase images are on the right. In Figure VIII-8a and 8b, there is no applied bias voltage. In Figure VIII-8c and 8d, a 1 V bias was applied to the stage puck producing a negative charge on PFSI membrane surface in contact with the substrate. No significant change in surface roughness is observed when a 1 V bias is applied, but the average phase shift of the cantilever's response to the surface increases from 16.3˚ to 23.8˚, indicating an overall decrease in energy dissipation. The same trend is observed in Figure VIII-8f and 8h as the bias is increased from 1 to 3 V. At 3 V, the average phase shift of the cantilever increases to 29.8˚. Surface roughness and average phase shift data are summarized in Table VIII-1 below. Table VIII-1 shows that the

surface roughness remains relatively constant, while the phase shift increases with applied voltage. The disappearance of the darker, more energy dissipative features as the applied bias is increased indicates that the total surface has become more energy conservative. Since the presence of water on the surface of a membrane will increase the energy dissipative characteristics of the surface, the observed increase in energy conservation of the PFSI membrane surface suggests that the surface is becoming dehydrated. This observation is in complete agreement with the neutron imaging results above and further supports the mechanism of proton and water migration to the negatively charged substrate as shown in the schematic presented in Figure VIII-10b.

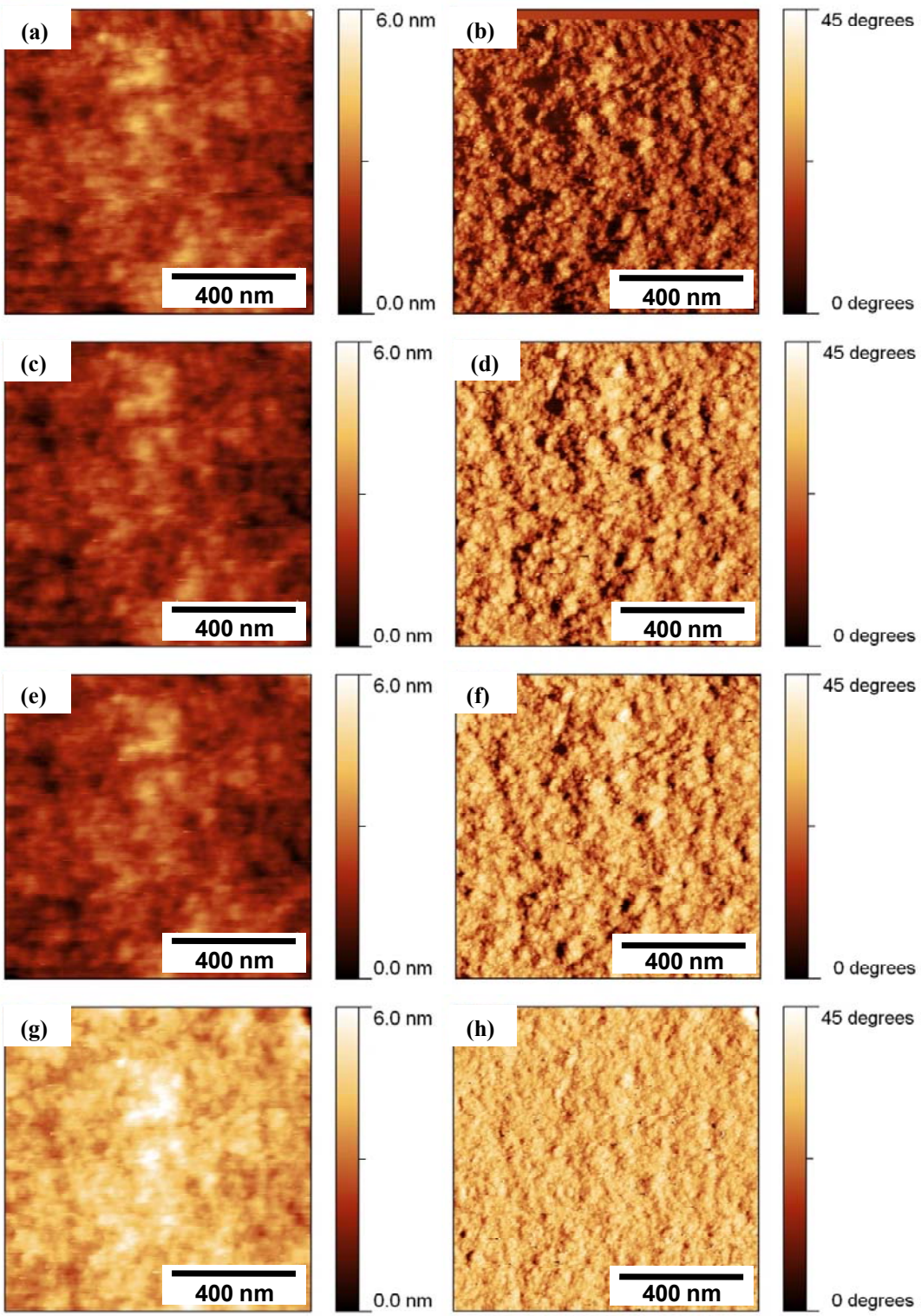


**Figure VIII-8**. APAFM topographical (left) and corresponding phase (right) images of PFSI film as a function of applied bias voltage: (a and b) 0 V, (c and d) 1 V, (e and f) 2 V, (g and h) 3 V (These data were acquired in collaboration with Prof. Sarah E. Morgan at the University of Southern Mississippi.)

Further examination of the electrically-stimulated gradients was conducted using the CSAFM method (operating in the contact regime) and presented in Figure VIII-9 with topographical images on the left, and the corresponding current images on the right. In Figure VIII-9a (topography) and Figure VIII-9b (current), a +2V bias was applied to the metal stage puck giving the substrate surface of the PFSI membrane a negative charge. The conductive domains (brighter areas, see scale bar) in Figure VIII-9b correspond to the high regions of the topographical image in Figure VIII-9a. Current flow is isolated to the bright areas that indicate measurable current. The average current, calculated from every point measured across the surface of Figure VIII-9b is 2.8 pA. It should be pointed out that the image scale in Figure VIII-9b is reduced to increase contrast. In Figure VIII-9c (topography) and Figure VIII-9d (current), the polarity is now reversed and –2V bias is applied to the substrate, yielding a positive charge at the substrate surface of the sample. The average current of Figure VIII-9d is –90.6 pA, which suggests that conduction occurs over the entire surface. The regions of high current flow in this image are the dark features, and correspond to the dark, lower regions of the topography image (see scale bar). Average diameter of the conductive domains determined by image analysis is 41 nm with a standard deviation of 8nm.

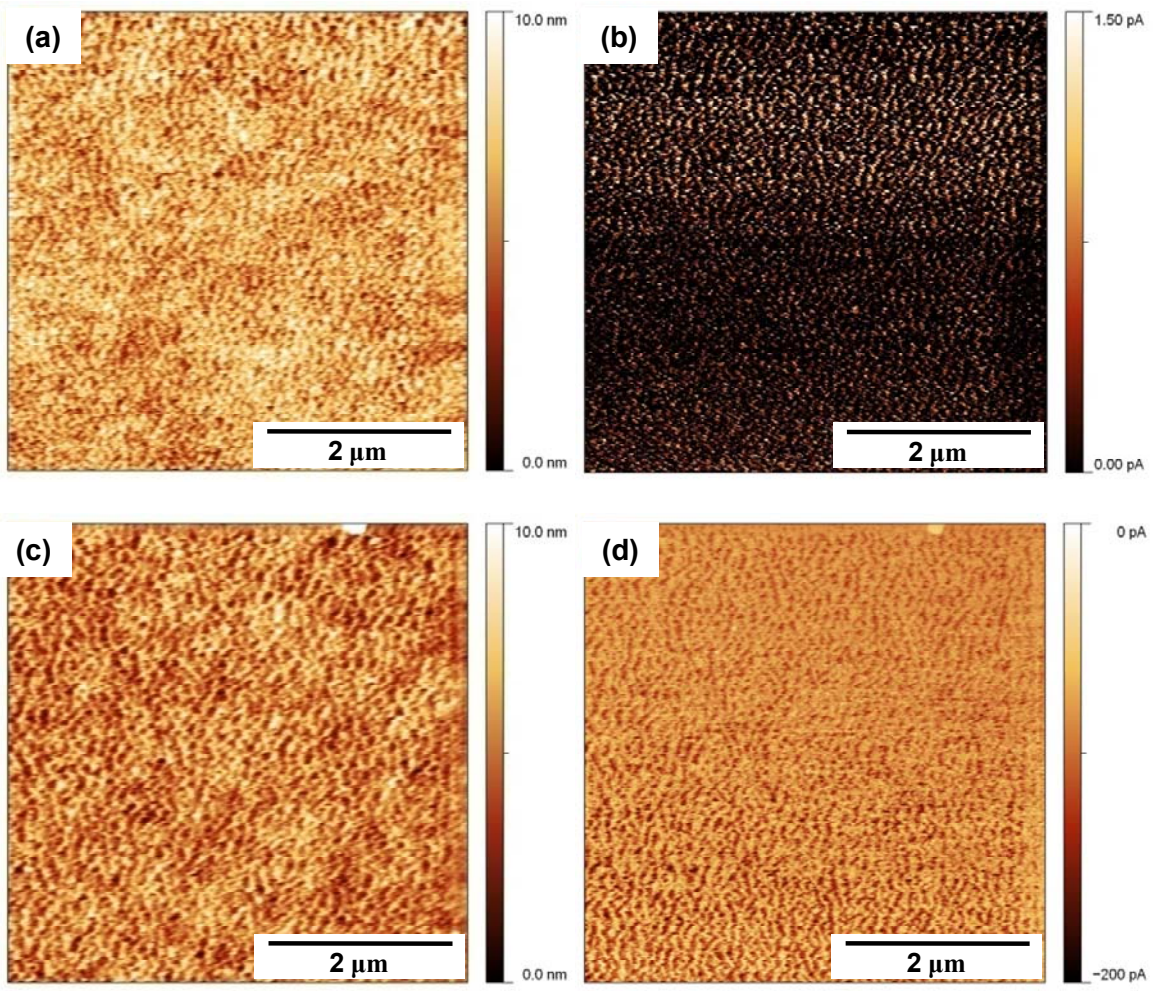


**Figure VIII-9**. CSAFM topographical (left) and current (right) images of PFSI film: (a and b) +2 V, (c and d) –2 V. (These data were acquired in collaboration with Prof. Sarah E. Morgan at the University of Southern Mississippi.)

The PFSI investigated in this study is known to form a phase-separated morphology where the ionic domains, termed ionic clusters, are distributed throughout the non-polar polytetrafluoroethylene (PTFE) matrix, and continuous ionic channel formation in a hydrated condition provides the percolation pathway for ionic conduction.[10,12,42] When no charge is applied to the membrane, the sulfonate groups residing in the interfacial region between the PTFE matrix and the ionic channel are in equilibrium with protons in solution, and the sulfonate groups residing on the top surface of the PFSI membrane are in equilibrium with protons residing in the thin liquid layer present on the top surface of the PFSI membrane.

This is illustrated schematically in Figure VIII-10a.

The light features in Figure VIII-9b correspond to the dark features in Figure VII-9a and indicate that these are actively conductive channels. The direction of positive current flow in Figure VIII-9b suggests that the light features represent the immobile, negatively charged sulfonate groups producing positive current flow to the grounded, platinum coated cantilever. The dark, continuous region of Figure VIII-9b corresponds to the light continuous region of Figure VIII-9a, suggesting that this is the nonconductive PTFE matrix. The direction of current flow indicates that the surface is absent of positively charged cations and suggests that these species have migrated to the negatively charged substrate as shown in the schematic presented in Figure VIII-10b.

In Figure VIII-9d the darker features correspond to the dark features in Figure VIII-9c, providing further evidence that these domains represent the actively conductive channels. The direction of negative current flow in Figure VIII-9d suggests that the mobile protons and water have migrated to the surface giving it a positive charge. The magnitude of the negative current flow and the presence of current flow over the entire surface suggest that the cationic fluid has not only migrated to the surface of the actively conducting domains but has actually formed a cationic film on the top surface of the PFSI membrane, which is illustrated schematically in Figure VIII-10c.

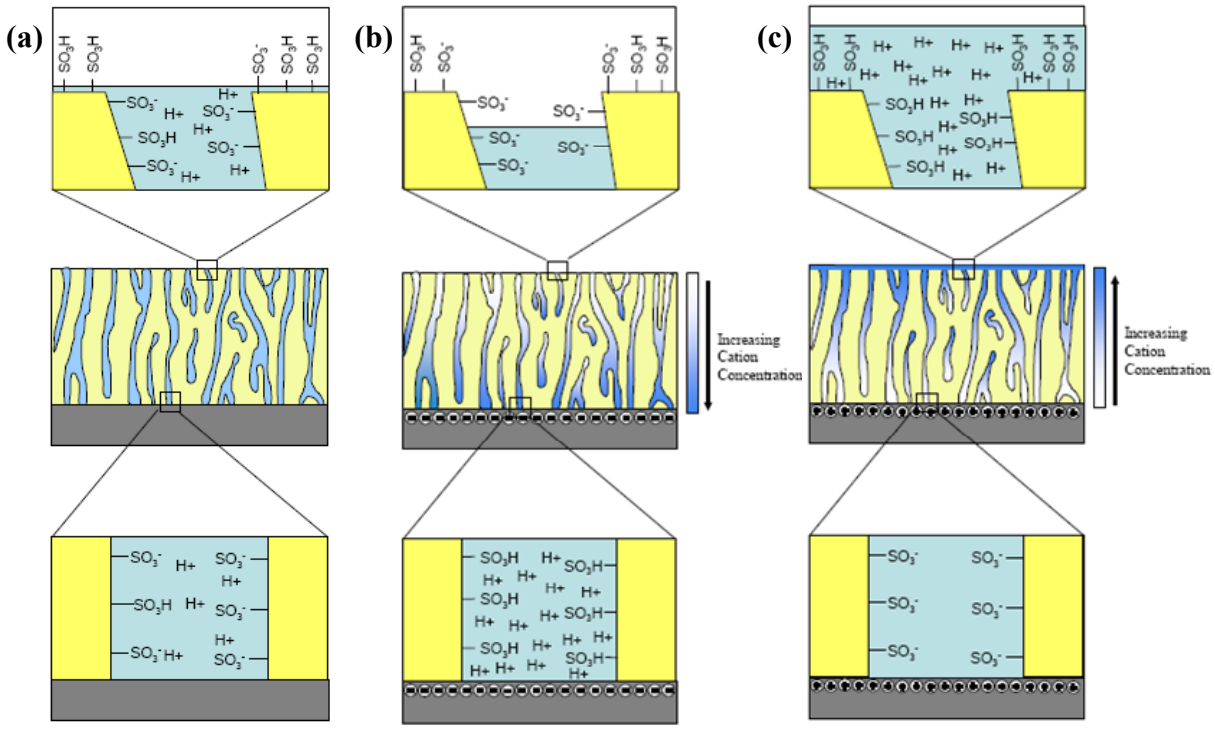


**Figure VIII-10**. (a) Illustration of the equilibrium state between sulfonate groups and protons in the PFSI membrane with no applied bias, (b) illustration of proton and water migration to the negatively charged substrate and formation of isolated sulfonate-rich domains and dehydration on the top surface of the PFSI membrane, and (c) illustration of proton and water migration away from the positively-charged substrate forming a cationic film on the top surface of the PFSI membrane and neutralization of the positively charged substrate by non-mobile sulfonate ions.

**Table VIII-1**. Summary of average height and phase variations as a function of applied voltage. The root mean square deviation associated with each value is presented in italics.

| | Topography (nm) | | Phase Shift (degrees) | |
|---|---|---|---|---|
| | Average Height | *RMS Roughness* | Average | *RMS* |
| 0 V | 2.13 | *0.62* | 16.3 | *7.03* |
| 1 V | 1.80 | *0.58* | 23.8 | *7.36* |
| 2 V | 1.93 | *0.58* | 26.1 | *6.78* |
| 3 V | 4.17 | *0.60* | 29.8 | *4.49* |

## D. Conclusions

We employed two different techniques, neutron imaging and atomic force microscopy, in an effort to fundamentally characterize electrically-stimulated water/counterion redistribution which has been suggested to be an important consideration in the IPMC actuation mechanism. While the neutron imaging method provided a bulk characterization (cross-sectional analysis) of water/counterion migration across the IPMC thickness, AFM allowed surface characterization of the nanoscale morphology and local surface properties due to migration of water/counterion under electrical stimulation. The time and space-resolved neutron imaging experiment showed that water gradients were established along the IPMC cross-section during 30 sec under 3 DCV stimulation. With a sudden switch in polarity, the gradient reversed rapidly, in agreement with the rapid actuation response typically observed with IPMCs. Moreover, under this DC stimulation, the water gradient was observed to persist over an extended time period (300 sec). While not specifically probed in this initial investigation, this persistent gradient suggests that the often observed back-relaxation in strain and bending force of DC stimulated IPMCs may be related to a segmental relaxation of the polymer matrix as opposed to a back-diffusion of water and/or ions. IPMCs neutralized with $TMA^+$ ions and swollen with $D_2O$ were used to directly probe counterion redistribution under electrical stimulation. Under 3V, a distinct sloping in the optical density profile was observed. A positive sign of optical density near the cathode indicated that counterions were attracted toward the negatively charged electrode.

Water/counterion migration in response to various voltages was characterized using APAFM. The increase in energy conservation of the PFSI membrane surface suggested that the surface was being dehydrated due to migration of protons and water to the negatively

charged substrate, which correlates very well with the neutron imaging results. Water/counterion migration was further supported by CSAFM. Under a +2 V bias, only a low 2.8 pA of average current was detected over the PFSI surface. This indicated that positively-charged cations were essentially absent on the surface. On the contrary, application of –2 V bias to the substrate/sample interface led to a high average current of –90.6 pA on the opposing surface, which suggests that the protons and water have migrated to the surface away from the positively-charged substrate.

While the true mechanism of actuation in IPMCs has remained under debate, the direct evidence in this study has demonstrated for the first time that the actuation response involves a strong hydraulic contribution. With an electrical field established between the IPMC electrode layers, mobile cations and their water molecules of hydration rapidly migrate to the cathode (negative electrode). This electrically-stimulated gradient in water concentration across the ionic polymer membrane creates opposing swelling (cathode side) and deswelling (anode side) pressures that induce a bending of the actuator toward the anode. With a switch in polarity, the water and ions move rapidly across the ionic polymer film to establish a reverse gradient that yields a subsequent reversal in the IPMC curvature.

## E. Acknowledgement

The authors wish to acknowledge support for this work provided by the National Science Foundation, (CMMI-0707364 and CBET-0756439), and the Materials Research Science and Engineering Center (MRSEC) program at the University of Southern Mississippi (DMR-0213883). This work was also supported by the U.S. Department of Commerce, the NIST Ionizing Radiation Division, the Director's office of NIST, the NIST Center for Neutron

Research, and the Department of Energy interagency agreement No. DE-AI01-01EE50660. Authors also would like to sincerely thank Paul J. Jones, Chris Sahagun, and Prof. Sarah E. Morgan for their collaboration, discussion and for running the Atomic Force Microscopy (AFM) experiments.

## F. References

(1) Duncan, A. J.; Leo, D. J.; Long, T. E. *Macromolecules* **2008**, *41*, 7765-7775.
(2) Park, J. K.; Moore, R. B. *ACS Appl. Mater. Interfaces* **2009**, *1*, 697-702.
(3) Phillips, A. K.; Moore, R. B. *Polymer* **2005**, *46*, 7788-7802.
(4) Shahinpoor, M. *Electrochim. Acta* **2003**, *48*, 2343-2353.
(5) Shahinpoor, M.; Kim, K. J. *Smart Mater. Struct.* **2001**, *10*, 819-833.
(6) Shahinpoor, M.; Bar-Cohen, Y.; Simpson, J. O.; Smith, J. *Smart Mater. Struct.* **1998**, *7*, R15-R30.
(7) Shahinpoor, M. *Smart Mater. Struct.* **1992**, *1*, 91-95.
(8) Sadeghipour, K.; Salomon, R.; Neogi, S. *Smart Mater. Struct.* **1992**, *1*, 172-179.
(9) Asaka, K.; Oguro, K.; Nishimura, Y.; Mizuhata, M. *Polym. J.* **1995**, *27*, 436-440.
(10) Mauritz, K. A.; Moore, R. B. *Chem. Rev.* **2004**, *104*, 4535-4585.
(11) Page, K. A.; Cable, K. M.; Moore, R. B. *Macromolecules* **2005**, *38*, 6472-6484.
(12) Schmidt-Rohr, K.; Chen, Q. *Nat. Mater.* **2008**, *7*, 75-83.
(13) Kim, M.-H.; Glinka, C. J.; Grot, S. A.; Grot, W. G. *Macromolecules* **2006**, *39*, 4775-4787.
(14) Rubatat, L.; Rollet, A. L.; Gebel, G.; Diat, O. *Macromolecules* **2002**, *35*, 4050-4055.
(15) Bennett, M. D.; Leo, D. J. *Sensor Actuat. A-Phys* **2004**, *115*, 79-90.
(16) Bennett, M. D.; Leo, D. J. *Smart Mater. Struct.* **2003**, *12*, 424-436.
(17) Shahinpoor, M.; Kim, K. J. *Smart Mater. Struct.* **2000**, *9*, 543-551.
(18) Onishi, K.; Sewa, S.; Asaka, K.; Fujiwara, N.; Oguro, K. *Electrochim. Acta* **2001**, *46*, 1233-1241.
(19) Nemat-Nasser, S.; Wu, Y. *J. Appl. Phys.* **2003**, *93*, 5255-5267.
(20) Nemat-Nasser, S.; Wu, Y. *Smart Mater. Struct.* **2006**, *15*, 909-923.
(21) Nguyen, V. K.; Lee, J. W.; Yoo, Y. *Sensor Actuat. B-Chem.* **2007**, *120*, 529-537.
(22) De Gennes, P. G.; Okumura, K.; Shahinpoor, M.; Kim, K. J. *Europhys. Lett.* **2000**, *50*, 513-518.
(23) Shahinpoor, M. *Smart Mater. Struct.* **1994**, *3*, 367-372.
(24) Weiland, L. M.; Leo, D. J. *Smart Mater. Struct.* **2004**, *13*, 323-336.
(25) Nemat-Nasser, S.; Li, J. Y. *J. Appl. Phys.* **2000**, *87*, 3321-3331.
(26) Naji, L.; Chudek, J. A.; Baker, R. T. *Soft Matter* **2008**, *4*, 1879-1886.
(27) Naji, L.; Chudek, J. A.; Baker, R. T. *J. Phys. Chem. B* **2008**, *112*, 9761-9768.
(28) Bellows, R. J.; Lin, M. Y.; Arif, M.; Thompson, A. K.; Jacobson, D. *J. Electrochem. Soc.* **1999**, *146*, 1099-1103.
(29) Hickner, M. A.; Siegel, N. P.; Chen, K. S.; McBrayer, D. N.; Hussey, D. S.; Jacobson, D. L.; Arif, M. *J. Electrochem. Soc.* **2006**, *153*, A902-A908.
(30) Satija, R.; Jacobson, D. L.; Arif, M.; Werner, S. A. *J. Power Sources* **2004**, *129*, 238-245.
(31) Moore, R. B.; Martin, C. R. *Anal. Chem.* **1986**, *58*, 2569-2570.
(32) Lu, J.; Kim, S.-G.; Lee, S.; Oh, I.-K. *Adv. Funct. Mater.* **2008**, *18*, 1290-1298.
(33) Affoune, A. M.; Yamada, A.; Umeda, M. *J. Power Sources* **2005**, *148*, 9-17.
(34) Lehmani, A.; Durand-Vidal, S.; Turq, P. *J. Appl. Polym. Sci.* **1998**, *68*, 503-508.
(35) McLean, R. S.; Doyle, M.; Sauer, B. B. *Macromolecules* **2000**, *33*, 6541-6550.

(36) Xie, X.; Kwon, O.; Zhu, D.; Nguyen, T. V.; Lin, G. *J. Phys. Chem. B* **2007**, *111*, 6134-6140.
(37) Bussian, D. A.; O'Dea, J. R.; Metiu, H.; Buratto, S. K. *Nano Lett.* **2007**, *7*, 227-232.
(38) Tamayo, J.; Garca, R. *Langmuir* **1996**, *12*, 4430-4435.
(39) Tamayo, J.; Garcia, R. *Appl. Phys. Lett.* **1997**, *71*, 2394-2396.
(40) Tamayo, J.; Garcia, R. *Appl. Phys. Lett.* **1998**, *73*, 2926-2928.
(41) James, P. J.; Antognozzi, M.; Tamayo, J.; McMaster, J.; Newton, J. M.; Miles, M. J. *Langmuir* **2001**, *17*, 349-360.
(42) Gierke, T. D.; Munn, G. E.; Wilson, F. C. *J. Polym. Sci. Polym. Phys. Ed.* **1981**, *19*, 1687-1704.

# CHAPTER IX

# COUNTERION MOTIONS AND THERMAL ORDERING EFFECTS IN PERFLUOROSULFONATE IONOMERS PROBED BY SOLID-STATE NMR

*This chapter is reformatted from [Park, Jong Keun; Moore, Robert B.; Sungsool Wi, "Counterion Motions and Thermal Ordering Effects in Perfluorosulfonate Ionomers Probed by Solid-State NMR", *Polymer* **2009**, 50, 5720-5727].

## A. Introduction

With greater system efficiencies and environmental benefits, proton-exchange membrane electrolyte fuel cells (PEMFCs) have become an attractive system as an alternative to nonrenewable, traditional energy sources. Currently, perfluorosulfonate ionomers (PFSIs), particularly Nafion®, are the benchmark proton exchange membranes due to their unique morphology, chemical stability, and excellent transport properties.[1] Nafion®, having the chemical structure shown below, is a copolymer of tetrafluoroethylene and generally less than 15 mol % of perfluorovinylether units terminated with sulfonic acid functionalities.

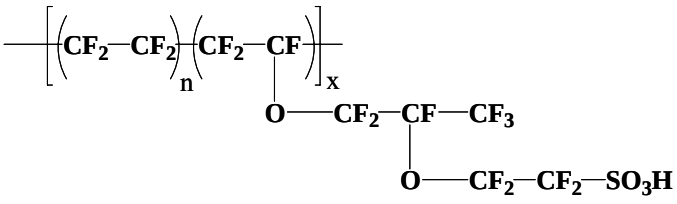


**Figure IX-1**. Chemical structure of Nafion®

With a sufficient length of polytetrafluoroethylene (PTFE) segments between side chains, Nafion® is capable of organizing into crystalline domains that are generally less than ca. 10 wt % in 1100 equivalent weight of Nafion® (EW, the grams of dry polymer per equivalent of sulfonic

acid units).[1] Greater efforts, however, have been given to the unique nanophase-separated morphology observed upon aggregation of the polar, ionic side chains within the matrix of hydrophobic PTFE. These ionic clusters, and specifically their shape, spatial distribution, and connectivity, precisely define the supramolecular organization and function of this technologically important material as an ionic conductor.

Recognizing the complex nature of the Nafion® morphology, numerous structural models have been proposed based mostly on small angle X-ray and neutron scattering studies. Hsu and Gierke suggested swollen inverse micelles of roughly spherical geometry that are connected by nanoscale hydrophilic channels concurrent with the unique transport properties exhibited by PFSIs.[2] In addition to the early work of Hsu and Gierke, the most common ones include the core-shell model by Fujimura et al.[3], the local order model by Dreyfus et al.[4], the rod-like aggregate model by Rubatat and coworkers[5], the fringed-micelle model by Kim et al.[6], and most recently, parallel cylindrical water channel model by Schmidt-Rohr[7]. Although each model differs significantly in the shape and order of ionic domains, they all recognize the presence of ionic aggregates that are dispersed throughout the PTFE matrix.

It has been shown that ionic aggregates in PFSIs can act as multifunctional physical cross-links that significantly restrict chain mobility.[8,9] However, the motional constraint imposed by ionic clustering in PFSIs may be weakened by hydration processes and/or control of electrostatic interactions. Page et al. showed that the strength of Columbic interactions within the ionic domain can effectively be manipulated by varying the size of neutralizing counterions, such as $Na^+$, tetramethylammonium ($TMA^+$), tetraethylammonium ($TEA^+$), tetrapropylammonium ($TPA^+$), and tetrabutylammonium ($TBA^+$) ions.[10-12] Dynamic mechanical analysis (DMA), and small angle X-ray scattering (SAXS) analysis have revealed that

tetraalkylammonium ion neutralized PFSIs exhibit two distinct thermo-mechanical relaxations in the range of 70–300 ˚C that have been assigned as the β- and α-relaxations.[1,10] The α-relaxation temperatures of $TMA^+$–, $TEA^+$–, $TPA^+$– and $TBA^+$–PFSIs are 240 ˚C, 160 ˚C, 130 ˚C, and 100 ˚C, respectively. On the other hand, the β-relaxation temperatures of $TMA^+$–, $TEA^+$–, $TPA^+$–, and $TBA^+$–PFSI membranes are 130 ˚C, 111 ˚C, 100 ˚C, and 73 ˚C, respectively.[10] Compared to the sulfonic acid form of the polymer, small $TMA^+$ ions cause dramatic increases in both the α and β relaxation temperatures due to the great strength of the electrostatic interactions between the ion-pairs, while larger $TPA^+$ or $TBA^+$ counterions cause the α- and β-relaxations to systematically shift to significantly lower temperatures.[10,11,13] As the size of the counterion increases, the larger counterions significantly weaken the strength of the electrostatic interactions and the bulky, organic counterions can effectively plasticize the ionomer, which in turn yields lower α- and β-relaxation temperatures.[10-12] More specifically, the low temperature β-relaxation, which is assigned to the genuine $T_g$ of Nafion®, is associated with the onset of thermally activated chain motions (primarily the backbone motions), within the framework of an electrostatically croslinked network.[10] However, the onset of long-range mobility of both the main- and side-chains facilitated by a significant destabilization of the electrostatic network has been assigned to motions associated with the high temperature α-relaxation.[10]

To gain a fundamental insight into the thermomechanical behavior, ionic motions, and morphological transformations within these complex materials, solid state NMR (ssNMR) sprctroscopy is recognized as a powerful method for probing site-specific, molecular dynamics. SsNMR spectroscopy has been widely used for investigating the characteristics of segmental movements of the chain and side-groups in polymers by monitoring the time-dependent, anisotropic NMR frequencies of specific nuclear sites of interest.[14-19] Variable temperature $^{19}F$

chemical shift anisotropy (CSA) measurements have been used to determine the degree of crystallinity and investigating macromolecular motions in PTFE-like backbone.[20] $^{19}F$ and $^{13}C$ CSAs, as well as $^{19}F$-$^{13}C$ dipolar couplings, have been utilized to probe fast, large-amplitude dynamics of both backbone and side-chain segments in Nafion® at ambient temperature.[21] On the basis of the observed counterion effects in Nafion®, Page and coworkers employed $^{19}F$ ssNMR spectroscopy to explore the influence of electrostatic interactions on the local and global chain dynamics in Nafion® samples that are neutralized with $Na^+$, $TMA^+$, and $TBA^+$.[12]

A fundamental understanding of the link between the morphology of PFSIs and their thermomechanical properties can be obtained by investigating the structural organization and molecular motions of the ionic species within the ionic aggregates as a function of counterion size and temperature. In this study, the variable temperature $^1H$ spin-lattice relaxation time, $T_1$, of tetraalkylammonium ions within the ionic domains of PFSIs is measured over temperatures ranging from 24 to 190 $^oC$. Because the spin-lattice relaxation time is governed by high-frequency motions in the order of tens or hundreds of MHz (usually associated with local motions of atoms or molecular segments near the nucleus under investigation [22]), the information obtained from this study will help to better understand the local-order origins of the thermomechanical relaxations of tetraalkylammonium-form PFSIs. To further explore the effect of ion size, electrostatic interactions, and ion-pair packing in the aggregates on the counterion mobility, we have also employed variable temperature static $^{13}C$ ssNMR spectroscopy to probe counterion dynamics on the molecular-level.

## B. Experimental

***Materials***: The perfluorosulfonate ionomer, Nafion® 117CS membranes (1100g / equivalent, 7 mil thickness) were purchased from E.I. Dupont de Nemours & Co. and cleaned by refluxing in 8M nitric acid for 2 hr, and then in deionized (DI) water for 1 hr. These PFSI samples were then completely neutralized to contain tetramethylammonium ($TMA^+$), tetraethylammonium ($TEA^+$), tetrapropylammonium ($TPA^+$), and tetrabutylammonium ($TBA^+$) counterions by soaking the $H^+$-form membranes in excess (ca. 5×) methanolic or aqueous solution of the appropriate alkylammonium hydroxide. The neutralized membranes were thoroughly rinsed of excess alkylammonium hydroxide and dried in a vacuum oven at 70 °C overnight.

***NMR Spectroscopy***: The NMR experiments were performed on a Bruker Avance II-300 wide-bore NMR spectrometer (7.05 T) operating at Larmor frequencies of 75.47 MHz for $^{13}C$ and 300.13 MHz for $^{1}H$ nuclei. Static $^{13}C$ ssNMR spectra of tetraalkylammonium ions bound in the ionic domains of PFSI membranes were acquired by employing a cross-polarization (CP) sequence shown in Figure IX-2a. The NMR signal averaging for $^{13}C$ spectral acquisition was achieved by co-adding 4096 transients with a 5s acquisition delay time. An inversion recovery method[23], implemented with a static CP-based $^{13}C$-detection scheme (Figure IX-2b), was incorporated to measure the $T_1$ relaxation times of the methylene or methyl protons adjacent to the nitrogen atoms of the alkylammonium ions. The proton $T_1$-relaxation of tetraalkylammonium ions was detected indirectly via the $^{13}C$ signals, incorporating a short one-bond $^{1}H$–$^{13}C$ Lee–Goldburg cross-polarization (LGCP)[24,25] (~ 150 μs) transfer as shown in Figure IX-2b. Proton equilibrium magnetizations are inverted by a 180° pulse, followed by a variable delay time, τ, and consecutively detected by a 90° read pulse. This read pulse was

combined with a LGCP scheme for signal encoding along the directly bonded $^{13}C$ sites. The NMR signal averaging for $^{1}H$ $T_1$ measurement was achieved by co-adding 4096 transients with a 10 s acquisition delay time. The sample temperature in the NMR probe was regulated by an air flow, which was under the control of a BVT-3000 digital temperature control unit of a Bruker console and a BCU-X precooling and stabilization accessory. The sample temperatures used in our NMR experiments were 24 ˚C, 40 ˚C, 80 ˚C, 120 ˚C, 160 ˚C, and 190 ˚C for acquiring static $^{13}C$ NMR spectra, and 24 ˚C, 120 ˚C, and 190 ˚C for measuring the $^{1}H$ $T_1$ relaxations. $^{1}H$ $\pi/2$ and $\pi$ pulse lengths were 4.5 and 9 μs, respectively. The SPINAL-64 decoupling sequence [26] at 62.5 kHz power was used for proton decoupling during $^{13}C$ signal detection.

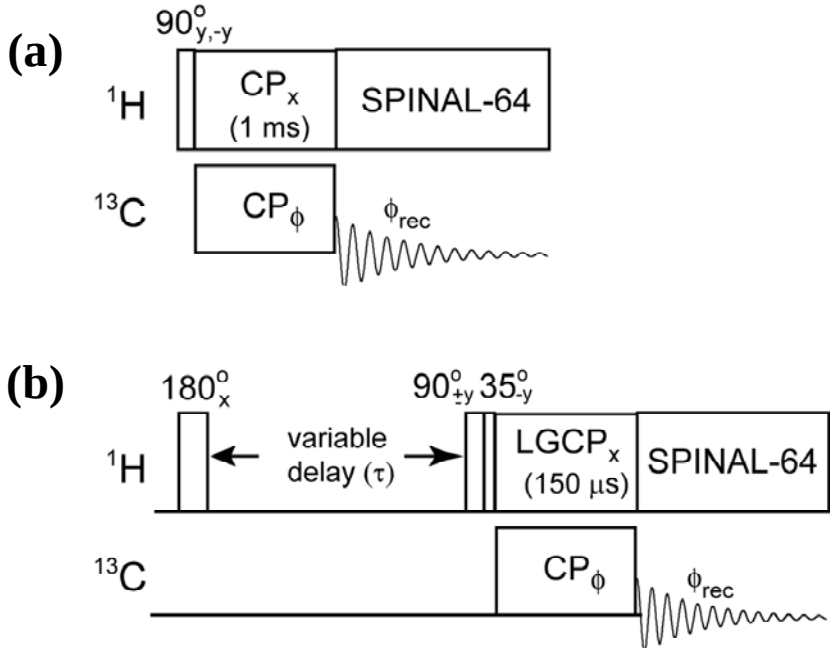


**Figure IX-2**. The pulse sequences used in our experiments for obtaining $^{13}C$ static CP spectra (a) and $^{1}H$ $T_1$s (b). A CP mixing time of 1 ms was applied for obtaining $^{1}H$-$^{13}C$ polarization transfer with a 2 s acquisition delay (A). A variable delay time $\tau$ following the initial 180 degree pulse was allowed for measuring $T_1$ of protons in alkylammonium ions, which are monitored indirectly via the $^{13}C$ signals of the directly bonded $^{13}C$ nuclei, obtained using a short (~ 150 μs) LGCP scheme for selective detection (B). The pulse phase $\phi$ and the signal acquisition phase $\phi_{rec}$ in both sequences are: $\phi$ = x, x, y, y, -x, -x, -y, -y; $\phi_{rec}$ = x, -x, y, -y, -x, x, -y, y.

***Small-angle X-ray Scattering (SAXS)***: Synchrotron small-angle X-ray scattering (SAXS) experiments were performed at Station 4C1 of the Pohang Accelerator Laboratory (PAL) (Pohang, Korea). The incident X-ray beam was tuned to a wavelength of 1.30 Å and the sample-to-detector distance was 1075 mm. The two dimensional scattering images were recorded using a Mar CCD camera with 30 sec exposure time. The relationship between pixel and the momentum transfer vector $q$ was determined by calibrating the scattering data with a silver behenate standard. All scattering intensities were corrected for transmission, incident beam flux, and background scatter due to air and Kapton windows. The $TMA^+$ and $TBA^+$-form membranes were annealed at 150 and 200 $^oC$ for 10 min and then cooled to room temperature prior to SAXS experiments.

***Dynamic Solid-state NMR lineshape Simulation***: For understanding the dynamic nature of variable temperature, static $^{13}C$ ssNMR spectra, a semiclassical exchange formalism [27] was incorporated to simulate the spectral characteristics associated with motons of the tetraalkylammonium ions. Anisotropic lineshapes of $^{13}C$ sites in $TMA^+$, $TEA^+$, $TPA^+$, and $TBA^+$ ions, which possess a tetrahedral local symmetry at the center of the molecule, that potentially undergo local $C_2$, $C_3$, or tetrahedral jumps or tumbling motions[28] have been simulated. An expression describing the $^{13}C$ CSA and $^{13}C$-$^{14}N$ dipolar interactions required for the calculation of $^{13}C$ ssNMR frequencies [29] of our sample system is given by:

$$\omega(m_s) = [\delta_{iso} + R_{2,0}^{CSA}]\omega_0 + 2R_{2,0}^{D} m_s, \qquad \textbf{Eq IX-1}$$

where $\omega_0$ is the Larmor frequency of $^{13}C$, $\delta_{iso}$ is the orientation-independent isotropic $^{13}C$ chemical shift, $R_{2,0}^{CSA}$ and $R_{2,0}^{D}$ the orientation-dependent CSA and dipolar tensors, respectively, expressed in the spherical tensor representation, and $m_s$ the nuclear spin state of $^{14}N$ which is 1 ,

0, or -1. Eq IX-1 can be used for calculating the NMR frequencies and the effect of chemical exchange, provided that the spatial components of the $^{13}C$ CSA and $^{13}C$-$^{14}N$ dipolar tensors of all the interconverting sites are expressed simultaneously in a common reference frame. The spatial part of the tensors, $R^{\lambda}_{2,0}$ ($\lambda$ = *CSA* or *D*), defined in the laboratory frame (LAB) can be related to the corresponding tensor elements defined in the principal axes frame (PAF), $\rho^{\lambda}_{2,\pm m}$ $(m = \text{-}2, \text{-}1, .., 2)$, via a common molecular frame (MOF), $M^{\lambda}_{2,\pm n}$ $(n = \text{-}2, \text{-}1, .., 2)$, according to

$$\rho^{\lambda}_{2,\pm m}(PAF) \xrightarrow{(\alpha,\beta,\gamma)} M^{\lambda}_{2,\pm n}(MOF) \xrightarrow{(\phi,\theta,0^{\circ})} R^{\lambda}_{2,0}(LAB) \qquad \textbf{Eq IX-2}$$

where $(\alpha,\beta,\gamma)$ denotes Euler angles specifying the tensor transformation from the PAF to the MOF. In addition, $(\phi, \theta, 0^{\circ})$ is a common, powder angle set specifying a transformation from the MOF to the LAB, which must be integrated over the solid sphere in order to sample the random orientations of sample molecules with respect to the external magnetic field $B_0$. The actual transformation in Eq IX-2 can be carried out in terms of the second-rank Wigner rotation matrices according to

$$R^{\lambda}_{2,0} = \sum_{n=-2}^{2} d^{2}_{n,0}(\theta) \sum_{m=-2}^{2} e^{-im\alpha} d^{2}_{m,n}(\beta) e^{-in(\gamma+\phi)} \rho^{\lambda}_{2,m} \qquad \textbf{Eq IX-3}$$

where, the CSA tensor elements are defined by $\rho^{CSA}_{2,0} = \delta_{csa}$, $\rho^{CSA}_{2,\pm 1} = 0$, and $\rho^{CSA}_{2,\pm 2} = \delta_{csa}\eta/\sqrt{6}$, and the dipolar tensor elements by $\rho^{D}_{2,0} = D_{zz}$, $\rho^{D}_{2,\pm 1} = 0$, and $\rho^{D}_{2,\pm 2} = 0$, respectively, in the PAF. The magnitude of the CSA tensor elements in the PAF is defined by $\delta_{csa} = \delta_{zz} - \delta_{iso}$ and $\eta = (\delta_{yy} - \delta_{xx})/\delta_{csa}$, where $|\delta_{zz} - \delta_{iso}| \geq |\delta_{xx} - \delta_{iso}| \geq |\delta_{yy} - \delta_{iso}|$ and $\delta_{iso} = (\delta_{xx} + \delta_{yy} + \delta_{zz})/3$. The magnitude of the dipolar vector in the PAF, $D_{zz}$, is provided by $(\mu_0\hbar/4\pi)(\gamma_i\gamma_j/r^3_{ij})$, where $r_{ij}$ designates the interatomic distance between atoms *i* and *j* whose magnetogyric ratios are given

by $\gamma_i$ and $\gamma_j$, respectively, and $\mu_0$ is the permeability constant ($4\pi \times 10^{-7}$ kg m $s^{-2}$ $A^{-2}$). For a directly bonded $^{13}C$-$^{14}N$ site in a tetraalkylammonium ion, the strength of a $^{13}C$-$^{14}N$ dipolar coupling is $D_{zz} \approx 700$ Hz ($r$(C-N) ≈ 1.4 Å). In this simulation, we assumed a coinciding $^{13}C$-$^{14}N$ dipolar vector with respect to the $^{13}C$ CSA tensor for simplicity ($\alpha = \beta = \gamma = 0^\circ$).

Multiple exchanging sites will thus be defined by multiple $(\alpha_j, \beta_j, \gamma_j)_{1 \le j \le N}$ sets of Euler angles. For sites undergoing $C_2$, $C_3$ or tetrahedral jumps, angle sets needed for achieving a full exchange averaging are: [29,30]

$$(\alpha,\beta,\gamma) = \begin{cases} (0^\circ, \beta, 0^\circ) \\ (0^\circ, \beta, \mathbf{18}0^\circ) \end{cases}, \text{ ($\beta$ is an arbitrary angle)} \qquad \textbf{Eq IX-4}$$

for $C_2$,

$$(\alpha,\beta,\gamma) = \begin{cases} (0^\circ, 125.3^\circ, 0^\circ) \\ (120^\circ, 125.3^\circ, 0^\circ) \\ (240^\circ, 125.3^\circ, 0^\circ) \end{cases} \qquad \textbf{Eq IX-5}$$

for $C_3$, and

$$(\alpha,\beta,\gamma) = \begin{cases} (315^\circ, 54.7^\circ, 240^\circ) \\ (225^\circ, 125.3^\circ, 150^\circ) \\ (135^\circ, 54.7^\circ, 150^\circ) \\ (45^\circ, 125.3^\circ, 240^\circ) \end{cases} \qquad \textbf{Eq IX-6}$$

for tetrahedral jumping, respectively.

Stochastic jumps of molecules or molecular segments occurring between these sites result in exchanging local fields of nuclear sites. This dynamic effect can be admixed into the NMR spectral calculation of sites, which is simply provided by Eq IX-1 when the motion among these sites is negligible, via kinetic modifications of Bloch's equation [31] as shown below. The

complete magnetization vector in the equation of motion for describing jumping motions among chemically and/or magnetically inequivalent sites can be written as: [27,29,30,32,33]

$$\frac{d}{dt}M(t) = (i\varpi + \bar{\pi})M(t) \qquad \textbf{Eq IX-7}$$

Here, $\bar{\pi}$ defines a matrix describing the topology and the rates (κs) of a jumping process, $\varpi$ is a diagonal matrix with elements $\omega_j(m_s) + i/T_{2j}$, where, $\omega_j(m_s)$ is the classical precessional frequency of each exchanging site provided in Eq IX-1, and $T_{2j}$ is the respective transverse relaxation time. Eq IX-7 can be formally solved as:

$$M(t) = [U \exp(\lambda t) U^{-1}] M_{eq} \qquad \textbf{Eq IX-8}$$

where $M_{eq}$ is a column vector describing the equilibrium population of each site at $t$ = 0, and $U$ and λ are the eigenvectors and eigenvalues of the $(i\varpi + \bar{\pi})$ matrix, respectively. Addition of $M(t)$s over all $m_s$ values and over all the powder orientations followed by Fourier transform provide a motionally averaged exchange spectrum at a particular topology and jumping rate.

## C. Results and Discussion

Figure IX-3 compares variable temperature, $^{13}C$ static CP ssNMR spectra of tetraalkylammonium ions in $TMA^+$– and $TEA^+$–form PFSIs measured at 24 ˚C, 40 ˚C, 80 ˚C, 120 ˚C, 160 ˚C, and 190 ˚C. The spectral lineshapes of these spectra provide a means to monitor the motional dynamics of these ions within the ionic domains, which are strongly influenced by the packing order and the strength of ionic interactions. In these spectra, the $^{13}C$ linewidths of the methyl and methylene groups of $TMA^+$ and $TEA^+$ ions show remarkably narrower linewidths

than that of $TPA^+$ or $TBA^+$ ions (vide infra) throughout the temperatures investigated. The smaller magnitude of the observed chemical shift anisotropy (CSA) might be correlated to the stronger ordering of $TMA^+$ and $TEA^+$ ions in the ionic domains because the smaller $TMA^+$ and $TEA^+$ ions make stronger Columbic interactions with sulfonyl groups than those bulkier $TPA^+$ and $TBA^+$ ions in the ionic domains. This interpretation matches well with the observed melting points from our differential scanning calorimetry (DSC) experiments — the melting temperatures of $TMA^+$-, $TEA^+$-, $TPA^+$-, and $TBA^+$-PFSI ionomers are 253 $^oC$, 187 $^oC$, 123 $^oC$, and 66 $^oC$, respectively (data are not shown). The remarkably higher melting temperatures observed in $TMA^+$- and $TEA^+$-PFSIs are probably due to the existence of local crystalline-like ordering of $TMA^+$ and $TEA^+$ ions in the ionic domains. Interestingly, the spectral linewidths of the spectra of $TMA^+$ and $TEA^+$ ions measured at 40 ˚C, 80 ˚C, and 120 ˚C are somewhat broader than those measured at room temperature or temperatures above 120 ˚C. This slight peak broadening effect is not understood at this point. It should be pointed out that this phenomenon occurred at temperatures that are well below the $T_g$ of main chain of polymers, which are 130 ˚C and 110 ˚C for the $TMA^+$– and $TEA^+$–PFSIs, respectively.

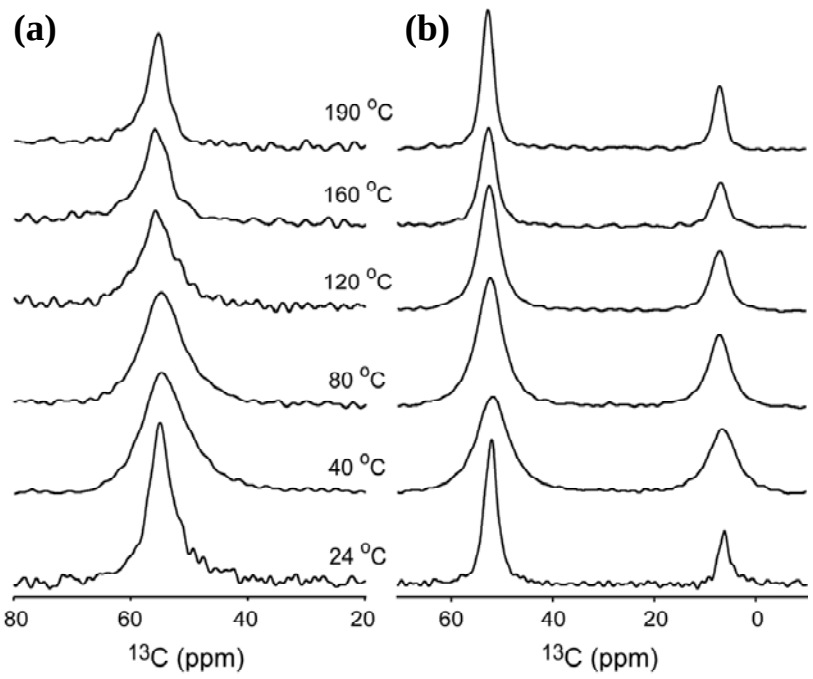


**Figure IX-3**. Experimental static $^{13}C$ CP NMR spectra of $TMA^+$–PFSI (a) and $TEA^+$–form (b) PFSI membranes over the temperature range of 24 ˚C – 190 ˚C. Note the slight line broadening effect around 40 ˚C – 80 ˚C which can be related to a thermal disordering phenomenon.

Figure IX-4 compares static $^{13}C$ CP NMR spectra of $TPA^+$ and $TBA^+$ ions in $TPA^+$– and $TBA^+$–PFSIs measured at 24 ˚C, 40 ˚C, 80 ˚C, 120 ˚C, 160 ˚C, and 190 ˚C. At temperatures in the range of 24 to 120 ˚C, the $^{13}C$ spectra of $TPA^+$ and $TBA^+$ ions exhibit broader linewidths than those of $TMA^+$ and $TEA^+$ ions, resulting in unresolved $^{13}C$ peaks among various carbon sites, except for the methylene groups that are adjacent to the nitrogen atoms. The increased CSAs of the $^{13}C$ sites in $TPA^+$ and $TBA^+$ ions might be resulted from the decreased packing order of these bulkier ions in ionic domains because of their less tightly bound nature to sulfonyl groups compared to the smaller $TMA^+$ and $TEA^+$ ions, and/or the less favorable segmental motions of alkyl arms of these ions due to the increased steric hindrance in the ionic domains. Interestingly, the $^{13}C$ spectra of $TPA^+$ and $TBA^+$ ions acquired at higher temperatures, 160 and 190 ˚C, demonstrate motionally averaged sharp peaks, while providing resolved peaks of all carbon sites in $TPA^+$ and $TBA^+$ ions in the spectra. This line narrowing effect is probably resulted from the

onset of overall molecular tumbling/jumping motions of $TPA^+$ and $TBA^+$ ions under high temperatures above the α-relaxation temperature. After the onset of molecular tumbling motions above the α-relaxation temperature (the α-relaxation temperatures of $TPA^+$– and $TBA^+$–PFSIs are 130 ˚C and 100 ˚C, respectively), $TPA^+$ and $TBA^+$ ions become more independent from the Columbic restraint of the sulfonyl groups of PFSIs because the onset of the thermal tumbling motions may remarkably counterbalance the force field of the electrostatic interactions — the bulkier $TPA^+$ or $TBA^+$ ions have considerably weaker electrostatic interactions with sulfonyl groups than that of either $TMA^+$ or $TEA^+$ ions. As we have seen in Figure IX-3, the $TMA^+$– and $TEA^+$ ions do not demonstrate this behavior in the same temperature range probably because $TMA^+$ and $TEA^+$ ions are bound more tightly to sulfonyl groups, resulting in higher α-relaxation temperatures. It must be noticed that the α-relaxation temperature of the $TMA^+$–PFSI system is 230 ˚C which is even beyond the test range of our current temperature setting. Because the β-relaxation temperatures of both $TPA^+$– and $TBA^+$–PFSIs are lower than that of the $TMA^+$– and $TEA^+$–PFSIs, a similar type of peak broadening effect would be observed in $TPA^+$– and $TBA^+$–PFSI systems at temperatures near or lower than 40 ˚C or 60 ˚C. Although the linewidth of $TPA^+$ ions measured at 40 ˚C is somewhat broader than the one measured at 24 ˚C, the step of our temperature variation might be too big to observe this effect for the $TBA^+$–PFSI system.

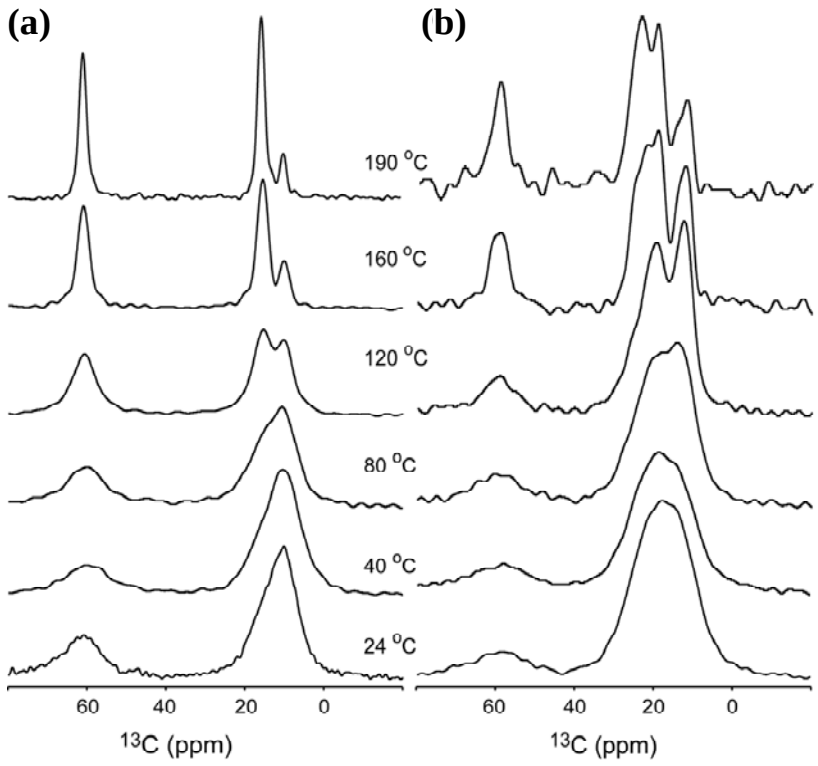


**Figure IX-4**. Experimental static $^{13}C$ CP NMR spectra of $TPA^+$–PFSI (A) and $TBA^+$–PFSI (B) membranes over the temperature range of 24 ˚C–190 ˚C. A motionally averaged line-narrowing effect observed in these sample systems can be related to the tetrahedral jump/hop motions of the tetraalkyl ammonium ions at elevated temperatures, particularly at 190 ˚C which is well above the α-relaxation temperatures of these sample systems.

To understand the fundamental characteristics of the onset of the molecular tumbling motions of tetraalkylammonium ions, we carried out theoretical simulations of $C_2$, $C_3$, and tetrahedral jumping motions that a tetraaalkylammonium ion can potentially undergo with a variable jumping rate according to the procedure described in the theoretical section. Figure IX-5 shows the calculated lineshapes of a $^{13}C$ site, possessing a CSA tensor ($\delta_{CSA}$ = 10 ppm; $\eta$ = 0.3) and a $^{13}C$-$^{14}N$ dipolar coupling vector (d($^{13}C$-$^{14}N$) = 700 Hz, assuming coinciding dipolar and CSA tensor orientations), undergoing $C_2$ (a and d), $C_3$ (b and e), and tetrahedral (c and f) jumps with various jumping rates, with (d, e and f) and without (a, b and c) considering $^{13}C$-$^{14}N$ dipolar coupling strength. As demonstrated in Figure IX-5, regardless whether the $^{13}C$-$^{14}N$ dipolar

coupling is considered or not, only the tetrahedral jumping mode is capable of providing a motionally averaged, sharp line at a rate of $\kappa$ = 1000 Hz or above. As compared to the spectra shown in Figure IX-4, this prediction matches reasonably well with the experimental spectra of $TPA^+$ and $TBA^+$ ions observed at 160 and 190 ˚C, regardless whether a carbon site is adjacent to or away from the nitrogen atom. Based on these observations, it can be inferred that $TPA^+$ and $TBA^+$ ions exhibit random, rapid tetrahedral jumping/ tumbling motions at a temperature well above the α-relaxation temperature, at which tetraalkylammonium ions in the ionic domains effectively overcome the constraints of the ionic interactions. Unlike the simulated CSA/dipolar lineshapes that are obtained assuming a sample state of microcrystalline powders, the experimental spectra measured on the actual samples provide ill-defined random powder lineshapes because of the amorphous nature of the sample's morphology. Page and coworkers have reported that tetraalkylammonium ions in PFSIs make translational hopping motions at an elevated temperature above the α-relaxation temperature based on the previous SAXS analysis.[10] In ssNMR spectra the observed line-narrowing effect evidences rotational tumbling/jumping motions of tetraalkylammonium ions. These rotational motions evidenced in ssNMR spectra provide complementary information to the SAXS data, which provide information of translational hopping motions of molecules indirectly.

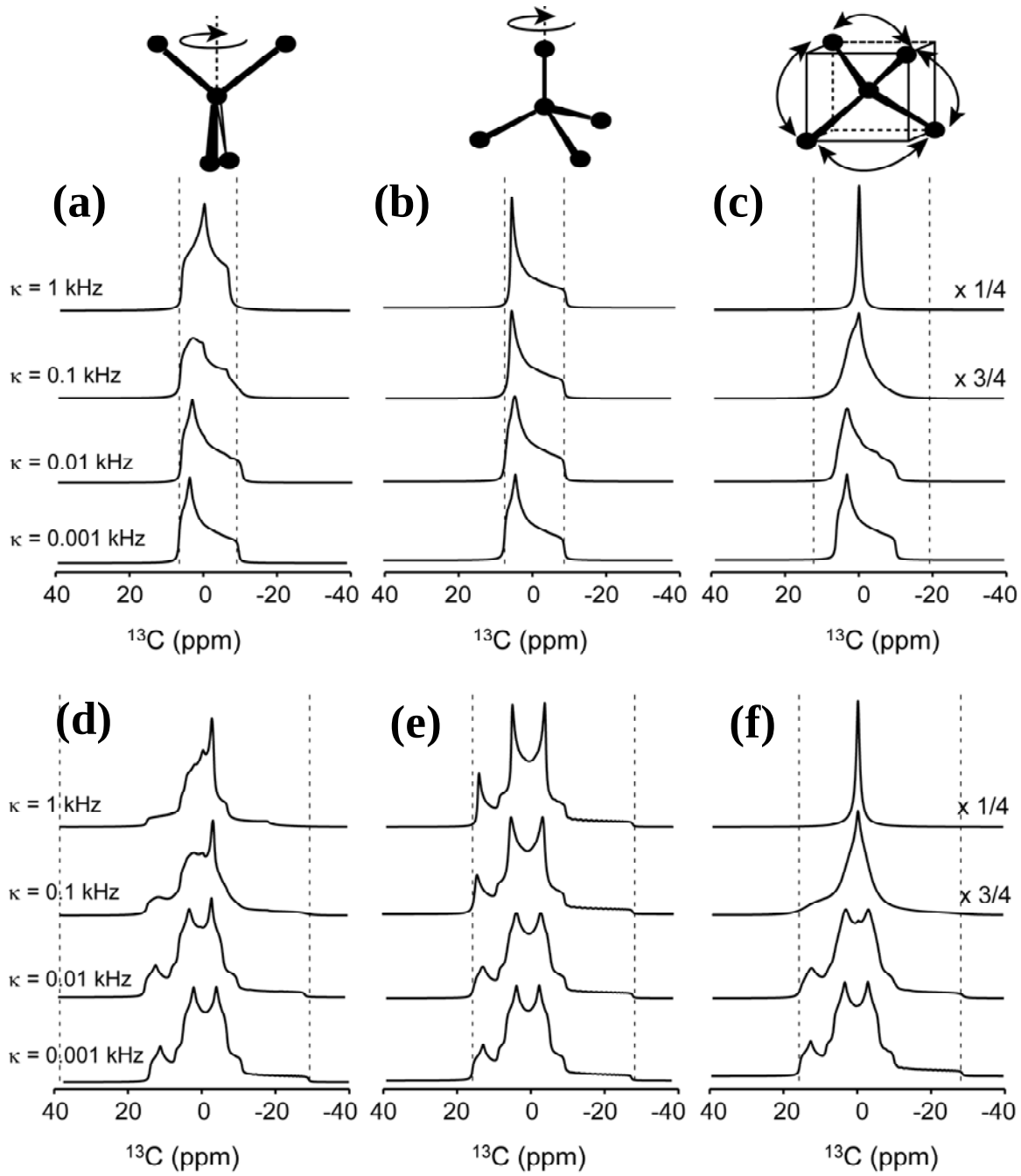


**Figure IX-5**. Simulated CSA powder lineshapes of a $^{13}C$ site, with (e-f) and without (a-c) considering $^{13}C$-$^{14}N$ dipolar interaction, undergoing random $C_2$ (a and d), $C_3$ (b and e), and tetrahedral jumps/hops (c and f) with variable jump/hop rates of $\kappa$ = 1, 0.1, 0.01, and 0.001 kHz. The CSA tensor parameters considered in the simulations are $\delta$ = 10 ppm and $\eta$ = 0.3. A 700 Hz of the coupling strength for the directly bonded $^{13}C$-$^{14}N$ dipolar pair was considered additionally in d-f. The Larmor frequency of $^{13}C$ is 75 MHz. While a site undergoing a $C_2$ or $C_3$ rotation jump/hop motion results in a motionally averaged tensor with reduced linewidth (a, b, d, and e), a $^{13}C$ site undergoing a fast tetrahedral jump/hop motion provides a motionally averaged isotropic peak (c and f).

Figure IX-6 shows the $^1H$ $T_1$ relaxation data of methylene or methyl groups that are adjacent to the nitrogen atoms of tetraalkylammonium ions in $TMA^+$- (a), $TEA^+$- (b), $TPA^+$- (c), and $TBA^+$-form PFSIs (d) at 24 ˚C, 120 ˚C, and 190 ˚C. When the observed data are correlated to the variable delay time, $\tau$, in a plot according to a formula $\ln[1-M(\tau)] = \ln 2 - \tau/\mathbf{T_1}$, where $M(\tau)$ is the measured magnetization at a variable delay time $\tau$, a straight line yielding a slope and an intercept of $-1/T_1$ and ln 2, respectively, is expected if a $T_1$ relaxation is governed by a single exponential function of time $e^{-\tau/T_1}$. $TPA^+$ (c) and $TBA^+$ (d) ions provide shorter $T_1$ times as the temperature increases. This means that ions constrained in ionic domains of ionomeric matrix undergo faster molecular collisions and therefore experience more frequent energy exchange with lattice at higher temperatures (shorter correlation times). Thus, it is natural that tetraalkylammonium ions with increased thermal energy lose their rf-induced energy states faster to the surrounding lattice, resulting in a decrease in $T_1$.[33] Interestingly, however, the methyl protons in $TMA^+$ of $TMA^+$-form PFSI (a) show the opposite behavior; that its $T_1$ relaxation time increases as the temperature increases over the range 24-190 ˚C. In general, warming the sample makes the fluctuations of molecules or molecular skeletons faster, reducing the correlation time. One possibility is that the observed $T_1$ behavior would simply correspond to the case involving an opposite regime with a short correlation time, in which $T_1$ increases as temperature increases—a common $T_1$ behavior of small organic molecules dissolved in a non-viscous solvent.[33] But it is very difficult to postulate the existence of a non-viscous, solution-like environment around $TMA^+$ ions that are bound in the ionic domains of solid state PFSI ionomers. Moreover, a small $TMA^+$ ion binds more tightly to a sulfonate group in the ionic domain of PFSI than those bulkier $TEA^+$, $TPA^+$, or $TBA^+$ ions. One plausible explanation, which receives an indirect support from a small angle X-ray scattering (SAXS) experiment that will be discussed

below, is that the observed trend in $T_1$ evidences a thermally induced molecular ordering effect of $TMA^+$ ions in the ionic domains. Individual ions or smaller ionic domains of $TMA^+$s scattered around polymer matrix under low temperature can conglomerate into a bigger ionic domain by thermal annealing because smaller $TMA^+$ ions which interact strongly with sulfonyl groups can easily be accommodated into a well packed array of $TMA^+$ ions in an ionic domain. Under this situation, the portion of $TMA^+$ ions colliding with neighboring polymer matrix or segments of molecules other than $TMA^+$ ions themselves decreases as the size of ionic array increases, therefore, $TMA^+$ ions can maintain their rf-induced energy identities longer, resulting in an increase in $T_1$ time.

The $TEA^+$-form PFSI system (b) demonstrates an intermediate response between these two extreme cases discussed above. The $T_1$ curve of $TEA^+$-PFSI system shows a clear deviation from a straight line at each temperature — a probable bi-exponential $T_1$ decay behavior. Currently, this behavior is not clearly understood, but perhaps the two opposite tendencies of having faster molecular tumbling and thermal ordering at higher temperature might contribute simultaneously. For the best-fit curve fitting of a $T_1$ relaxation time we have used only the initial trend in each curve. Table IX-1 summarizes $^1H$ $T_1$ relaxation times of alkylammonium ions of $TMA^+$–, $TEA^+$–, $TPA^+$–, and $TBA^+$–PFSI ionomers measured at 24 ˚C, 120 ˚C, and 190 ˚C.

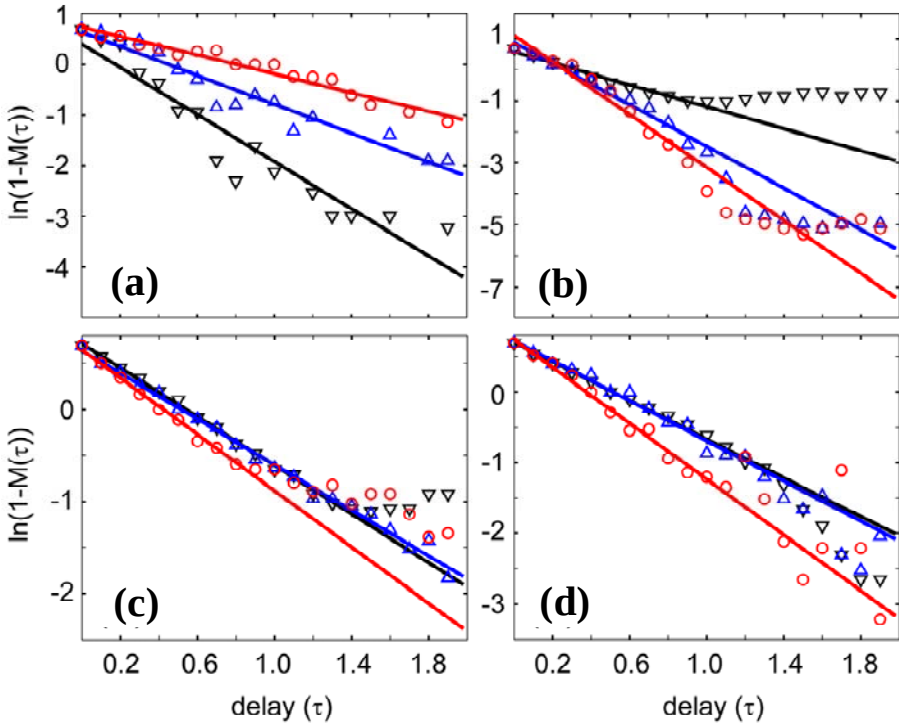


**Figure IX-6**. Temperature dependence of $T_1$ relaxation times measured on the methylene or methyl protons, which are closest to the nitrogen atom, of tetraalkylammonium ions bound to PFSI ionomers. Experimentally obtained (symbols) and best-fit (lines) $^1$H $T_1$ relaxation data of $TMA^+$– (a), $TEA^+$– (b), $TPA^+$– (c), and $TBA^+$–form (d) PFSIs are shown over variable temperatures. Symbols represent experimental data at 24 ˚C (black circle), 120 ˚C (blue triangle), and 190 ˚C (inverted red triangle), respectively, and lines represent the best-fit curves at 24 ˚C (black lines), 120 ˚C (blue lines), and 190 ˚C (red lines), respectively. A formula $\ln[1-M(\tau)] = \ln 2 - \tau/T_1$, where $\tau$ and $M(\tau)$ are a delay time and the longitudinal magnetization measured at $\tau$, respectively, is used for the curve fitting. From the slope of the curve we obtain $-1/T_1$. We considered a portion in the graph demonstrating an initial slope, experimental data with delay times less than 1.0 s, for the curve fitting when a graph exhibited multi-exponential $T_1$ behavior.

**Table IX-1**. $^1$H $T_1$ relaxation times of tetraalkylammonium ions[a] in PFSI ionomers neutralized by tetraalkylammonium ions.

| *Temperature* | *$TMA^{+b}$–PFSI* | *$TEA^+$–PFSI* | *$TPA^+$–PFSI* | *$TBA^+$–PFSI* |
|---|---|---|---|---|
| 24 ˚C | 0.43 s | 0.57 s | 0.76 s | 0.73 s |
| 120 ˚C | 0.70 s | 0.30 s | 0.81 s | 0.70 s |
| 190 ˚C | 1.08 s | 0.23 s | 0.65 s | 0.51 s |

[a] $T_1$ relaxation times of methylene or methyl groups that are directly bonded to nitrogen are recorded although other protons also exhibited $T_1$ values in the similar range, probably due to an exchange process established by $^1$H-$^1$H spin diffusion

In addition to ssNMR experiments, we have performed SAXS experiments on $TMA^+$ and $TBA^+$-form PFSI membranes to further explore the possibility of thermal ordering of the aggregated counterions. Figure IX-7 shows SAXS profiles of $TMA^+$-Nafion® (a) and $TBA^+$-Nafion® (b) subjected to thermal annealing at 150 °C and 200 °C for 10 min and then cooled to room temperature prior to SAXS experiment. The insets in Figure IX-7 also show 2-dimensional SAXS patterns comparing before (left) and after (right) thermal annealing at 200 °C, for each countetrion form. A diffuse and broad scattering halo of maximum intensity at ca. $q = 2$ $nm^{-1}$ can be observed for both $TMA^+$ and $TBA^+$ PFSI membranes and is attributed to scattering from the ionic aggregates dispersed in the ionomer matrix. While ssNMR probes directly how counterions (thus, strictly ionic domains) behave under the thermal stimulation, SAXS offer the ability to characterize phase homogeneity of the ionic and hydrophobic domains by comparing the relative sharpness of the ionomer peak. As $TBA^+$-Nafion® (Figure IX-7b) is annealed at 150 °C for 10 min, the ionomer peak shifts slightly to higher $q$ with a relatively constant peak width. Annealing at even higher temperature, 200 °C (beyond the α-relaxation temperature of $TBA^+$-form) does not seem to modify the SAXS profile significantly, except for the low $q$ region that is influenced by changes in the crystalline order of the PTFE segments of the ionomer.[1,34] For $TMA^+$-Nafion® (Figure IX-7a), annealing at 150 °C for 10 min also causes the ionomer peak to shift to higher $q$ as observed in $TBA^+$-form Nafion®. However, thermal annealing at 200 °C induces a profound change in the scattering pattern. The diffuse scattering ring observed for the as-received (low temperature) state is transformed into a very distinct scattering ring with a much narrower peak width (Table IX-2). A greatly reduced width in the ionomer peak after thermal annealing simply means that the distribution of the ionic domain separations became narrower most likely due to the improved counterion packing order within the ionic domains. It is

postulated that some of the ionic clusters become more well-ordered ones by losing loosely held interfacial ions from the aggregates or by incorporating lone ion-pairs into a bigger ionic aggregates.

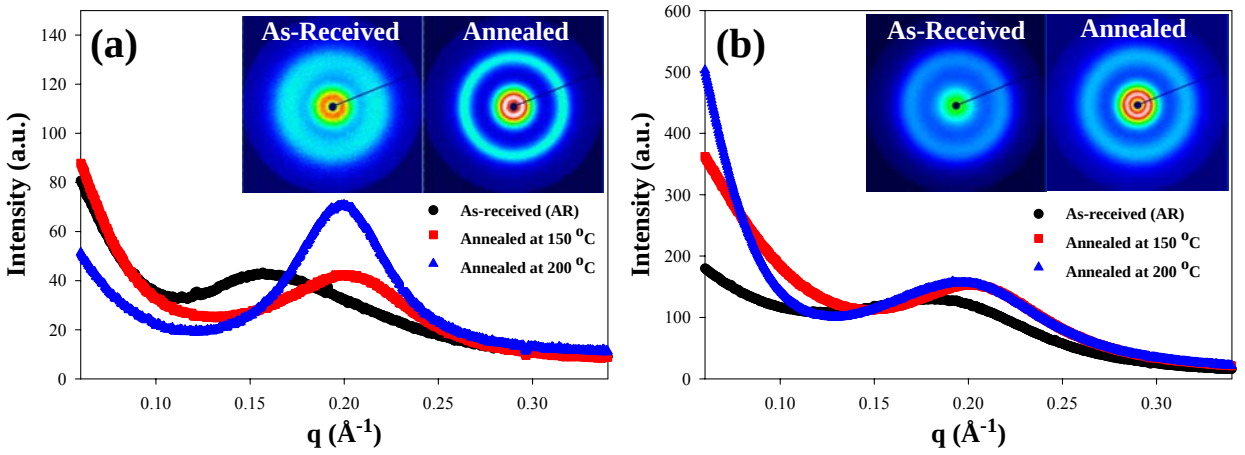


**Figure IX-7**. Small angle X-ray scattering (SAXS) profiles of $TMA^+$ (a) and $TBA^+$-Nafion (b) subjected to thermal annealing at 100 and 200 °C for 10 min. Each plot contains two-dimensional SAXS images before (left) and after (right) thermal annealing at 200 °C .

**Table IX-2**. Full width at half maximum (FWHM) of the ionomer peaks for $TMA^+$-, and $TBA^+$-form Nafion®

| *Temperature* | *$TMA^+$–PFSI* | *$TBA^+$–PFSI* |
|---|---|---|
| 24 ˚C | 0.0876 | 0.0853 |
| 150 ˚C | 0.0754 | 0.0765 |
| 200 ˚C | 0.0571 | 0.0826 |

Our observation is also in line with the previous ionomer annealing studies carried out by other groups utilizing ssNMR experiments. O'Connell *et al.* employed $^{23}Na$ ssNMR to investigate $Na^+$ neutralized sulfonated polystyrene ionomers under thermal stimulation.[35] They

observed that the center of the gravity of $Na^+$ peaks had shifted to upfield from about -17 ppm to -23 ppm at thermal treatment at 160 $^oC$ for 24 hr. They attributed this shift to a thermally-induced ordering of $Na^+$ ions in ionic aggregation domain, most likely by the loss of loosely held interfacial ions from the aggregates. Nosaka *et al.* have focused on $^1H$ NMR signals of water confined in the PFSIs as a function of annealing temperatures.[36] Interestingly, the initially observed broad $^1H$ NMR spectra at 297K were strongly affected by the thermal annealing at 358K,which lead to a decreased line width to about one-third of that of the sample before the thermal annealing. Based on this observation, they suggested that thermal annealing provided an increased homogeneity in the chemical environments of water molecules. These NMR studies demonstrate that thermal annealing can have a significant effect on the state of ionic aggregation in Nafion®, and our SAXS results confirm that depending on counterion type, the morphological changes can apparently involve short and long-range ordering in the ionic domains. This interesting phenomenon will be the subject of future studies.

Based on the clear ordering effect observed in the SAXS data of Figure IX-7a and the supporting NMR experimental data carried out by other groups on the related compounds, we thus attribute the abnormal $T_1$ behavior of the ionomer peak observed in the $TMA^+$-form PFSI samples to a thermally induced ordering in the packing of $TMA^+$ ions in ionic domains of the PFSIs. The small $TMA^+$ ions would be suitable for producing efficiently packed ionic multiplets due to their compact size and rigid structure, and much stronger electrostatic interactions between ion pairs.[37] One may need more experimental evidences to understand the detailed mechanism why the $TMA^+$-form PFSI system shows thermal ordering effect under an elevated temperature. We hypothesize that the strongly associated nature of $TMA^+$-PFSI system makes rotational tumbling or translational hopping movements of $TMA^+$ ions unfavorable. Instead,

smaller $TMA^+$ ions may fill up gaps occurring when the polymeric matrices undergo thermally induced movements, resulting in the reinforcement of the integrity of the electrostatically aggregated states between cationic $TMA^+$ ions and anionic PFSI ionomers. Then, a $TMA^+$ ion confined more tightly in an electrostatically aggregated domain under elevated temperature would end up with a longer spin-lattice relaxation time. This may also explain why the α-relaxation temperature of the $TMA^+$-form PFSI system is much higher than those from $TEA^+$-, $TPA^+$- and $TBA^+$-form PFSIs. Reorganization of the ionic domains toward the increased order by incorporating the $TMA^+$ ions may give us a clue to design/process the novel membrane with high performance, such as proton conductivity, water diffusion, and fuel cell performance. Indeed, we have observed greatly improved fuel cell performance based on the thermally-stimulated $TMA^+$-Nafion® and these results will be published in the near future.

## D. Conclusions

Variable temperature $^1H$ and $^{13}C$ SSNMR spectroscopy has been incorporated to study the thermally induced transitions of PFSI ionomers neutralized by tetraalkylammonium ions by observing $T_1$ relaxation times and CSAs of methyl or methylene groups in tetraalkylammonium ions. For PFSIs neutralized to contain bulkier $TPA^+$- and $TBA^+$-counterions, thermally induced ionic tumbling behaviors were observed at temperatures above the α-relaxation temperature, indicating the occurrence of a significant destabilization in the electrostatic network between sulfonyl groups and alkylammonium ions.[17] According to our simulations, the molecular tumbling motions of alkylammonium ions observed in $TPA^+$- and $TBA^+$-form PFSI complexes correspond to tetrahedral jumping with rate constants $\kappa \approx 1$ kHz. Interestingly, the $TMA^+$-form

PFSI system demonstrated a dramatic increase in the $^{1}H$ $T_1$-relaxation time of the methyl groups in $TMA^+$ ions over the temperature range we employed, indicating that a type of thermally induced ordering effect is present even before the α-relaxation temperature. A similar type of thermally induced, molecular ordering effect had been observed in $^{19}F$ $T_1$ relaxation times, regardless of the position of $^{19}F$ nuclei in the main- or side-chains, measured over temperature ranges 25-250 ˚C.[12] The effects of thermal stimulation were also investigated with SAXS techniques. Depending on the type of counterions used to neutralized the PFSIs, SAXS profiles were significantly modified after thermal annealing at elevated temperatures. For example, FWHM of the ionomer peak for $TMA^+$-Nafion® clearly narrowed after thermal stimulation at 200 $^{o}$C while that of $TBA^+$-Nafion® ionomer peak remained relatively unchanged. Significant narrowing of the ionomer peak is another evidence of increased order within the ionic domains.

## E. Acknowledgements

The authors wish to acknowledge support for this work provided by the National Science Foundation, (CMMI-0707364, and CBET-0756439). The small-angle X-ray scattering experiments at PAL were supported in part by the Ministry of Science and Technology of Korea and Pohang Steel Co.

## F. References


(1) Mauritz, K. A.; Moore, R. B. *Chem. Rev.* **2004**, *104*, 4535-4585.
(2) Gierke, T. D.; Munn, G. E.; Wilson, F. C. *J. Polym. Sci. Polym. Phys. Ed.* **1981**, *19*, 1687-1704.
(3) Fujimura, M.; Hashimoto, T.; Kawai, H. *Macromolecules* **1982**, *15*, 136-144.
(4) Dreyfus, B.; Gebel, G.; Aldebert, P.; Pineri, M.; Escoubes, M.; Thomas, M. *Journal de Physique, France* **1990**, *51*, 1341-1354.
(5) Rubatat, L.; Rollet, A. L.; Gebel, G.; Diat, O. *Macromolecules* **2002**, *35*, 4050-4055.
(6) Kim, M.-H.; Glinka, C. J.; Grot, S. A.; Grot, W. G. *Macromolecules* **2006**, *39*, 4775-4787.
(7) Schmidt-Rohr, K.; Chen, Q. *Nat. Mater.* **2008**, *7*, 75-83.
(8) Moore, R. B.; Cable, K. M.; Croley, T. L. *J. Membrane Sci.* **1992**, *75*, 7.
(9) Eisenberg, A.; Hird, B.; Moore, R. B. *Macromolecules* **1990**, *23*, 4098-4107.
(10) Page, K. A.; Cable, K. M.; Moore, R. B. *Macromolecules* **2005**, *38*, 6472-6484.
(11) Page, K. A.; Landis, F. A.; Phillips, A. K.; Moore, R. B. *Macromolecules* **2006**, *39*, 3939-3946.
(12) Page, K. A.; Jarrett, W.; Moore, R. B. *J. Polym. Sci. Part B: Polym. Phys.* **2007**, *45*, 2177-2186.
(13) Phillips, A. K.; Moore, R. B. *J. Polym. Sci. Part B: Polym. Phys.* **2006**, *44*, 2267-2277.
(14) Spiess, H. W. *J. Chem. Phys.* **1980**, *72*, 6755-6762.
(15) Spiess, H. W. *Adv. Polym. Sci.* **1985**, *66*, 23-58.
(16) Schmidt, C.; Wefing, S.; Blümich, B.; Spiess, H. W. *Chem. Phys. Lett.* **1986**, *130*, 84-90.
(17) Pschorn, U.; Rössler, E.; Sillescu, H.; Kaufmann, S.; Schaefer, D.; Spiess, H. W. *Macromolecules* **1991**, *24*, 398-402.
(18) Schmidt-Rohr, K.; Kulik, A. S.; Beckham, H. W.; Ohlemacher, U.; Pawelzik, U.; Boeffel, C.; Spiess, H. W. *Macromolecules* **1994**, *27*, 4733-4745.
(19) Schmidt-Rohr, K.; Spiess, H. W. *Multidimensional Solid-State NMR and Polymers*; Academic Press: San Diego, 1994.
(20) Kimmig, M.; Strobel, G.; Stuhn, B. *Macromolecules* **1994**, *27*, 2481-2495.
(21) Chen, Q.; Schmidt-Rohr, K. *Macromol. Chem. Phys.* **2007**, *208*, 2189-2203.
(22) Holsteina, P.; Schelerb, U.; Harris, R. K. *Polymer* **1998**, 4937-4941
(23) Harris, R. K. *Nuclear Magnetic Resonance Spectroscopy*; Pitman, 1983.
(24) van Rossum, B.-J.; de Groot, C. P.; Ladizhansky, V.; Vega, S.; de Groot, H. J. M. *J. Am. Chem. Soc.* **2000**, *122*, 3465-3472.
(25) Ladizhansky, V.; Vega, S. *J. Chem. Phys.* **2000**, *112*, 7158-7168.
(26) Fung, B. M.; Khitrin, A. K.; Ermolaev, K. *J. Magn. Reson.* **2000**, *142*, 97–101.
(27) McConnell, H. M. *J. Chem. Phys.* **1958**, *28*, 430-431.
(28) In NMR spectroscopy, m. j. o. h. m. r. a. r. m. o. m. w. r. t. t. e. m. f.
(29) Mehring, M. *High Resolution NMR in Solids*; Springer-Verlag: Berlin, 1983.
(30) Schurko, R. W.; Wi, S.; Frydman, L. *J. Phys. Chem. A* **2002**, *106*, 51-62.
(31) Bloch, F. *Phys. Rev.* **1946**, *70*, 460-474.
(32) Spiess, H. W. *Dynamic NMR Spectroscopy*; Springer-Verlag: Berlin, 1978.
(33) Abragam, A. *Principles of Nuclear Magnetism*; Oxford University Press: New York, 1961.
(34) Rubatat, L.; Rollet, A. L.; Gebel, G.; Diat, O. *Macromolecules* **2002**, *35*, 4050 - 4055.
(35) O'Connell, E. M.; Root, T. W.; Cooper, S. L. *Macromolecules* **1995**, *28*, 4000-4006.
(36) Nosak, A. Y.; Watanabe, S.; Toyoda, I.; Nosaka, Y. *Macromolecules* **2006**, *39*, 4425-4427.
(37) Eisenverg, A.; Kim, J.-S. *Introduction to Ionomers*; Wiley-Interscience: New York, 1998.

# CHAPTER X

# FUTURE WORK: EVIDENCE OF LOCAL ORDERING OF COUNTERION IN PERFLUOROSULFONATE IONOMERS

## A. Introduction

The perfluorosulfonate ionomers (PFSIs), (e.g., Nafion®) are currently the benchmark material for proton exchange membrane fuel cells (PEMFCs) due to their excellent chemical and thermal stability, as well as permselective ion transport abilities.[1-3] Nafion® consists of a polytetrafluoethylene (PTFE) backbone and perfluorovinylether side chains terminated with sulfonic acid functionalities. Nafion® is currently available from E.I. du Pont de Nemours and Company and has the following structure: [2]

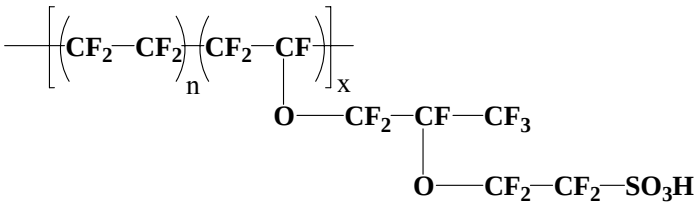


Due to the difference in polarity between the non-polar PTFE matrix and polar ionic moieties, the hydrophilic ionic groups are separated from hydrophobic PTFE matrix to form ionic domains (or ionic clusters).[2] With electron differences between the ionic domains and the PTFE matrix, a scattering maximum appears in small-angle X-ray scattering (SAXS) profiles at ca. $q$ = 0.2 Å$^{-1}$, which has been termed the "ionomer peak".[2] Along with the ionic clusters are the crystalline domains involving runs of PTFE segments between side chains, which have unit cell dimensions virtually identical to that of pure PTFE.[4]

To date, numerous structural models have been proposed, mainly based on small-angle X-ray and neutron scattering studies to accurately describe Nafion®'s complex, phase-separated morphology.[2,3] Hsu and Gierke suggested swollen inverse micelles of roughly spherical geometry that are connected by nanoscale hydrophilic channels concurrent with the unique transport properties exhibited by PFSIs.[5] In addition to the early work of Hsu and Gierke, the most common ones include the core-shell model by Fujimura et al. [6], the local order model by Dreyfus et al. [7], the rod-like aggregate model by Rubatat and coworkers [8], the fringed-micelle model by Kim et al. [9], and most recently, parallel cylindrical water channel model by Schmidt-Rohr [3]. Although each model differs significantly in the shape and order of ionic domains, they all recognize the presence of ionic aggregates that are dispersed throughout the PTFE matrix.

While ionic clusters, and specifically their size, shape, spatial distribution and connectivity in PFSIs have received a significant research attention, arrangement of ions inside the ionic clusters is the topic which has not been fully investigated. In this chapter, we present preliminary results of the differential scanning calorimetry (DSC), wide- and small-angle X-ray scattering behavior of alkylammonium ion neutralized Nafion® membranes, which indicated the existence of structural ordering within the ionic clusters for alkylammonium-neutralized Nafion® membranes.

## B. Experimental

***Materials.*** The perfluorosulfonate ionomer, Nafion® 117CS membrane (1100g / equivalent, 7 mil thickness) was purchased from E.I. Dupont de Nemours & Company and cleaned by refluxing in aqueous 8M nitric acid for 2 hr, and then in deionized (DI) water for 1 hr. These PFSI membranes were then completely neutralized to contain tetramethylammonium

($TMA^+$), tetraethylammonium ($TEA^+$), tetrapropylammonium ($TPA^+$), and tetrabutylammonium ($TBA^+$) counterions by soaking the $H^+$-form membranes in excess (ca. 5×) methanolic or aqueous solution of the appropriate alkylammonium hydroxide. The neutralized membranes were thoroughly rinsed of excess alkylammonium hydroxide and dried in a vacuum oven at 70 °C for 12 hr.

***Differential Scanning Calorimetry (DSC)***. DSC data were collected using a TA differential scanning calorimeter (DSC 2000). $TMA^+$-, $TEA^+$-, $TPA^+$-, and $TBA^+$-form Nafion® membranes were dried at 70 $^oC$ under vacuum for 12 hr prior to thermal analysis. All samples (ca. 10 mg) were scanned at a rate of 20 $^oC$/min under $N_2$ purge.

***Wide-angle X-ray Diffraction (WAXD)***. WAXD experiment was performed on the Gemini diffractometer system from Oxford Diffraction equipped with a two-dimensional position sensitive area detector. A sealed tube source was used to produce the Cu Kα radiation (λ=1.54 Å) with sample-to-detector distance of 55 cm. Scattering patterns were corrected for background scattering and integrated using the GADDS software package.

***Small-angle X-ray Scattering (SAXS).*** Synchrotron small-angle X-ray scattering (SAXS) experiments were performed at Station 4C1 of the Pohang Accelerator Laboratory (PAL) (Pohang, Korea). The incident X-ray beam was tuned to a wavelength of 1.30 Å and the sample-to-detector distance was 1075 mm. The two dimensional scattering images were recorded using a Mar CCD camera with 30 sec exposure time. The relationship between pixel and the momentum transfer vector $q$ was determined by calibrating the scattering data with a silver behenate standard. All scattering intensities were corrected for transmission, incident beam flux, and background scatter due to air and Kapton windows. The $TMA^+$ and $TBA^+$-form membranes

were annealed at 150 and 200 $^{o}$C for 10 min and then cooled to room temperature prior to SAXS experiments.

## C. Results and Discussion

Previous DSC studies of as-received $Na^{+}$- or $Cs^{+}$-form Nafion® membranes showed a broad endotherm in the initial scan between 200 and 250 $^{o}$C.[10] After melt-quenching from 330 $^{o}$C, this endotherm disappeared upon rescan and thus was attributed to the melting of PTFE-like crystallite in PFSIs. Figure X-1 shows the DSC thermograms of various tetraalkylammonium ion-neutralized Nafion® 117CS. In an agreement with the previous DSC studies with as-received $Na^{+}$- or $Cs^{+}$-form Nafion® membranes, tetramethylammonium ($TMA^{+}$) neutralized Nafion® shows one broad, asymmetric endotherm between 200 and 260 $^{o}$C. However, we observe that with an increase in the size of counterion, this endotherm shifts systematically to lower temperature. Quite interestingly, the temperature at which the endotherm is observed for each counterion is closely related to the previously observed α-relaxation temperature (Table X-1). To investigate the origin of this endotherm, $TMA^{+}$-form Nafion® was heated up to 330 $^{o}$C, held for 5 min to eliminate the crystalline component and then quickly quenched to room temperature. Small-angle X-ray scattering (SAXS) evidently confirmed a complete melting of PTFE-like crystallites by examining the intercrystalline peak typically observed at ca. 0.05 $Å^{-1}$ in the as-received state (data now shown). Upon rescan, the endotherm centered at ca. 257 $^{o}$C still remains but now narrower in its width. To examine the effects of isothermal annealing, melt-quenched samples were subjected to isothermal crystallization at 200 $^{o}$C for various time frames and their DSC thermograms are shown in Figure X-2. Isothermal crystallization for 5 min induces a small peak at around 200 $^{o}$C. This peak grows in its intensity and shifts to higher temperature under extended periods of time. Thus, undoubtedly, this melting endotherm is

attributed to the existence of PTFE-like crystals in the sample. Then, the other melting endotherm which remains even after quenching from 330 °C and is essentially insensitive to isothermal annealing at 200 °C can likely be linked to the presence of ordered counterion packing within the ionic clusters.

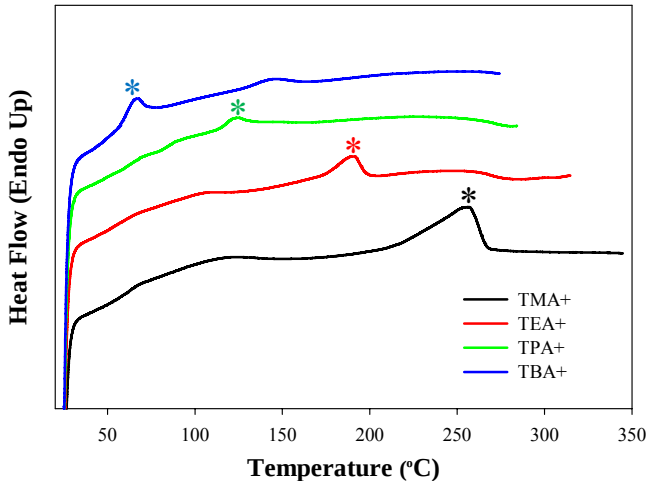


**Figure X-1**. DSC thermograms of tetramethylammonium ($TMA^+$), tetraethylammonium ($TEA^+$), tetrapropylammonium ($TPA^+$), and tetrabutylammonium ($TBA^+$) neutralized Nafion® 117CS. All membranes were dried at 70 °C under vacuum for 12 hr. Thermograms are shifted along the y-axis for comparison (1st scan with 20 °C /min)

**Table X-1**. Transition temperatures measured by DSC, DMA, and SAXS for $TMA^+$, $TEA^+$, $TPA^+$, and $TBA^+$ Nafion®

| | *$TMA^+$–PFSI* | *$TEA^+$–PFSI* | *$TPA^+$–PFSI* | *$TBA^+$–PFSI* |
|---|---|---|---|---|
| *DSC* | 257 | 187 | 123 | 66 |
| *[a]DMA* | 240 | 160 | 130 | 100 |
| *[b]SAXS* | 240-260 | 165-185 | 120-130 | 80-100 |

[a,b] Transition temperatures attributed to α-relaxation where significant destabilization of the electrostatic network may be observed and thus results in the activation of a *dynamic* network facilitated through the ion-hopping process

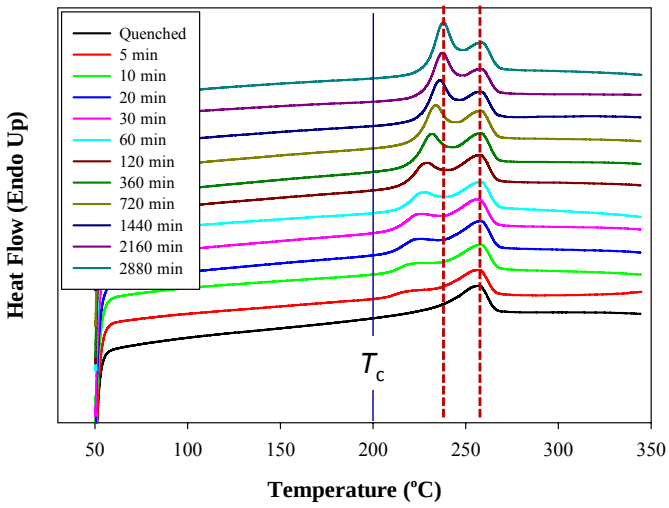


**Figure X-2**. DSC thermograms of $TMA^+$-form Nafion® 117CS. Samples were isothermally crystallized at 200 °C for various times after melt-quenching from 330 °C. Thermograms are shifted along the y-axis for comparison. (scanning rate: 20 °C /min)

To further explore the effects of thermal annealing on endotherms observed in tetraalkylammonium ion-neutralized Nafion®, vacuum-dried, as-received samples were subjected to simple annealing at various temperatures, immediate quenching to room temperature and rescanning at 20 °C/min. Annealing temperatures were selected in a way that covers above, near and below the α-relaxation temperature for each counterion form. Figure X-3a shows DSC thermograms of $TMA^+$-form Nafion® 117CS that were scanned from 25 to 340 °C directly after annealing at temperatures ranging from 175 to 275 °C. Samples annealed below 250 °C show two endotherms, one that is the low temperature endotherm and observed to occur at ca. 20-30 °C above the respective annealing temperature and the other (i.e., the high temperature endotherm centered at 257 °C) which remains reasonably constant. In an agreement with the study by Page et al., we attribute the low temperature endotherm which is sensitive to annealing temperatures to melting of PTFE-like crystallites.[10] Interestingly, annealing at 250 °C leads to a very narrow endotherm peak centered at 264 °C. Annealing at even higher temperature, 275 °C, shows single endotherm which looks similar to the one observed after melt-quenching from 330

$^{o}$C. This is most likely because annealing at 275 $^{o}$C leads to melting of the PTFE-like crystallites and thus the observed single endotherm should be attributed to the melting of ordered counterions within the ionic clusters. Figure X-3b shows DSC thermograms of $TEA^{+}$-form Nafion® 117CS that were scanned from 25 to 290 $^{o}$C directly after annealing at temperatures ranging from 125 to 225 $^{o}$C. Essentially, $TEA^{+}$-form membranes behaves in a similar manner as for $TMA^{+}$-form samples. It should be pointed out that annealing near the temperature at which the endotherm is observed narrows the peak width in $TMA^{+}$ and $TEA^{+}$ samples, which means greatly improved counterion packing orders. Figure X-3c and d show DSC thermograms of $TPA^{+}$-(annealing temperature ranging from 125 to 225 $^{o}$C), and $TBA^{+}$ (annealing temperature ranging from 75 to 200 $^{o}$C)-form Nafion® membranes, respectively. Unlike $TMA^{+}$-and $TEA^{+}$-form membranes, annealing of $TPA^{+}$-and $TBA^{+}$-form membranes does not induce any crystallization of PTFE-like crystallite, nor show endotherms which we attributed to the melting of ordered counterion within ionic clusters. While it needs further studies to explain this behavior, it is possible that bulky counterions may experience a difficulty in packing into a well-ordered structure within the ionic domains. On the contrary, relatively small ions such as $TMA^{+}$ and $TEA^{+}$ can be treated as small hard spheres and thus can be accommodated into a well-ordered structure within an ionic domain.

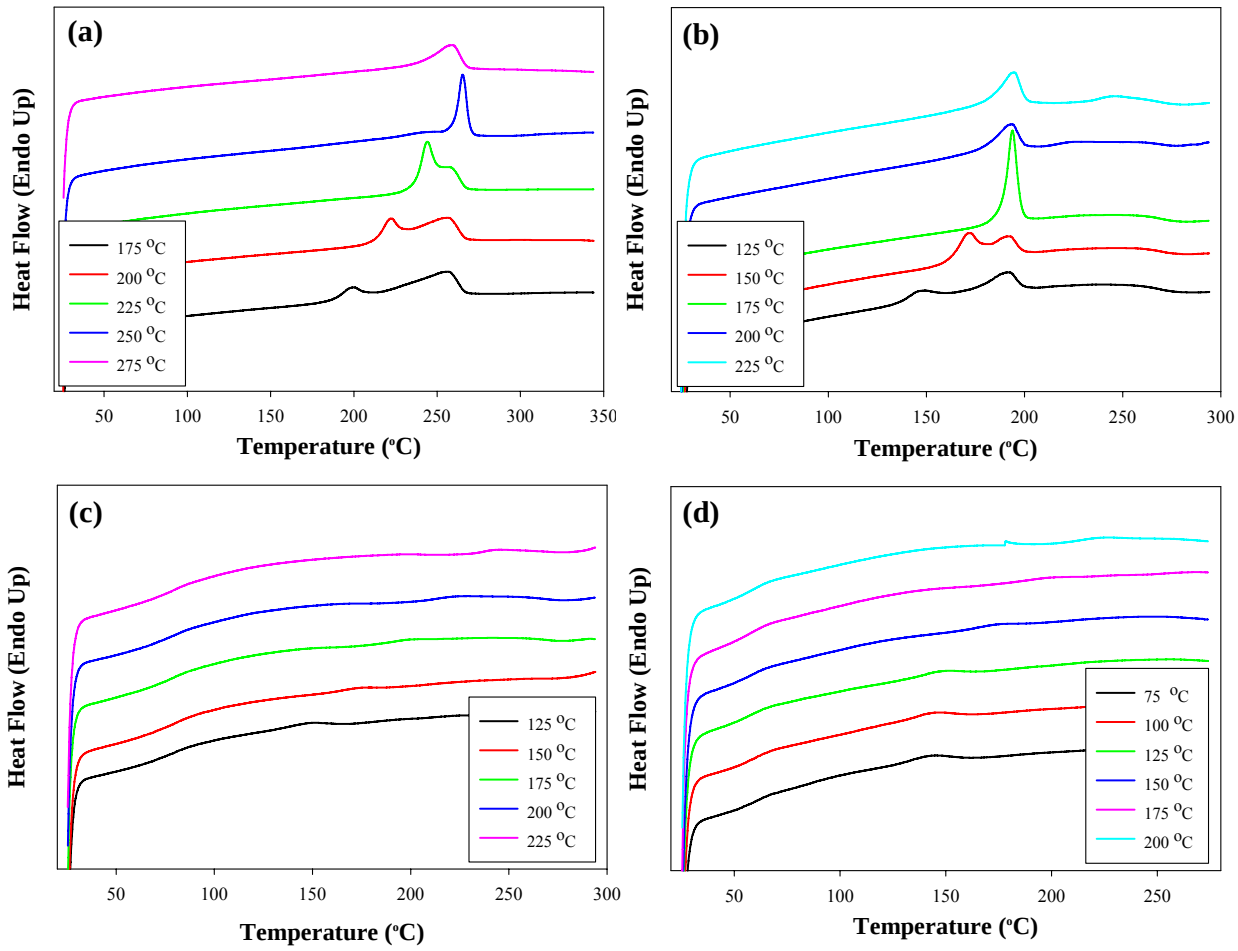


**Figure X-3**. DSC thermograms of vacuum-dried, as-received Nafion® 117CS neutralized to contain $TMA^+$(a), $TEA^+$ (b), $TEA^+$ (c), and $TBA^+$ (d). Each membrane was annealed at various temperatures for 30 min.

Additional support for local ordering of counterions inside the ionic clusters comes from wide-angle X-ray diffraction on tetraalkylammonium ion-neutralized Nafion®. Figure X-4 shows WAXD scattering curves obtained for $H^+$-, $TMA^+$-, $TEA^+$-, $TPA^+$- and $TBA^+$-form Nafion® 117CS membranes. For the $H^+$-form membrane, two peaks can be observed, where the inner peak is attributed to the weak reflection of PTFE-like crystallite, $hkl$ = 100 at $2\theta = 18^o$, which is superimposed as a shoulder on a broad amorphous halo. The outer peak centered at $2\theta$

= 39° is attributed to the PTFE crystalline reflection *hkl* = 101. For the $TMA^+$-form, it is observed that on the low angle ($2\theta$) side of the amorphous halo there is the presence of a shoulder, which systematically shifts to lower angle with an increase in counterion size. For $TBA^+$-form, there is a presence of a distinct maximum. Although not shown here, this maximum is also seen for the larger counterion (i.e., tetrahexylammonium through tetradecylammonium ions) and shifts to lower angle as the counterion size increases. Very interestingly, the same type of X-ray scattering behavior was observed in different polymer systems, such as n-alkyl acrylate polymer (n-PA)[11], n-alkyl methacrylate polymers (n-PMA)[11], and poly(di-n-alkyl itaconate)s[12]. For example, Arrighi et al. investigated the poly(di-n-alkyl itaconate)s with various alkyl chain length (n = 1-5, 8, and 10) and observed the "extra" peak which shifts systematically with side-chain length.[12]

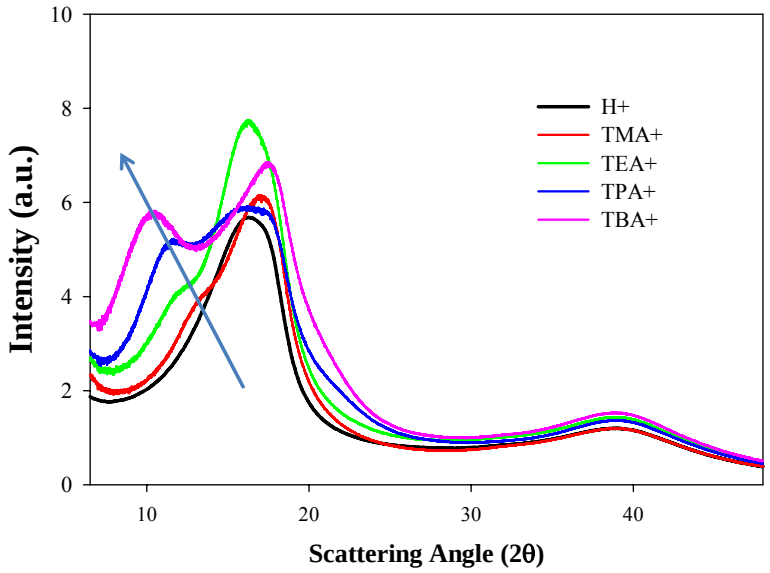


**Figure X-4**. WAXD scattering curves of vacuum dried, as-received $H^+$-, $TMA^+$-, $TEA^+$-, $TPA^+$- and $TBA^+$-form Nafion® 117CS membranes

To investigate the effects of thermal annealing on the new peak showing up for tetraalkylammonium ion-neutralized Nafion® in WAXD profiles, membranes were annealed at

various temperatures for 10 min. Acquired WAXD curves are shown in Figure X-5 for $TMA^+$-(a), $TEA^+$-(b), $TPA^+$-(c) and $TBA^+$-(d) form membranes. It is immediately noticeable that for $TMA^+$-, and $TEA^+$-form Nafion®, the extra new peaks are sensitive to thermal annealing and becomes more pronounced (i.e., an increase in packing order) with an increase in annealing temperatures. Furthermore, for $TMA^+$-form, an additional sharp peak appeared at $2\theta = 17.5^o$ after annealing at high temperature. On the contrary, the extra new peaks in $TPA^+$-, and $TBA^+$-form Nafion® fairly remain unaffected during thermal annealing and does now show any sign of improved packing ordering.

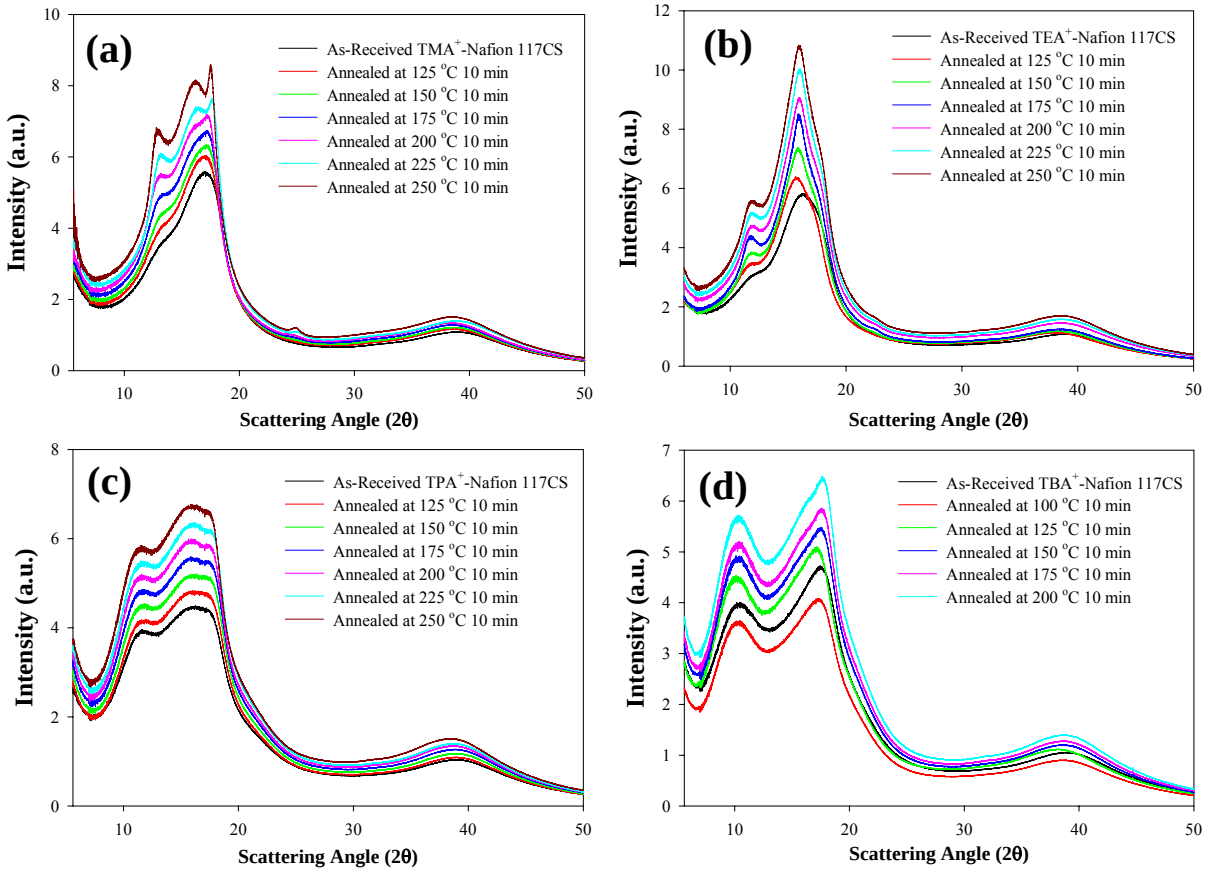


**Figure X-5.** WAXD scattering curves of $TMA^+$-(a), $TEA^+$-(b), $TPA^+$-(c) and $TBA^+$-(d) form Nafion® 117CS membranes annealed at various temperature for 10 min and then quenched to room temperature before data acquisition.

While DSC and WAXD methods allowed us to investigate short range order of counterions inside the ionic clusters, SAXS can offer the ability to characterize phase homogeneity of the ionic and hydrophobic domains by comparing the relative sharpness of the ionomer peak. As $TBA^+$-Nafion® (Figure X-6b) is annealed at 150 °C for 10 min, the ionomer peak shifts slightly to higher *q* with a relatively constant peak width. Annealing at even higher temperature, 200 °C (beyond the α-relaxation temperature of $TBA^+$-form) does not seem to modify the SAXS profile significantly, except for the low *q* region that is influenced by changes in the crystalline order of the PTFE segments of the ionomer.[13,14] For $TMA^+$-Nafion® (Figure X-6a), annealing at 150 °C for 10 min also causes the ionomer peak to shift to higher *q* as observed in $TBA^+$-form Nafion®. However, thermal annealing at 200 °C induces a profound change in the scattering pattern. The diffuse scattering ring observed for the as-received (low temperature) state is transformed into a very distinct scattering ring with a much narrower peak width. A greatly reduced width in the ionomer peak after thermal annealing simply means that the distribution of the ionic domain separations became narrower most likely due to the improved counterion packing order within the ionic domains. Depending on counterion type, the SAXS results along with DSC and WAXD clearly indicate that the morphological changes can apparently involve short and long-range ordering in the ionic domains. Reorganization of the ionic domains toward the increased order by incorporating the $TMA^+$ ions may give us a clue to design/process the novel membrane with high performance, such as proton conductivity, water diffusion, and fuel cell performance.

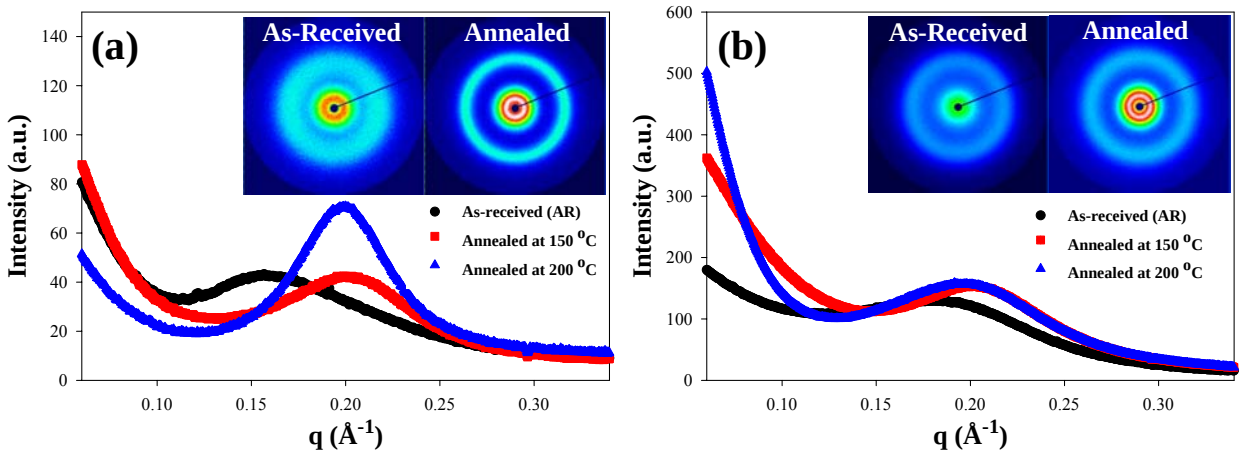


**Figure X-6.** Small angle X-ray scattering (SAXS) profiles of $TMA^+$ (a) and $TBA^+$-Nafion (b) subjected to thermal annealing at 100 and 200 °C for 10 min. Each plot contains two-dimensional SAXS images before (left) and after (right) thermal annealing at 200 °C.

## D. Conclusions

In this work, we observed an evidence of local ordering of counterions inside the ionic clusters. DSC thermograms of $TMA^+$-, $TEA^+$-, $TPA^+$- and $TBA^+$- form membranes showed a endotherm which shifts systematically to lower temperature with an increase in the counterion size. Furthermore, the temperature at which this endotherm is observed is closely related to the α-relaxation temperature proved by DMA and SAXS methods. Very interestingly, short range orders are significantly improved for small ions ($TMA^+$, and $TEA^+$) but not for bulky ions ($TPA^+$ and $TBA^+$) under thermal annealing and thus membranes processing using organic ions offers the ability to control electrostatic interactions that govern morphological development. Further research is needed to investigate whether or not structural ordering within the ionic domains leads to significantly improvements in polymer electrolyte membrane fuel cell (PEMFC) performance. Because the morphological changes are quite different depending on counterion type, various processing protocols such as uniaxial/biaxial orientation, solution-processing, and

melt-processing need to be also explored as a function of counterion type to fully understand this interesting phenomenon.

## E. Acknowledgements

The authors wish to acknowledge support for this work provided by the National Science Foundation, (CMMI-0707364, and CBET-0756439). The small-angle X ray scattering experiments at PAL were supported in part by the Ministry of Science and Technology of Korea and Pohang Steel Co.

## F. References

(1) Doyle, M.; Rajendran, G. In *Handbook of Fuel Cells-Fundamentals, Technology and Applications*; Wielstich, W., Lamm, A., Gasteiger, H. A., Eds.; John Wiley & Sons: Chichester, 2003; Vol. 3; pp 351-395.
(2) Mauritz, K. A.; Moore, R. B. *Chem. Rev.* **2004**, *104*, 4535-4585.
(3) Schmidt-Rohr, K.; Chen, Q. *Nat. Mater.* **2008**, *7*, 75-83.
(4) Starkweather, H. W. *Macromolecules* **1982**, *15*, 320-323.
(5) Gierke, T. D.; Munn, G. E.; Wilson, F. C. *J. Polym. Sci. Polym. Phys. Ed.* **1981**, *19*, 1687-1704.
(6) Fujimura, M.; Hashimoto, T.; Kawai, H. *Macromolecules* **1982**, *15*, 136-144.
(7) Dreyfus, B.; Gebel, G.; Aldebert, P.; Pineri, M.; Escoubes, M.; Thomas, M. *Journal de Physique, France* **1990**, *51*, 1341-1354.
(8) Rubatat, L.; Rollet, A. L.; Gebel, G.; Diat, O. *Macromolecules* **2002**, *35*, 4050-4055.
(9) Kim, M.-H.; Glinka, C. J.; Grot, S. A.; Grot, W. G. *Macromolecules* **2006**, *39*, 4775-4787.
(10) Page, K. A.; Cable, K. M.; Moore, R. B. *Macromolecules* **2005**, *38*, 6472-6484.
(11) Miller, R. L.; Boyer, R. F. *J. Polym. Sci. Part B: Polym. Phys.* **1984**, *22*, 2021-2041.
(12) Arrighi, V.; Triolo, A.; McEwen, I. J.; Holmes, P.; Triolo, R.; Amentisch, H. *Macromolecules* **2000**, *33*, 4989-4991.
(13) Mauritz, K. A.; Moore, R. B. *Chem. Rev.* **2004**, *104*, 4535-4585.
(14) Rubatat, L.; Rollet, A. L.; Gebel, G.; Diat, O. *Macromolecules* **2002**, *35*, 4050 - 4055.